UNIVERSITY OF
NEWCASTLE UPON TYNE

UNIVERSITY OF
NEWCASTLE

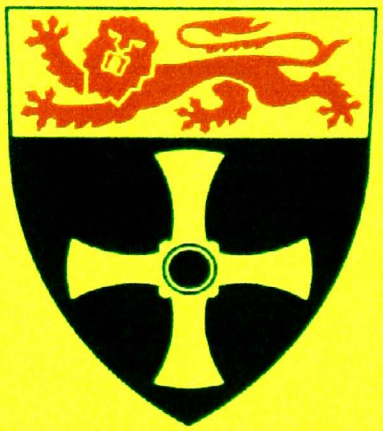

Energy Based Models to Determine Fracture Toughness of Thin Coated Systems by Nanoindentation

Jinju Chen

A thesis submitted for the Degree of
Doctor of Philosophy

July 2006

Declaration

This thesis records work carried out in School of Chemical Engineering and Advanced Materials at the University of Newcastle upon Tyne between October 2003 and July 2006 under the supervision of Prof. Steve. J. Bull. All the work is original except where reference has been made to the work of others.

No part of this work has been or is currently being submitted for any other degree, diploma or other qualification at any other University.

Several sections of this work have been already published (or are in press) in different journals, these papers are summarised below, along the relevant chapters from which they are drawn.

1. *Assessment of the toughness of thin coatings using nanoindentation under displacement control*, **J. Chen** and S.J. Bull, Thin Solid Films. **494** (2006) 1-7. (Chapter 5)

2. *A critical examination of the relationship between plastic deformation zone size and Young's modulus to hardness ratio in indentation testing*, **J. Chen** and S. J. Bull, Journal of Materials Research. **21** (2006) 2617-2627. (part of this paper is in Chapter 3)

3. *A new method based on the work-displacement curve to asses the toughness of coated systems*, **J. Chen** and S. J. Bull, Mat. Res. Soc. Symp. Proc. **890** (2006) Y0202 (Chapter 5)

4. *On the relationship between plastic deformation zone radius and maximum depth during nanoindentation*, **J. Chen** and S. J. Bull, Surf. Coat & Technol., (2006), in press (part of this paper is in Chapter 3)

5. *An energy based model to estimate coating toughness in the case that there is no excursion in the load-displacement curve*, **Jinju Chen** and S. J. Bull , Proc. Int. Conf. Materials Science and Technology (MS&T) 2006: Fundamentals and Characterization: Vol.**2**, 61-70, (Chapter 7)

6. *Assessment of the adhesion of ceramic coatings*, **Jinju Chen** and S.J. Bull, 11th International Ceramics Congress Advanced in Science and Technology. **45** (2006) 1299-1308, Trans Tech Publications Ltd, Switzerland (Chapter 8)

7. *A modified model to determine the limiting values of coating toughness by nanoindentation*, **J. Chen** and S.J. Bull, **submitted** to Wear, 2005, in the Proceedings of the 4th International Colloquium Micro-Tribology 2005, Karwica, Poland. (Chapter 6)

8. *Assessment of the nanoindentation response of brittle coated systems by analysing the loading curves*, **J. Chen** and S.J. Bull, ***submitted*** to Zeitschrift fur Metallkunde, 2005 (Chapter 9)

Acknowledgements

I would like to express my sincere thanks to all of the people who helped me during the course of this project in the last three years. I am in particularly indebted to the following people:

My supervisor, Prof. Steve Bull, for sharing his invaluable knowledge and experience; and for offering me the best support and encouragement during this work. Great thanks for his patience with my endless questions and giving me much opportunity to learn new things! Also, his kindness and friendship, whenever I met a problem, he was always ready to help.

All the colleagues and staff in the Advanced Materials Group for providing a friendly atmosphere. A special thanks to Jose for being my colleague at work, who is like an elder brother. Prof. White, Thompson, Dr.Charles, Siller, Kath, Isabel, Paul for their kindness.

The University of Newcastle Upon Tyne and Overseas Research Students Award Scheme (ORSAS) for financial support for this project.

Pilkington Technology Centre for providing the multilayer optical coatings on float glass samples.

Other respectful friends such as Lance,Viv, Zygmunt, especially for Lance. Some former colleagues and respectful friends in China, Prof. Jin, Yin, Xie, Su, Dr. Tao, Zhou, Zhu, and Mr. Guo, Cheng, Miss Lu, Zhu for their kindness and friendship, in particular for Prof. Jin who always provides encouragement.

My family, especially my grandparents, for their never-ending support.

Abstract

This project aims to determine the fracture toughness of thin coated systems by nanoindentation. The development of techniques for the assessment of coating toughness lags behind the determination of Young's modulus and hardness of thin coatings. No universal model or technique has been agreed to estimate coating toughness. With the development of complex coating stacks (e.g. multilayered coated systems) and the presence of variable crack patterns, the difficulty of generating a solution by stress analysis based models is dramatically increased. Therefore, there is an urgent need for the development of models to deal with complex coatings and varied cracking patterns. The most successful models in this respect are energy-based.

In this thesis the existing models and techniques to assess coating toughness and adhesion have been critically reviewed. The stress analysis based models usually require empirical fitting parameters and they only deal with specific crack patterns. In contrast, the energy based models can deal with different cracking patterns without empirical constants; but they usually require that the crack propagates during loading cycle only, whilst, stress analysis based models do not have such a restriction.

Several new models have been developed to assess coating toughness in this work. Two of them are based on excursions in load–displacement (P-δ) curves resulting from fracture during nanoindentation. The first model (W_t-dp method) is based on extrapolating the plot of total work during indentation versus displacement. Compared to a literature model based on extrapolating P-δ curve, this approach removes the influence on fracture dissipated energy from plastic deformation of the substrate. The second is a modified model to estimate the limiting value of coating toughness which could equally give the upper and lower boundary for toughness from nanoindentation performed under load control and displacement control, thus improving on the initial boundary model by *Toonder et al* which could only provide an upper boundary of coating toughness for nanoindentation under displacement control. However, it is often observed that fracture does not result in an excursion in the P-δ curve, which requires a different modelling approach. The third model (W_{irr}-W_p model) developed addresses this problem. All the previous models address through-thickness fracture which is widely observed in nanoindentation testing of hard coatings. In addition, another energy based method is

proposed to estimate the adhesion of coatings by analysing the extra linear recovery of unloading curve associated with the rebound of the coating during unloading.

Models were validated by experiments carried out by a range of nanoindentation techniques. The low load tests were performed by a Hysitron Triboindenter fitted with a sharp cube corner tip and a Berkovich tip. The maximum penetration was in the range of 40~400nm. Higher load tests were performed using a Nanoindenter II ™ fitted with a Berkovich tip in the range of 10mN~500mN. Atomic force microscopy (AFM), high-resolution scanning electron microscopy (SEM) and reflected light microscopy have been employed to investigate the fracture behaviour.

To examine the models developed in this work, two different coated systems were investigated: one is multilayer optical coatings (total thickness <500nm) including ITO, SnO_2, ZnO, and TiO_xN_y on glass, which is the case of harder coating on hard (but relatively softer) substrate and they are the main samples investigated in this project; the other is a 1μm fullerene-like CN_x coating on various ceramic substrates such as SiC, Si, and Al_2O_3, which is the case of hard (but relatively softer) coating on a harder substrate. Some common brittle bulk materials (e.g. Si) were also tested to examine the applicability of the models. Reasonable toughness values for both coated systems and bulk materials have been obtained by the new models developed in this work.

To gain more insight into the fracture mechanisms of coated systems, the threshold of fracture is also an important issue to be addressed. The loading rate may influence the critical load for fracture in brittle materials. It was observed that within the penetration rate range used in this study (10~40nm/s) the higher the penetration rate the higher was the threshold for cracking in the optical multilayer coatings on glass indented by a cube corner tip. When analysing the P-δ curves at different loading rates, significantly different behaviour was observed for ITO and SnO_2 coatings which is possibly due to a pressure-induced phase transformation in these coatings.

List of Abbreviations

A	Area
A_c	Contact area
A_{fra}	Fracture area
A_{int}	Area of interfacial failure
AE	Acoustic Emission
AFM	Atomic Force Microscopy
BEI	Backscattered Electron Imaging
c	Crack length
C_R	Crack radius of delamination or chipping
C-AFM	Contact Mode Atomic Force Microscopy
CIM	Conventional Indentation Method
CL	Cathodoluminiscence
COD	Crack Opening Displacement
CRIT	Continuous Recording Indentation Technique
CRT	Cathode-Ray-Tube
CSM	Continuous Stiffness Measurement
DCB	Double Cantilever Beam
ECP	Electron Channelling Pattern
EDX	Energy Dispersive X-Ray Analysis
E	Young's modulus
E_c	Young's modulus of the coating
E_i	Young's modulus of the indenter
E_{int}	Young's modulus of interface
E_s	Young's modulus of the substrate
E_r	Reduced Modulus
FEM	Finite Element Method
FIP	Fracture initiation point
G_{IC}	Energy release rate for mode I cracking
G_{int}	Energy release rate for interfacial failure
H	Hardness
ISE	Indentation Size Effect
ITO	Indium doped tin oxide
L_c	Critical load in scratch test
K_{IC}	Toughness for mode I cracking
K_{int}	Interface toughness
K_{exp}	Experimental slope of P-δ^2
Ld-dp	Load-displacement method
LEFM	Linear elastic fracture mechanics
LFM	Lateral Force Microscopy
NC-AFM	Non-Contact Mode Atomic Force Microscopy
P_m	Maximum load
P-δ	Load-displacement
PVD	Physical Vapour Deposition
$\%R$	% Elastic recovery
RID	Relative Indentation Depth

RLM	Reflected Light Microscopy
RT	Room temperature
S	Contact stiffness
S_l	Slope of loading curve
S_u	Slope of unloading curve
SACP	Selected Area Channelling Pattern
SEI	Secondary Electron Image
SEM	Scanning Electron Microscopy
SEAM	Scanning Electron Acoustic Microscopy
TEM	Transmission Electronic Microscopy
t	Coating thickness
V_i	Indentation volume
W_e	Elastic work of indentation
W_t-dp	Total work –displacement method
W_{irr}	Irreversible work
W_{irr}-W_p	Irreversible work-plastic work method
W_p	Plastic work of indentation
W_t	Total work of indentation
δ_c	Contact depth
δ_e	Elastic depth
δ_m	Maximum depth
δ_r	Residual depth
ν	Poisson ratio
ν_i	Poisson ratio of the indenter
θ	Half-included indenter angle
σ	Stress
σ_B	Buckling stress
σ_r	Residual stress
β	The angle that crack propagate along the thickness
s	Crack spacing

Table of Contents

Chapter 1:

Introduction

Chapter 1: Introduction

1.1. Introduction and objectives

Multilayer coated systems (e.g. solar control coatings on glass which consist of a selective absorbing layer, antireflection layers and barrier layers) are widely used in industrial applications. Whatever the application, the coating lifetime which is controlled by the mechanical properties of the coated system, is a key issue that industry needs to address. In many cases, the life-limiting failure modes are produced during handling or by contact damage in service. Therefore, it is necessary to analyse and understand the mechanical response of these coating/substrate systems in a range of contact conditions.

The work in this thesis was motivated by the challenges in the development of the latest generation of solar control coatings for architectural glass. Current coatings show low transmission in the infrared (almost down to the theoretical limit) but tend to fail due to mechanical damage or the effects of environmental exposure. Therefore, it is very important to understand the mechanical behaviour of the coatings.

In the last 2 decades, nanoindentation techniques have been widely applied to investigate the mechanical properties of bulk materials and coatings at sub-micron scale or even at nanoscale [(Oliver and Pharr, 1992),(Page et al., 1992),(Page and Hainsworth, 1993),(Tuck et al., 2001, Bull, 2005),(Malzbender et al., 2002)]. With regard to the determination of hardness and elastic modulus of the coatings, there are many well-established techniques and models available [e.g.(Korsunsky et al., 1998),(Korsunsky and Constantinescui, 2006),(Bull, 2001)] . In contrast, the determination of the coating toughness from nanoindentation is less well-developed. However, it is crucial to understand the fracture behaviour (such as fracture

toughness, fracture initiation) of hard coatings in particular in the case of thin hard films. For solar control coatings, fracture produces very visible damage which is unacceptable to users and thus improving fracture resistance properties is a key part of coating development. Some models (stress based models and energy based models) and techniques [e.g. (Li et al., 1997),(Malzbender and de With, 2000),(den Toonder et al., 2002)] have been advanced to assess coating toughness. However, these have been developed in a range of systems and as the coatings are becoming more complex (such as multilayer stacks) and the coatings are becoming very thin (tens of nanometeres or less) the suitability of the existing methods is questionable. There is thus a great challenge in the assessment of coating toughness and interfacial toughness, which this work aims to address.

The work in this thesis is aimed at further understanding the fracture mechanisms of coated systems during nanoindentation. Thus different aspects have been investigated such as how to analyse the effect of different crack patterns, and how the loading rate influences the fracture behaviour. The coated systems investigated here include the main components of solar control coatings on glass as well as CN_x coatings on various hard substrates (e.g. SiC). These two coated systems have several applications in industry which brings them into the scope of this work. For example, the former coatings are applied to architectural glass for their optical properties and the latter have a good tribological property which enables their use as protective layer for hard disk drives. Further, these two sets of materials are representative of different coated systems. The former set is a harder coating on hard (but relatively softer) substrate, whilst, the other is a hard coating on harder substrate. Both of them are brittle. In addition, some common brittle bulk materials (such as Si, Ge, SiC) have been investigated to validate the models developed in this study.

In order to investigate the fracture behaviour at different scales, low load nanoindentation tests(<5mN) by a Hysitron Triboindenetr fitted with a sharp cube corner tip and high load nanoindentation tests (up to 500mN) by Nanoindenter II fitted with a Berkovich tip were performed. Although, many indenter geometries are available such as spherical, conical, Berkovich, Vickers, Cube corner and North star etc, the cube corner tip is commercially available and is very suitable for fracture

assessment at low load because it could significantly reduce the threshold for fracture compared to the more common Berkovich indenter (e.g.(Pharr, 1998),(Harding et al., 1995)) which is why it was selected to investigate fracture at low loads where less plastic deformation of the substrate occurs.

1.2. Motivation

In solar control coatings on glass, transit scratches are observed during the delivery of the glass from the coating plant to the assembler of double glazing units. (Fig.1.1). transit scratches are caused by the sliding of polymer intervelant balls over the surface during transit. High tensile stresses generated at the trailing edge of an essentially Hertzian elastic contact generate through-thickness cracks which can divert along the interface; these cracks do not tend to propagate into the glass substrate. Thus the coating toughness and interface toughness are key parameters dictating coating performance.

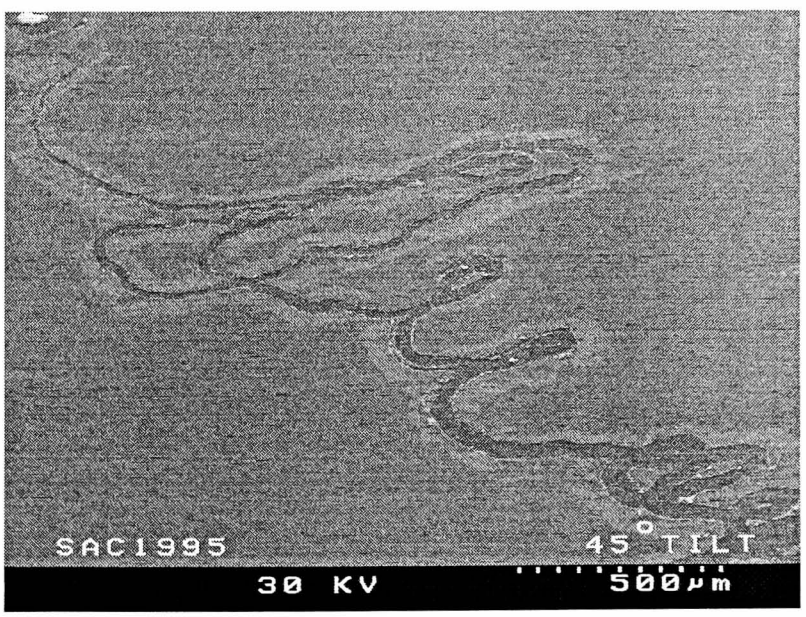

Figure 1.1. SEM image of a transit failure in solar control coatings on glass.

What is more, if current mechanical performance models (e.g. the Bull model [(Bull et al., 2004),(G-Berasategui et al., 2004)]) which are based on energy dissipation) used to predict the hardness and Young's modulus of the complex coated systems are to be improved, it is necessary to understand the fracture behaviour and include the effect of cracks in the model.

The motivation for the development of new models to assess coating toughness in this study is that the conventional indentation models (e.g.(Anstis et al., 1981)) and the existing energy based models [e.g. (Li and Bhushan, 1998), (Malzbender et al., 2000)] do not work well with the very thin coatings used for optical or computer hard disk applications in this study.

In this thesis, different models have been developed to assess coating toughness based on observations of different types of fracture. Also, the fracture initiation point is discussed together with the influence of loading rate on the fracture behaviour.

1.3. Structure of this thesis

The body of this thesis is split into the following 4 parts.

I. Introducing and analysing the problems.

The literature review is mainly covered by chapters 2 to 4. Chapter 2 introduces the problems of fracture assessment by indentation and critically reviews the existing models and techniques for the assessment of coating toughness. Chapter 3 explains why nanoindentation techniques are powerful tools and introduces their application to coating mechanical property assessment. Chapter 4 describes the experimental tools used for solving the problems. A complete review for all existing literature in this field is beyond the scope of this thesis and the literature review is concentrated on the most representative methods and techniques.

II. Energy based models

Chapters 5 to 8 introduce new models to assess the coating toughness and adhesion measurement. Chapter 5 presents an energy based model to assess coating toughness in the case of the fracture resulting in an excursion in the load-displacement curve. Chapter 6 presents a new boundary model to estimate the upper and lower limit of coating toughness, which also requires an excursion in the load-displacement curve. Chapter 7 proposes a model to deal with the situation that the fracture does not cause any excursion in load-displacement curve. Chapter 8 outlines a method to assess adhesion based on extra elastic linear recovery in unloading curve. The results obtained by various methods are compared.

III. Loading rate influence on fracture mechanisms

Chapter 9 explores the possible mechanisms to account for rate-dependent fracture behaviour and highlights this behaviour in SnO_2 and ITO coatings.

IV. Conclusions and further work

In Chapter 10, some conclusions about the toughness results for various coatings are drawn and some brief comments about the suitability of the models developed in this study are made. To generate further understanding and insight into fracture mechanisms, further work regarding both experimental techniques and modelling is suggested.

Reference:

Anstis, G. R., Chantikul, P., Lawn, B. R. and Marshall, D. B. (1981) A Critical-Evaluation of Indentation Techniques for Measuring Fracture-Toughness .1. Direct Crack Measurements,*Journal of the American Ceramic Society,* **64,** 533-538.

Bull, S. J. (2001) Modelling the hardness response of bulk materials, single and multilayer coatings,*Thin Solid Films,* **398,** 291-298.

Bull, S. J., Berasetegui, E. G. and Page, T. F. (2004) Modelling of the indentation response of coatings and surface treatments,*Wear,* **256,** 857-866.

Bull, S. J. (2005) Nano-indentation of coatings,*Journal of Physics D-Applied Physics,* **38,** R393-R413.

den Toonder, J., Malzbender, H., de With, G. and Balkenende, R. (2002) Fracture toughness and adhesion energy of sol-gel coatings on glass,*Journal of Materials Research,* **17,** 224-233.

G-Berasategui, E., Bull, S. J. and Page, T. F. (2004) Mechanical modelling of multilayer optical coatings,*Thin Solid Films,* **447,** 26-32.

Harding, D. S., Oliver, W. C. and Pharr, G. M. (1995) "Cracking During Nanoindentation and Its Use in the Measurement of Fracture Toughness",*Materials Research Society Symposium Proceedings* **356,** pp. 663-668.

Korsunsky, A. M., McGurk, M. R., Bull, S. J. and Page, T. F. (1998) On the hardness of coated systems,*Surface & Coatings Technology,* **99,** 171-183.

Korsunsky, A. M. and Constantinescui, A. (2006) Work of indentation approach to the analysis of hardness and modulus of thin coatings,*Materials Science and Engineering a-Structural Materials Properties Microstructure and Processing,* **423,** 28-35.

Li, X. D., Diao, D. F. and Bhushan, B. (1997) Fracture mechanisms of thin amorphous carbon films in nanoindentation,*Acta Materialia,* **45,** 4453-4461.

Li, X. D. and Bhushan, B. (1998) Measurement of fracture toughness of ultra-thin amorphous carbon films,*Thin Solid Films,* **315,** 214-221.

Malzbender, J. and de With, G. (2000) Energy dissipation, fracture toughness and the indentation load-displacement curve of coated materials,*Surface & Coatings Technology,* **135,** 60-68.

Malzbender, J., de With, G. and den Toonder, J. M. J. (2000) Elastic modulus, indentation pressure and fracture toughness of hybrid coatings on glass,*Thin Solid Films,* **366,** 139-149.

Malzbender, J., den Toonder, J. M. J., Balkenende, A. R. and de With, G. (2002) Measuring mechanical properties of coatings: a methodology applied to nano-particle-filled sol-gel coatings on glass,*Materials Science & Engineering R-Reports,* **36,** 47-103.

Oliver, W. C. and Pharr, G. M. (1992) An Improved Technique for Determining Hardness and Elastic Modulus Using Load and Displacement Sensing Indentation Experiments,*Journal of Materials Research,* **7,** 1564-1583.

Page, T. F., Oliver, W. C. and McHargue, C. J. (1992) The Deformation-Behavior of Ceramic Crystals Subjected to Very Low Load (Nano)Indentations,*Journal of Materials Research,* **7,** 450-473.

Page, T. F. and Hainsworth, S. V. (1993) Using Nanoindentation Techniques for the Characterization of Coated Systems - a Critique,*Surface & Coatings Technology,* **61,** 201-208.

Pharr, G. M. (1998) Measurement of mechanical properties by ultra-low load indentation,*Materials Science and Engineering a-Structural Materials Properties Microstructure and Processing,* **253,** 151-159.

Tuck, J. R., Korsunsky, A. M., Bhat, D. G. and Bull, S. J. (2001) Indentation hardness evaluation of cathodic are deposited thin hard coatings,*Surface & Coatings Technology,* **139,** 63-74.

Chapter 2:

Assessment of fracture toughness of coated materials by nanoindentation

Chapter 2: Assessment of fracture toughness of coated materials by nanoindentation

2.1. Introduction

For Bulk brittle materials and sufficiently thick brittle coatings, the indentation methods to measure the toughness have been well-established [(Lawn et al., 1980), (Anstis et al., 1981)]. However, due to limitations of their thickness, complex composition and structure, it is tricky to find a universal method to measure the fracture toughness of thin films. Many efforts have been made to address this. This chapter will summarize and compare these methods so that the optimised methods could be selected according to the actual coated systems and testing conditions required. Due to the advantage of simplicity and economy in testing, indentation (nanoindentation) techniques have been widely used to assess coating toughness. The existing models used to estimate the coating toughness can be divided mainly into two catalogues, i.e. stress analysis based models and energy based models. With the development of new coated systems and different demands for the mechanical properties of coated systems, the adhesion between the coating and substrate is also an important issue to be addressed. Therefore, the main approaches to measure adhesion such as the pull-off test, bending test, bulge test, superlayer test, and scratch and indentation tests are also reviewed with the emphasis on indentation.

2.2. Models and techniques to assess the indentation fracture toughness of coating

In the indentation testing of brittle bulk materials there are five major types of cracks depending on the load, material, environment conditions and indenter (Cook and Pharr, 1990), which are summarized in the following:

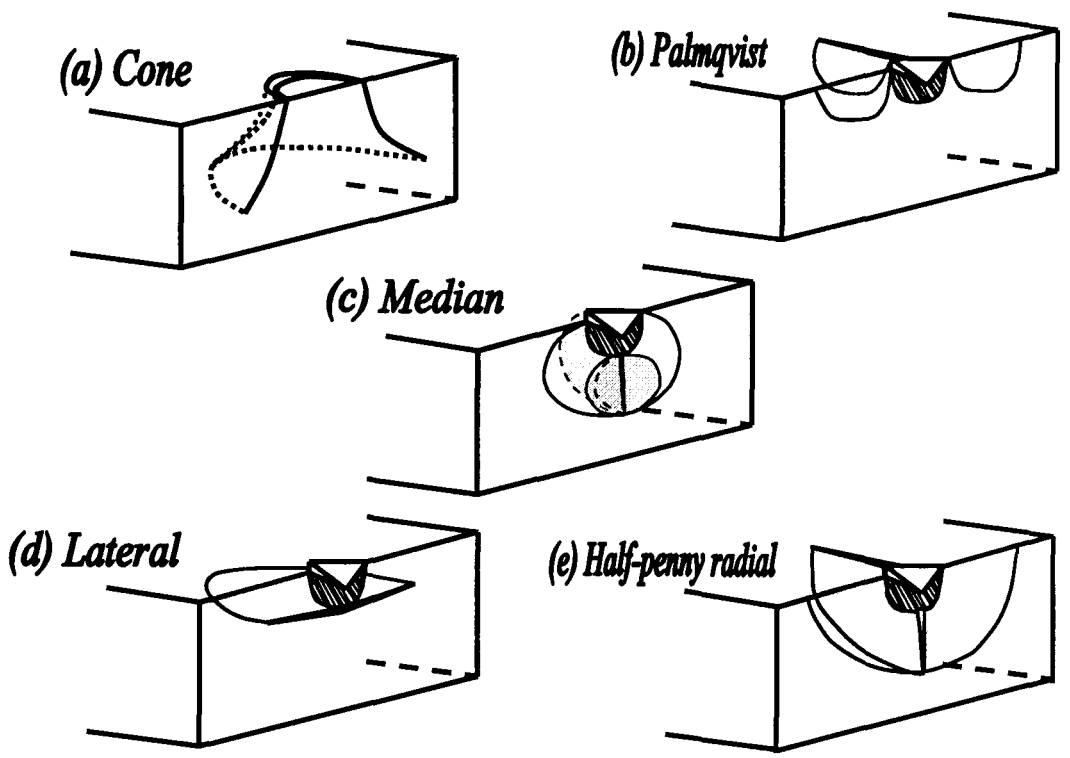

a) **Cone Cracks**: typically generated by flat punch indenters or spherical ones. Related only to the elastic deformation, they initiate in a ring crack because of the high tensile stresses near the edge of the contact. With increasing load, the maximum tensile stresses distribute around a cone producing a cone crack.

b) **Palmqvist cracks**: related to the plastic deformation of the material when indented with sharp indenters or blunt indenters at high loads, beyond the Hertzian regime. They are created parallel to the axis of the load starting from the edge of the plastic impression left by the indenter, which are driven by tensile hoop stress. These usually occur in the materials which are much tougher than glass.

c) **Median cracks**: also propagate parallel to the axis of the load but are created beneath the plastic deformation zone due to the wedging action of a conical or pyramidal indenter.

d) **Lateral cracks**: are also created beneath the plastic deformation zone and propagate initially almost parallel to the surface of the material before turning upwards to the surface and forming a chip. They usually originate during the unloading cycle (for most ceramics), although for some glasses they also appear during the loading cycle.

e) **Half Penny cracks**: This type of crack may be formed on unloading starting from a radial crack running downwards or a median crack running upwards or a mixture between the two of them.

2.2.1. Stress analysis based models

2.2.1.1 Half–penny like radial crack

Experimental observations found that the toughness K_{Ic} of indented materials was proportional to applied load P multiplied by crack length, c, raised to the power of -1.5, in the case of well-developed radial/median crack system (half-penny like cracking) caused by indentation. Combining stress analysis based on the model of the analogous expanding spherical cavity problem and simplistic dimensional analysis, Lawn et al (Lawn et al., 1980) developed the following expression to assess the toughness of ceramics and glass,

$$K_{Ic} = \chi P / c^{3/2} = \xi_v^R (E/H)^m P / c^{3/2} \qquad (2.1)$$

where ξ_v^R is a calibration coefficient which depends on indenter geometry and crack pattern; the exponent m is usually treated as ½, and E and H are Young's modulus and hardness, respectively. For well developed radial cracking produced by a Vickers or Berkovich indenter, ξ_v^R =0.016±0.004 (Anstis et al., 1981). There is a considerable uncertainty (±25%) in the constant itself, leading to an inherent uncertainty in the calculated toughness. For median cracking, the coefficient ξ_v^R will be lower for bulk materials (Lawn et al., 1980) and coatings as well (Malzbender et al., 2000) which indicates that median cracking tends to occur at higher loads. This was observed by Cook and Pharr (Cook and Pharr, 1990). With the decrease of indenter semi-angle (θ), ξ_v^R increases since it is proportional to $(\cot\theta)^{2/3}$ which was derived based on the expanding cavity model by (Lawn et al., 1980) and was verified by indentation in different brittle materials (Jang et al., 2004). Such geometry dependent phenomena

have been verified in different tip angles in the range of 35.3 ° to 75 ° (Jang et al., 2004).

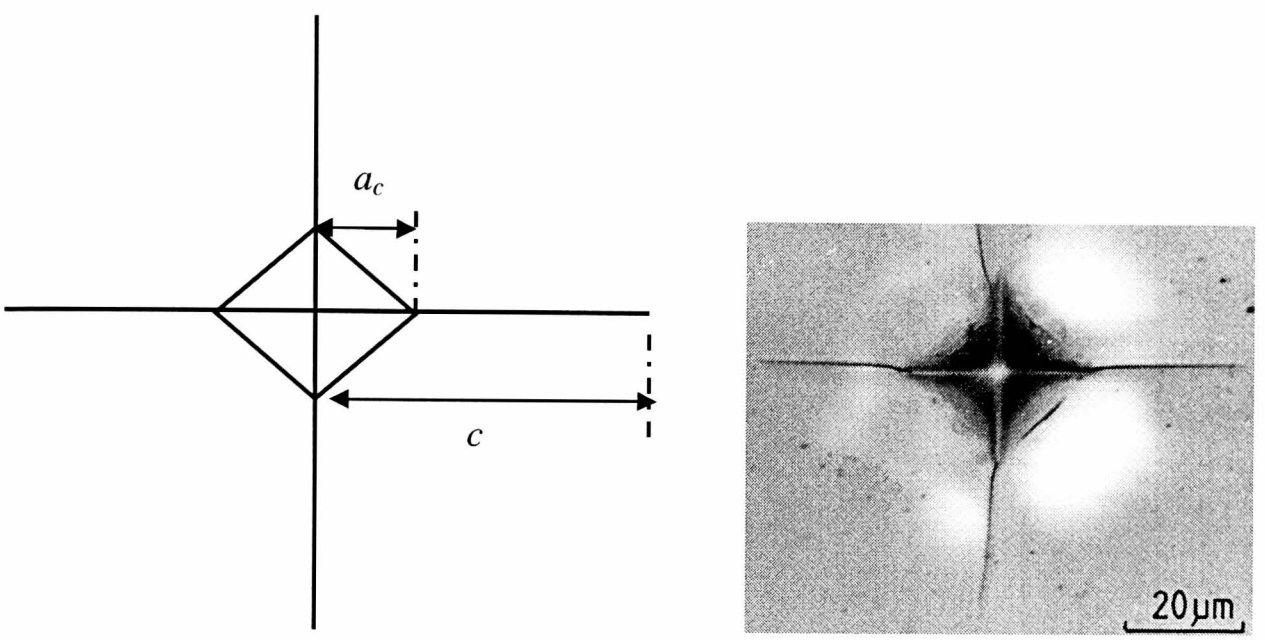

(a) (b)

Fig. 2.1. (a) Schematic of well developed radial cracking caused by indentation with a Vickers indenter, (b) radial crack in glass.

E and H can be easily measured by nanoindentation and crack length c can be determined by SEM, AFM or reflected light microscopy. The simplicity and reliability of this method leads to its convenience of application and thus it becomes a common method for bulk materials indented at high loads. However, it requires the crack to be sufficiently developed (i.e. $c >> 2a_c$, where a_c is the contact impression radius as depicted in Fig. 2.1) which accordingly requires a high load. For thin films, high loads lead to large penetration which may result in plastic deformation in the substrate. In such cases, the initial residual stress field to drive the fracture may be disturbed by the interface and substrate so that the fracture shape will also change. This reduces the reliability of the conventional indentation method.

Harding et al (Harding et al., 1995) found that the threshold for cracking could be dramatically lowered by using a sharper tip such as a cube corner tip. At a fixed load, the cube corner tip deforms a greater volume of material than a Berkovich indenter (by more than 3 times) which leads to much higher stress intensity. It was suggested that a cube corner indenter could reduce the critical load for fracture by more than 10 times for most brittle materials (Pharr, 1998). In addition to the advantage of reducing the critical load, at the same penetration the more confined plastic deformation compared to a Berkovich indenter is also a merit of a cube corner tip which could eliminate the influence from the substrate (Stein, 2005), (Chen and Bull, 2006b). Therefore, it is preferable to use a cube corner tip when assessing the toughness of thin films [e.g.(Harding et al., 1995) , (Pharr, 1998), (Li et al., 1997), (Chen and Bull, 2006c)]. However, different researchers reported different values of the coefficient ξ_v^R for a cube corner tip in Eq.(2.1). If it is assumed that ξ_v^R is related to tip angle (θ) only ($\xi_V^R = \xi_r^R(\cot\theta)^{\frac{2}{3}}$, where ξ_r^R is a constant), it can be expected to have a value of 0.0335; however, 0.0319 (Pharr et al., 1993), 0.032 (Li and Anderson, 2004), 0.036(Harding et al., 1995), 0.04 (Pharr, 1998), and 0.0535 (Scharf et al., 1997) have been reported as different values for the constant.

The different materials tested by different authors are a very important factor in this. As analysed by Anstis et al (Anstis et al., 1981) and Lawn et al (Lawn et al., 1980), Eq.(2.1) did not take account of pile-up and sink-in. For many ceramics the relatively high *H/E* leads to sink-in during nanoindentation, while, pile-up tends to occur in materials with low *H/E*. If the materials display the conventional plasticity, the pile-up may generate at high stress concentrators at slip steps even if the *H/E* is not very low. Both pile-up and sink-in will disturb the cracking dimensions and shape; also they may influence the residual stress field. The different magnitude of sink-in and pile-up between different materials may thus cause the variations from Eq.(2.1) as well. Another possible reason is that the flaw size and distribution may vary significantly with different materials and surface treatments. When the indenter becomes sharper, individual defects may play a vital role in the fracture mechanism. In addition, when indenting hard materials a sharp tip is much easier to wear or even be broken which is a very important issue if performing indentations by a cube corner tip.

Although some problems exist, Eq.(2.1) has still been widely used to estimate the fracture toughness of relatively thick coatings (>10μm). Due to the mismatch between the coatings and their substrates and the different coating processes used, it is inevitable that pre-existing residual stress will occur which has not been considered in Eq. (2.1). This residual stress may be small compared to indentation stress but it becomes significant for systems with big thermal expansion mismatch in coating and substrate deposited at high temperature. In order to solve this problem, a modified expression considering residual stress (can be pre-existing surface stress in bulk materials or residual stress in coatings) has been suggested [(Marshall and Lawn, 1977), (Malzbender and de With, 2000c), (Emiliani, 1993)],

$$K_c = \xi_v^R (E/H)^{1/2} P/c^{3/2} + 2\sigma(c/\pi)^{1/2} \tag{2.2}$$

However, it should be noted that the constant π is crack geometry dependent and corresponds to well-developed half-penny crack. It can be expected that both the stress field and crack shape will be disturbed by the substrate. Malzbender et al (Malzbender and de With, 2000c) argued that the radial cracks are mainly confined to the surface of coating so that the influence of substrate on stress field can be ignored. Such an assumption seems to be reasonable for their relatively thick coatings (2μm and 4 μm in thickness in (Malzbender and de With, 2000c) tested at low load). Plotting $\xi_v^R (E/H)^{1/2} P/c^{3/2}$ versus $2(c/\pi)^{1/2}$ both toughness (the intercept with the ordinate axis) and residual stress (the slope) can be obtained. When the substrate effect becomes more important, a shape factor initially defined by Broek (Broek, 1997) can be introduced to account for crack shape modification. Therefore, Eq. (2.2) can be modified as,

$$K_c = \xi_v^R (E/H)^{1/2} P/c^{3/2} + Z\sigma c^{1/2} \tag{2.3}$$

$$Z = 1.12\sqrt{\pi}\,\frac{d/c}{(3\pi/8) + (\pi/8)(d/c)^2} \tag{2.4}$$

Where d is the depth of the radial crack. Although it is difficult to accurately measure the crack depth, den Toonder et al (den Toonder et al., 2002) argued that the fracture

toughness can be obtained without the knowledge of Z and Z is only important when determining the residual stress.

Eq.(2.2) works well for a coating with significant residual stress compared to its toughness such as organic-inorganic hybrid coatings with thickness of more than 3μm on glass (Malzbender et al., 2000) and SiO_2- filled methyltrimethoxysilane coatings with thickness of more than 2μm on glass (Malzbender and de With, 2000c). Otherwise, the scatter in data for $\xi_v^R (E/H)^{1/2} P/c^{3/2}$ and $2(c/\pi)^{1/2}$ leads to Eq. (2.3) losing its merit. In addition, it needs to be pointed out that the sol-gel coatings on float glass are a case of hard coatings on a much harder substrate and there is no reason to believe that models will equally apply to systems with different material combinations. With harder coatings on a softer substrate (e.g. harder ceramics on glass, ceramics on metal or polymer), plastic deformation of the substrate may occur during the propagation or even initiation of a radial crack in the coating and an additional bending stress will be imposed on coating which totally changes the initial fracture mechanism which Eqs.(2.1) to (2.3) rely on. The mismatch between coatings and substrate will also influence the stress field when it propagates into the interface region.

Furthermore, when the coating thickness decreases, well-developed radial cracking may not be observed (e.g. for 400nm Solar control coatings on glass in (Chen and Bull, 2006c); 500nm SiO_2 filled methyltrimethoxysilane coatings on glass in (Malzbender and de With, 2000c). In such cases, the usefulness of the above equations will be in doubt. For example, Laugier (Laugier, 1987) and Nihara (Nihara et al., 1982) reported that the linear relation between K_{Ic} and $P/c^{3/2}$ stopped when $c<2.5a_c$. However, Jang et al (Jang et al., 2004) argued that such a scaling relationship is still maintained even for small crack in Si (100). Aslo, Scholz et al (Scholz et al., 2004) found that such a scaling relationship remained even when the radial crack length was down to $1.1a_c$ for typical ceramics such as fused silica, sapphire etc.

For a radial crack confined within the contact region, Tanaka et al (Tanaka, 1984) argued that the coefficient in Eq. (2.1) should be bigger if the crack was not sufficiently developed. Extrapolating the experimental results by Scholz et al (Scholz

et al., 2004), a smaller coefficient can be expected. These deviations between different research workers may demonstrate that the accuracy of Eq.(2.1) will also be influenced by contact scale, microstructure and materials properties. Alternatively, for a sub-threshold crack, a model relating the toughness to the hardness and strength of the material was presented by Jung et al (Jung et al., 2004) and reasonable estimations were obtained for common brittle materials such as soda-lime glass, Si, and sapphire. The disadvantage is that it gives numerical results and the constants in the model are empirical varying with materials (Jung et al., 2004).

If it is assumed that Eq. (2.1) holds for small crack lengths (i.e. $c>a_c$, but not by much), the difficulty to accurately measure the crack length will be a major issue so a method to estimate crack length in the absence of any imaging system was suggested by Field et al (Field et al., 2003) based on the concept of crack opening displacement and utilizing the feature of a pop-in in the load-displacement curve. For a typical pyramid indenter, the crack opening displacement (COD) δ_{COD} can be given by,

$$\delta_{COD} = 2h_{ex} \cot\varphi \tan 30^{o} \tag{2.5}$$

Where φ is the face-to-centre angle of the tip, and h_{ex} is the extra penetration caused by the entry of the indenter into the crack. Field et al (Field et al., 2003) suggested that h_{ex} can be estimated as the difference between the actual displacement with pop-in and the extrapolated displacement without pop-in (i.e. h_{m2}-h_{m1} is regarded to be h_{ex} as depicted in Fig. 2.2).

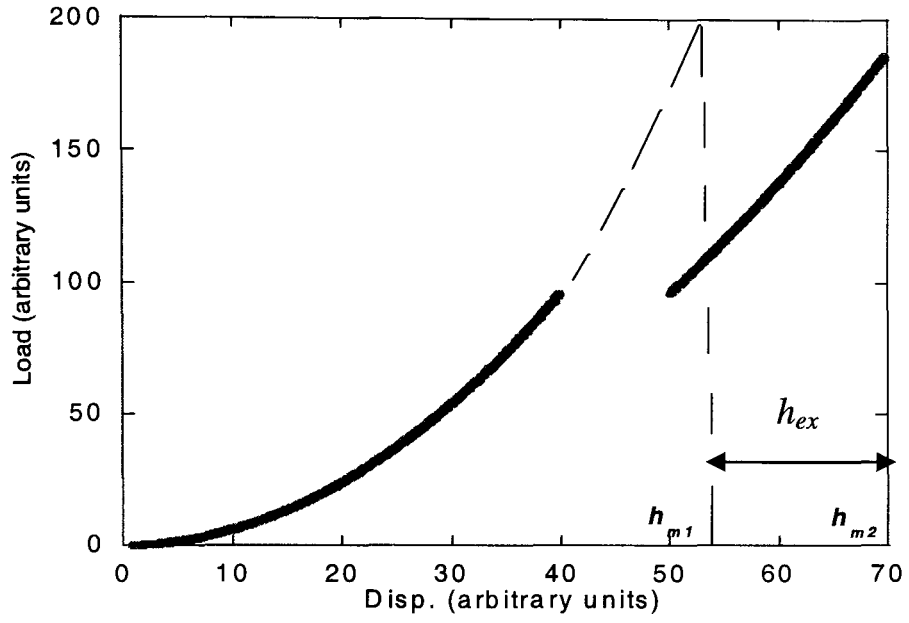

Fig. 2.3. Schematic of a pop-in in a load-displacement curve.

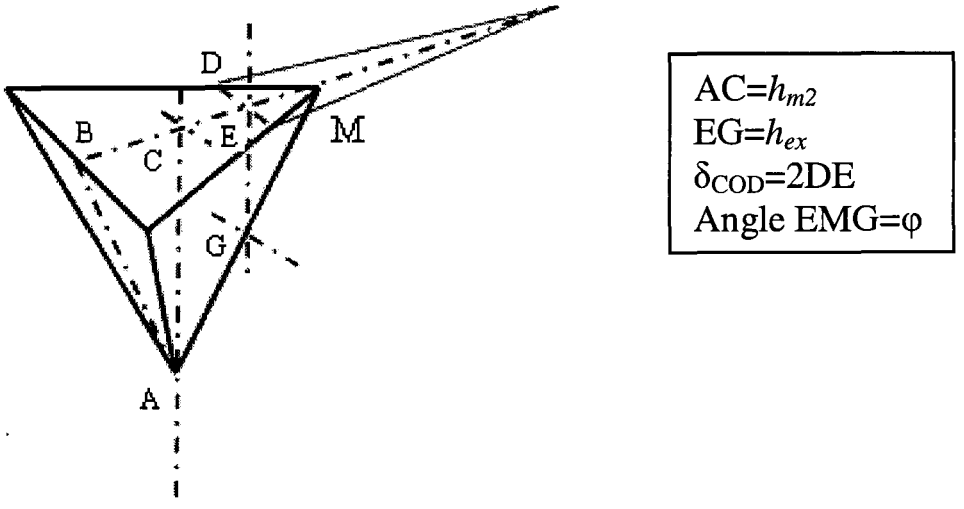

Fig. 2.4 Schematic of a triangular pyramid indenter wedging open radial/median crack in the brittle material surface.

By geometrical analysis for a pyramid indenter (see Fig.2.4) with crack length c, the distance from crack tip to the indentation centre is given by,

$$c = (h_{m2} - h_{ex})\cot\varphi + \frac{\pi E_r h_{ex}\cot\varphi\tan 30^o}{4pD} \tag{2.6}$$

Where E_r is reduced Young's modulus; p is the pressure at the centre of the crack, and D is a constant.

Since p is likely to be proportional to the Meyer's hardness, H_M (Mencik, 1996), Eq.(2.6) can be rewritten as follows,

$$c = h_{m2}\cot\varphi + \left(Q\frac{E_r}{H_M} - 1\right)h_{ex}\cot\varphi \tag{2.7}$$

Where Q is a combined constant which can be obtained by curve fitting the relationship between c and h_{ex}.

Reasonable results were reported and it was found that Q was similar (with a difference of ~10%) for two different materials in (Field et al., 2003). Although it is not sufficiently justified to assume a valued constant Q, it leads to the possibility to extend the method to other bulk materials whose cracks are not easily measured even at high load and avoids the time consuming work of imaging the cracks. Further, it leads to the possibility of calculating the threshold of radial crack formation if a favourable initiating microcrack did not significantly delay the pop-in. However, data is relatively scattered in these plots, in particular for fused silica. For materials that have significant densification below the indenter, the stresses adjacent to the indenter will be reduced thus leading to a decrease of crack length, therefore, the conventional indentation method based on measurement of radial crack length will result in a gross over-prediction of fracture toughness (Marshall and Lawn, 1979) which is also the reason that Anstis et al (Anstis et al., 1981) emphasised the precautions necessary to be taken when the indented specimen has an open-network structure. Unfortunately, the fused silica selected to obtain Q in (Field et al., 2003) falls into this category, which restricts in the reliability of the value of Q.

Another important issue that needs to be highlighted is the interaction between different crack types. A cone crack can appear prior to radial/median cracking and it provides a confining bound for the development of radial or median crack systems. Also it is possible that lateral cracks will accompany radial cracking and the

expansion of the lateral cracking will affect the propagation of the radial cracking. Usually, lateral cracks occur at the end of the unloading cycle, by which time crack systems are fully developed and constrain the lateral cracks,

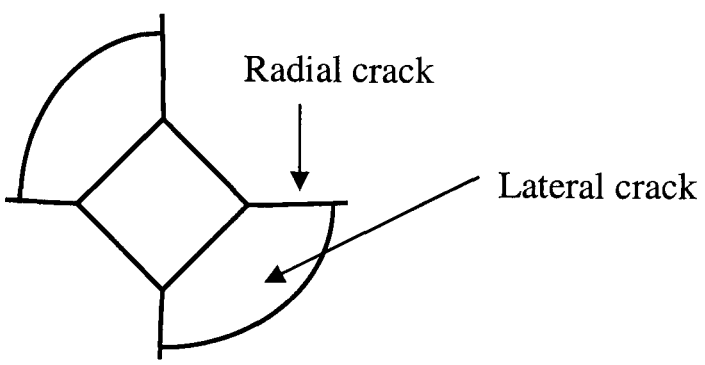

Hence,

Rather than,

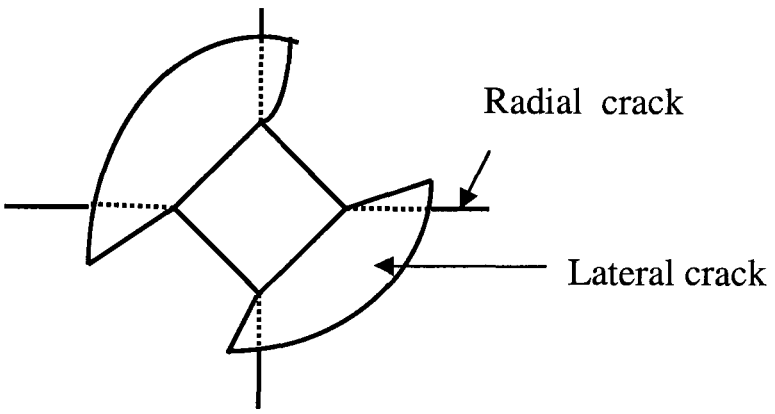

For some coated systems with relatively poor adhesion, delamination at the interface may be associated with radial fracture in the coatings before the radial cracks can extend which will seriously affect the residual stress field to drive the radial cracks and thus the final dimension of the radial crack. In such cases, Eqs.(2.1) to (2.3) become invalid or at least less reliable depending on the extent of the effect. Further, for some coated systems indented by a Berkovich indenter even at high load, only

ring-like cracks, or picture frame cracks are observed (e.g.(Page and Hainsworth, 1993)) in which case, all the models above cannot work.

In order to avoid the constraint of crack length impacted by other factors such as densification, another COD method was proposed requiring no knowledge of crack length. It only requires that the crack in quasi-equilibrium (crack propagation stops ignoring the slow crack growth effect) which is the case immediately after indentation with sharp tips (Marshall and Lawn, 1979).With the aid of the solution of the near-tip displacement field (Lawn, 1993), a numerical solution of crack driving force can be obtained. Reasonable results were obtained for soda-lime glass (Burghard et al., 2004). This method avoids the influence of densification only if the displacement field is not changed appreciably but can provide the intrinsic toughness.

Crack Opening Displacement has been directly correlated with fracture toughness (Fett, 2002), (Kruzic and Ritchie, 2003). Based on linear elastic fracture mechanics, the near-tip stress intensity K_{tip} for a crack related to the crack opening displacement (COD) is given by Fett (Fett, 2002),

$$u(r)=\frac{4K_{tip}b^{1/2}}{\pi E_r}\left[A\left(1-\frac{r}{a}\right)^{1/2}+B\left(1-\frac{r}{a}\right)^{3/2}+C\left(1-\frac{r}{a}\right)^{5/2}\right] \tag{2.8}$$

Where *r, b, a* are the radial position of the crack tip, the contact radius, and the crack length, respectively, as measured from the indent centre. Here the constants A, B, C are given by,

$$A=\left(\frac{\pi a}{2b}\right)^{1/2} \tag{2.9}$$

$$B\approx 0.011+1.8179\ln\frac{a}{b}$$

$$C\approx -0.6513+2.121\ln\frac{a}{b}$$

Usually K_{tip} is regarded as the material toughness. Compared to the conventional indentation method (CIM), this approach was argued to be non-empirical. CIM is sensitive to R-curve behaviour (i.e. increasing toughness with crack growth(Lutz et al., 1994)) because of extrinsic toughening mechanisms such as crack bridging (Briard et al., 2005) whilst this effect will not influence the COD method. Since hardness is not required in the approach, unlike CIM, it is not expected to be influenced by indentation size effect (ISE) unusually observed in ceramics (Bull, 2003),(Bull et al., 1989). But this method was found to be influenced by the secondary radial cracking which releases some of the residual stress thus affecting the COD of the main radial crack (Kruzic and Ritchie, 2003).

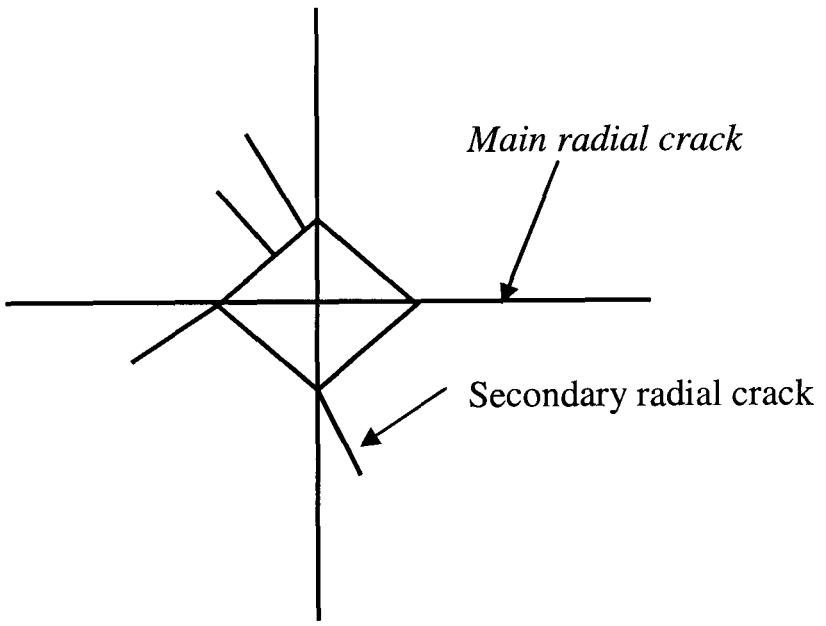

Fig. 2.5 Schematic of main radial crack and secondary radial crack produced during indentation.

Also, the COD method will also be influenced by subsurface fracture (such as lateral cracking) which may reduce the opening displacement of the radial crack. This method is not very suitable for nanoindentation at low loads in which case the COD is of the order of a few nanometers. The measurement uncertainties will lead to large errors when plotting COD versus the distance from the crack tip.

Clearly, there is need to reduce the errors in all of the previous methods. A strength method was also proposed by Chantikul at al (Chantikul et al., 1981) based on indentation which could avoid some of the systematic errors in Eq. (2.1) and it also eliminated the need for fracture imaging. By combining indentation and strength tests (see (Chantikul et al., 1981)) the following expression to determine toughness can be derived,

$$K_c = \eta_v^R (E/H)^{1/8} (\sigma P^{1/3})^{3/4} \tag{2.10}$$

Where $\eta_v^R = \left[(256/27)(\pi\Omega)^{3/2}\xi_v^R\right]^{1/4}$. Here Ω is a crack-geometry factor which takes into account free-surface effects, cracking interactions such as the lateral-radial cracking interaction mentioned previously, and the deviation from penny-like shape. It can be seen that the constant η_v^R in Eq. (2.10) still relies on ξ_v^R from Eq. (2.1), which indicates that all the errors in ξ_v^R will be introduced into η_v^R. Therefore, it cannot be expected that this method will significantly improve the accuracy compared to Eq.(2.1). In addition, it requires an indentation at the centre of the tensile face of a bend test piece and only one result can be obtained for a single specimen, which is a possible reason that the method is not as popular as the CIM by Eq. (2.1). In addition, this method is very difficult to apply to thin coatings.

In addition to half-penny (or approximately half-penny) crack patterns, palmqvist radial cracks are also observed for stiff and hard bulk materials such as WC [e.g. (Laugier, 1985)]. These usually occur at high load for much tougher materials compared to glass. Palmqvist cracks tend to appear during loading, initiating at corners due to the high stress concentration and are driven by the hoop tensile stress. In this case, the proportional relationship between toughness K_{IC} and $P/c^{1.5}$ as shown in Eq.(2.1) is still valid, however, the exponent of E/H was found to be 2/3 and an additional term depending on the crack dimension over contact size (c/a_c) is required to get reasonable toughness values. The c/a_c term will affect the proportional coefficient (Dukino and Swain, 1992). It was found that the toughness values of a range of ceramics based on the half-penny cracking pattern and the Palmqvist radial morphology did not deviate too much (within 10%) (Dukino and Swain, 1992). Since

this kind of crack tends to occur at relatively high loads in relatively tough bulk materials, it is not suitable to be considered for the assessment of thin coatings because a high load cannot be used without a substrate influence. However, this model can be treated as another explanation for the lower coefficient in Eq. (2.1) in the case of smaller crack which supports the arguments of Scholz et al (Scholz et al., 2004) regarding the constants when the radial cracks are not fully developed as discussed previously.

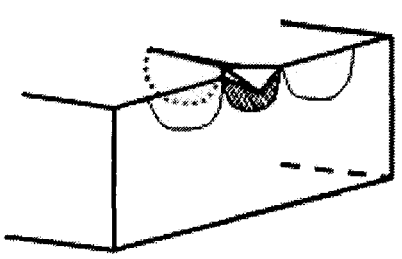

Fig.2.6 Schematic of palmqvist radial crack.

2.2.1.2 Lateral cracking

For lateral cracking, based on the expanding cavity model as used in the analysis of radial/median crack pattern (Lawn et al., 1980) and a simple plate theory, Marshall et al (Marshall et al., 1982) proposed a model to relate the toughness of brittle bulk materials to the critical load where lateral cracks occur during unloading.

$$K_c^4 = \frac{P_0 A_0^2}{\delta_0}(\cot\theta)^{\frac{2}{3}}\left(\frac{H^4}{E}\right) \tag{2.11}$$

Here P_0 is threshold load for lateral cracking; A_0 and δ_0 are dimensionless constants, A_0 =3/4 and δ_0 =1200; θ is the half-included angle for an indenter (Marshall et al., 1982).

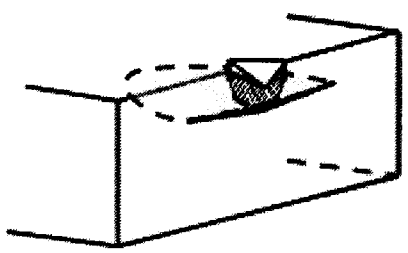

Fig. 2.7. Schematic of lateral crack.

Under certain circumstance, this method can be extended to assess the interfacial failure of a coated system which will be discussed in Chapter 8.

2.2.2 Energy based models

2.2.2.1 Assessment of coating toughness based on features in the indentation load-displacement curve

2.2.2.1.1 Models based on individual P-δ curve

With the development of complex coating stacks (e.g. multilayered coated systems) and the presence of variable crack patterns, the difficulty of generating a solution by stress analysis based models is dramatically increased. Therefore, there is an urgent need for the development of models to deal with complex coatings and varied cracking patterns. The most successful models in this respect are energy-based which are critically reviewed in this section.

A widely used energy-based model was initially proposed by Li et al (Li et al., 1997, Li and Bhushan, 1998) based on extrapolating the loading curve when there is a step associated with through-thickness fracture in it. In this model the load-displacement curve is extrapolated from the step start point (assumed to be the onset of fracture) to

its end point, and the difference between the extrapolated curve and the measured curve is regarded as the fracture dissipated energy. For convenience, this method will be denoted as the ld-dp method in this thesis.

With regard to through thickness cracking in carbon films on silicon substrate during nanoindentation, three different stages have been described (Li et al., 1997) (See Fig. 2.8 as well):

I. **First ring-like through–thickness crack formation**.

The tensile stresses at the contact edge are very high hence the first ring-like through thickness cracks form. In this stage the film under the indenter is separated from the rest of the film via this first crack. A discontinuity would occur in the load-displacement curve given sufficient load and displacement resolution.

II. **Delamination and buckling**.

In this stage, nanoindentation fracture is mainly produced by the lateral volume expansion and residual compression stresses of the material under the indenter. After the first stage, the film under the indenter is separated from the rest of the film and sticks to the indenter. The indentation is no longer with a sharp indenter but a blunt 'indenter-film'. As the indenter pushes, the film around it is pressed laterally and when the pressure is larger than a critical value, delamination can occur. This does not produce a step in the load-displacement curve, but a sudden change in slope can be observed because of the decrease of the stiffness.

III. **Second ring-like through thickness crack formation and spalling.**

As the indenter penetration increases, the height of the buckle increases, when this height reaches a critical value, a second ring-like through thickness crack and spalling at the edge of the buckled film is produced.

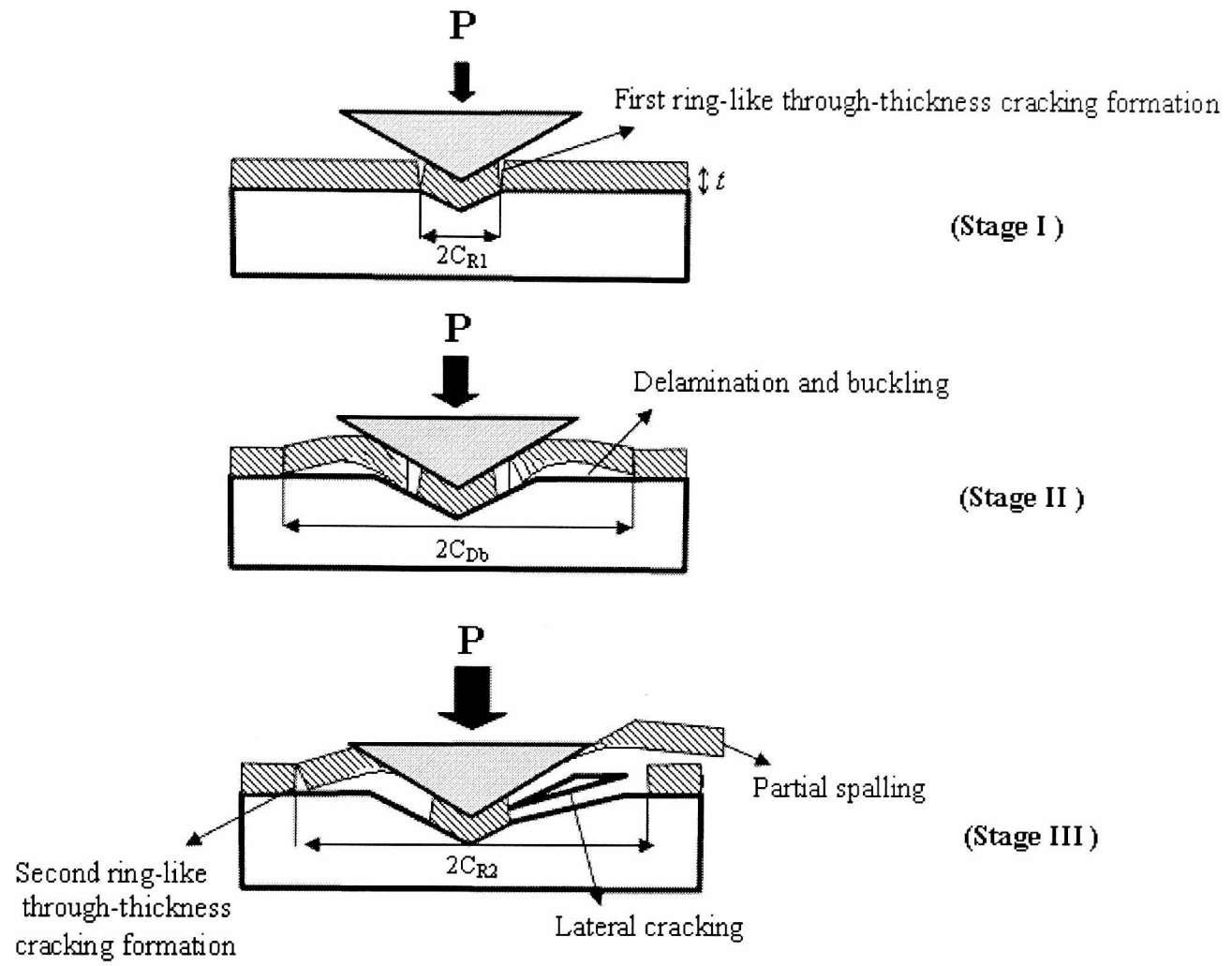

Figure 2.8. Schematic drawing of the different stages in nanoindentation fracture for carbon coatings on silicon.

The fracture toughness is related to the released elastic strain energy during fracture, U, the film thickness, t, the total length of the crack in the film plane $2\pi C_R$, Young's modulus of the film, E, and Poisson's ratio of the film, ν, and it is given by,

$$K_{IC} = \left[\left(\frac{E}{(1-\nu^2)2\pi C_R}\right)\left(\frac{U}{t}\right)\right]^{1/2} \tag{2.12}$$

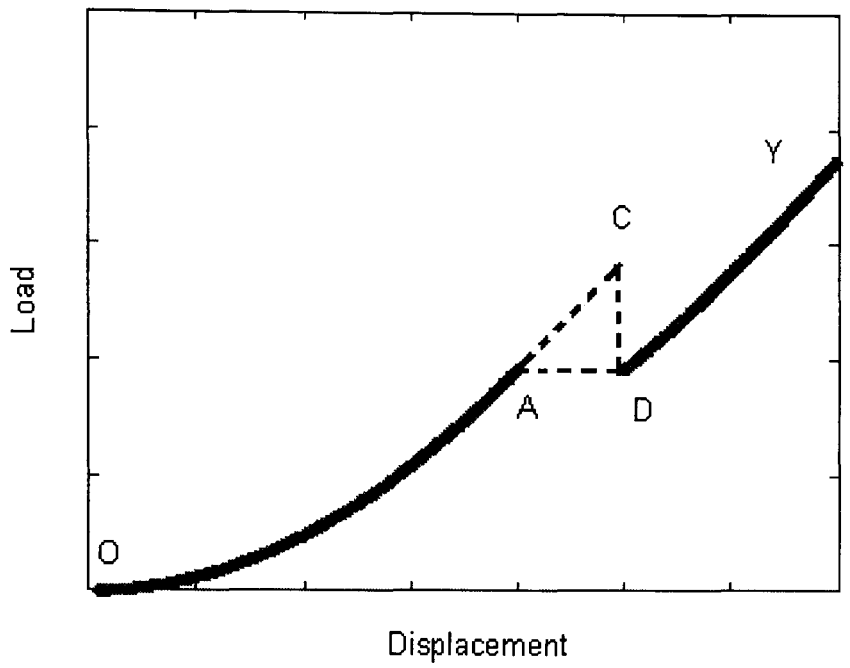

Fig. 2.9. Schematic of the ld-dp method to determine the fracture dissipated energy, i.e. area ACD. See text.

This was slightly modified by den Toonder et al by considering the effective coating thickness and the number of chippings (den Toonder et al., 2002). Thus, the toughness is,

$$K_{IC} = \sqrt{\frac{U_{fra} E}{(1-\nu^2) 2N\pi C_R t'}} \tag{2.13}$$

where $t' = \frac{t}{\sin\beta}$, since the crack may propagate at an angle of β rather than exactly perpendicular to the coating/substrate interface. β can be measured by microscopy (e.g. Fig. 2.10).

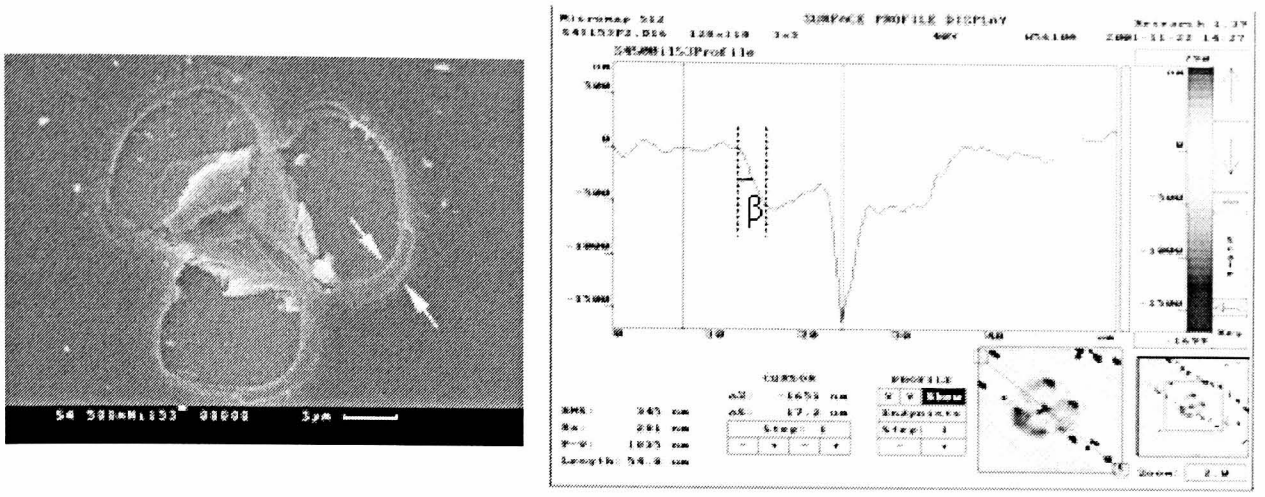

Fig.2.10. SEM image and the measurement of cracking propagation angle by optical profilmeter for a 1μm CN_x on Si(100) indented by a Berkovich tip at 500mN. (Fernandez-Palacio et al., 2004)

However, through thickness fracture may change the stress field around the indenter and thus change the elastic-plastic behaviour of the coated system. This influence has been completely ignored in this model. The actual coating cannot survive to the extrapolated load and during fracture event the indenter still does the work which is mainly dissipated by elastic plastic deformation. There is no distinct relation between the actual fracture dissipated energy and the energy enclosed in area ACD. It was also argued elsewhere (den Toonder et al., 2002) that the area ACD in Fig. 2.9 is not the actual energy dissipated by fracture. Therefore, this model has been further developed in this thesis based on analysing the total work versus displacement curve (W_t-dp method). The method to determine fracture events is explained in Figure 2.11. First, it is proposed to extrapolate the initial W_t-dp curve from the cracking start point A to the cracking end point C, to get the work difference CD (with the units of J) after fracture; then extrapolate the W_t-dp curve after cracking backward to the cracking start point and thus obtaining the work difference AB (with the units of J) at the onset of fracture. AB represents the work caused by different elastic-plastic deformation behaviour of the material before and after fracture whereas CD represents the total work difference caused by the presence of cracking which consists of the change of elastic-plastic deformation behaviour between the uncracked system and cracked system plus the fracture dissipated energy. The difference between the two (i.e. CD minus AB in Fig.2.11) will be the fracture dissipated energy.

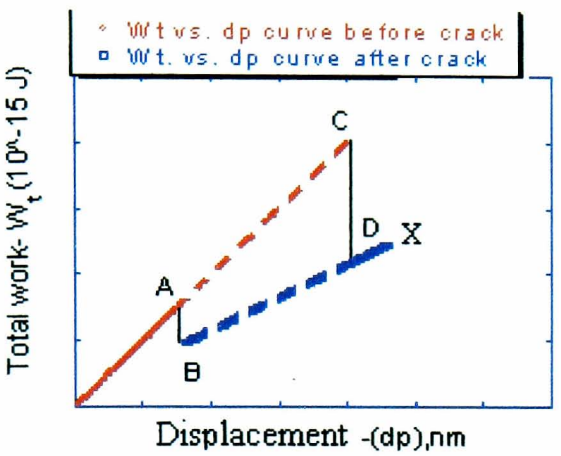

Fig.2.11 Schematic of extrapolating the total work vs. displacement curve before and after cracking to determine the fracture dissipated energy CD-AB.

Evidence of underestimation of the coating toughness by the ld-dp method for softer coatings on harder and stiffer substrates such as sol-gel coatings on glass has been reported (Malzbender et al., 2000). Malzbender et al (Malzbender and de With, 2000c) attributed this deviation to the different stress intensity in directions perpendicular and parallel to the interface. Correcting their results by multiplying by a factor of $2^{1/2}$ (Hu et al., 1988) , leads to a reasonable agreement with other methods, however, it is doubtful that the crack propagation occurs in the manner that this would imply. Chips can be formed by different mechanisms such as by fracture of material detached by buckling at regions of tensile stress, radial cracking which deflects along the interface, or lateral cracking along the interface which propagates upwards to the surface. Only for the second mechanism is this model valid. Otherwise, the complex crack extension path may make it difficult to apply such an approach. However, when the W_t-dp method was utilized, reasonable results can be obtained (see details in Chapter 5).

The disadvantage of the W_t-dp method is that two-step extrapolation may lead to more fitting errors.

2.2.2.1.2 Models based on a range of P-δ curves

An alternative energy based model was proposed by Malzbender and de With (Malzbender and de With, 2000a) based on plotting the irreversible work W_{irr} over the total work done by indenter W_t at a range of loads. For thicker sol-gel coatings on glass in (Malzbender and de With, 2000a), a slope change of the curve of W_{irr} versus applied load (W_{irr} -P) curve was observed when delamination occurred. At higher loads, a step occurred in the P-δ curve which leads to a jump in the W_{irr}-P curve which is found to correlate with the chipping. The irreversible work is obtained from a completed loading-unloading curve at a given load. The difference between the energy at a given delamination dimension r_d to the extrapolated energy for the plastic deformation of coatings before delamination, ΔW_{irr}^{d} (see Fig. 2.12) was assumed to be the energy dissipated by delamination. The difference between the irreversible work of the delaminated coated system and the chipped system, ΔW_{irr}^{c} (as depicted in Fig. 2.12) is regarded to be the energy dissipated by chipping.

The energy release rate for delamination G_{int} is given by,

$$G_{\text{int}} = \frac{\Delta W_{irr}^{d}}{\pi r_d^2} \tag{2.14}$$

and the interfacial toughness K_{int} is given by,

$$K_{\text{int}} = \sqrt{G_{\text{int}} E_{\text{int}}} \tag{2.15}$$

where E_{int} is the interfacial modulus which is given by (Hutchinson and Suo 1992)

$$\frac{1}{E_{\text{int}}} = \frac{1}{2}\left(\frac{1}{E_c} + \frac{1}{E_s}\right) \tag{2.16}$$

Where E_c and E_s are the Young's modulus of coating and substrate, respectively.

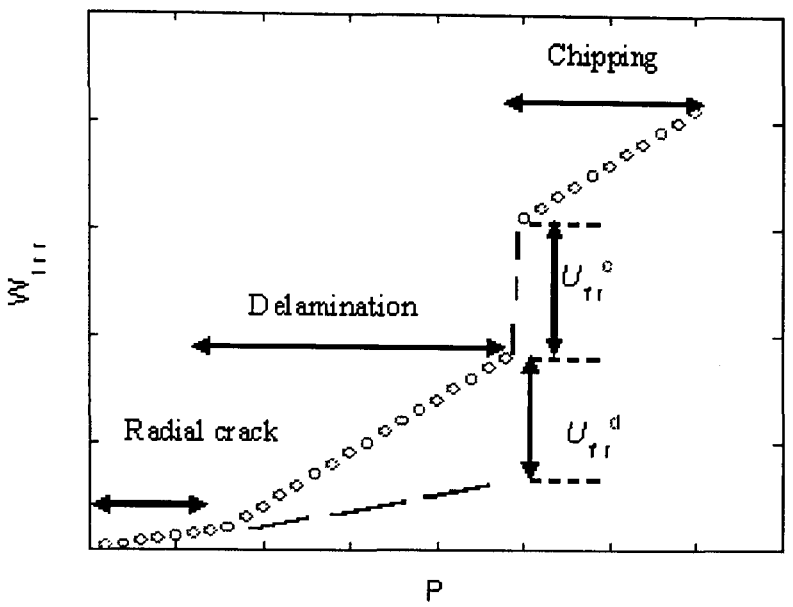

Fig.2.12 Schematic of irreversible energy dissipated as a function of applied load when different fracture events occur during indentation. After (Malzbender and de With, 2000a).

For chipping, the toughness can be given by a similar formula replacing the delamination area in Eq.(2.14) with chipping area ($3\times 2\pi rt$). Here t is a so- called effective thickness of coating as mentioned in the previous section, the factor 3 accounts for the fact that usually three chips appear simultaneously when a three-sided pyramid tip is used, and r is the radial dimension of the crack. However, caution needs to be used since for some coated system, one or two chips were observed rather than three.

It was argued (Malzbender and de With, 2000a) that this method is more accurate than the ld-dp method. When extrapolating the irreversible work before delamination, it is assumed that the relationship between the extent of the plastic deformation and the applied load will maintain the same linear relationship independent of applied load if no delamination occurs. However, once radial cracking occurs the deformation pattern may change with an increase of load in a coated system. Furthermore, the threshold load for delamination in a 2μm sol-gel coating (composition H see details in initial paper (Malzbender and de With, 2000a) is about 100mN where the indentation depth of about 1.8μm is comparable to the coating thickness which means the substrate has already begun to influence the plastic deformation of the whole coated

system. With a further increase of the load, the extent of the deformation of the substrate will also change significantly. Therefore, the model will drop in accuracy and it can be expected that the method will significantly overestimate the interfacial toughness for a softer coating on a hard substrate (e.g. sol-gel coatings on glass in (Malzbender and de With, 2000a)). The energy release rate for delamination in some sol-gel coatings (i.e.Coating A and B in (Malzbender and de With, 2000a)) is calculated to be between 11 and 290 J/m^2, which is unrealistically high for such coatings with relatively poor adhesion and it was much higher than results ($< 4J/m^2$) in the literature determined by other methods (Malzbender and de With, 2000c). In order to eliminate the substrate influence (and the change of apparent Young's modulus and hardness caused by cracking and delamination), it was further suggested by Malzbender et al to estimate the fracture dissipated energy by extrapolating the plots of ΔW_{irr}^{d} and ΔW_{irr}^{c} versus the inverse of coating thickness to infinite coating thickness (Malzbender and de With, 2000a). In this way a reasonable approximation (same order of magnitude) of interfacial toughness can be achieved. Also, the fracture toughness of coatings with composition A is 0.06 ± 0.02 MPam $^{0.5}$ by this approach which is close to previous reported values. However, the toughness for coatings with composition B is 3.4 ± 2.5 MPam $^{0.5}$ which is still significantly overestimated compared to their previous results of 0.18 MPam $^{0.5}$. The measurement error is thus relatively big (up to 75%) and the approach cannot be regarded as reliable. Since different fracture behaviour is observed for the same coating composition with different thickness not only for sol-gel coating (Malzbender et al., 2000) but also PVD coatings such as ITO on glass, it is unlikely that any method which does not attempt to account for this will give good results. It has also been argued elsewhere that for a given coating the fracture toughness can increase or decrease with coating thickness [(Harry et al., 1998), (Volinsky et al., 2002),(Volinsky et al., 2003)]. It is difficult to separate out this effect.

This method requires many tests at a number of different loads which is quite time consuming and it requires the same coatings with different thickness which is not economic for practical application. It is also important to note that the W_{irr} method is only valid in the case of a feature in P-δ curve otherwise no obvious characteristic

change is observed which invalidates the method (see such example for inorganic-organic coating on glass in (Etienne-Calas et al., 2004)).

Another approach based on plotting irreversible work versus load has been proposed (Nakonechna et al., 2004). It was suggested that the position of the W_{irr} jumps (i.e. ΔW_{irr}) on the W_{irr}-P curve correlates with the evidence of the first crack in micrographs, and reasonable results for toughness were reported. However, there are lots of events in a plot of W_{irr}-P after the critical load (see Fig.2.13 which makes it difficult to repeat the calculations for different crack dimensions. Therefore, the method actually depends on detecting the first event associated with a measurable crack dimension which may not be easily done, the extension of the cracks subsequently to the find position at the end of the test is not known in all cases.

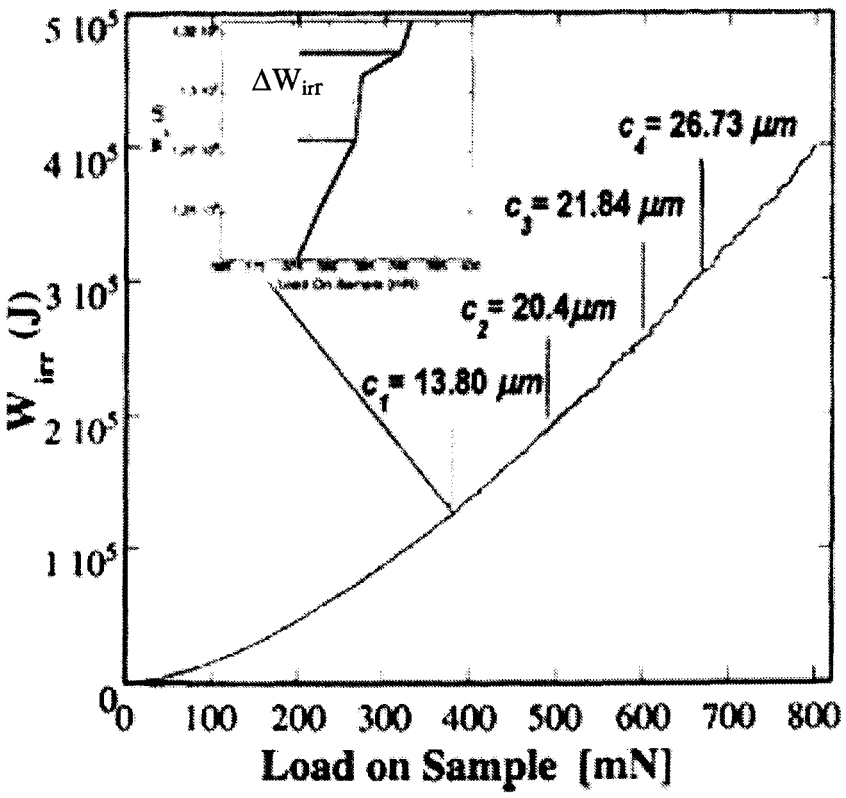

Fig. 2.13. Irreversible work (W_{irr}) versus load (P) for a gradient film AlTiSiN. ΔWirr is regarded to be fracture dissipated energy by the first crack. After (Nakonechna et al., 2004).

2.2.2.2. Limiting values of coating toughness

Given the doubt about the method proposed by Li et al, den Toonder et al (den Toonder et al., 2002) proposed so-called bound methods to determine the upper and /or lower bound for fracture toughness from nanoindentation carried out under load control and displacement control. The approach assumes the load (P) scales with displacement squared (δ^2) in the loading part and in the unloading procedure before cracking and after cracking. At the same time, it is supposed that fully elastic behaviour (i.e. final depth δ_f =0) or fully plastic behaviour (i.e. δ_f =δ_m, δ_m is the maximum depth) in the coated system before and after crack events determines the lower bound (i.e. area OAB in Fig. 2.14) or upper bound (i.e. area ABDC in Fig.2.14) for fracture dissipated energy under load control, which is given by (den Toonder et al., 2002),

$$\frac{2}{3}P_{cr}(\delta_2-\delta_1)\le U\le P_{cr}(\delta_2-\delta_1), \qquad \text{for load control} \qquad (2.17)$$

where P_{cr}, is the critical load for a step caused by fracture, and δ_1, δ_2 are the indentation penetration before and after the fracture event (see Fig. 2.14), respectively. For displacement control, only the upper limit for fracture dissipated energy (i.e. area OST in Fig. 2.15) is obtained,

$$U\le\tfrac{1}{3}\delta_{cr}(P_2-P_1), \qquad \text{for displacement control} \qquad (2.18)$$

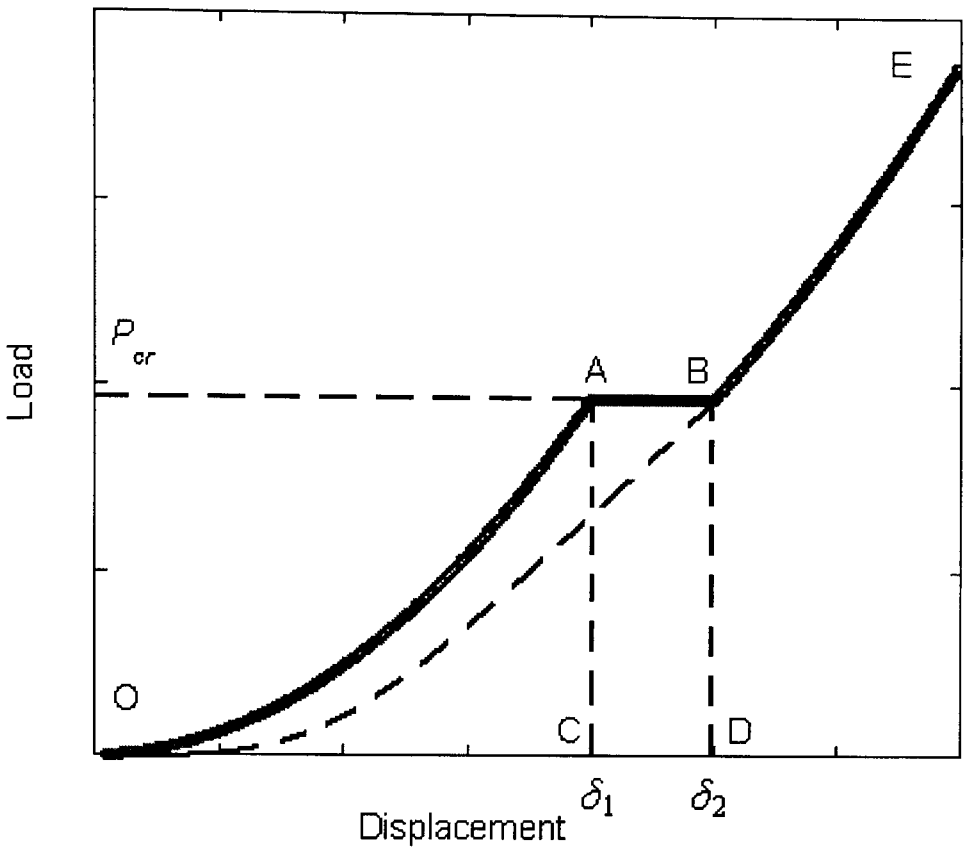

Fig.2.14. Schematic of the lower bound method by den Toonder et al under load control. The areas OAB and ACDB are regarded as the lower and upper bound of fracture dissipated energy, respectively.

The fact that plastic deformation dominates or fracture occurs leads to the result that the final depth cannot be zero. In real situations, therefore, it may significantly deviate from the assumptions above. Also, it is not reasonable to regard the area OAB (see Fig.2.14) as the lower bound of fracture dissipated energy. Actually, the area OAB is the upper bound of fracture dissipated energy under the assumption of fully elastic behaviour. It is incorrect to assume the area enclosed by ABDC (see Fig.2.14) is the maximum irreversible work for the indenting procedure, because the area ABDC is the work done by indenter which can be elastic, plastic deformation plus other factors. There is no reason to argue that the work done by indenter for a ductile material will be the upper limit of fracture dissipated energy. For displacement control, with the assumption of a fully elastic behaviour as mentioned previously the area OST in Fig. 2.15 will be the maximum elastic strain energy which could supply the fracture dissipated energy. However, for actual coated systems, the fracture occurs at relatively high load where the plastic deformation may have been well-developed, it is

necessary to derive a more general expression to describe the upper bound for the fracture dissipated energy.

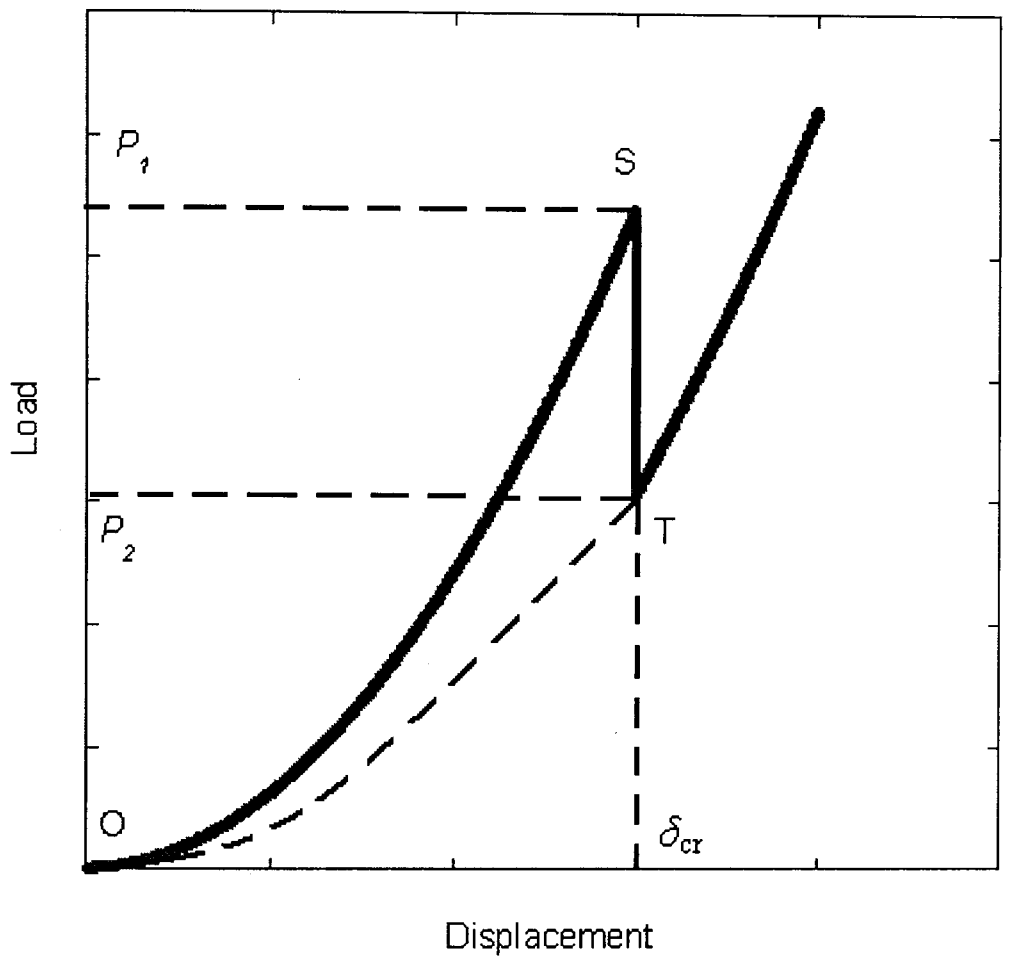

Fig.2.15. Schematic of the upper bound method by den Toonder et al under displacement control. The area of OST is regarded as the upper bound of fracture dissipated energy.

Thus a modified bound model has been developed in this thesis. The key point is to estimate the final depth rather than assuming it equals zero and the lower limit can be obtained by assuming the final depth does not change due to the presence of the fracture event. If unloading the curve at point B, the associated final depth should be between the δ_f and δ_m because it is obvious that the residual depth will not recover during the further indentation (usually the reversible plasticity is ignored). The upper limit of the fracture dissipated energy can be obtained by assuming the final depth after fracture is equal to the penetration where the excursion stops (i.e. all the stored

elastic strain energy supplies fracture dissipated energy). By this approach the upper and lower bound of coating toughness can be obtained for nanoindentation under load control and displacement control as well. The areas EAB and EABF in Fig. 2.16 are the lower and upper bound of fracture dissipated energy for indentation under load control; areas AEB and AEG in Fig. 2.17 are the lower and upper bound of fracture dissipated energy for indentation under displacement control. Actually, the lower and upper bound in this thesis is referred to the lower and upper limits of the upper bound. A more detailed discussion is provided in Chapter 6.

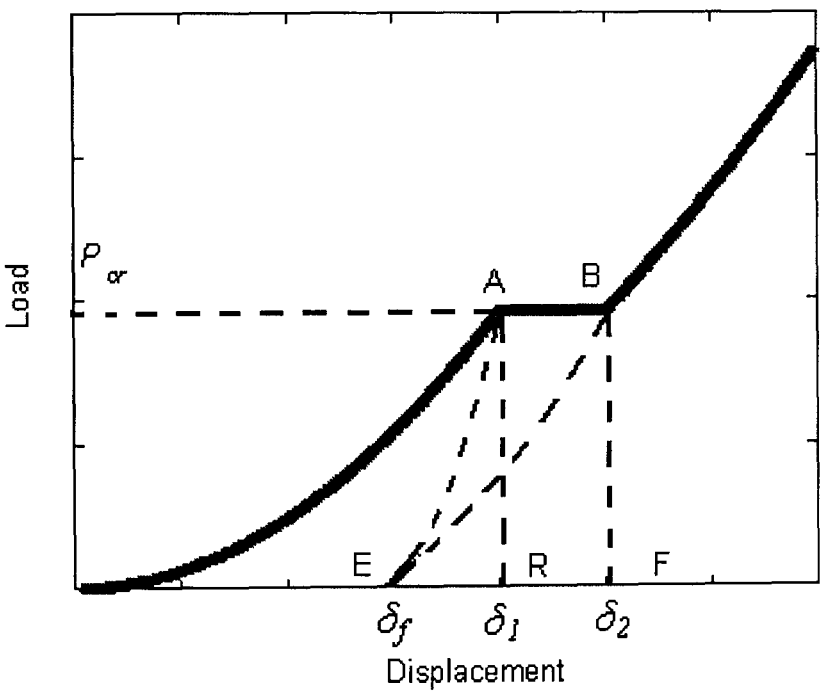

Fig.2.16. Schematic of the lower bound method developed in this work under load control. The areas EAB and EABF are regarded as the lower and upper bound of fracture dissipated energy, respectively.

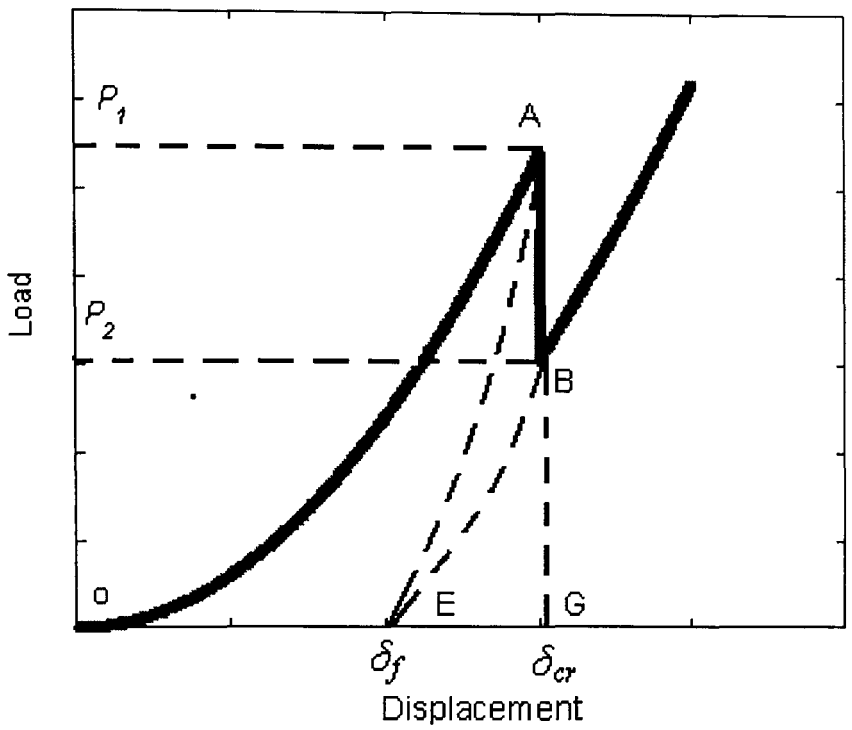

Fig.2.17. Schematic of the upper and lower bound methods developed in this work under displacement control. The areas AEB and AEG are regarded as the lower and upper bound of fracture dissipated energy, respectively.

2.2.2.3 Energy based models in the case of no obvious excursion in the P-δ curve

All the energy based models introduced in previous sections are based on features in the load-displacement curve associated with fracture, otherwise, no slope change or jump in the plot of W_{irr}-P and W_t-dp can be observed. However, it is not unusual that fracture does not cause an excursion in the load-displacement curve. For example, for the Solar control coatings (with the main components of being ITO, ZnO, SnO_2 and TiO_xN_y) on glass indented by a Berkovich indenter, a number of picture-frame cracks have been observed in the SEM whilst no obvious slope change or excursions have been observed in the load–displacement curve even from high load tests (500mN) using a Nanoindenter II. (see Fig. 2.18).

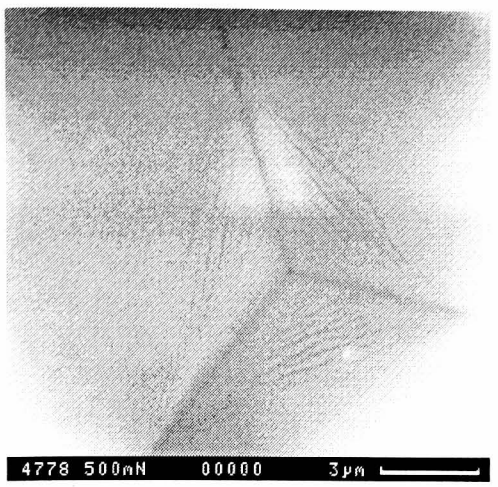

(a)

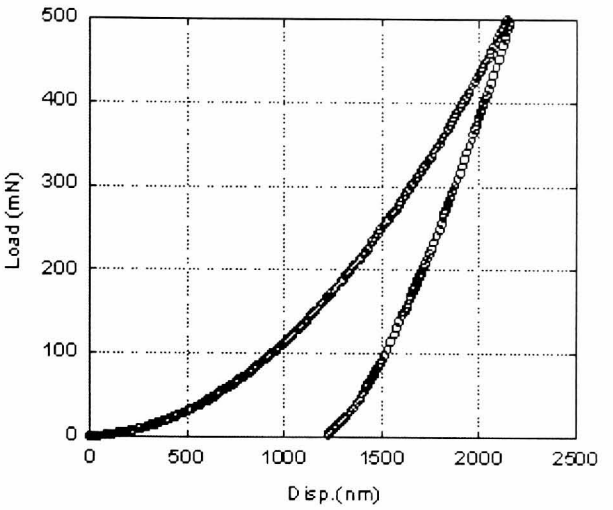

(b)

Fig. 2.18 (a) SEM image of picture frame cracks in a 400nm ZnO coating on glass indented by a Berkovich tip at 500mN and (b) its associated load-displacement curve. No excursion in the P-δ curve was observed.

2.2.2.3.1 Model based on change of composite hardness

An energy based model to estimate coating toughness was first suggested by Tuck and Korsunsky (Tuck and Korsunsky, 2000) based on picture-frame cracks in nitride coatings on steel. They related the hardness increment of a coated system over the uncoated substrate to the coating deformation which includes plastic deformation, fracture and interfacial delamination. The hardness can be defined in terms of applied load or plastic work as follows,

$$H = \gamma P / d^2 \tag{2.19}$$

$$H = \frac{3\gamma W}{d^3} \tag{2.20}$$

where P is the applied load, d is the diagonal of the Vickers indenter impression; γ is a dimensionless coefficient and equal to 18.544 for a Vickers indenter, and W is the plastic work of indentation.

Thus the increment of the hardness of the coated systems is given by,

$$H - H_s = \frac{3\gamma W_f}{d^3} \tag{2.21}$$

Where $W_f = (H_f V_f + G_c A_c + G_i A_i)$; H, H_s and H_f are the hardness of composite, substrate and film, respectively; V_f is the volume of the plastic deformation zone in the film; G_c and G_i are the strain energy release rate of the coating and interface, respectively; A_c and A_i are the areas of cracks in the coating and at the interface.

A range of indentation mechanisms for a hard coating on a soft substrate are observed as a function of contact scale [e.g.(Korsunsky et al., 1998),(Tuck et al., 2001)]. The indentation mechanisms for a hard coating on soft substrate can be described by (Fig. 2.19).

(1) Stage I: At low load, provided the indenter is sufficiently sharp, the hard coating is plastically deformed in a region of high compressive stress immediately under the indenter. With an increase of the load, the film undergoes membrane flexure, altering the stress distribution and postponing the tendency for plastic deformation of the substrate.

(2) Stage II: A critical load is reached, and the first circumferential through thickness crack (i.e. picture frame crack) occurs and the membrane stress is relieved. When load increases further, multiple through thickness cracks form and the retard on substrate plastic deformation caused by film flexure is removed. Substrate deformation begins to become significant.

(3) Stage III: Plastic deformation of the substrate completely dominates and the hardness of the composite reduces to close to the substrate hardness.

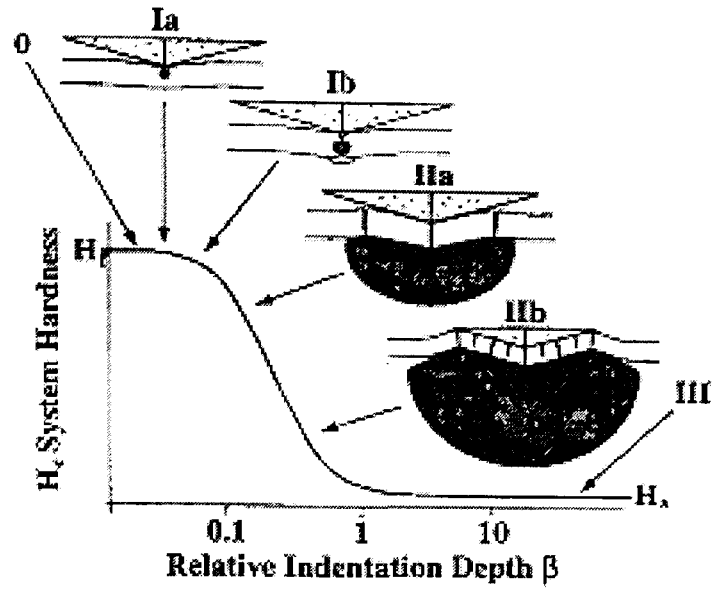

Figure 2.19 Schematic showing the evolution of nanoindentation response of a hard coating on a softer substrate where the different regimes states are indicated. After (Korsunsky et al., 1998).

Assuming that crack initiation can be described by a critical strain criterion, it can be expected that the spacing (s) between the parallel cracks is equal. Thus, for the picture-frame cracks produced by a Vickers indenter, as depicted in Fig. 2.20, the total crack length L is given by,

$$L = (d^2 - d_0^2)/2s \tag{2.22}$$

For well-established picture frame cracks, it is usually observed that $d_0 << d$ so that equation (2.22) can be simplified to $L = d^2/2s$. Assuming A_c scales with the area under the indenter and V_f is proportional to the volume of coating under indenter, W_f can be expressed by,

$$W_f = (G_c/s + \chi G_i/t + \eta H_f)td^2/2 \tag{2.23}$$

Where χ and η are dimensionless coefficients.

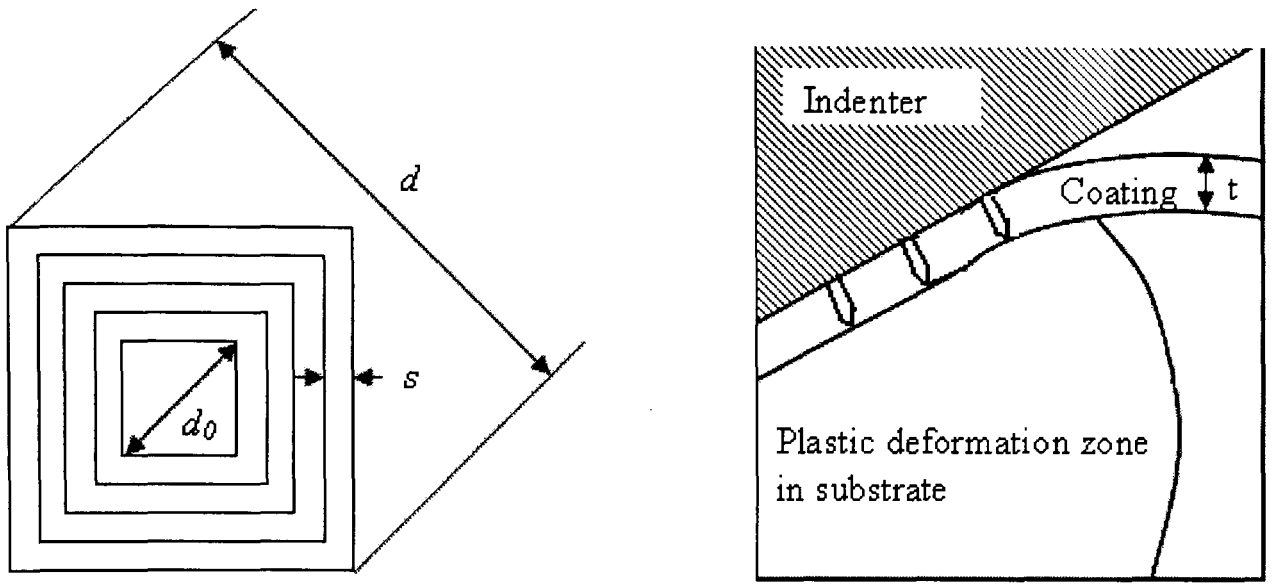

Figure 2.20. A schematic illustration of the picture-frame crack pattern developed by a Vickers indentation in a coated system, after Tuck and Korsunsky (Tuck and Korsunsky, 2000).

For a coated system, the change of hardness can be given by another expression (Tuck and Korsunsky, 2000, Korsunsky et al., 1998),

$$H - H_s = \frac{H_f - H_s}{1 + k\beta^X} \tag{2.24}$$

Where k, X are dimensionless coefficients and β is relative indentation depth (RID),i.e. the ratio of penetration over coating thickness. This can be rewritten as,

$$H - H_s = \frac{g}{\beta^X} \tag{2.25}$$

where g is used to assess the transition of hardness from coating to substrate dominance and can be obtained by fitting the H-β curve (i.e. Fig. 2.21); it has units of hardness.

Finally, it is found that g is given by,

$$g = \frac{3}{14}\gamma t G \tag{2.26}$$

where $G = (G_c t / s + \chi G_i + \eta t H_f)$

This method requires a lot of experiments to determine the H-β curve to estimate the value of g and the procedure is relatively complex. It can be used as a good indictor of fracture behaviour for comparison between different coatings on the same substrate. However, it can not be treated as quantitive assessment because the parameter G in Eq. (2.26) used to estimate the coating toughness is a combined term which depends on different deformation mechanisms and leads to overestimation of fracture toughness by more than one order of magnitude (even by more than 100 in some cases).

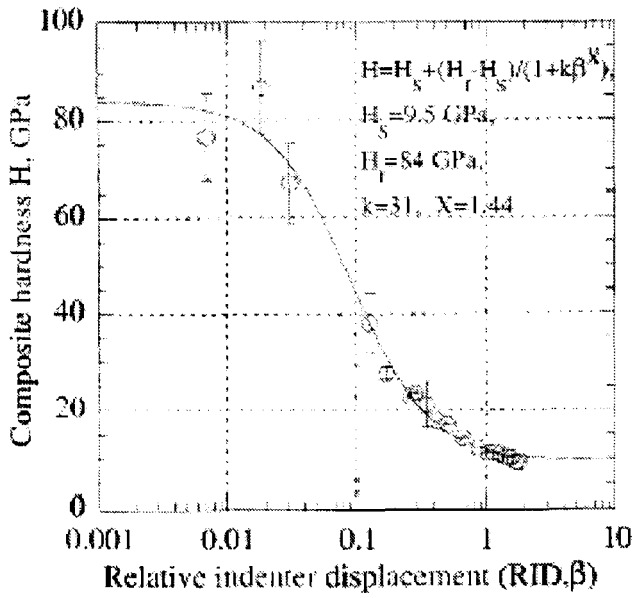

Fig.2.21 Composite hardness versus the relatively indentation depth (β) for a 3.5μm TiN coatingon M2 steel substrate (Tuck and Korsunsky, 2000).

2.2.2.3.2 W_{irr}-W_p method

Another energy based model to estimate coating toughness in the case of no excursion in *P-δ* curve was proposed in this thesis (see Chapter 7). The key requirement is to obtain the plastic work during nanoindentation. The method of irreversible work difference (denoted as W_{irr}-W_p) is explained as follows.

The method of irreversible work difference (denoting as W_{irr}-W_p) is explained as follows.

1. The load-displacement curve shows no evidence for fracture, either in the form of large excursions in the loading or unloading curve or smaller invisible excursions which lead to an increase indenter displacement at a fixed load on loading. This will be compared with the experimental data which shows evidence of cracking.
2. Therefore, the influence of cracking on the mechanical properties of the whole coated system after cracking applies to the whole loading part of the experimental curve, i.e. averaging the crack influence on the plastic and elastic deformation over the whole loading cycle. This is a reasonable assumption since *E/H* remains almost constant despite the presence of fracture in the case that no excursion and no slope change in the *P-δ* curve is observed.
3. In such case the coated system can be treated as equivalent to a bulk material.
4. Ignoring the energy dissipated by heat etc, $W_t = W_P + U_{fra} + W_e$, the fraction of plastic work remains the same as in the equivalent bulk materials i.e. $W_t = W_P + W_e^{'}$ (where $W_e^{'} = U_{fra} + W_e$). The total work does not change because fracture only plays a role in converting some stored elastic energy into irreversible work.

The irreversible work minus plastic work can be regarded to be the fracture dissipated energy. This will be discussed in detail in Chapter 7.

2.2.3 Summary

In summary, the stress analysis based models usually require empirical fitting parameters and only deal with specific crack patterns. For instance, it will require different models when dealing with picture frame cracks, spiral cracks etc. In contrast, the energy based models can deal with different cracking patterns without empirical constants given that the specific assumptions outlined in the models can be satisfied. However, they usually require that the crack propagates during the loading cycle only and that residual stress contributions are small, whilst, stress analysis based models can take account of this if carefully constructed.

2.3 Assessment of Interfacial toughness

Prior to evaluation of interfacial toughness, it is necessary to distinguish the different interfacial failure mechanisms. The general failure modes that may generate adhesive failure in coated systems are outlined in the following

Coating failure induced interfacial failure:

(a) Median/radial cracks propagate to the interface and deflect (Warren et al., 1994, Malzbender et al., 2000)

(b) A periodic array of cracks growing through the film may divert to the interface (Thouless, 1991)

Failure starts at the interface:

(a) Crack initiates at the interface and propagates along the interface, or extends into coating or substrate; no buckling occurs

(b) After initial defect formation, the high compressive residual stress leads to buckling (Hutchinson and Suo 1992), (Evans and Hutchinson, 1984), (Chiang et al., 1981)

Substrate failure induced interfacial failure:

A substrate crack may occur at or close to the interface, and divert along it to cause interfacial failure.

The different types of crack modes are also summarized in Fig. 2.22.

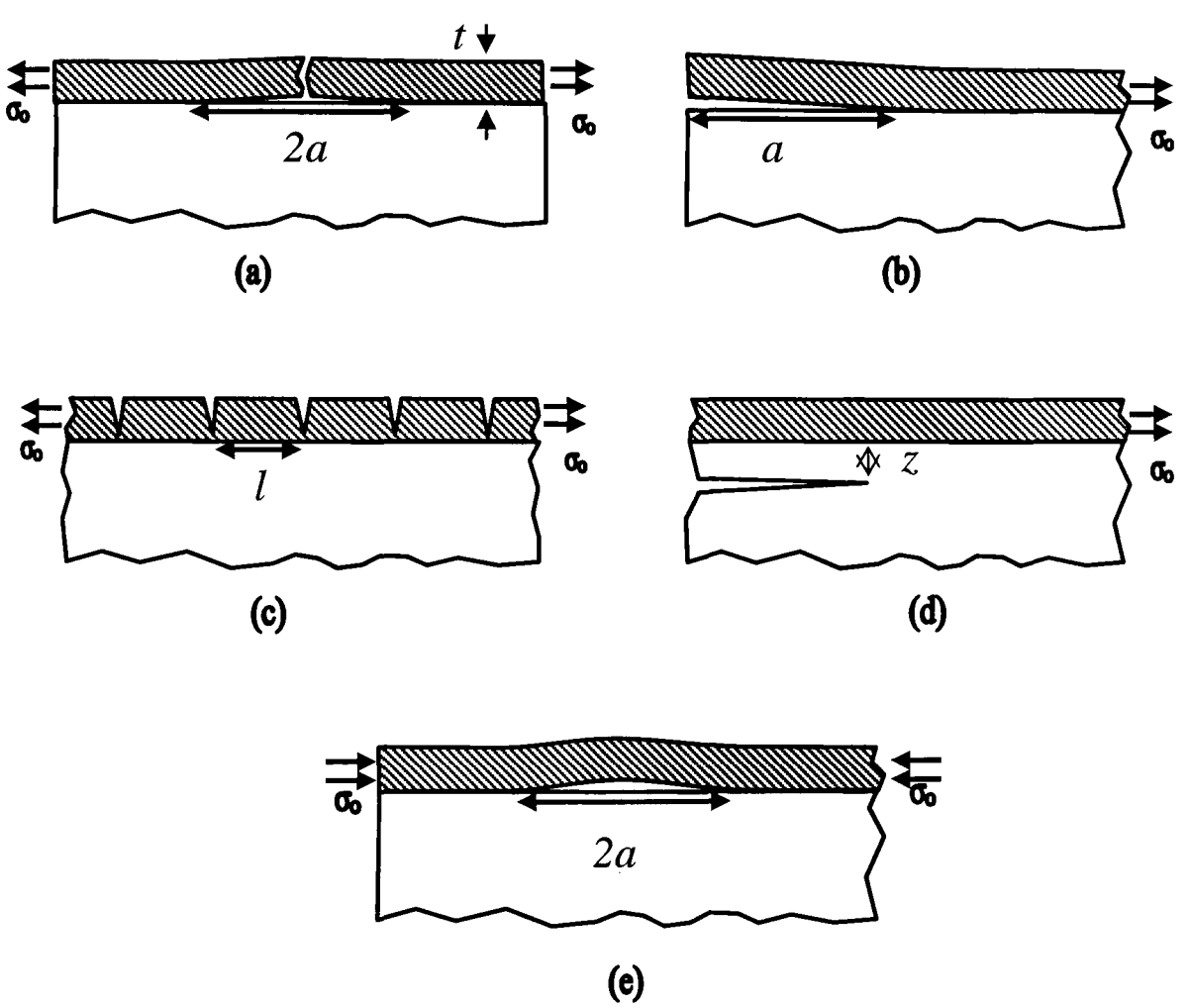

Fig. 2.22. Schematic of different failure modes in coated systems. (a) Delamination at interface from a crack in the coating; (b) delamination resulting from an edge flaw at the interface; (c)multiple cracks in the film (d) fracture in the substrate (e) buckling in the film. After (Thouless, 1991).

2.3.1. Brief review of the techniques for adhesion assessment

There are numerous methods to generate interfacial failure and to assess the interfacial toughness [(Ritter et al., 1989b), (Rosenfeld et al., 1990), (Bull, 1992), (Malzbender and de With, 2002), (Volinsky et al., 2003), (Volinsky et al., 2002), (Malzbender et al., 2003), (Malzbender and de With, 2000b), , (Bull and Berasetegui, 2006)] which are outlined in the following.

Pull-off methods: These methods such as the tape peel test or the tangential shear technique [e.g. (Jacobsson, 1976), (Katz, 1976)]. The tape test uses a pressure sensitive adhesive tape to pull off the coating to determine peel force per unit tape width. It is quite easy to apply. The main disadvantage is that it can be only applied to thick and rather weakly bonded coatings. Alternatively, one may bond rods to the coating and substrate by a structural adhesive and then perform a tensile test to pull off the coating (see Fig. 2.23), which can measure tougher interfaces. However, the perfect alignment necessary to ensure uniform loading across the interface is difficult to achieve in particular for small samples. The mixture of tensile and shear stress during the test leads to difficulty in the interpretation of the results. Also, when the coating becomes thinner, diffusion of the adhesive to the interface may be important. The test is limited by the strengths of available adhesives to interfacial strength less than ~50MPa. For some coating/substrate systems it is possible to braze or weld the rods to increase this maximum strength but with penalty that considerable residual stresses are introduced and the coating/substrate system may be damaged by the bonding process. It actually measures the strength of the interface.

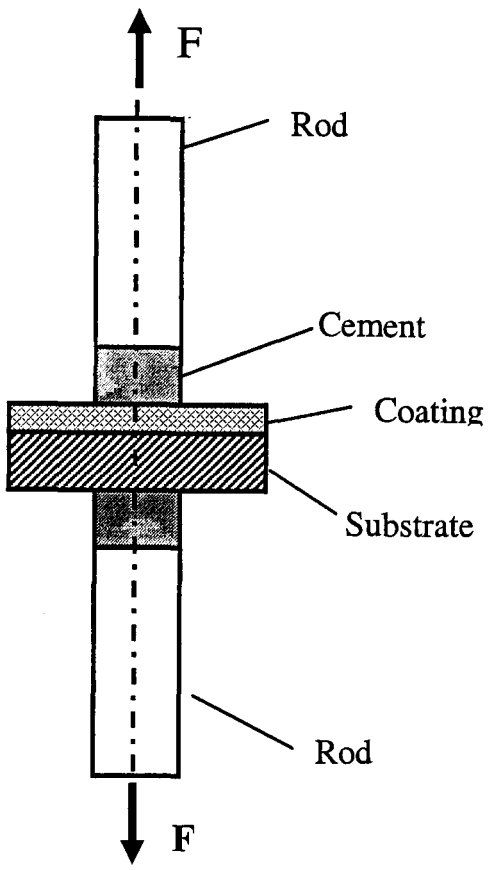

Fig. 2.23. Pull-off adhesion test.

Superlayer test: This requires depositing a thick superlayer on the top of the film of interest so that it increases the apparent film thickness and the total residual stress in the combined coating without altering the tested interface [(Bagchi et al., 1994),(Volinsky et al., 2002)]. This makes it easier to debond the interface. This method is almost always applied to metal-ceramic systems. Although an accurate adhesion strength can be measured by this technique, it requires tedious tests to alter the thickness of and stress within superlayer until controlled delamination occurs and it requires careful choices of a suitable material for the superlayer, which most have a higher adhesion to the test coating than this has to the substrate

.

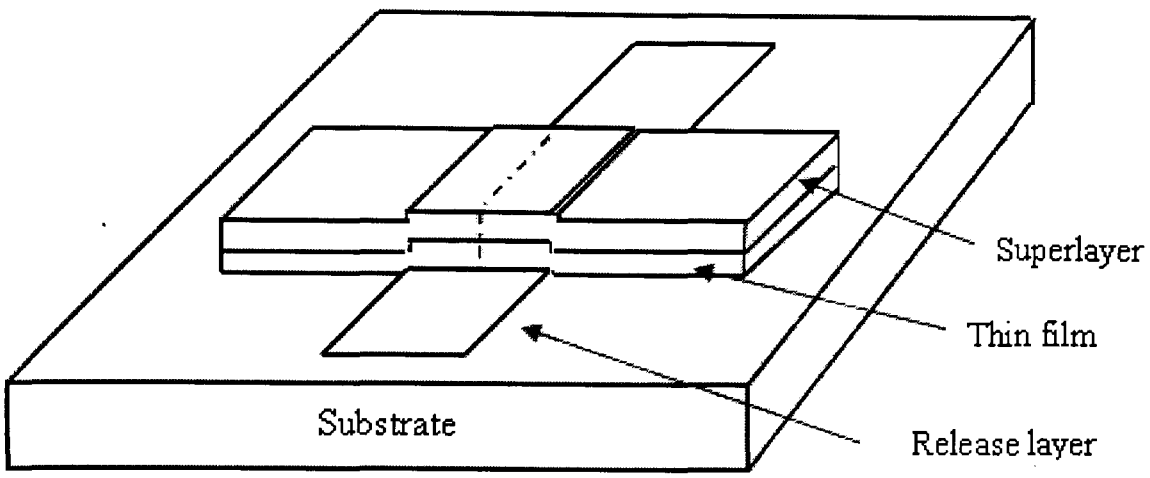

Fig. 2.24 Superlayer adhesion test.

Bending test: This is usually used for metal-ceramics system where through-thickness fracture in the coating diverts to the interface to cause interfacial failure [e.g. (Charalambides et al., 1989), (Harry et al., 1998)]. This method requires a relatively big sample and it cannot account for pre-existing residual stress in the coating (Volinsky et al., 2002). Also this method does not work for ceramic-ceramic systems since it is more likely to cause catastrophic failure of the whole coated system due to the brittle nature of the coating and substrate. However, it is widely used to assess the adhesion of thick ceramic coatings on metallic substrate (e.g. (Harry et al., 1998)).

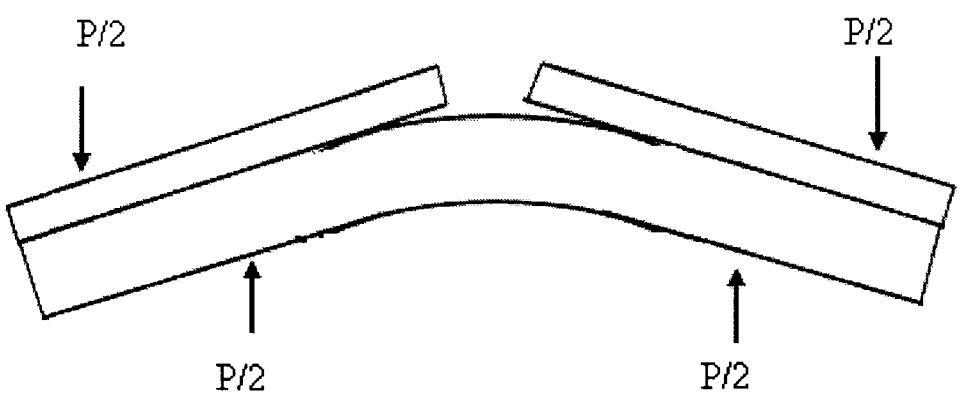

Fig. 2.25 Schematic of the four point bending test for adhesion measurement.

Bulge test: This requires etching the substrate to obtain a free-standing thin film window and the application of pressure on one side to cause deflection of the film. It is relatively straight-forward method to analyse the delamination stresses. However, the etch may lead to contamination of the interface especially for thin ceramic films on ceramic substrates during processing of the free-standing films. It was also argued that it may not work for thin films (<2μm) due to possible wrinkling effects (Small and Nix, 1992).

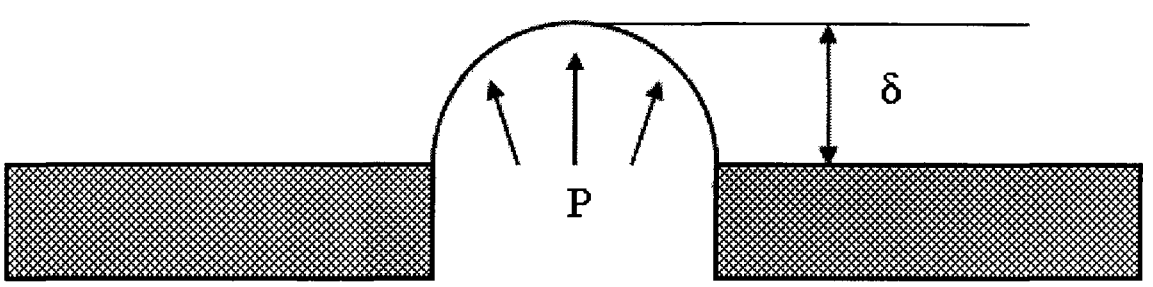

Fig. 2.26. Schematic of Bulge test.

Double Cantilever Beam test: In this test the test coating is bonded between two rigid plates. The energy release rate can be determined by measuring the fracture load, precrack length and the height of specimen [(Ostojic and McPherson, 1988) (Volinsky et al., 2002)]. The advantage is that this method leads to almost pure mode I failure which makes it easier to be analysed. It works well for relatively thick coatings; however, it is difficult to be applied to thin films because it is almost impossible to create a suitable pre-crack.

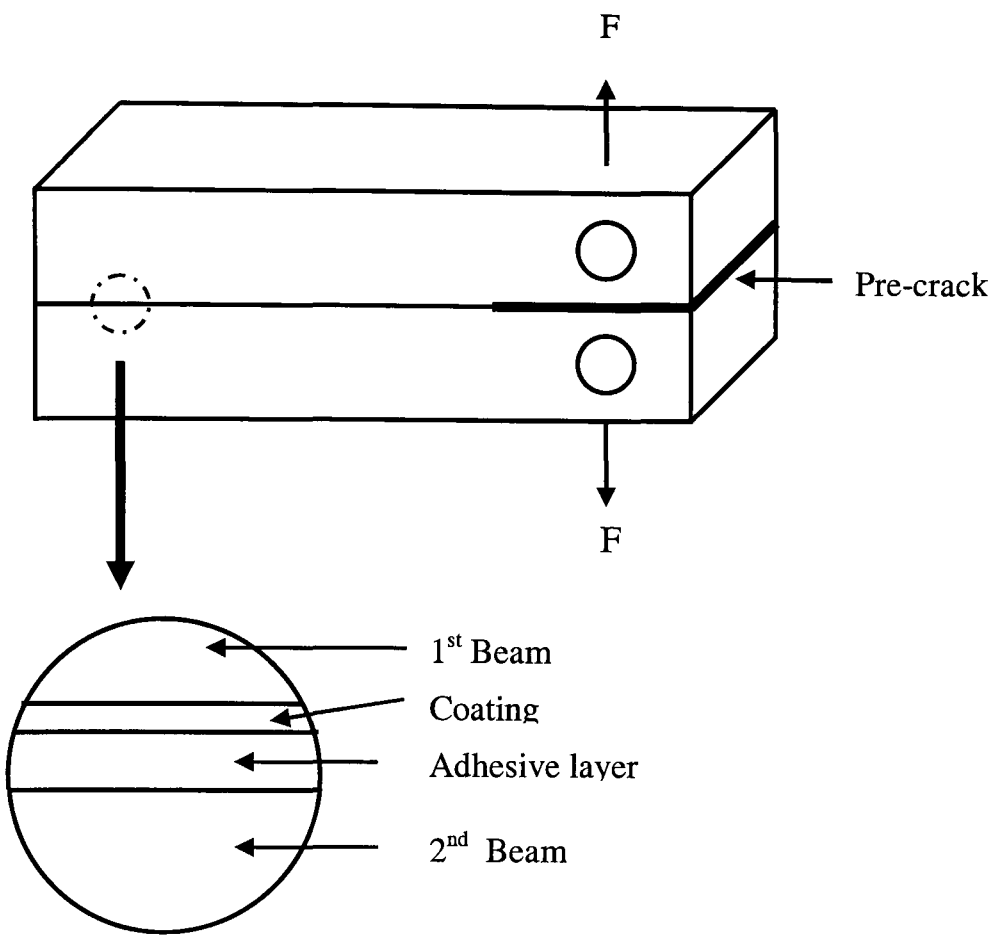

Fig. 2.27 Schematic of the DCB test for the adhesion measurement of plasma sprayed coatings (Ostojic and McPherson, 1988).

Shockwave tests: In this group of tests delamination is produced by shockwave (Gupta et al., 1990). The fracture dissipated energy may come from impact of the erosive particles or from an impinging laser beam. The main problem is that the process of creating the shockwave may influence the surface in particular for thin films. It is also difficult to couple the laser radiation to the surface if the coating or substrate is transparent at the laser wavelength.

Scratch test: This is a simple way to estimate adhesion, which is usually regarded as semi-quantitative because there are a lot of intrinsic (such as instrument-specific) and extrinsic parameters (e.g. coating thickness, substrate hardness) which influence the results. It is very useful for qualitative assessment of hard coatings on a softer substrate (e.g. (Bull, 1992), (Malzbender and de With, 2001a), (Malzbender and de With, 2001b), (Malzbender and de With, 2000b), (Malzbender and de With, 1999),

(Bull and Berasetegui, 2006)). The test involves dragging a stylus across the surface of the coating with a stepwise or continuously increasing normal load until an adhesion related failure occurs at what is termed the critical load, L_c. This critical load is often used to compare different materials but this is only valid if the same failure mode occurs.

For a thin hard coating (<10μm), buckling is the most common failure mode which is usually caused by the compressive stress generated ahead of the moving indenter (see Fig.2.28). Unlike for the case of spontaneous buckling, where a pre-existing interfacial defect is required, the shear stresses associated with plastic deformation in the substrate tend to create a suitable defect with dimensions comparable to scratch width, and buckle failure is widely observed. However, since plastic deformation is responsible for the initial defect the critical load is dependent on substrate hardness and comparisons between coatings on different substrates are difficult to make reliably. For a thicker coating, through thickness cracking is preferred to occur during scratch testing which can lead to wedge spallation (see Fig.2.29). This is because the bending stiffness of the coating has increased. When such wedge spallation occurs comparisons between different coatings are more meaningful and reliable quantification is possible (Bull and Berasetegui, 2006).

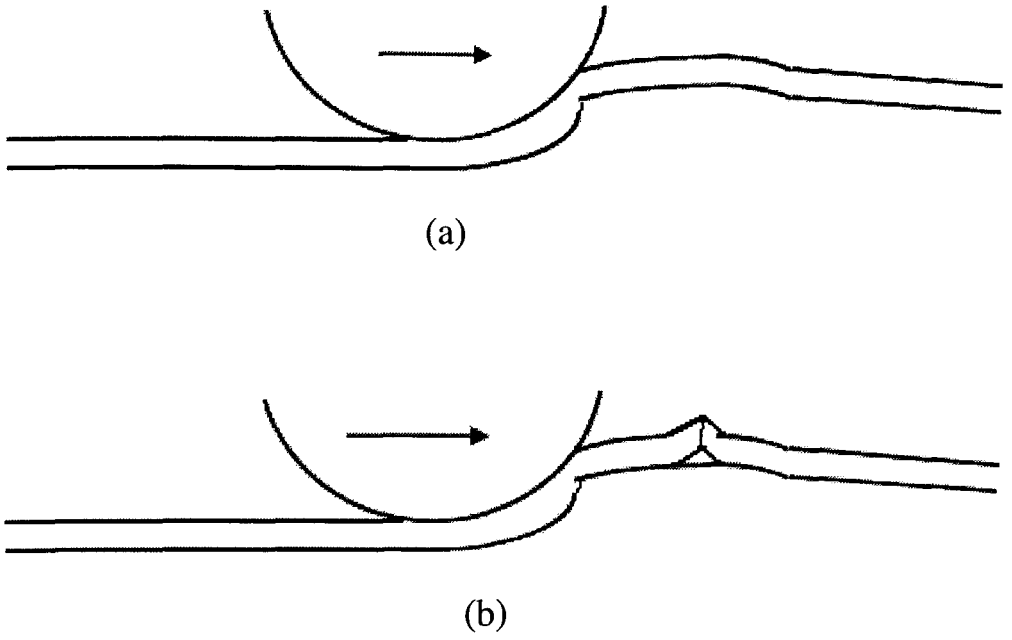

Fig. 2.28. Buckling failure mode in thin coatings during scratch testing : (a) pile-up ahead of the moving indenter; (b) interfacial failure resulting in buckling. After (Bull and Berasetegui, 2006).

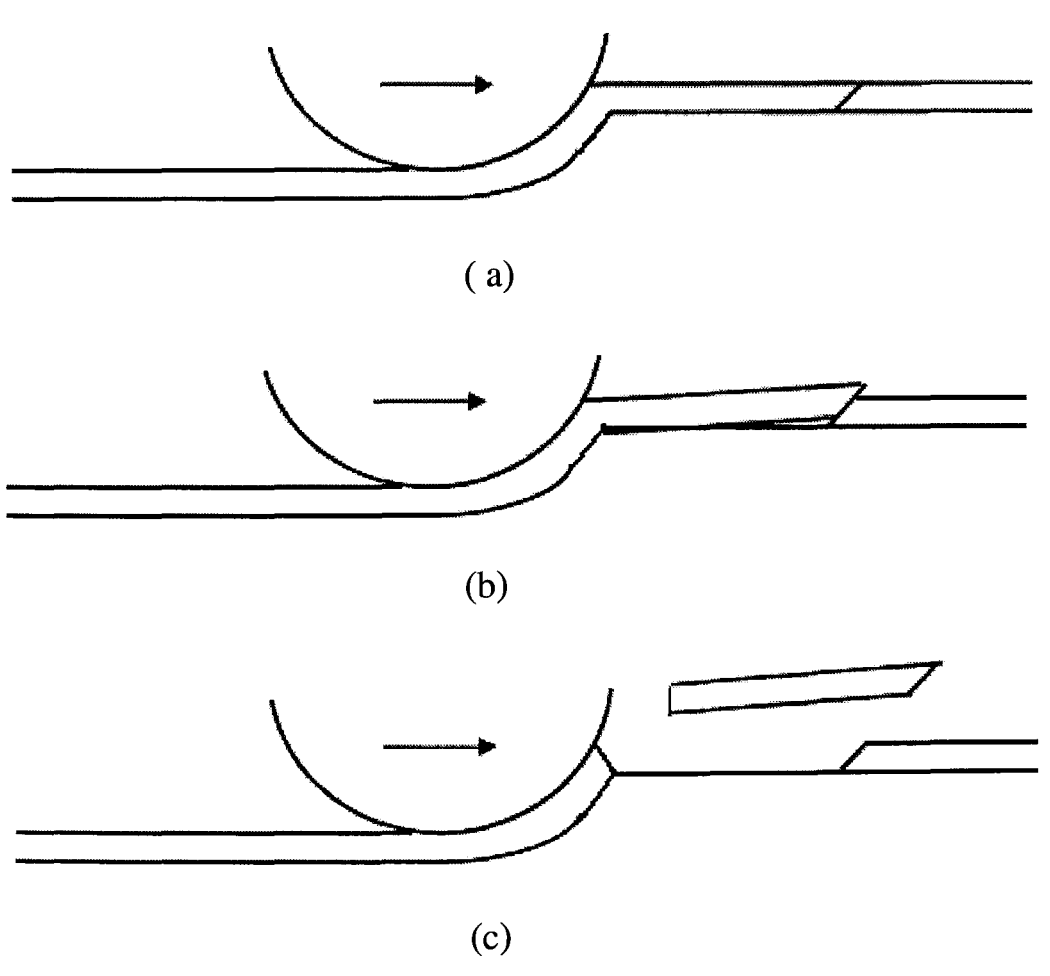

Fig.2.29. Wedge spallation failure mode in thick coatings during scratch testing: (a) wedge crack is generated some distance ahead of the moving indenter; (b) the coating is driven up the wedge opening an interfacial crack (c) through thickness cracking close to indenter leads to spallation. After (Bull and Berasetegui, 2006)

Indentation: For thin films, nanoindentation is a very effective technique to measure the mechanical properties (Oliver and Pharr, 1992) of the coatings such as Young's modulus, hardness, and fracture toughness. If delamination is caused during nanoidentation, the interfacial toughness can also be measured [(Malzbender and de With, 2000a), (den Toonder et al., 2002), (Chen and Bull, 2006a)]. Indentation may cause the nucleation and propagation of an interfacial crack. If the indenter penetration reaches a critical value, the high compressive stress in the coating will lead to double buckling as depicted in Fig.2.31 (if the interfacial toughness is not too high and there is an appropriate interfacial defect). If the crack length does not reach its critical buckling length on each side of indenter, single buckling may occur during unloading cycle (Fig. 2.30). The initial double buckling may change into single buckling during the unloading because the constraint of the coating underneath the indenter is removed. It is also possible that the double buckling remains even after removing the indenter.

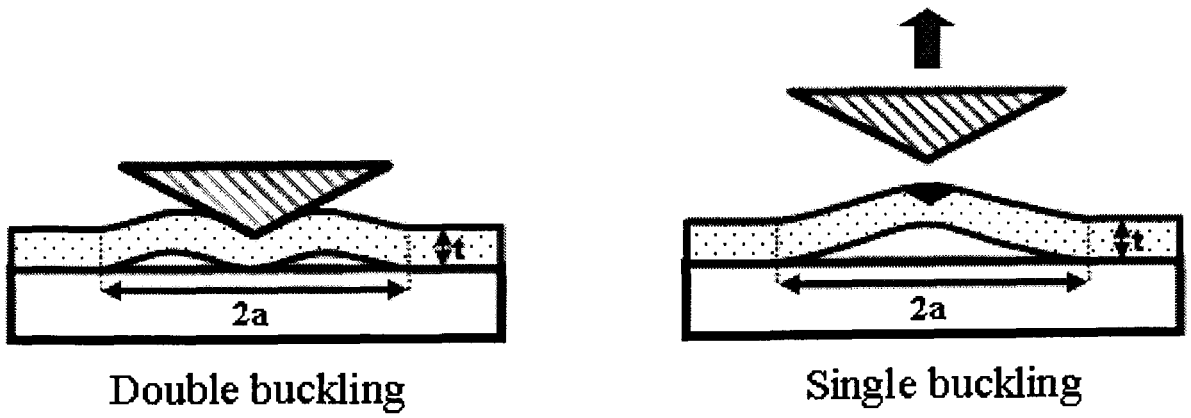

Fig.2.30. Schematic of (a) double buckling forms during loading and (b) single buckling during unloading.

2.3.2 Critical review on adhesion assessment by indentation techniques

Considering the advantage of the ease of test and the convenience of interpretation of the results, the indentation test will be emphasised here. With regard to interfacial toughness assessment by indentation induced delamination, many models have been developed. The existing analytical models mainly are based on linear elastic fracture mechanics (LEFM) but the models have been modified to account for plastic deformation. Energy based models are also valid. The most important models are outlined in the following.

It should be pointed out that all the energy based models in the previous sections can be applied to assess adhesion given that the phenomena described in these models are observed, and they will not be discussed further in this section.

2.3.2.1 Models based on normal indentation techniques

The theoretical approach by He et al (He et al., 1994) analyses the kinking of a crack at and out of the interface between two dissimilar elastic solids, and this forms the basis for the indentation analysis of other workers.

For a soft coating on a rigid substrate, approaches based on contact radius at the initiation of delamination under the indenter have been proposed (Ritter et al., 1989a). The following expression linking interfacial shear strength to coating hardness was given by (Ritter et al., 1989a),

$$\tau_c = \frac{0.56H_c}{K_1'(\phi a_c / t)/\phi K_1(\phi a_c / t) + \nu t / a_c \phi^2} \tag{2.27}$$

Where H_c is the hardness of the coating, K_1 is a modified Bessel function of the second kind, $K_1^{'}$ is the derivative of the function K_1; a_c is the contact radius, and

$$\phi = [6(1-\nu)/(4+\nu)]^{1/2} \tag{2.28}$$

The interfacial toughness, K_{int} is then given by (Mencik, 1996),

$$K_{\text{int}} = \tau_c \sqrt{\pi c_{\text{int}}} \tag{2.29}$$

where interfacial failure was treated as mode I failure and c_{int} is the appropriate flaw size at interface. In this way, Malzbender et al (Malzbender et al., 2000) obtained an average interfacial toughness of 0.18 MPam $^{0.5}$ for their hybrid coatings on glass which falls into the range of results determined previously based on the work by He et al (He et al., 1994). This indicates that this model works well, however, c_{int} is not easy to accurately determine. Therefore, it may be more convenient to relate the interfacial toughness to a crack dimension that can be readily measured.

Thouless (Thouless, 1988) analysed the interfacial fracture toughness based on the decohesion of films with axisymmetric geometries. Following this analysis, Rosenfeld et al (Rosenfeld et al., 1990) proposed the following expression which relates interfacial fracture toughness to coating hardness H, applied load P, and delamination size c,

$$K_{\text{int}} = \frac{0.792H\sqrt{(1-\nu^2)t}}{[1+\nu+2(1-\nu)Hc^2/P]} \tag{2.30}$$

This model assumes that the pressure at the interface is approximately equal to the hardness of the coating, which is reasonable for a sufficiently soft coating compared to its substrate provided that the coating is sufficiently thick. The simplistic form makes it easy to apply (because all the parameters in Eq. (2.30) can be easily obtained), but it may considerably overestimate or underestimate the adhesion in the case that the mechanical property mismatch between the coating and substrate is big

or the plastic deformation of substrate dominates before the delamination occurs. For instance, overestimation was found when applying Eq. (2.30) to sol-gel coatings with the thickness of several micrometers). To account for this deviation, Malzbender et al treated the delamination occurring between radial cracks as three separate circular clamped plates with deflection at the centre instead of the initial assumption (Rosenfeld et al., 1990) of a clamped circular plate without deflection at centre. Thus the buckling stress and shear stress at interface can be reduced by approximately one third (He et al., 1994) and Malzbender et al (Malzbender et al., 2000) obtain reasonable results for interfacial toughness. However, it should be noted that the hybrid coating (H~1.6GPa) is not sufficiently soft compared to its substrate (H~5.9GPa) and the critical indentation penetration of delamination approaches the coating thickness, so that, the deformation of substrate cannot be ignored. This is probably the reason for the overestimation of interfacial fracture toughness by Eq.(2.30). A similar overestimation has also been observed elsewhere (Garcia, 2002). In addition, friction between the fracture faces may also contribute overestimation of the interfacial fracture toughness especially for mode II failure (Suresh et al., 1990).

Alternative approaches were proposed by Thouless (Thouless, 1998) and further developed by den Toonder et al (den Toonder et al., 2002). It was assumed that during indentation or scratch testing the delaminated coating is a partial disk which extends with increasing load and it will buckle when the in-plane stress reaches a critical value. Supposing the driving force for delamination equals critical load for buckling, Thouless derived the following equation for interfacial fracture energy, (Thouless, 1998)

$$G_{\text{int}} = 0.35\frac{Et^5}{L^4}\left(\frac{\tan\beta + 2a/L}{\tan\beta + a/L}\right)^2 \tag{2.31}$$

Where L, a, β are the geometry parameters for the chip as depicted in Fig. 2.31.

Initially, Thouless treated the chip as triangular shape. By considering the curved geometry and the residual stress, σ_r, den Toonder et al modified the model giving [(den Toonder et al., 2002), (Malzbender and de With, 2002)]

$$G_{\text{int}} = 1.42\frac{Et^5}{L^4}\left(\frac{\frac{a}{L}+\frac{\beta\pi}{2}}{\frac{a}{L}+\beta\pi}\right)^2 + \frac{t(1-\nu)\sigma_r^2}{E} + \frac{3.36(1-\nu)t^3\sigma_r}{L^2}\left(\frac{\frac{a}{L}+\frac{\beta\pi}{2}}{\frac{a}{L}+\beta\pi}\right) \qquad (2.32)$$

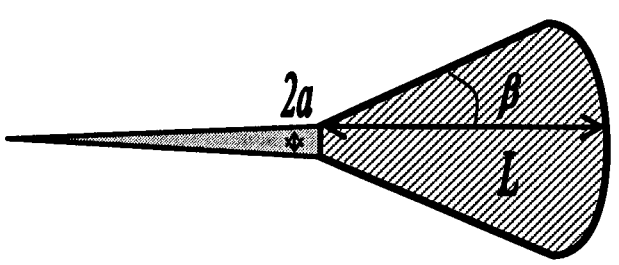

Fig.2.31 Schematic of a chipped area in analysis by Thouless (1998).

Eq.(2.32) provides similar results for experiments carried out by indentation or scratch for sol-gel coatings on glass [(Malzbender and de With, 2001b), (Malzbender and de With, 2001a), (Malzbender et al., 2000)]. The method has been used by other researchers and reasonable results were obtained [(Fernandez-Palacio et al., 2004), (Garcia, 2002)].

Alternatively, Marshall et al developed a model to determine the energy release rate by delamination from comparisons between the unbuckled and buckled coating (Marshall and Evans, 1984). The analysis for a thin film is given for delamination caused by a conical indenter. The strain energy release rate is,

$$G_{\text{int}} = \frac{\frac{1}{2}t\sigma_i^2(1-\nu_f^2) + t(1-\alpha)(1-\nu_f)\left(\sigma_r^2 - (\sigma_i - \sigma_B)^2\right)}{E_f} \tag{2.33}$$

where the subscript f denotes the properties of film, σ_i and σ_B are the indentation stress and buckling stress, respectively. The parameter α is the slope of the buckling load versus the edge displacement which is 0.38 for materials with Poisson's ratio of 1/3. The other parameters are as defined previously.

In the case of non-buckling fracture (α=1), delamination is only driven by the indentation stress and the residual stress does not make contribution. The term α is defined zero if the film does not buckle. The indentation stress is,

$$\sigma_i = \frac{V_i E_f}{2\pi(1-\nu_f)ta^2} \tag{2.34}$$

where V_i is the indentation volume which can estimated based load-displacement curve or the profile of indentation impression; and a is the crack length .

Assuming the crack tip is far from the indenter, then

$$\sigma_B = \frac{\mu^2 t^2 E_f}{12(1-\nu_f)a^2} \tag{2.35}$$

where μ is a boundary condition-dependent constant.

This model was further developed by Hutchinson and Suo (Hutchinson and Suo 1992), such that

$$G_{\text{int}} = \frac{t(1-\alpha)(1-\nu_f)\left(\sigma^2 - {\sigma_C}^2\right)}{E_f} \tag{2.36}$$

$$\alpha = 1 - \frac{1}{1 + 0.902(1 - \nu_f)} \tag{2.37}$$

$$\sigma = \sigma_r + \frac{V_i E_f}{2\pi(1 - \nu_f)ta^2} \tag{2.38}$$

$$\sigma_C = \frac{kt^2 E_f}{12(1 - \nu_f^2)a^2} \tag{2.39}$$

where k=42.67 for a double blister and k=14.68 for a single blister, a is crack length.

All these models treat the buckling as an elastic blister which is reasonable when the crack tip is far from the plastic deformation zone; otherwise plastic deformation must be accounted for (Li and Siegmund, 2004).

2.3.2.2 Some special indentation techniques

In addition to the development and improvement of the models described above, some special indentation techniques have also been proposed. For instance, a test with a special indenter such as the wedge indentation test was proposed to measure adhesion of thin metal lines [(DeBoer and Gerberich, 1996b), (DeBoer and Gerberich, 1996a)] This method is less sensitive to the measurement accuracy of crack length and it is easier to induce interfacial failure compared to the normal indentation test by conical indenters or pyramids due to its geometry. Later it was applied to a brittle coating on a ductile substrate (Vlassak et al., 1997) . For a brittle coating on ductile substrate, a stress analysis based model was derived based on the expanding cavity model. The schematic of the wedge delamination test is depicted in Fig.2.32.

Compared to the axisymmetric indenter test, the radial crack is not a problem in this technique because no tensile hoop stress develops in the coating (Vlassak et al., 1997). The other significant advantage is that this technique is suitable to the study of brittle coatings which has very good adhesion to their substrate which may not be assessed

by the normal axisymmetric indenter. But this model ignores the bending effect in the film and substrate during the indenting cycle thus causing errors especially for ductile substrates (Volinsky et al., 2002).

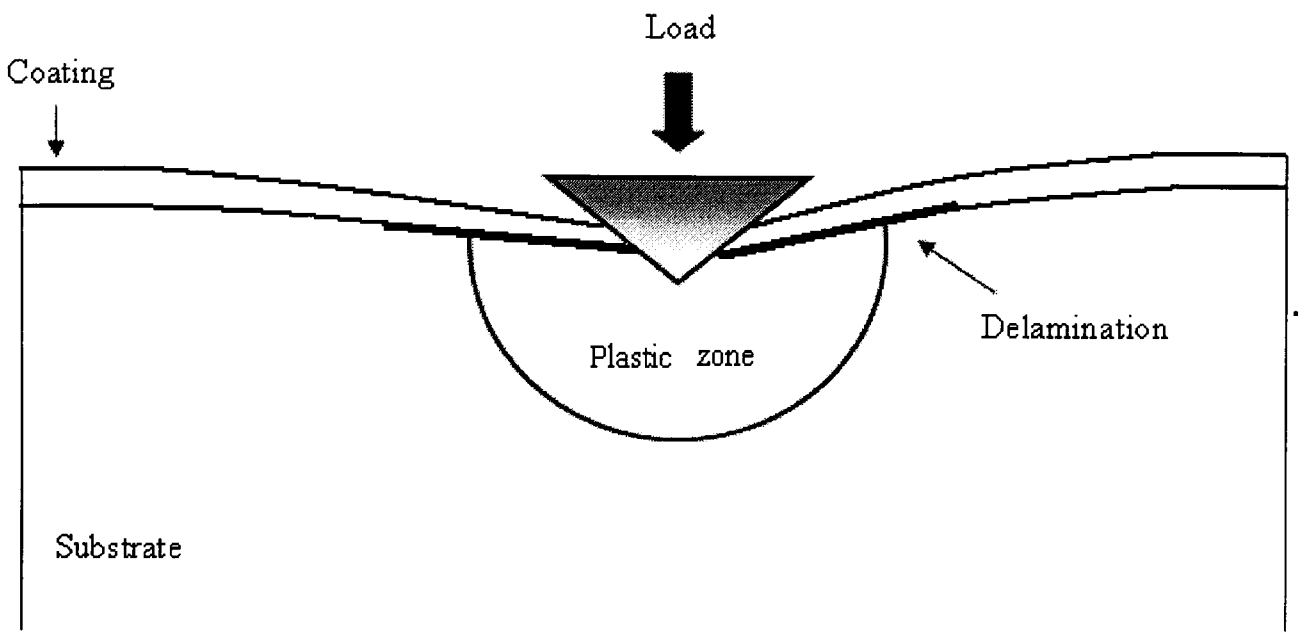

Fig. 2.32. Schematic of the wedge delamination test.

If a ductile coating adheres strongly to the substrate, the above methods will not work since no delamination will occur during normal indentation tests. For this reason, a superlayer indentation test was introduced. A highly stressed hard superlayer was deposited onto the ductile coating which causes addition stress to enhance delamination and eliminate pile-up around the indenter during indentation. By altering the residual stress in the superlayer, it is possible to measure interfacial toughness at different phase angles (Kriese et al., 1999).

In order to eliminate the influence resulting from plastic deformation, in particular, for a ductile coating on a much stiffer substrate, a cross-sectional indentation test was suggested (Demarecaux et al., 1994, Chicot et al., 1996a, Chicot et al., 1996b,

Sanchez et al., 1999). An indentation is made in a polished cross-section in the substrate close to the film interface which then causes delamination (see Fig.2.33). Assuming the interface is a homogeneous material with the Young's modulus and hardness as combined parameters of coating and substrate, analogy to an equivalent bulk material is made and the interfacial toughness is given by (Chicot et al., 1996b),

$$K_{\text{int}} = 0.015(E/H)_{\text{int}}^{1/2} P/a^{3/2} \tag{2.40}$$

where P and a are the critical load and contact radius for the delamination at the interface, respectively.

$$(E/H)_{\text{int}}^{1/2} = \frac{(\frac{E}{H})_s^{1/2}}{1+(\frac{H_f}{H_s})^{1/2}} + \frac{(\frac{E}{H})_f^{1/2}}{1+(\frac{H_s}{H_f})^{1/2}} \tag{2.41}$$

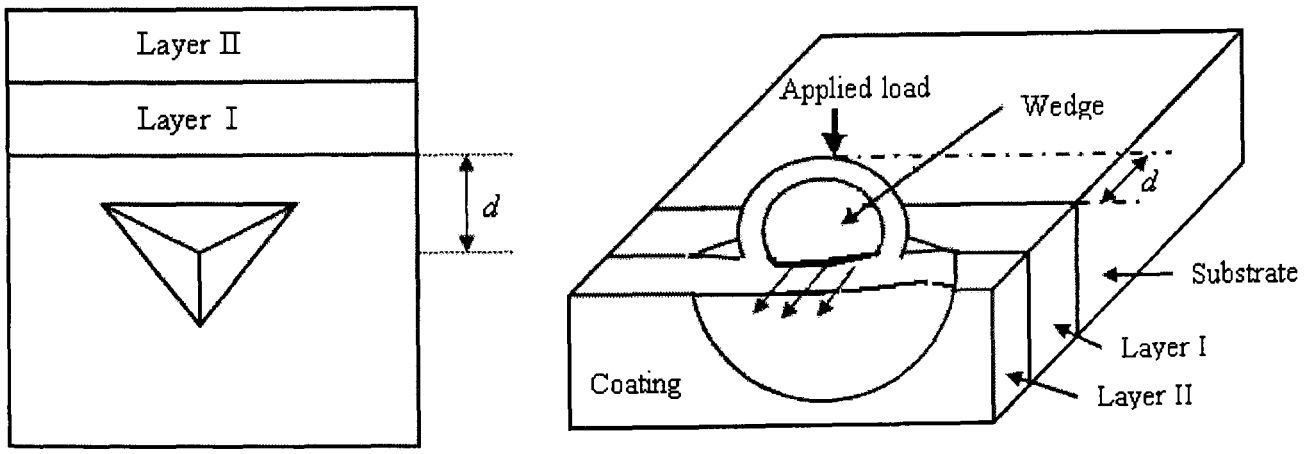

Fig.2.33 Schematic of the cross-section indentation test.

Equations (2.40) and (2.41) provide reasonable results for very thick ceramic (hundreds of micrometers) coatings on steel. However, if the mismatch between the coating and substrate properties is very significant, it is not reasonable to treat the interface as an equivalent bulk as given in equation (2.41).

This method was further developed by Sanchez et al (Sanchez et al., 1999). Based on a plate model, the energy release rate for the interface is given by (Sanchez et al., 1999),

$$G_{\text{int}} = \frac{Et^3 u_0^2}{12(a-b)^4}(1-\lambda)^4(2F+\lambda F') \tag{2.42}$$

$$F(\lambda) = \frac{2\ln\lambda + \frac{1+\lambda}{1-\lambda}\ln^2\lambda}{\left[(1+\lambda)\ln\lambda + 2(1-\lambda)\right]^2} \tag{2.43}$$

where a, b are the delamination radius and contact radius, respectively ; u_0 is the maximum film deflection, t is film thickness, $\lambda=a/b$, and $F' = dF/d\lambda$.

This method is particularly useful for a brittle or ductile coating on a brittle substrate. The crack initiates in the brittle substrate and it will propagate along the weaker interface. The essence of this method is that it induces a pre-crack at the interface. The disadvantage of this method is that there are some critical parameters such as orientation of the indenter tip and the indentation position with respect to the interface (e.g. d in Fig.2.33) for controlled delamination, which must be accurately known.

Interfacial failure can be also assessed based on the phenomena of extra linear elastic recovery during unloading [e.g. (Hainsworth et al., 1998), (Chen and Bull, 2006a)] which will be addressed in Chapter 8.

2.4 Summary

Various models and experimental techniques to assess coating toughness and interfacial toughness have been discussed, among which the models based on nanoindentation experiments have been emphasised. In the next Chapter, the nanoindentation technique will be discussed in detail.

References :

Anstis, G. R., Chantikul, P., Lawn, B. R. and Marshall, D. B. (1981) A Critical-Evaluation of Indentation Techniques for Measuring Fracture-Toughness .1. Direct Crack Measurements,*Journal of the American Ceramic Society,* **64,** 533-538.

Bagchi, A., Lucas, G. E., Suo, Z. and Evans, A. G. (1994) A New Procedure for Measuring the Decohesion Energy for Thin Ductile Films on Substrates,*Journal of Materials Research,* **9,** 1734-1741.

Briard, R., Heitz, C. and Barthel, E. (2005) Crack bridging mechanism for glass strengthening by organosilane water-based coatings,*Journal of Non-Crystalline Solids,* **351,** 323-330.

Broek, D. (1997) *Elementary engineering fracture mechanics,* Kluwer, Dordrecht, The Netherlands.

Bull, S. J., Page, T. F. and Yoffe, E. H. (1989) An Explanation of the Indentation Size Effect in Ceramics,*Philosophical Magazine Letters,* **59,** 281-288.

Bull, S. J. (1992) In *Advanced techniques for Surface Engineering*(Eds, Gissler, W. and Jehn, H. A.) ECSC, EEC, EAEC, Brussels and Luxembourg., pp. 31-68. .

Bull, S. J. (2003) On the origins and mechanisms of the indentation size enect,*Zeitschrift Fur Metallkunde,* **94,** 787-792.

Bull, S. J. and Berasetegui, E. G. (2006) An overview of the potential of quantitative coating adhesion measurement by scratch,*Tribology International,* **39,** 99-114.

Burghard, Z., Zimmermann, A., Rodel, J., Aldinger, F. and Lawn, B. R. (2004) Crack opening profiles of indentation cracks in normal and anomalous glasses,*Acta Materialia,* **52,** 293-297.

Chantikul, P., Anstis, G. R., Lawn, B. R. and Marshall, D. B. (1981) A Critical-Evaluation of Indentation Techniques for Measuring Fracture-Toughness .2. Strength Method,*Journal of the American Ceramic Society,* **64,** 539-543.

Charalambides, P. G., Lund, J., Evans, A. G. and McMeeking, R. M. (1989) A test specimen for determining the fracture resistarim of bimaterial interfaces,*Journal of Applied Mechanics-Transactions of the Asme,* **56,** 77-82.

Chen, J. and Bull, S. J. (2006a) Assessment of adhesion of ceramic coatings,*Proc. 11th International Ceramic Conference, Acireale Sicily, Italy, International*

Conference on Modern Materials & Technologies (CIMTEC 2006) June 4~9, 2006 , in press.

Chen, J. and Bull, S. J. (2006b) A critical examination of the relationship between plastic deformation zone size and Young's modulus to hardness ratio in indentation testing, *J. Mater. Res.2006, in press.*

Chen, J. and Bull, S. J. (2006c) Assessment of the toughness of thin coatings using nanoindentation under displacement control,*Thin Solid Films,* **494,** 1-7.

Chiang, S. S., Marshall, D. B., Lawn, B. R. and Evans, A. G. (1981) In *Surfaces and interfaces in ceramic and ceramic metal systems*(Ed, Evans, P.) Plenum, New York, pp. 603-617.

Chicot, D., Demarecaux, P. and Lesage, J. (1996a) Apparent interface toughness of substrate and coating couples from indentation tests,*Thin Solid Films,* **283,** 151-157.

Chicot, D., Demarecaux, P. and Lesage, J. (1996b) Measurement of the apparent interface toughness by interfacial indentation tests,*Revue De Metallurgie-Cahiers D Informations Techniques,* **93,** 245-&.

Cook, R. F. and Pharr, G. M. (1990) Direct Observation and Analysis of Indentation Cracking in Glasses and Ceramics,*Journal of the American Ceramic Society,* **73,** 787-817.

DeBoer, M. P. and Gerberich, W. W. (1996a) Microwedge indentation of the thin film fine line .1. Mechanics,*Acta Materialia,* **44,** 3169-3175.

DeBoer, M. P. and Gerberich, W. W. (1996b) Microwedge indentation of the thin film fine line .2. Experiment,*Acta Materialia,* **44,** 3177-3187.

Demarecaux, P., Lesage, J., Chicot, D. and Mesmacque, G. (1994) An Examination of the Validity of the Interface Indentation Test - Application to Thermal Sprayed Coatings,*Vide-Science Technique Et Applications,* 524-527.

den Toonder, J., Malzbender, H., de With, G. and Balkenende, R. (2002) Fracture toughness and adhesion energy of sol-gel coatings on glass,*Journal of Materials Research,* **17,** 224-233.

Dukino, R. D. and Swain, M. V. (1992) Comparative Measurement of Indentation Fracture-Toughness with Berkovich and Vickers Indenters,*Journal of the American Ceramic Society,* **75,** 3299-3304.

Emiliani, M. L. (1993) Debond Coating Requirements for Brittle-Matrix Composites,*Journal of Materials Science,* **28,** 5280-5296.

Etienne-Calas, S., Duri, A. and Etienne, P. (2004) Fracture study of organic-inorganic coatings using nanoindentation technique,*Journal of Non-Crystalline Solids,* **344,** 60-65.

Evans, A. G. and Hutchinson, J. W. (1984) On the Mechanics of Delamination and Spalling in Compressed Films,*International Journal of Solids and Structures,* **20,** 455-466.

Fernandez-Palacio, J., Arce-Garcia, I. and Bull, S. J. (2004) Indentation response of fullerene-like CNx,*Tribology International,* **37,** 929-940.

Fett, T. (2002) In *Report. No. FZKA 6757*Forschungszentrum Karlsruhe, , Karlsruhe, Germany.

Field, J. S., Swain, M. V. and Dukino, R. D. (2003) Determination of fracture toughness from the extra penetration produced by indentation-induced pop-in,*Journal of Materials Research,* **18,** 1412-1419.

Garcia, I. A. (2002) Mechanical properties of fullerene-like CNx, Ph.D thesis,University of Newcastle Upon Tyne

Gupta, V., Argon, A. S., Cornie, J. A. and Parks, D. M. (1990) Measurement of Interface Strength by Laser-Pulse-Induced Spallation,*Materials Science and Engineering a-Structural Materials Properties Microstructure and Processing,* **126,** 105-117.

Hainsworth, S. V., McGurk, M. R. and Page, T. F. (1998) The effect of coating cracking on the indentation response of thin hard-coated systems,*Surface & Coatings Technology,* **102,** 97-107.

Harding, D. S., Oliver, W. C. and Pharr, G. M. (1995) "Cracking During Nanoindentation and Its Use in the Measurement of Fracture Toughness",*Materials Research Society Symposium Proceedings* **356,** pp. 663-668.

Harry, E., Rouzaud, A., Ignat, M. and Juliet, P. (1998) Mechanical properties of W and W(C) thin films: Young's modulus, fracture toughness and adhesion,*Thin Solid Films,* **332,** 195-201.

He, M. Y., Evans, A. G. and Hutchinson, J. W. (1994) Crack Deflection at an Interface between Dissimilar Elastic-Materials - Role of Residual-Stresses,*International Journal of Solids and Structures,* **31,** 3443-3455.

Hu, M. S., Thouless, M. D. and Evans, A. G. (1988) The Decohesion of Thin-Films from Brittle Substrates,*Acta Metallurgica,* **36,** 1301-1307.

Hutchinson, J. W. and Suo , Z. (1992) Mixed mode cracking in layered materials.,*Adv. Appl. Mech.,* **29,** 63–191.

Jacobsson, R. (1976) Measurement of Adhesion of Thin-Films,*Thin Solid Films,* **34,** 191-199.

Jang, J., Wen, S., Lance, M. I., Anderson, I. M. and Pharr, G. M.2004Cracking and Phase transformation in Silicon during nanoindentationBoston,MA

Jung, Y. G., Pajares, A., Banerjee, R. and Lawn, B. R. (2004) Strength of silicon, sapphire in the subthreshold flaw and glass region,*Acta Materialia,* **52,** 3459-3466.

Katz, G. (1976) Adhesion of Copper-Films to Aluminum-Oxide Using a Spinel Structure Interface,*Thin Solid Films,* **33,** 99-105.

Korsunsky, A. M., McGurk, M. R., Bull, S. J. and Page, T. F. (1998) On the hardness of coated systems,*Surface & Coatings Technology,* **99,** 171-183.

Kriese, M. D., Gerberich, W. W. and Moody, N. R. (1999) Quantitative adhesion measures of multilayer films: Part I. Indentation mechanics,*Journal of Materials Research,* **14,** 3007-3018.

Kruzic, J. and Ritchie, R. (2003) Determining the toughness of ceramics from Vickers indentations using the crack-opening displacements: An experimental study *Journal of the American Ceramic Society,* **86** 1433-1436

Laugier, M. (1985) Palmqvist crack extension and the center-loaded penny crack analogy *J.Am.Ceram. Soc.,* **68,** C51-C52.

Laugier, M. T. (1987) Palmqvist Indentation Toughness in Wc-Co Composites,*Journal of Materials Science Letters,* **6,** 897-900.

Lawn, B. (1993) *Fracture of Brittle Solids,* Cambridge University Press, Cambridge,UK.

Lawn, B. R., Evans, A. G. and Marshall, D. B. (1980) Elastic/Plastic Indentation Damage in Ceramics: The Median/Radial Crack System,*J. Am. Ceram. Soc.,* **63,** 574.

Li, D. and Anderson, T. (2004) In *http://www.hysitron.com/PDF/1115-001%20Kic%20Sic.pdf*, Vol. 11Oct.2004.

Li, W. Z. and Siegmund, T. (2004) An analysis of the indentation test to determine the interface toughness in a weakly bonded thin film coating substrate system,*Acta Materialia,* **52,** 2989-2999.

Li, X. D., Diao, D. F. and Bhushan, B. (1997) Fracture mechanisms of thin amorphous carbon films in nanoindentation,*Acta Materialia,* **45,** 4453-4461.

Li, X. D. and Bhushan, B. (1998) Measurement of fracture toughness of ultra-thin amorphous carbon films,*Thin Solid Films,* **315,** 214-221.

Lutz, E. H., Swain, M. V. and Cook, P. S. (1994) Significance of Specimen Size for the K(R)-Curve Behavior of Quasi-Brittle Materials,*Journal of the European Ceramic Society,* **13,** 501-507.

Malzbender, J. and de With, G. (1999) Sliding indentation, friction and fracture of a hybrid coating on glass,*Wear,* **236,** 355-359.

Malzbender, J. and de With, G. (2000a) Energy dissipation, fracture toughness and the indentation load-displacement curve of coated materials,*Surface & Coatings Technology,* **135,** 60-68.

Malzbender, J. and de With, G. (2000b) Modeling of the fracture of a coating under sliding indentation,*Wear,* **239,** 21-26.

Malzbender, J. and de With, G. (2000c) Elastic modulus, hardness and fracture toughness of SiO2-filled methyltrimethoxysilane coatings on glass substrates,*Journal of Non-Crystalline Solids,* **265,** 51-60.

Malzbender, J., de With, G. and den Toonder, J. M. J. (2000) Elastic modulus, indentation pressure and fracture toughness of hybrid coatings on glass,*Thin Solid Films,* **366,** 139-149.

Malzbender, J. and de With, G. (2001a) Analysis of scratch testing of organic-inorganic coatings on glass,*Thin Solid Films,* **386,** 68-78.

Malzbender, J. and de With, G. (2001b) Scratch testing of hybrid coatings on float glass,*Surface & Coatings Technology,* **135,** 202-207.

Malzbender, J. and de With, G. (2002) A model to determine the interfacial fracture toughness for chipped coatings,*Surface & Coatings Technology,* **154,** 21-26.

Malzbender, J., Steinbrech, R. W. and Singheiser, L. (2003) Determination of the interfacial fracture energies of cathodes and glass ceramic sealants in a planar solid-oxide fuel cell design,*Journal of Materials Research,* **18,** 929-934.

Marshall, D. B. and Lawn, B. R. (1977) "An Indentation Technique for Measuring Stresses in Tempered Glass Surfaces",*J. Am. Ceram. Soc.,* **60,** 86

Marshall, D. B. and Lawn, B. R. (1979) Residual-Stress Effects in Sharp Contact Cracking .1. Indentation Fracture-Mechanics,*Journal of Materials Science,* **14,** 2001-2012.

Marshall, D. B., Lawn, B. R. and Evans, A. G. (1982) Elastic/Plastic Indentation Damage in Ceramics: The lateral crack system,*J. Am. Ceram. Soc.,* **65.,** 561.

Marshall, D. B. and Evans, A. G. (1984) Measurement of Adherence of Residually Stressed Thin-Films by Indentation .1. Mechanics of Interface Delamination,*Journal of Applied Physics,* **56,** 2632-2638.

Mencik, J. (1996) *Mechanics of components with treated coated surface,* Kluwer, Dordrecht, The Netherlands.

Nakonechna, O., Cselle, T., Morstein, M. and Karimi, A. (2004) On the behaviour of indentation fracture in TiAlSiN hard thin films,*Thin Solid Films,* **447,** 406-412.

Nihara, K., Morena, R. and Hasselman, D. P. H. (1982) Evaluation of KIC of Brittle Solids by the Indentation Method with Low Crack-to-Indent Ratio, *J. Mater. Sci. Lett.* , **1,** 13.

Oliver, W. C. and Pharr, G. M. (1992) An Improved Technique for Determining Hardness and Elastic Modulus Using Load and Displacement Sensing Indentation Experiments,*Journal of Materials Research,* **7,** 1564-1583.

Ostojic, P. and McPherson, R. (1988) Determining the Critical Strain-Energy Release Rate of Plasma-Sprayed Coatings Using a Double-Cantilever-Beam Technique,*Journal of the American Ceramic Society,* **71,** 891-899.

Page, T. F. and Hainsworth, S. V. (1993) Using Nanoindentation Techniques for the Characterization of Coated Systems - a Critique,*Surface & Coatings Technology,* **61,** 201-208.

Pharr, G. M., Harding, D. S. and Oliver, W. C. (1993) *Mechanical Properties and deformation behaviour of materials having ultra-fine microstructure,* Klumer Academic press.

Pharr, G. M. (1998) Measurement of mechanical properties by ultra-low load indentation,*Materials Science and Engineering a-Structural Materials Properties Microstructure and Processing,* **253,** 151-159.

Ritter, J., Lardner, T., Rosenfeld, L. and Lin, M. (1989a) Measurement of adhesion of thin polymer coatings by indentation.,*J. Appl. Phys.,* **66,** 3626-3634.

Ritter, J. E., Lardner, T. J., Rosenfeld, L. and Lin, M. R. (1989b) Measurement of Adhesion of Thin Polymer-Coatings by Indentation,*Journal of Applied Physics,* **66,** 3626-3634.

Rosenfeld, L. G., Ritter, J. E., Lardner, T. J. and Lin, M. R. (1990) Use of the Microindentation Technique for Determining Interfacial Fracture Energy,*Journal of Applied Physics,* **67,** 3291-3296.

Sanchez, J. M., El-Mansy, S., Sun, B., Scherban, T., Fang, N., Pantuso, D., Ford, W., Elizalde, M. R., Martinez-Esnaola, J. M., Martin-Meizoso, A., Gil-Sevillano, J., Fuentes, M. and Maiz, J. (1999) Cross-sectional nanoindentation: A new technique for thin film interfacial adhesion characterization,*Acta Materialia,* **47,** 4405-4413.

Scharf, T. W., Deng, H. and Barnard, J. A. (1997) Mechanical and fracture toughness studies of amorphous SiC-N hard coatings using nanoindentation,*Journal of Vacuum Science & Technology a-Vacuum Surfaces and Films,* **15,** 963-967.

Scholz, T., Schneider, G. A., Munoz-Saldana, J. and Swain, M. V. (2004) Fracture toughness from submicron derived indentation cracks,*Applied Physics Letters,* **84,** 3055-3057.

Small, M. K. and Nix, W. D. (1992) Analysis of the Accuracy of the Bulge Test in Determining the Mechanical-Properties of Thin-Films,*Journal of Materials Research,* **7,** 1553-1563.

Stein, W. (2005), Private communication

Suresh, S., Shih, C. F., Morrone, A. and Odowd, N. P. (1990) Mixed-Mode Fracture-Toughness of Ceramic Materials,*Journal of the American Ceramic Society,* **73,** 1257-1267.

Tanaka, K. (1984) Evaluation of Elastic Plastic Indentation Stress to Determine Fracture-Toughness,*Journal of the Japan Institute of Metals,* **48,** 1157-1162.

Thouless, M. D. (1988) Decohesion of Films with Axisymmetric Geometries,*Acta Metallurgica,* **36,** 3131-3135.

Thouless, M. D. (1991) Cracking and Delamination of Coatings,*Journal of Vacuum Science & Technology a-Vacuum Surfaces and Films,* **9,** 2510-2515.

Thouless, M. D. (1998) An analysis of spalling in the microscratch test,*Engineering Fracture Mechanics,* **61,** 75-81.

Tuck , J. R. and Korsunsky, A. M. (2000) In *13th European Conference on Fracture, http://www.eng.ox.ac.uk/~ftgamk/ecf13.pdf 27Nov.2004*san sebastian, Spain.

Tuck, J. R., Korsunsky, A. M., Bhat, D. G. and Bull, S. J. (2001) Indentation hardness evaluation of cathodic are deposited thin hard coatings,*Surface & Coatings Technology,* **139,** 63-74.

Vlassak, J. J., Drory, M. D. and Nix, W. D. (1997) A simple technique for measuring the adhesion of brittle films to ductile substrates with application to diamond-coated titanium,*Journal of Materials Research,* **12,** 1900-1910.

Volinsky, A. A., Moody, N. R. and Gerberich, W. W. (2002) Interfacial toughness measurements for thin films on substrates,*Acta Materialia,* **50,** 441-466.

Volinsky, A. A., Vella, J. B. and Gerberich, W. W. (2003) Fracture toughness, adhesion and mechanical properties of low-K dielectric thin films measured by nanoindentation,*Thin Solid Films,* **429,** 201-210.

Warren, P. D., Hills, D. A. and Roberts, S. G. (1994) Surface Flaw Distributions in Brittle Materials and Hertzian Fracture,*Journal of Materials Research,* **9,** 3194-3202.

Chapter 3:

Nanoindentation techniques

Chapter 3: Nanoindentation techniques

Nanoindentation techniques have been widely used to investigate the mechanical behaviour of coated systems (e.g.(Oliver and Pharr, 1992b), (Page et al., 1992), (Page and Hainsworth, 1993), (Bull et al., 1994, Page and Hainsworth, 1995), (Berasategui and Page, 2003) because this allows measurement at very small scales (i.e. submicrometer or nanometer scale) and it makes it feasible to obtain a range of mechanical properties such as hardness, elastic modulus and fracture toughness of coatings independent of their substrates. This chapter aims to explain the use of nanoindentation and the factors which limit its application for coated systems.

3.1 What is nanoindentation?

Nanoindentation is a technique in which a continuous record of the applied load and displacement is made during indentation. The nanoindentation load-displacement (P-δ) curve provides a "mechanical fingerprint" of a material response (Hainsworth and Page, 1994a). Nanoindentation not only reduces the spatial scale of the test compared to traditional indentation methods but also makes it possible to estimate properties such as hardness and elastic modulus without reliance on post-facto microscopy to measure the small indentations formed for many materials. However, post-facto microscopy is still very important if more details (such as pile-up, cracking, delamination, phase transformation etc) about the deformation response are required.

The basic parameters in a load-displacement curve are introduced in the following; they are very useful to derive the mechanical properties of both bulk materials and coatings. Fig. 3.1 displays a typical load-displacement curve (P-δ) from a

nanoindentation test. The basic parameters available from the curve are (Page and Hainsworth, 1993),

- P_{max}, the maximum applied load.
- S, the contact stiffness at peak load calculated from the slope of the upper part of the unloading curve (Doerner and Nix, 1986, Oliver and Pharr, 1992a).
- δ_{max}, the maximum displacement at the indenter at the maximum applied load. This indicates both the plastic depth of the impression and the elastic deflection of the surface.
- δ_c, the contact depth, which is the actual depth that the indenter in contact with material in the absence of elastic deflection of the surface.
- δ_{res}, the residual displacement after the elastic recovery of the material.
- W_p, the plastic work of indentation (the area within the loading and unloading curves, see Fig. 3.1)
- W_e, the elastic work of indentation (the area under the unloading curve from δ_{res} up to δ_{max}, see Fig. 3.1)
- W_t, the total work of indentation (the area under the loading curve up to δ_{max}).
- $\%R$, the percentage of elastic recovery, *i.e.* $R = \frac{\delta_{max} - \delta_{res}}{\delta_{max}} x100\%$, which is a good indicator for the extent of elastic recovery.
- **Segment AB**, the elastic portion of the loading curve where $P \alpha \delta^{1.5}$.
- **Segment BC,** the transition from elastic behaviour to elastic-plastic behaviour.
- **Segment CD,** the plastic portion of the loading curve where $P \alpha \delta^2$
- **Segment DE,** the initial part of the unloading curve where the recovery of the surface flexure occurs. No change of indent shape occurs in this range.
- **Segment EF,** the region in which full elastic recovery occurs, and the impression changes shape.

Based on the parameters above, the basic mechanical properties such as elastic modulus and hardness can be obtained as discussed in section 3.2.1. However, Fig.3.1 only provides a standard load-displacement curve which does not include many features occurring in actual bulk materials and coatings. For example, creep in metals

(Lucas and Oliver, 1999, Asif and Pethica, 1997), cracks in brittle materials (McGurk and Page, 1999), (Li et al., 1997), (Li and Bhushan, 1998), dislocation bursts in crystalline materials (Page et al., 1992), (Page et al., 1998), phase transformations in many semi-conductors (Pharr et al., 1991), (Page et al., 1992), all may result in additional features in the load-displacement curves which can be used to derive other mechanical properties which will be discussed in section 3.3.

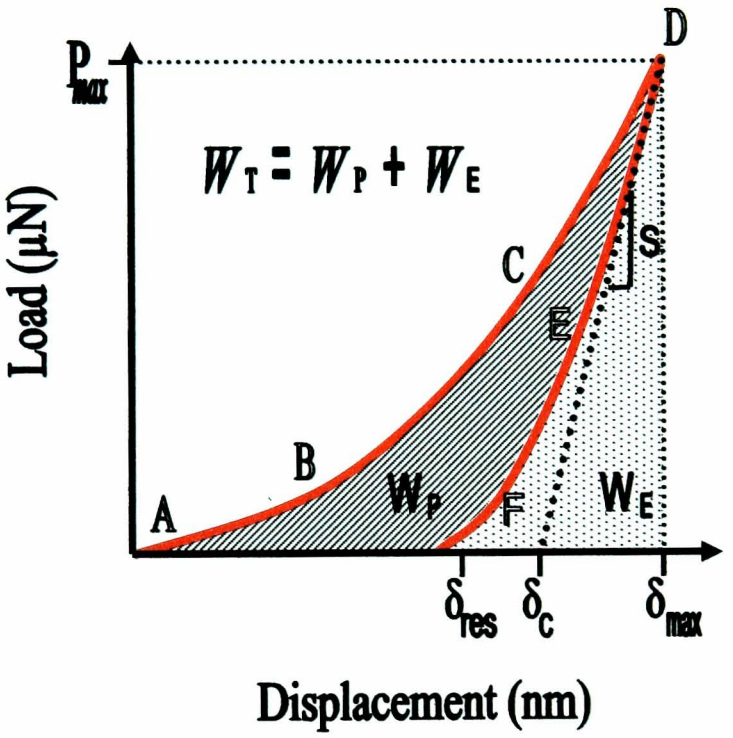

Figure 3.1 Schematic of a typical load displacement-curve for an elastic-plastic material indented by a pyramidal tip, with the basic parameters explained in text.

3.2 Extracting mechanical properties from P-δ curves

3.2.1 Extracting elastic modulus and hardness

3.2.1.1 Unloading curve analysis

By extending the methods proposed by Loubet et al (Loubet et al., 1984) and Doerner and Nix (Doerner and Nix 1986), Oliver and Pharr (Oliver and Pharr, 1992b) developed the normally used method to obtain hardness and elastic modulus.

Based on the analysis for the elastic unloading of a flat punch, it was suggested that the elastic modulus can be given by (Sneddon, 1965),

$$S = \frac{2}{\sqrt{\pi}} E_r \sqrt{A_C} \tag{3.1}$$

Considering that a Berkovich tip is actually not axially symmetric, an extra parameter β (β=1.034) is introduced to correct this (King and Osullivan, 1987), which has been widely adopted. If considering a flat-ended triangular tip, the value of β will be a little higher (Vlassak and Nix, 1994). Since most indenters are not flat punches, a correction for the elastic radial inward displacement (see Fig.3.2) in the Sneddon equation (i.e. Equation (2.2) in section 2) when indenting an elastic half space by a rigid indenter is required. This correction factor γ is given by Hay et al (Hay et al., 1999) .

$$\gamma = \pi \frac{\frac{\pi}{4} + 0.15483073 \cot\theta \frac{(1-2\nu)}{4(1-\nu)}}{\left(\frac{\pi}{2} - 0.83119312 \cot\theta \frac{(1-2\nu)}{4(1-\nu)}\right)^2} \tag{3.2a}$$

where θ is the half included angle of the indenter (which in the case of a Berkovich is 70.32°) and ν is the Poisson's ratio of the material indented. For a very sharp tip (e.g. cube corner indenter (θ= 42.28°)) the expression derived for γ is:

$$\gamma = 1 + \frac{(1-2\nu)}{4(1-\nu)\tan\theta} \tag{3.2b}$$

Taking these corrections into consideration, equation (3.1) can be re-written,

$$S = \beta\gamma \frac{2}{\sqrt{\pi}} E_r \sqrt{A_C} \tag{3.3}$$

Where the E_r is the reduced modulus which is given by,

$$\frac{1}{E_r} = \frac{(1-\nu_s{}^2)}{E_s} + \frac{(1-\nu_i{}^2)}{E_i} \tag{3.4}$$

The subscripts i and s refer to the indenter and specimen, respectively. For a diamond tip (used in this study), E_i =1141 GPa and the Poisson's ratio, ν_i is 0.070. For many ceramics and metals, a value of ν=0.25 can be used without introducing significant errors into the moduli values calculated.

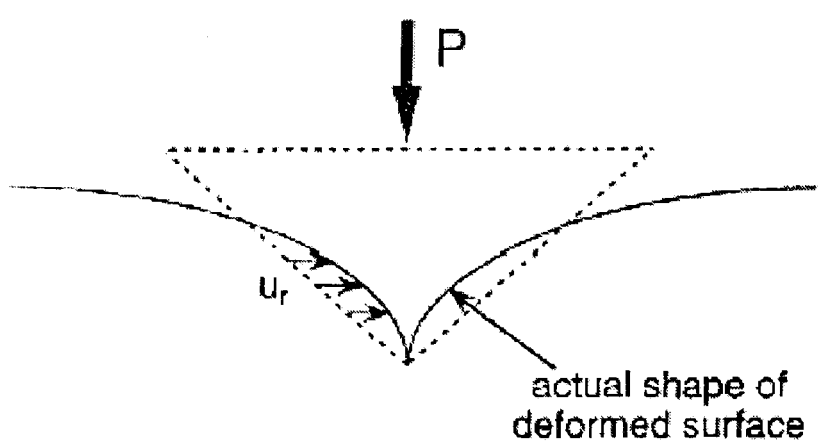

Fig. 3.2 Schematic representation of the actual deformed surface which considers the radial displacement. The inward displacement taken from (Hay et al., 1999) is exaggerated .

In order to obtain the stiffness S, it is necessary to analyse the unloading curve. Oliver and Pharr found that the unloading curve or even the upper part of the unloading curve generated by flat punch in contact with a flat surface is better described by a power law rather than linear relationship proposed by Sneddon, i.e. the unloading curve is given by,

$$P = B\left(\delta - \delta_{res}\right)^{m} \tag{3.5}$$

where B and m are fitting constants. Thus, the initial unloading slope (i.e. stiffness) is given by,

$$S = \left.\frac{dP}{d\delta}\right|_{\delta=\delta_{\max}} = mB\left(\delta_{\max} - \delta_{res}\right)^{m-1} \tag{3.6}$$

The analytical solution was initially developed for a flat punch indenter, but it was shown that equation (3.6) is valid for any self-similar indenter which could be described as a solid of revolution of a smooth function, such as a cone, sphere, paraboloid of revolution, or ellipsoid of revolution. It provides reasonable results for often used pyramids which can not be considered as a body of revolution (Pharr et al., 1992b), analysed in terms of an equivalent cone (Johnson,1970).

A schematic drawing of a cross section of an indentation given by Oliver and Pharr is displayed in Fig. 3.3.

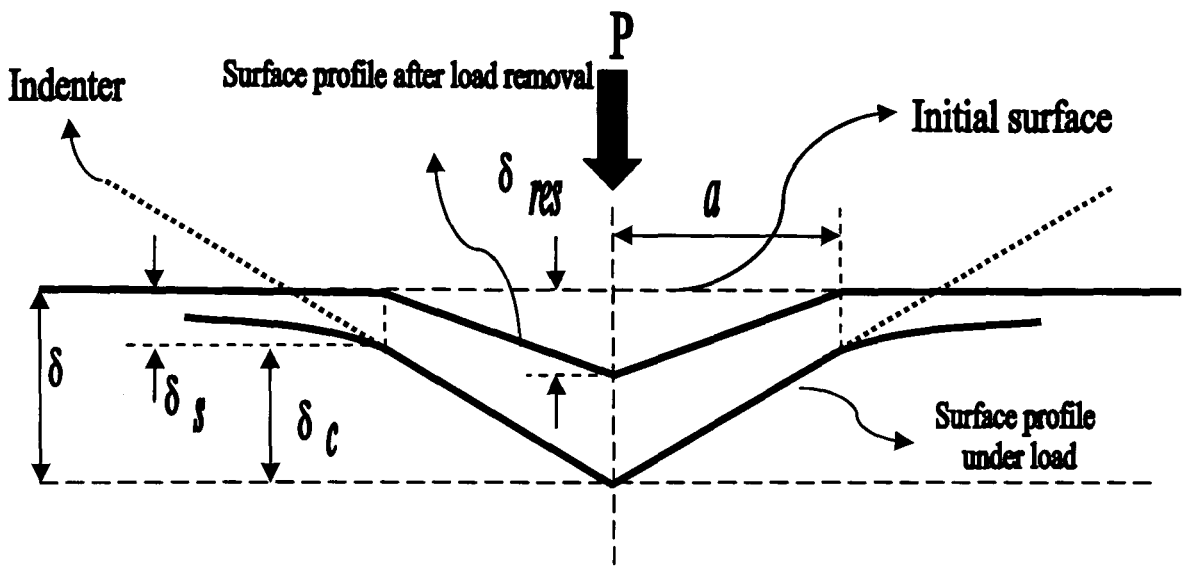

Figure 3.3. Schematic drawing of a cross-section of an indentation marking various parameters used in the analysis of Oliver and Pharr (1992a). Pile-up and sink-in is ignored here.

The total displacement, δ, is given by,

$$\delta = \delta_c + \delta_s \tag{3.7}$$

where δ_c is the contact depth as depicted in Fig. 3.3. δ_s is the vertical distance from the original surface to the perimeter of the indentation under load and is given by,

$$\delta_s = \varepsilon \frac{P_{\max}}{S} \tag{3.8}$$

where ε is a geometric constant which can be experimentally determined or calculated from Finite Element Analysis (FEA). For a typical pyramid indenter (such as a Berkovich tip) $\varepsilon = 0.75$; for a conical tip equivalent to a Berkovich tip, $\varepsilon = 0.72$; for a flat punch, $\varepsilon = 1$.

The hardness is given by,

$$H = \frac{P}{A(\delta_C)} \tag{3.9}$$

From equation (3.3) and equation (3.9), it can be seen that it is necessary to determine the contact area A_c so that the mechanical properties hardness and elastic modulus can be determined. Given that the deformation of the indenter during nanoindentation can be ignored (i.e. it is much stiffer than the materials under test), it is assumed that the contact area can be expressed as a function of the contact depth (Pethica et al., 1983, Oliver et al., 1986).

No indenter is perfect and thus for a pyramid tip or its equivalent conical tip, the area function at high load is given by,

$$A_C(\delta_C) = C_0\delta_C{}^2 + C_1\delta_C^1 + C_2\delta_C^{1/2} + C_3\delta_C^{1/4} + \cdots + C_8\delta_C^{1/128} \tag{3.10}$$

where, C_0=24.5 and 2.596 for Berkovich and cube corner indenters, respectively. The constants C_1 to C_8 are fitting parameters which are obtained by calibration tests on fused quartz, a material with well known mechanical properties which shows homogeneity of mechanical properties with depth. For a perfect tip, constants C_1 to C_8 are zero. The reason about the choice of this fitting function is strictly for its ability to fit data over a wide range of depths and not because it has any physical significance. It is quite convenient in describing a number of important indenter geometries.

Actually, the main additional factors which influence the measurement of hardness and elastic modulus by Oliver and Pharr method are pile-up and sink-in which will be discussed in Section 3.3.

3.2.1.2 Method based on work of indentation

The hardness of a material can also be obtained through the energy expenditure per unit volume during indentation, which is the work of indentation method first proposed by Stilwell and Tabor in 1961 (Stilwell and Tabor, 1961). The hardness can be expressed by plastic work (W_p) divided by the plastically deformed volume (V_p), i.e,

$$H = \frac{P}{A} = \frac{W_p}{V_p} \tag{3.11a}$$

$$W_p = W - W_e \tag{3.11b}$$

Where W, the total work of indentation (i.e. the total area under the loading curve) and W_e, the elastic work (i.e. the area under the unloading curve) can be easily obtained from load-displacement curve.

If it is assumed that the maximum depth over contact depth (δ_m / δ_c) is a constant, the contact area can be given by $A_c = k\delta_m^2$, where δ_m is the maximum penetration and k is a constant dependent on the geometry. Thus,

$$\left.\begin{aligned} P_m &= Hk\delta_m^2 \\ W &= \int_0^{\delta m} P d\delta \end{aligned}\right\} \Rightarrow W = \frac{kH}{3}\delta_m^3 \tag{3.12}$$

Therefore,

$$\left.\begin{aligned} P_m &= Hk\delta_m^2 \\ H &= \frac{3W}{k\delta_m^3} \end{aligned}\right\} H = \frac{P_m^3}{9kW^2} \tag{3.13}$$

It was shown that hardness obtained by this method agrees well with the values determined by Oliver and Pharr method at big loads, in which case the tip geometry effects are not important (Tuck et al., 2001, Bull, 2002). However, Malzbender and de With (Malzbender and de With, 2002b) demonstrated that for highly elastic materials, this method leads to big errors, up to 70% when the *H/E* ratio is higher than 0.025. The problem of this method is that *k* is a material dependent parameter rather than a geometrical related constant because it depends on the ratio of contact depth over maximum depth which is actually not a constant which is discussed in the following.

Combining the analysis about nanoindentation discussed previously, we obtain,

$$\left.\begin{aligned} \delta_m - \delta_c &= \varepsilon\frac{P_m}{S} \\ S &= \frac{2E_r}{\sqrt{\pi}}\sqrt{A_c} \\ H &= \frac{P_m}{A_c} \end{aligned}\right\} \delta_m = \left[1 + \frac{\pi}{2}\varepsilon\frac{H}{E_r}\tan(\theta)\right]\delta_c \tag{3.14}$$

From Equation (3.14), it is obvious that the ratio between the contact depth and maximum depth is not a constant but related to the hardness over elastic modulus of the materials.

3.2.1.3 Method of Loading curve analysis

During loading, for a non-adhesive conical punch with apical angle θ in contact with a smooth flat elastic body (Sneddon, 1965), the load can be expressed as ,

$$P = \frac{2E\tan\theta}{(1-\nu^2)\pi}\delta^2 \tag{3.15}$$

Based on dimensional analysis, a similar relationship between applied load and displacement is found (Cheng and Cheng, 1998b) and it is given by,

$$P = K_m\delta^2 \tag{3.16}$$

where K_m is a constant dependent on E, ν, the yield stress, Y, and the half-included angle of the indenter, θ. It is assumed that the elastic and plastic behaviour could be split in two parts (Loubet et al., 1986),

$$P = K_p{\delta_p}^2 \tag{3.17a}$$

$$P = K_e{\delta_e}^2 \tag{3.17b}$$

where K_p is a function of Y and K_e is a function of E, ν and θ.

Since $\delta = \delta_p + \delta_e$, combining Eq.(3.16) and (3.17) yields,

$$(K_m)^{-\frac{1}{2}} = \left[(K_e)^{-1/2} + (K_p)^{-1/2}\right] \tag{3.18}$$

Equation (3.18) can be expressed in terms of the Vickers Hardness (H_V) (Loubet et al., 1986) as,

$$K_m = \left[0.92 \left(\frac{1-\nu^2}{E} \right) \sqrt{H_V} + \frac{0.194}{\sqrt{H_V}} \right]^{-2} \tag{3.19}$$

This work was further developed by Hainsworth et al (Hainsworth et al., 1996) . Since for conical and pyramidal indenters, the plastic depth is directly related to the characteristic contact radius, which is given by,

$$\delta_p = \varphi \cdot a_c = \phi \sqrt{\frac{P}{H}}, \quad \phi = \pi\varphi \tag{3.20}$$

Here ϕ is an empirical constant which depends on the geometry of the indenter used. By dimensional analysis, the elastic displacement is given by,

$$\delta_e = \psi \frac{P}{E a_c} = \psi \frac{P}{E} \sqrt{\frac{H}{P}} \tag{3.21}$$

where ψ is another empirical constant.

Thus,

$$\delta = \delta_p + \delta_e = \phi \sqrt{\frac{P}{H}} + \psi \frac{P}{E} \sqrt{\frac{H}{P}} \tag{3.22}$$

If it is assumed that $P=K_m\delta^2$, then,

$$K_m = E \left(\phi \sqrt{\frac{E}{H}} + \psi \sqrt{\frac{H}{E}} \right)^{-2} \tag{3.23}$$

For a used Berkovich tip, it was experimentally found that ϕ =0.194 and ψ=0.930 (Hainsworth et al., 1996) which is identical to equation (3.19).

A similar equation was derived by Malzbender et al (Malzbender et al., 2000c) and the reduced modulus was used instead of the Young's modulus, giving,

$$P = E_r\left(\frac{1}{\sqrt{C}}\sqrt{\frac{E_r}{H}} + \varepsilon\sqrt{\frac{\pi}{4}}\sqrt{\frac{H}{E_r}}\right)^{-2}\delta^2 \qquad (3.24)$$

For a perfect tip Berkovich tip, C=24.5, and ε=0.75, so that it yields $\phi = \frac{1}{\sqrt{C}} = 0.202$, and $\psi = \varepsilon\sqrt{\frac{\pi}{4}} = 0.638$. The value of ϕ is close to that given by Hainsworth et al which is not surprising given that it depends only on indenter geometry . There is more deviation in ψ. The deviation mainly results from the non-perfect tip and the use of elastic modulus instead of reduced modulus in Eq. (3.22). Also, experimental measurement errors may also be responsible for it since some of the calibration materials used show significant pile-up in the indentation test.

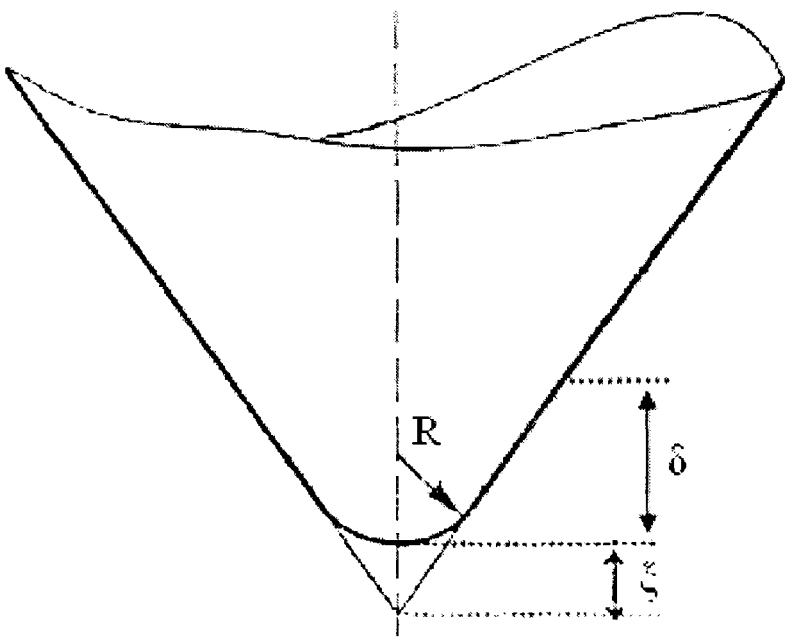

Fig. 3.4. Schematic of a truncated Berkovich indenter with a spherical tip end.

Considering the tip rounding as depicted in Fig. 3.4, it was suggested to modify Eq.(3.24) (Malzbender et al,2000),

$$P = E_r\left(\frac{1}{\sqrt{C}}\sqrt{\frac{E_r}{H}} + \frac{\varepsilon}{\beta}\sqrt{\frac{\pi}{4}}\sqrt{\frac{H}{E_r}}\right)^{-2}(\delta+\xi)^2 \qquad (3.25)$$

Where ξ is the distance between the rounded tip end and the extrapolated perfect tip as depicted in Fig. 3.4. However, it should be pointed out that in the real situation the tip may be more likely to be a truncated pyramid with a flat end rather than a spherical shape.

Despite this, the method is very useful to determine either H or E if one is already known without the need to consider other complex factors such as pile-up, sink-in or the change of slope in the initial part of unloading curve caused by creep etc. The main disadvantage of this method is that it requires fully plastic behaviour otherwise the assumption that load scales with the displacement squared fails. Also, any excursion in the load-displacement curve (e.g. fracture in brittle coated systems) and slope changes (e.g. hard coating in soft substrate) may also influence the results.

3.2.1.4 Slope ratio Method

This method is again based upon the assumption that the load scales with displacement squared (i.e. equations 3.23 to 3.25). Then the slope of the loading curve (see Fig. 3.5), S_l, is obtained by differentiating equation 3.25),

$$S_l = \left(\frac{dP}{d\delta}\right)_{loading} = 2E_r\left(\frac{1}{\sqrt{C}}\sqrt{\frac{E_r}{H}} + \frac{\varepsilon}{\beta}\sqrt{\frac{\pi}{4}}\sqrt{\frac{H}{E_r}}\right)^{-2}(\delta+\xi) \qquad (3.26)$$

The slope of the unloading curve, S_u, is taken from Equation 3.3. After arrangement and combination with the equation for hardness it gives (Joslin and Oliver, 1990),

$$\frac{P}{S_u^2} = \frac{\pi}{(2\beta)^2}\frac{H}{E_r^2} \tag{3.27}$$

Thus, the ratio between loading and unloading slopes is, (Joslin and Oliver, 1990) , (Oliver, 2001),

$$\frac{S_u}{S_l} = \frac{E_r}{H\sqrt{\pi C}} + \frac{\varepsilon}{2\beta} \tag{3.28}$$

After further rearrangement it can be shown that

$$H = \frac{\beta^2}{CP}\left(\frac{2\beta S_u - \varepsilon S_l}{S_u S_l}\right)^{-2} \tag{3.29}$$

$$E_r = \sqrt{\frac{\pi}{C}}\frac{\beta}{2P}\left(\frac{S_u^2 S_l}{2S_u - \varepsilon S_l}\right) \tag{3.30}$$

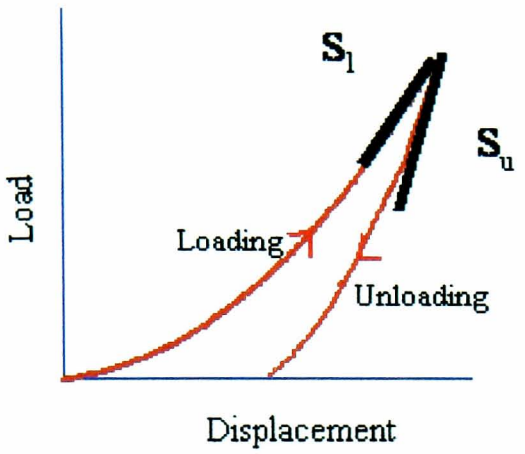

Figure 3. 5. A schematic representation of the loading and unloading stiffness which is the slope of the upper portion of loading half cycle and unloading half cycle, respectively.

The values of S_l and S_u can be continuously measured by employing the continuous stiffness method (CSM) (see the description of CSM in Chapter 4) (Pethica and Oliver, 1987). It was shown that this technique almost did not affect the shape of load-displacement curve but it may affect the initiation of fracture (Page et al., 1998).

Because it is based on the assumption that the load scales with squared displacement, this method is also strongly affected by the elastic-plastic transition which is critical for a hard coating on a soft substrate. Creep would also affect the results, reducing the values of the stiffness in the loading and increasing those of the unloading, which was found experimentally by Garcia (Garcia, 2002).

3.2.1.5 Other methods

A range of models have been derived to relate ratio of the hardness to elastic modulus (or reduced modulus) to measurable parameters such as the ratio of residual depth to maximum depth and the ratio of plastic work to total work.

It has been suggested by many authors [e.g.(Cheng and Cheng, 1998a, Cheng et al., 2002), (Malzbender and de With, 2000), (Malzbender, 2005), (Malzbender, 2006)]

that there is a linear relationship between the ratio of elastic work to total work and the ratio of hardness to Young's modulus, which is given by several authors (Cheng et al., 2002), (Malzbender, 2005), (Malzbender, 2006), (Alkorta et al., 2006), as

$$\frac{W_e}{W_t} = \kappa^{-1} \frac{H}{E_r} \tag{3.31}$$

Where κ^{-1} is a constant.

Initially Eq. (3.31) was proposed by Cheng et al (Cheng et al., 2002) based on finite element simulations to derive a value for κ^{-1}. The analytical assessment of κ^{-1} was achieved by Malzbender et al (Malzbender, 2005) and Alkorta et al (Alkorta et al., 2006). It was argued that κ^{-1} is a constant for a given indenter (Cheng et al., 2002), (Malzbender, 2005). Later, it was found (Alkorta et al., 2006) κ^{-1} is dependent on θ, δ_c/δ_m and m (the exponent of power law expression to describe the unloading curve in equation 3.5). When plotting equation (3.31) for a wide range of materials, κ^{-1} =5.3 in Eq. (3.31) seems to provide reasonable global agreement with the FEM results for a Berkovich indenter, but it was found that it strongly depends on work hardening behaviour in particular for soft metals (Alkorta et al., 2006).

The other approach is to relate the hardness to elastic modulus ratio, *H/E,* to residual depth over maximum depth, δ_r/δ_m. Initially, a few authors [e.g.(Cheng et al., 2002), (Malzbender and de With, 2000)] proposed that there was a linear relationship between δ_r/δ_m and *H/E.*

$$\frac{\delta_{res}}{\delta_{\max}} = 1 - \lambda \frac{H}{E_r} \tag{3.32a}$$

$$\lambda = 1.50 \tan\theta + 0.327 \quad for\ 60^\circ \le \theta \le 80^\circ \quad \text{(Cheng et al., 2002)} \tag{3.32b}$$

$$\lambda = 1 - 2\tan\theta \frac{H}{E_r} \quad \text{(Malzbender and de With, 2000)} \tag{3.32c}$$

Although these equations have been developed for indentation in homogeneous solids, the work by Malzbender and de With (Malzbender and de With, 2000a) suggested that it could be used in the study of coatings and thin films providing that fracture and delamination events do not significantly influence in the energy expenditure.

However, combining the numerical simulations and equations to derive Er and H by Oliver and Pharr et al, it can be shown that the relationship between δ_r/δ_m and H/E is actually not linear which is discussed as follows. Although the linear relationship given by Eq.(3.32) provides a good approximation for some materials, significant deviation occurs with the increase of H/E_r (especially when H/E_r >0.1).

Based on the analysis by Bao et al (Bao et al., 2005), we can derive the following expression,

$$\frac{\delta_r}{\delta_m} = 1 - \frac{1 - \left(\dfrac{1}{1 + \dfrac{\pi}{2} \varepsilon \dfrac{H}{E_r} \tan\theta} \right)}{1 - \dfrac{1}{\sqrt{\pi}} f(m)} \tag{3.33a}$$

Where $$f(m) = \frac{\Gamma[0.5(m-1)^{-1} + 0.5]}{\Gamma[0.5(m-1)^{-1} + 1]}, \tag{3.33b}$$

In this equation Γ is the gamma function.

When establishing the relationship between H and E in terms of a recovery resistance, a relation between maximum depth and contact was also obtained (Bao et al., 2005),

$$\delta_m = [1 + \frac{\pi}{2} \varepsilon \frac{H}{E_r} \tan(\theta)] \delta_c \tag{3.34}$$

Combining the equations in the following,

$$\left.\begin{aligned} S &= \frac{2E_r}{\sqrt{\pi}} \sqrt{A_c} \\ \delta_m - \delta_r &= mP_m / S \\ \delta_m &= [1 + \frac{\pi}{2} \varepsilon \frac{H}{E_r} \tan(\theta)] \delta_c \end{aligned}\right\}$$

another equation can be derived as follows (Chen and Bull, 2006a, Chen and Bull, 2006b) ,

$$\frac{\delta_r}{\delta_m} = 1 - \frac{m\pi}{2} \frac{H}{E_r} \tan\theta \left(\frac{1}{1 + \frac{\pi}{2} \varepsilon \frac{H}{E_r} \tan\theta} \right) \tag{3.35}$$

Alternatively, another equation can be obtained in a different way.

Combining the following equations,

$$\left.\begin{aligned} &\delta_m - \delta_r = mP_m / S \\ &\delta_m - \delta_r = mP_m / S \\ &P = E_r\left(\sqrt{\frac{1}{\pi\tan^2\theta}}\sqrt{\frac{E_r}{H}} + \varepsilon\sqrt{\frac{\pi}{4}}\sqrt{\frac{H}{E_r}}\right)^{-2}\delta^2 \\ &S = \frac{2E_r}{\sqrt{\pi}}\sqrt{A_c} \end{aligned}\right\}$$

We obtain,

$$\frac{\delta_r}{\delta_m} = 1 - \frac{m\pi}{2}\sqrt{\frac{H}{E_r}}\left(\cot\theta\sqrt{\frac{E_r}{H}} + \frac{\varepsilon\pi}{2}\sqrt{\frac{H}{E_r}}\right)^{-1} \tag{3.36}$$

where the value of m can be obtained by fitting finite element or experimental load-displacement results.

Eq. (3.33) to Eq. (3.36) indicates that the relationship between the δ_r/δ_m and H/E_r is actually not a simple linear relationship independent of the contacting materials. It can be shown that Equations (3.35) and (3.36) are the same after some simple mathematical analysis. Both equations are derived based on existing nanoindentation theories without any additional assumptions or additional empirical constants, which further supports their validity. Further discussion about this issue can be found in the paper (Chen and Bull, 2006a). The finite element simulations shows that Eq.(3.35) or (3.36) provides the best description of the relationship between δ_r/δ_m and H/E_r.

Since the values of H/E_r^2 can be obtained from the initial unloading slope (i.e. Equation 3.27), in principle the values for H and E can be obtained from the load displacement curve by combining various equations described in this section (i.e. equation (3.31) to (3.36)). However, an accurate knowledge of H/E is required and this is not directly available in all systems due to fracture. This is discussed further in the next section.

3.2.2 Extracting other mechanical properties

As well documented in Chapter 2, it is feasible to obtain the fracture toughness of bulk materials and coatings based on the load-displacement curves in the case that the fracture results in an excursion in load-displacement curve (e.g. Fig.3.6) and even in the case that the fracture does not lead to features in the load-displacement curve if the total work is well defined.

The pop-in in the load-displacement curve may also be caused by a dislocation burst in metals and ceramics. The energy absorbed in this process can be assessed (Page and Hainsworth, 1993), (Whitehead and Page, 1992).

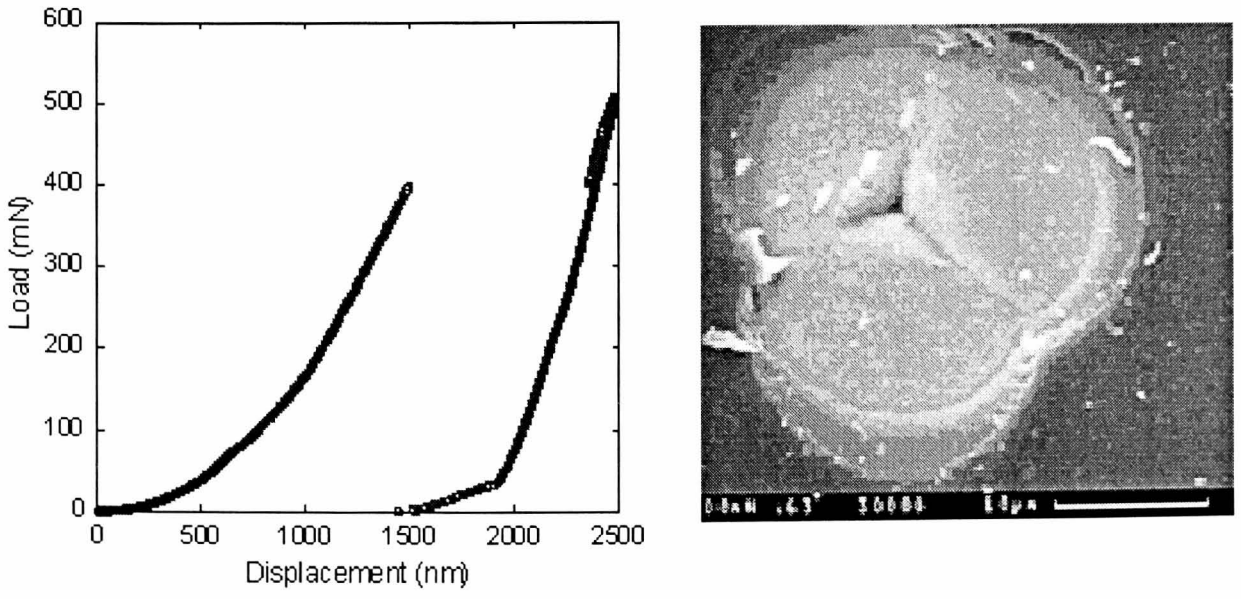

Fig. 3.6 (a) Load displacement curve and (b) SEM image of CN_x on a 3C SiC(100) substrate. An excursion in the load-displacement curve (pop-in) is clearly visible which is related to through thickness fracture in the CN_x coating.

In addition, it is also possible to extract the yield strength and work hardening exponent [(Cheng and Cheng, 1999), (Tunvisut et al., 2002),(Pelletier, 2006), (Taljat et al., 1998), (Nayebi et al., 2002)] from load-displacement curves in bulk materials. To obtain accurate data, other information such as the geometry of pile-up, must be taken into consideration. Also, analysis of the load-displacement curve helps to identify phase transformation, and creep (Pharr et al., 1991), (Page et al., 1992).

3.3 Factors affecting the mechanical properties derived from P-δ curve

3.3.1 Pile-up and sink-in

Pile-up can be described as the material adjacent to the indentation impression pushed up and away as a response to the penetration of the indenter, forming a ridge of material around the rim of the impression (see Figure 3.7), which is very common when indenting a soft material. Sink-in is a response to indentation test which is opposed to pile up. When a hard ceramic material is indented, the surface tends to sink in. Both will affect the hardness and modulus results obtained by the Oliver and Pharr method, but pile-up is by far the most serious effect (Berasategui, 2003).

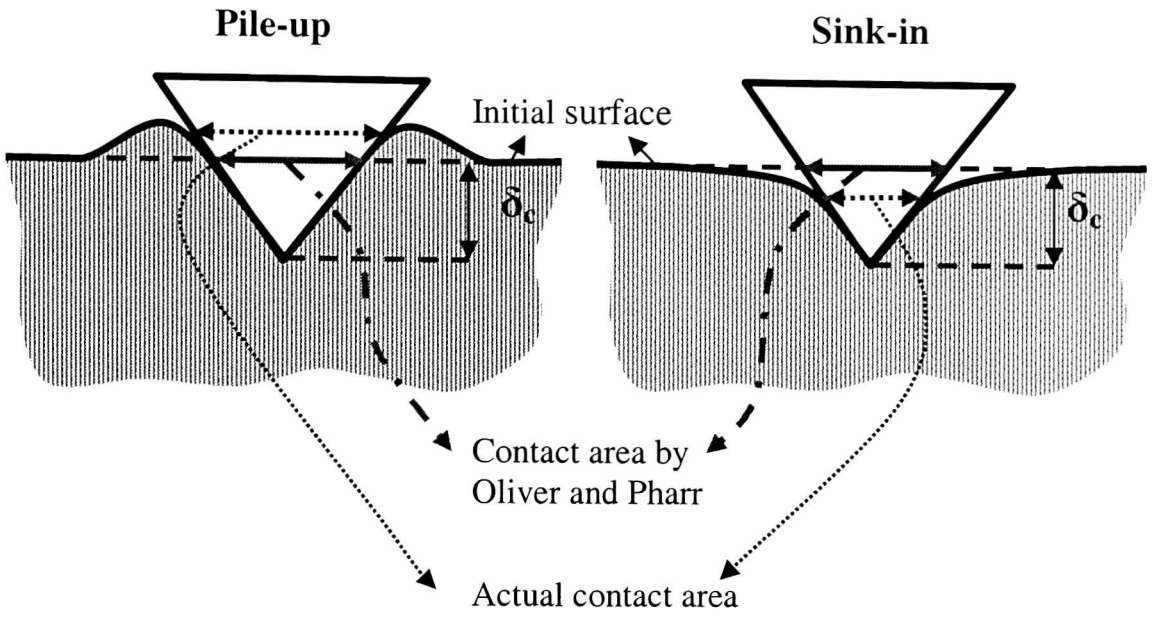

Figure 3.7. Schematic of pile-up and sink-in during nanoindneattion, which results in underestimation or overestimation of the contact area, respectivley. It may lead to inaccuracies in the calculation of the contact stiffness up to 50% (Bolshakov and Pharr, 1998).

When pile-up occurs, the Oliver and Pharr method underestimates the actual contact area thus overestimating hardness and Young's modulus, the overestimation can be up to 60% and 50% for hardness and elastic modulus, respectively (Bolshakov and Pharr, 1998, Oliver and Pharr, 2004, Cheng and Cheng, 1998a). On the contrary, in the case of sink-in, the Oliver and Pharr method overestimates the actual contact area resulting in the underestimation of hardness and elastic modulus. In both cases, post-facto microscopy such as AFM, SEM is necessary to measure the actual contact area. Also, FEM simulations are useful (Soare et al., 2004). It is possible to relate the pile up or (sink-in) behaviour to the yield stress to elastic modulus ratio, *Y/E*, and the work hardening behaviour (Cheng and Cheng, 1998a). The basic stress strain (σ-ε) relationship is given by,

$$\sigma = \begin{cases} E\varepsilon, & for\ \varepsilon \le \dfrac{Y}{E} \\ K\varepsilon^{n}, & for\ \varepsilon \ge \dfrac{Y}{E} \end{cases} \tag{3.37}$$

where K is a constant and n is the work hardening exponent.

It was found that for small values of Y/E and small work hardening exponent (i.e. the work hardening is not significant), e.g. $n=0.1$, materials show significant 'pile-up' while for the case of severe work hardening, e.g. $n=0.5$, materials may exhibit 'sink-in'. For large values of Y/E (e.g. ceramics), no matter what is the value of n, sink-in always occur (Cheng and Cheng, 1998a).

3.3.2 Creep

Creep can be defined as "the slow deformation of solid materials over extended periods under load" (Finnie and William, 1959). Nanoindentation creep has been reported in various materials such as metals (Lucas and Oliver, 1999, Asif and Pethica, 1997), ceramics (Grau et al., 1998, Han and Tomozawa, 1990a) and polymers (Briscoe et al., 1998)

Creep not only occurs during hold periods, but also occurs during the loading and unloading procedure. It may influence the loading curve (see Fig. 3.9a) as well as the initial part of the unloading curve (see Fig. 3.9b) if the loading rate and the hold period are not appropriate. It also affects the contact depth, maximum depth and irreversible work which will affect the results from the method of Oliver and Pharr and the various methods in section 3.2.1.5. As a result in some cases this behaviour may lead to errors of calculated hardness and Young's modulus by up to 20% (Chudoba and Richter, 2001, Feng and Ngan, 2002). Creep varies with materials and it may decrease from several nanometres per second down to less than 1nm/s after 10 or 20 second during a hold period (Chudoba and Richter, 2001).

The amount of measured creep also strongly depends on the loading rate and unloading rates and intuitively it is obvious that low loading rates affect it much more than high ones. The proper holding segment has to be *"long enough such that the creep rate has decayed where the depth increase in 1 minute is less than 1% of the indentation depth*" (Chudoba and Richter, 2001). Usually, for ceramics especially amorphous ceramics, the creep is not an important issue.

In order to remove the influence of creep, the constant loading rate over load (dP/P) experiments can be employed (Cheng and Cheng, 2001). For some hard coatings (e.g. CN_x), the creep may have significant influence on the load-displacement curve at low laod if the loading rate is very small. Fig. 3.9a displays a comparison of the load-displacement curves between (dP/P) technique and experiments under load control at different loading rates. It can be seen that at higher loading rate, the influence of creep on loading curve is invisible and its influence on unloading curve is obvious but not significant; however, the slope of upper part of the unloading curve is almost unaffected. In contrast, at very low loading rate, the creep significantly affects both the loading curve and the unloading curve. From Fig.3.9b, it can be seen that in the case of no holding period the creep obviously increases the slope of initial unloading curve compared to the experiments with long enough holding period. But, for the ceramics coatings investigated in this study, the influence of creep can be ignored (Berasategui, 2003). In addition, the loading rate in the experiments carried out in this work is high enough and the holding time is long enough so that the creep may is not a concern.

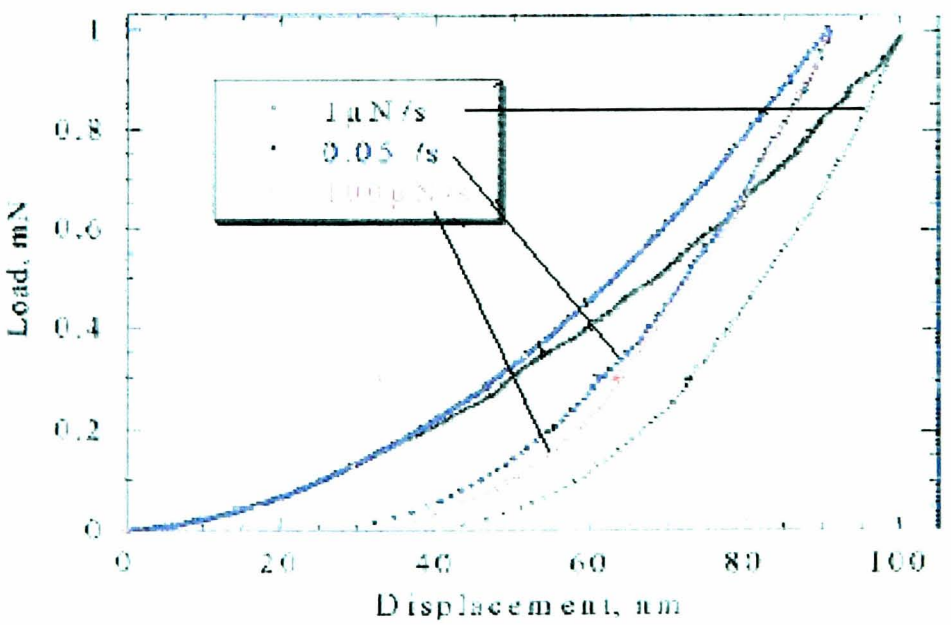

Fig.3.9a. Comparison between the loading curve at different loading rates (1μN/s and 100μN/s) and dP/P=0.05 for an indentation into CN_x on 3C SiC (001). At high loading rate the influence of creep is negligible, while, at low loading rate, the creep will significantly affect both the loading curve and unloading curve.(After (Arce-Garcia, 2002)).

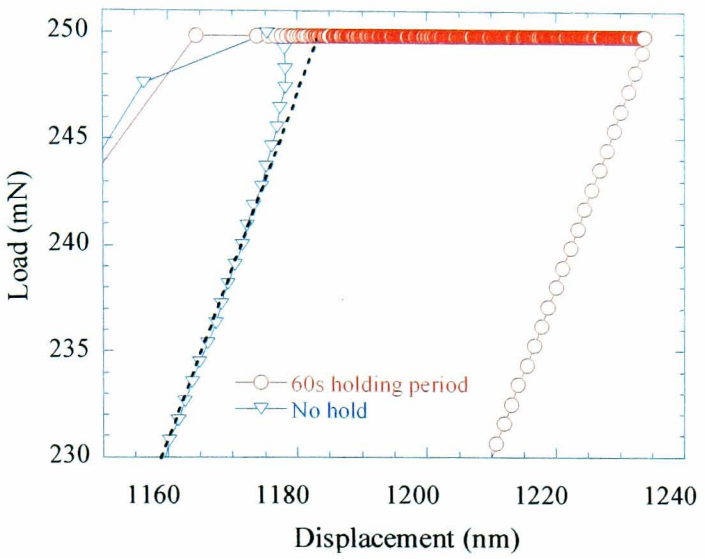

Fig.3.9b. Indentation creep at maximum load of 250mN for a 1μm thick CN_x coating on 3C SiC (001) showing a change in the slope of the upper portion of the unloading curve if a hold period is not included. After (Arce-Garcia, 2002).

3.3.3 Indentation Size Effect (ISE)

The Indentation Size Effect (ISE) describes the phenomenon that the hardness of most material changes with the indentation depth at very small contact scales which affects the measured mechanical properties of all the methods introduced in section 3.2. There are a number of mechanisms [e.g.(Bull et al., 1989), (Leipner et al., 2001), (Feng and Nix, 2004), (Bull, 2003a), (Manika and Maniks, 2006)] known to be responsible for the ISE (usually the ISE means that the hardness increases with the decrease of indentation size and hence depth), which vary with the intrinsic materials properties, different processes, and the working conditions. Negative ISE (hardness decrease with the decrease of penetration) can also occur. The causes of indentation size effects are summarized in the following.

Intrinsic materials-related effects:

It has been observed that by reducing the dislocation density the critical load for plasticity initiation increases thus the hardness is initially higher under the condition that dislocations are already present (Leipner et al., 2001). Another explanation is that

the highly curved dislocations formed around a small indentation are much more difficult to propagate and the hardness of the surface increases (Ma and Clarke, 1995), (Nix and Gao, 1998). The grain size is also an important factor when considering the grain size-dependent strength behaviour (Petch, 1953). Creep will also tend to reduce hardness for longer indentation cycles and in constant loading rate tests this leads to ISE.

Process related effects:

Some metals can increase their hardness after being polished because of a work hardening effect (Mott, 1956). In ceramics, however, polishing can induce cracks at shallow depths reducing the hardness of the material in the near surface region, which leads to the negative indentation size effect. The native oxides forming on a metal when exposed to air will also lead to an ISE at low penetration because the test is actually measuring the harder surface oxide layer.

Working conditions related effects:

Indenter/specimen friction resistance may lead to ISE for a sharp indenter. Diffusion between the indenter and specimen or other chemical effects may also lead to ISE (e.g. WC ball in contact with steel, or diamond in contact with steel). Surface contamination usually causes a negative ISE. Chemomechanical effects may cause ISE or reverse ISE.

A comparison for the main indentation size effect mechanisms for hard material and soft material is shown in table 3.1.

Table 3.1: Main indentation size effect mechanisms for different material classes. After (Bull, 2003a).

Soft material (e.g. metal)	Hard material (e.g. ceramic)
Geometrically necessary dislocations	Geometrically necessary dislocations
Strain gradient plasticity	Strain gradient plasticity
Microstructural scale	Microstructural scale
Oxide layers	Elastic-plastic transition
Polishing damage	Fracture
Lubrication	Chemomechanical effects
Creep	

3.3.4 Other factors

Fracture and phase transformation will also influence the different models to assess mechanical properties from load-displacement curves. For example, an excursion in the load-displacement curve (see Fig. 3.10) caused by fracture may result in the failure of the methods based on analysis of the loading curve (e.g. the model by Hainsworth et al, and slope ratio method). Also it may affect the method based on work of indentation because the irreversible work not only results from plastic work but also fracture dissipated energy. Further, the increase of maximum depth or decrease of load will make the standard Oliver and Pharr method underestimate H and E. Phase transformation may affect the unloading slope and residual depth which will affect the slope ratio method, the Oliver and Pharr method and the other methods described in Section 3.2.1.5. Fig.3.11 displays a load-displacement curve for Si (111) indented by a Berkovich tip at 100mN peak load, where a pop-out is observed in the unloading which is believed to relate to a phase transformation (Pharr et al., 1992, Page et al., 1992).

Delamination at the interface will also influence the methods described in section 3.2.1.5 if it causes additional elastic recovery which changes the residual depth.

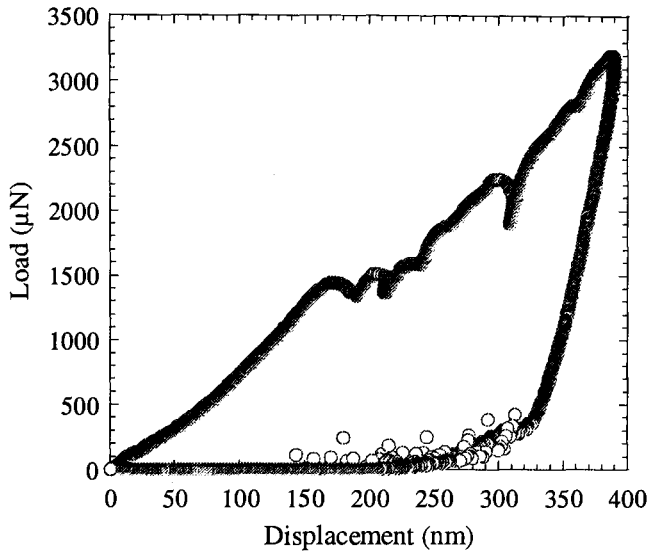

Fig. 3.10 Load-displacement curve for a 240nm ITO coating on glass indented by a cube corner tip under displacement control. The presence of fracture causes excursions and slope changes in the loading curve which will affect the mechanical properties obtained from the slope ratios method and the other methods described in Section 3.2.1.5.

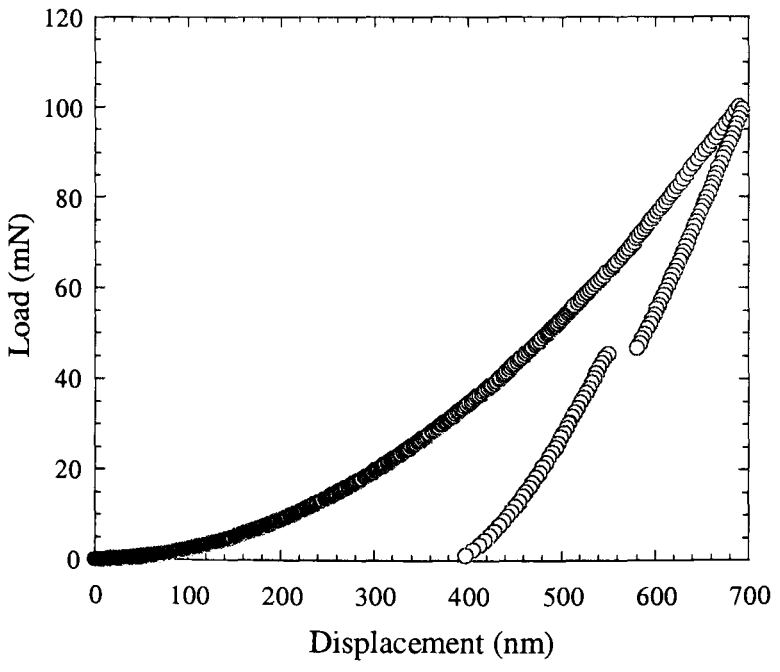

Fig.3.11. Load–displacement curve for Silicon (111) indented by a Berkovich tip at 100mN peak load. In the unloading curve, the pop-out is related to a phase transformation from metallic to amorphous silicon.

Finally, careful calibration of the tip area function, machine compliance and thermal drift is also very important if accurate values for hardness and Young's modulus are to be obtained. Oliver and Pharr proposed using a set of indentations in fused silica for this purpose, this material is elastically isotropic and its elastic modulus is independent of depth for the depth range in which the calibration should be done. The area can be derived from equation 3.1. By plotting the area versus the contact depth and fit the curve according to equation 3.10, area function can be obtained. An alternative method is to obtain the exact geometry of the indenter by microscopy (e.g. AFM, TEM) and derive a mathematical area function for it. Very careful calibration of the area function is critical for shallow penetration depth (<100nm). Also, it is necessary to frequently do the calibration if the hard and stiff materials have been tested because the tip is easily worn in such circumstances, especially for a sharp tip. Similarly indentation into materials in which carbon can dissolve often leads to tip blunting by chemical dissolution (e.g. tests on iron).

For the determination of the properties of coatings, usually it is necessary to avoid plastic deformation in the substrate. For the measurement of the hardness of thin films, an often-quoted rule of thumb is the 10% law (Pharr and Oliver, 1992), i.e. the penetration should be less than 10% of the film thickness. However, the critical penetration depends on the properties of coating and substrates. For some coated systems, 10% may be too strict (Xu, 2001), whereas for other coated systems, it may be too loose. However, even if the penetration exceeds the critical depth, it is still possible to obtain the coating hardness by a range of models if the mechanical properties of the hardness substrate is well known [(Korsunsky et al., 1998),(Tuck et al., 2000, Tuck et al., 2001)] . The 10% rule does not apply for Young's modulus measurements and extrapolating of coating/substrate composite data to zero depth is an effective way to extract coating data.

3.4 Summary

The different indentation methods to measure hardness and elastic modulus have been discussed together with the factors which affect them. If the materials under test do not display significant pile-up or creep, and H/E is not too high, all the methods will agree with each other at higher loads where the tip defect is ignorable. In the next chapter, the experimental indentation methods used in this study and the equipment to achieve them are outlined. The materials tested in this thesis are also discussed.

Reference:

Alkorta, J., Martinez-Esnaola, J. M. and Sevillano, J. G. (2006) Comments on "Comment on the determination of mechanical properties from the energy dissipated during indentation" by J. Malzbender J. Mater. Res. 20, 1090 (2005),*Journal of Materials Research,* **21,** 302-305.

Arce-Garcia, I. (2002) Mechanical properties of fullerene-like CNx : Ph. D Dissertation, ,University of Newcastle Upon Tyne

Asif, S. A. S. and Pethica, J. B. (1997) Nanoindentation creep of single-crystal tungsten and gallium arsenide,*Philosophical Magazine a-Physics of Condensed Matter Structure Defects and Mechanical Properties,* **76,** 1105-1118.

Bao, Y., Liu, L. Z. and Zhou, Y. C. (2005) Assessing the elastic parameters and energy-dissipation capacity of solid materials: A residual indent may tell all,*Acta Materialia,* **53,** 4857-4862.

Berasategui, E. G. (2003) Determining the mechanical properties of thin coated systems by nanoindentation,University of Newcastle Upon Tyne

Berasategui, E. G. and Page, T. F. (2003) The contact response of thin SiC-coated silicon systems - characterisation by nanoindentation,*Surface & Coatings Technology,* **163,** 491-498.

Bolshakov, A. and Pharr, G. M. (1998) Influences of pileup on the measurement of mechanical properties by load and depth sensing indentation techniques,*Journal of Materials Research,* **13,** 1049-1058.

Briscoe, B. J., Fiori, L. and Pelillo, E. (1998) Nano-indentation of polymeric surfaces,*Journal of Physics D-Applied Physics,* **31,** 2395-2405.

Bull, S. J., Page, T. F. and Yoffe, E. H. (1989) An Explanation of the Indentation Size Effect in Ceramics,*Philosophical Magazine Letters,* **59,** 281-288.

Bull, S. J., Chalker, P. R., Johnston, C. and Cooper, C. V. (1994) Indentation Response of Diamond Thin-Films,*Diamond and Related Materials,* **4,** 43-52.

Bull, S. J. (2002) Extracting hardness and Young's modulus from load-displacement curve,*Zeitschrift Fur Metallkunde,* **93,** 870-874.

Bull, S. J. (2003a) On the origins and mechanisms of the indentation size effect,*Zeitschrift Fur Metallkunde,* **94,** 787-792.

Chen, J. and Bull, S. J. (2006a) A critical examination of the relationship between plastic deformation zone size and Young's modulus to hardness ratio in indentation testing, *J. Mater. Res.2006, in press.*

Chen, J. and Bull, S. J. (2006b) On the relationship between plastic deformation zone radius and maximum depth during nanoindentation, *Surf. Coat & Technol.*, in press.

Cheng, Y. T. and Cheng, C. M. (1998a) Relationships between hardness, elastic modulus, and the work of indentation,*Applied Physics Letters,* **73,** 614-616.

Cheng, Y. T. and Cheng, C. M. (1998b) Scaling approach to conical indentation in elastic-plastic solids with work hardening,*Journal of Applied Physics,* **84,** 1284-1291.

Cheng, Y. T. and Cheng, C. M. (1998a) Effects of 'sinking in' and 'piling up' on estimating the contact area under load in indentation,*Philosophical Magazine Letters,* **78,** 115-120.

Cheng, Y. T. and Cheng, C. M. (1999) Can stress-strain relationships be obtained from indentation curves using conical and pyramidal indenters?,*Journal of Materials Research,* **14,** 3493-3496.

Cheng, Y. T. and Cheng, C. M. (2001) Scaling relationships in indentation of power-law creep solids using self-similar indenters,*Philosophical Magazine Letters,* **81,** 9-16.

Cheng, Y. T., Li, Z. Y. and Cheng, C. M. (2002) Scaling, relationships for indentation measurements,*Philosophical Magazine a-Physics of Condensed Matter Structure Defects and Mechanical Properties,* **82,** 1821-1829.

Chudoba, T. and Richter, F. (2001) Investigation of creep behaviour under load during indentation experiments and its influence on hardness and modulus results,*Surface & Coatings Technology,* **148,** 191-198.

Doerner, M. F. and Nix, W. D. (1986) A method for interpreting the data from depth-sensing indentation instruments,*Journal of Materials Research,* **1,** 601-609.

Doerner, M. F. and Nix , W. D. (1986) A method for the interpreting the data from depth-sensing indentation instruments,*Journal of Materials Research,* **1,** 601-609.

Feng, G. and Ngan, A. H. W. (2002) Effects of creep and thermal drift on modulus measurement using depth-sensing indentation,*Journal of Materials Research,* **17,** 660-668.

Feng, G. and Nix, W. D. (2004) Indentation size effect in MgO,*Scripta Materialia,* **51,** 599-603.

Finnie, I. and William, R. H. (1959) *Creep of engineering materials,* McGraw-Hill Book Company, Inc.

Garcia, I. A. (2002) Mechanical properties of fullerene-like CNx, Ph.D thesis,University of Newcastle Upon Tyne

Grau, P., Berg, G., Meinhard, H. and Mosch, S. (1998) Strain rate dependence of the hardness of glass and Meyer's law,*Journal of the American Ceramic Society,* **81,** 1557-1564.

Hainsworth, S. V. and Page, T. F. (1994a) Nanoindentation Studies of Chemomechanical Effects in Thin-Film Coated Systems,*Surface & Coatings Technology,* **68,** 571-575.

Hainsworth, S. V., Chandler, H. W. and Page, T. F. (1996) Analysis of nanoindentation load-displacement loading curves,*Journal of Materials Research,* **11,** 1987-1995.

Han, W. T. and Tomozawa, M. (1990a) Mechanism of Mechanical Strength Increase of Soda-Lime Glass by Aging - Reply,*Journal of the American Ceramic Society,* **73,** 1464-1465.

Hay, J. C., Bolshakov, A. and Pharr, G. M. (1999) A critical examination of the fundamental relations used in the analysis of nanoindentation data,*Journal of Materials Research,* **14,** 2296-2305.

Joslin, D. L. and Oliver, W. C. (1990) A New Method for Analyzing Data from Continuous Depth-Sensing Microindentation Tests,*Journal of Materials Research,* **5,** 123-126.

King, R. B. and Osullivan, T. C. (1987) Sliding Contact Stresses in a Two-Dimensional Layered Elastic Half-Space,*International Journal of Solids and Structures,* **23,** 581-597.

Korsunsky, A. M., McGurk, M. R., Bull, S. J. and Page, T. F. (1998) On the hardness of coated systems,*Surface & Coatings Technology,* **99,** 171-183.

Leipner, H. S., Lorenz, D., Zeckzer, A., Lei, H. and Grau, P. (2001) Nanoindentation pop-in effect in semiconductors,*Physica B-Condensed Matter,* **308,** 446-449.

Li, X. D., Diao, D. F. and Bhushan, B. (1997) Fracture mechanisms of thin amorphous carbon films in nanoindentation,*Acta Materialia,* **45,** 4453-4461.

Li, X. D. and Bhushan, B. (1998) Measurement of fracture toughness of ultra-thin amorphous carbon films,*Thin Solid Films,* **315,** 214-221.

Loubet, J. L., Georges, J. M., Marchesini, O. and Meille, G. (1984) Vickers Indentation Curves of Magnesium-Oxide (MgO),*Journal of Tribology-Transactions of the ASME,* **106,** 43-48.

Loubet, J. L., Georges, J. M. and Meille, G. (1986) In *Microindentation Techniques in Materials Science and Engineering*(Eds, Blau, P. J. and Lawn, B. R.) American Society for Testing and Materials,ASTM, Philadelphia, pp. 72-89.

Lucas, B. N. and Oliver, W. C. (1999) Indentation power-law creep of high-purity indium,*Metallurgical and Materials Transactions a-Physical Metallurgy and Materials Science,* **30,** 601-610.

Ma, Q. and Clarke, D. R. (1995) Size-Dependent Hardness of Silver Single-Crystals,*Journal of Materials Research,* **10,** 853-863.

Malzbender, J. and de With, G. (2000) Energy dissipation, fracture toughness and the indentation load-displacement curve of coated materials,*Surface & Coatings Technology,* **135,** 60-68.

Malzbender, J. and de With, G. (2000a) Energy dissipation, fracture toughness and the indentation load-displacement curve of coated materials,*Surface & Coatings Technology,* **135,** 60-68.

Malzbender, J., de With, G. and den Toonder, J. (2000c) The P-h(2) relationship in indentation,*Journal of Materials Research,* **15,** 1209-1212.

Malzbender, J. and de With, G. (2002b) Indentation load-displacement curve, plastic deformation, and energy,*Journal of Materials Research,* **17,** 502-511.

Malzbender, J. (2005) Comment on the determination of mechanical properties from the energy dissipated during indentation,*Journal of Materials Research,* **20,** 1090-1092.

Malzbender, J. (2006) Reply to the comments on "Comment on the determination of mechanical properties from the energy dissipated during indentation" by J. Malzbender J. Mater. Res. 20, 1090 (2005),*Journal of Materials Research,* **21,** 306-306.

Manika, E. and Maniks, J. (2006) Size effects in micro- and nanoscale indentation,*Acta Materialia,* **54,** 2049-2056.

McGurk, M. R. and Page, T. F. (1999) Using the P-delta(2) analysis to deconvolute the nanoindentation response of hard-coated systems,*Journal of Materials Research,* **14,** 2283-2295.

Mott, B. W. (1956) *Micro indentation hardness testing,* Butterworths, London.

Nayebi, A., El Abdi, R., Bartier, O. and Mauvoisin, G. (2002) New procedure to determine steel mechanical parameters from the spherical indentation technique,*Mechanics of Materials,* **34,** 243-254.

Nix, W. D. and Gao, H. J. (1998) Indentation size effects in crystalline materials: A law for strain gradient plasticity,*Journal of the Mechanics and Physics of Solids,* **46,** 411-425.

Oliver, W. C., Hutchings, R. and Pethica, J. B. (1986) In *Microindentation Techniques in Materials Science and Engineering*(Eds, Blau, P. J. and Lawn, B. R.) American Society for Testing and Materials,ASTM, Philadelphia, pp. 90-108.

Oliver, W. C. and Pharr, G. M. (1992a) An Improved Technique for Determining Hardness and Elastic- Modulus Using Load and Displacement Sensing Indentation Experiments,*Journal of Materials Research,* **7,** 1564-1583.

Oliver, W. C. and Pharr, G. M. (1992b) An Improved Technique for Determining Hardness and Elastic Modulus Using Load and Displacement Sensing Indentation Experiments,*Journal of Materials Research,* **7,** 1564-1583.

Oliver, W. C. (2001) Alternative technique for analyzing instrumented indentation data., *J. Mater. Res.2006, accepted,* **16,** 3202.

Oliver, W. C. and Pharr, G. M. (2004) Measurement of hardness and elastic modulus by instrumented indentation: Advances in understanding and refinements to methodology,*Journal of Materials Research,* **19,** 3-20.

Page, T. F., Oliver, W. C. and McHargue, C. J. (1992) The Deformation-Behavior of Ceramic Crystals Subjected to Very Low Load (Nano)Indentations,*Journal of Materials Research,* **7,** 450-473.

Page, T. F. and Hainsworth, S. V. (1993) Using Nanoindentation Techniques for the Characterization of Coated Systems - a Critique,*Surface & Coatings Technology,* **61,** 201-208.

Page, T. F. and Hainsworth, S. V.1995 Procedures for the nanoindentation testing of coated systemsSan Diego, CASpecial Publication of the National Institute of Standards & Technology, (Gaitherburg, USA)

Page, T. F., Pharr, G. M., Hay, J. C., Oliver, W. C., Lucas, B. N., Herbert, E. and Riester, L. (1998) In *Fundamentals of Nanoindentation and Nanotribology*, Vol. 522, pp. 53-64.

Pelletier, H. (2006) Predictive model to estimate the stress-strain curves of bulk metals using nanoindentation,*Tribology International,* **39,** 593-606.

Petch, N. J. (1953) The cleavage strength of polycrystals,

Iron Steel institute, **174,** 25-28.

Pethica, J. B., Hutchings, R. and Oliver, W. C. (1983) Hardness Measurement at Penetration Depths as Small as 20 nm,*Philosophical Magazine a-Physics of Condensed Matter Structure Defects and Mechanical Properties,* **48,** 593-606.

Pethica, J. B. and Oliver, W. C. (1987) Tip Surface Interactions in Stm and Afm,*Physica Scripta,* **T19A,** 61-66.

Pharr, G. M., Oliver, W. C. and Harding, D. S. (1991) New Evidence for a Pressure-Induced Phase-Transformation During the Indentation of Silicon,*Journal of Materials Research,* **6,** 1129-1130.

Pharr, G. M. and Oliver, W. C. (1992) Measurement of Thin Film Mechanical Properties Using Nanoindentation,*MRS Bulletin,* **17,** 28-33.

Pharr, G. M., Oliver, W. C., Cook, R. F., Kirchner, P. D., Kroll, M. C., Dinger, T. R. and Clarke, D. R. (1992) Electrical-Resistance of Metallic Contacts on Silicon and Germanium During Indentation,*Journal of Materials Research,* **7,** 961-972.

Pharr, G. M., Oliver, W. C. and Brotzen, F. R. (1992b) On the Generality of the Relationship among Contact Stiffness, Contact Area, and Elastic-Modulus During Indentation,*Journal of Materials Research,* **7,** 613-617.

Sneddon, I. N. (1965) The relationship between load and penetration in the axisymmetric Boussinesq problem for a punch of arbitrary profile,*International Journal of Engineering Science,* **3,** 47-57.

Soare, S., Bull, S. J., O'Neil, A. G., Wright, N., Horsfall, A. and dos Santos, J. M. M. (2004) Nanoindentation assessment of aluminium metallisation; the effect of creep and pile-up,*Surface & Coatings Technology,* **177,** 497-503.

Stilwell, N. A. and Tabor, D. (1961) Elastic Recovery of Conical Indentations,*Proceedings of the Physical Society of London,* **LXXVIII,** 169-179.

Taljat, B., Zacharia, T. and Kosel, F. (1998) New analytical procedure to determine stress-strain curve from spherical indentation data,*International Journal of Solids and Structures,* **35,** 4411-4426.

Tuck, J. R., Korsunsky, A. M., Davidson, R. I., Bull, S. J. and Elliott, D. M. (2000) Modelling of the hardness of electroplated nickel coatings on copper substrates,*Surface & Coatings Technology,* **127,** 1-8.

Tuck, J. R., Korsunsky, A. M., Bull, S. J. and Davidson, R. I. (2001) On the application of the work-of-indentation approach to depth-sensing indentation experiments in coated systems,*Surface & Coatings Technology,* **137,** 217-224.

Tunvisut, K., Busso, E. P., O'Dowd, N. P. and Brantner, H. P. (2002) Determination of the mechanical properties of metallic thin films and substrates from indentation tests,*Philosophical Magazine a-Physics of Condensed Matter Structure Defects and Mechanical Properties,* **82,** 2013-2029.

Vlassak, J. J. and Nix, W. D. (1994) Measuring the Elastic Properties of Anisotropic Materials by Means of Indentation Experiments,*Journal of the Mechanics and Physics of Solids,* **42,** 1223-1245.

Whitehead, A. J. and Page, T. F. (1992) Nanoindentation Studies of Thin-Film Coated Systems,*Thin Solid Films,* **220,** 277-283.

Xu, Z. H. (2001) Nanoindentation on coatings: Licentiate Thesis, ,Royal Institute of Technology, Sweden.

Chapter 4:

Experimental Methods

Chapter 4: Experimental Methods

4.1 Introduction

This chapter describes the samples investigated together with the reason for their selection and explains the main experimental techniques. After an introduction to the samples, the instruments employed to perform nanoindentation (i.e. Nanoindenter II and Triboindenter) are explained together with their working mechanisms and their characteristics. In order to gain more insight into deformation behaviour, microscopy is necessary. Therefore, the various microscopy techniques used for means of imaging the indentation impressions, such as high resolution Scanning electron Microscopy (SEM), Atomic Force Microscopy (AFM), and Reflected Light microscopy (RLM) used are discussed.

4.2. Description of the samples

Complex ultra thin multilayer coatings on glass were selected since these offer a great challenge for mechanical property characterisation. In order to further understand the fracture behaviour, some common brittle materials such as Si, Ge, Si on Sapphire, and SiC on Si were investigated as well. However, coated glass is the main concern of this work, since one of the major objectives was to understand the role of fracture in transit scratch formation during the delivery of coated architectural glass.

4.2.1 Solar control coatings on float glass

Solar control coatings are applied to architectural glass to help to keep internal building temperatures comfortable. Such coatings allow the sun's heat and light to pass trough the glass into the building, and at the same time these block heat from leaving the room, reducing heat loss considerably, which makes them helpful in both cold and hot places. To achieve this, the coatings must be transparent to visible wavelengths but opaque to radiation in the infrared. The glass substrate is reasonably opaque to UV radiation. Current solar control coatings almost reach the theoretical optical function; however, the mechanical failure which controls their life-time often occurs during transit. Polymer ball (PMMA) are sprayed onto the coated surface to separate the large glass sheets which are supported on a steel frame called a stillage during transport. Relative motion of the glass sheets causes the balls to slide, and the tensile stresses at the rear of the moving contact can cause fracture and stripping of the coating. Surface adsorption through cracks can also reduce the mechanical properties of the coating layers. Therefore, it is necessary to investigate the fracture behaviour of these coatings to help to optimise their design.

The coatings investigated here are the main oxide components of solar control coatings ITO, SnO_2, ZnO, TiO_xN_y, and silver. These coatings were sputtered on commercial soda-lime glass by an industrial scale coating plant at Pilkington PLC. The coated system tested is a multilayer stack consisting of very thin layers (<20nm) capped with a 400nm thick layer (such as ITO, SnO_2 and ZnO) for fracture assessment. This procedure is designed to produce coatings with the same microstructure as in commercial solar control layers. For ITO coatings, there were serious problems with adhesion, which prevented a 400nm coating being deposited– the coating thickness is limited to 240nm for this material deposited under these conditions. These coatings are designed for their optical properties. The use of conductive coatings such as ITO can reduce emissivity. ITO is also a barrier layer. The conducting silver layer acts as wavelength selective layer and it is the main layer to reduce heat loss.

Table 4.1a. Samples of the solar control coating stopped after each different layer in the multilayer stack with the final thickness increased to 400nm. N.B., this leads to spallation of the ITO so an extra sample was produced with a 240nm thickness top layer.

Sample 1: TiO_xN_y (400nm top layer) on substrate glass
Sample 2: TiO_xN_y / ZnO/ Ag/ ITO / SnO_2 /TiO_xN_y (400nm top layer) on substrate glass
Sample 3: TiO_xN_y / ZnO/ Ag/ ITO (240nm top layer) on substrate glass
Sample 4: TiO_xN_y / ZnO/ Ag/ ITO (400nm top layer) on substrate glass
Sample 5: TiO_xN_y / ZnO/ Ag/ ITO /SnO_2 (400nm top layer) on substrate glass
Sample 6: TiO_xN_y / ZnO (400nm top layer) on substrate glass

Table 4.1b. Samples of the solar control coating stopped after each different layer in the multilayer stack. Note: The thickness of the layers varies from several nanometers to 20 nm.

Sample 7 : TiO_xN_y (normal thickness) on substrate glass
Sample 8: TiO_xN_y / ZnO (normal thickness) on substrate glass
Sample 9: TiO_xN_y / ZnO/ Ag/ ITO / SnO_2 (normal thickness) on substrate glass
Sample 10: TiO_xN_y / ZnO/ Ag/ ITO (normal thickness) on substrate glass
Sample 11: TiO_xN_y / ZnO/ Ag/ ITO / SnO_2 /TiO_xN_y (normal thickness) on substrate glass

* Note the samples with the thicker cap layer are the emphasis of this study.

The thickness of the coatings below the cap layer is 10~20nm except for silver which is about 7nm. For convenience, these samples will be identified by their cap layers, for instance, 400nm TiO_xN_y single layer, 400nm ZnO multilayer.

4.2.2 Other brittle materials

In order to gain more information about contact fracture, some additional brittle materials such as bulk Silicon (100), Ge(100), SiC, 600nm Si on Sapphire, 1000nm SiC on Silicon etc were studied as well. These were standard semiconductor wafers obtained from commercial suppliers.

4.3. Indentation instruments

4.3.1 Nanoindenter II

The Nanoindenter® II (MTS, Knoxville, TN, USA) is an indentation system which has been commercially available for more than ten years. It allows indentation in the load range of 100μN to 500mN. The system consists of four major components: the indenter head, a reflected light microscope for remote viewing of the sample, a table with precise x-y position control where the specimen is placed, and a stiff frame as shown in Figure 4.1. The equipment is enclosed in a cabinet to ensure the thermal stability of the system. The cabinet is placed in a room with an air conditioning system which controls the temperature variance less than 1° C per day.

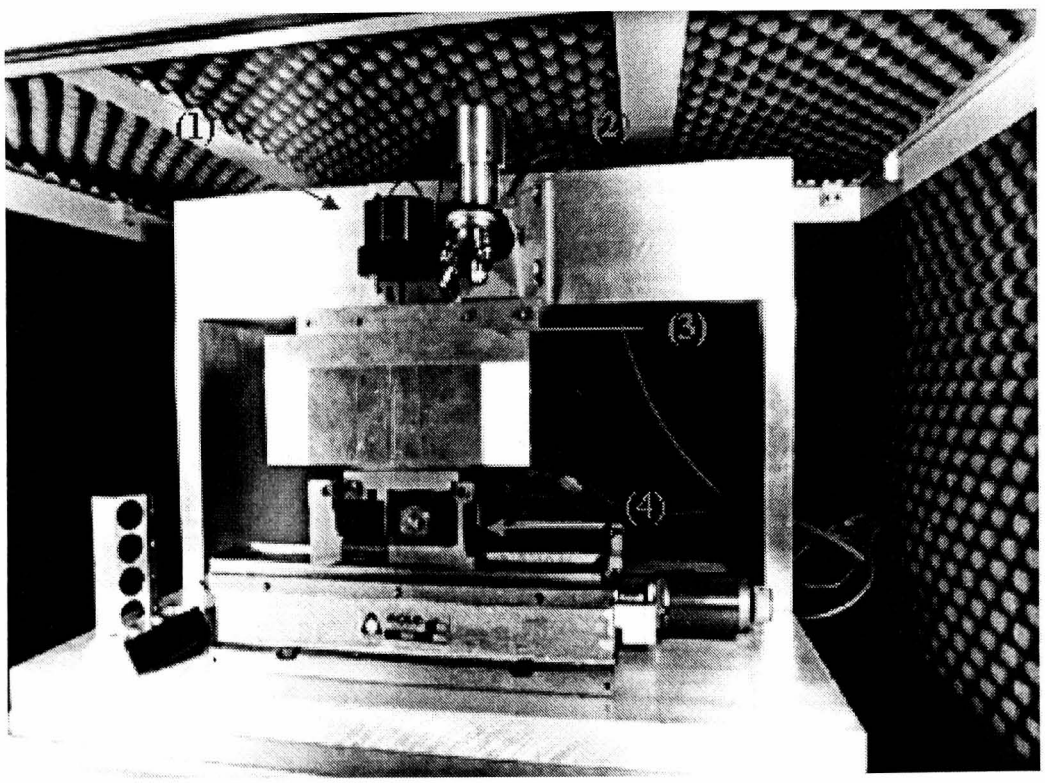

Figure 4.1: Image of Nanoindenter II: (1) indenter head, (2) optical microscope, (3) x, y, z table and (4) motors.

In the Nanoindenter® II load is applied via a roil and magnetic system and displacement is measured using a three plate capacitance gauge.

The load is applied by a precisely-controlled current through the coil, while the voltage is measured. The best load resolution is less than 100nN and the theoretical depth resolution is 0.04nm. Data from digital voltmeters on the coil and the capacitor is processed by computer which converts the output voltage to mN and nm. During this procedure, corrections are made to remove the effects of the intrinsic machine displacements and thermal drift. In the end, the data is stored on the control computer as depicted in Fig.4.2. The position of the indentations on a specimen is selected using the built-in reflected light microscope. The software records precise coordinates of the position on the table where the sample was placed in terms of a relative co-ordinate from a fixed position, which is very useful for post facto imaging (e.g. SEM).

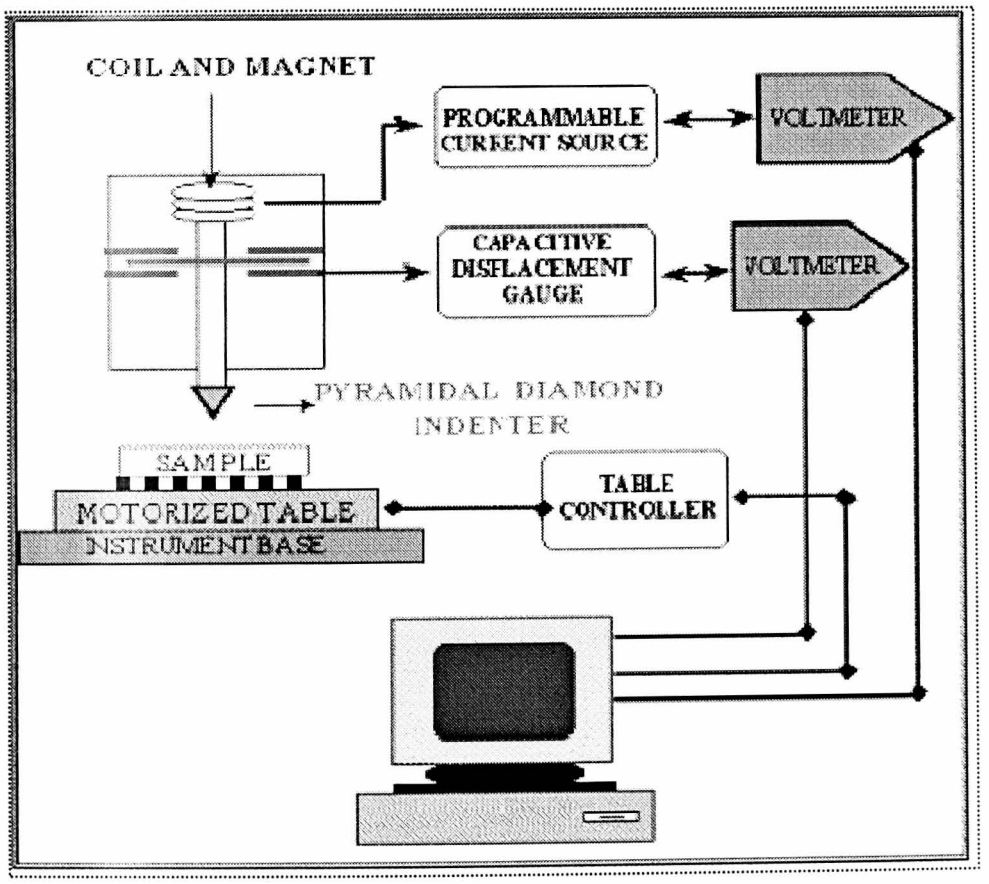

Figure 4.2: Schematic drawing of the Nano Indenter®.

The indentations are made using a procedure that allows loading rate or displacement limits to be set. A typical indentation cycle is:

- Approach segment: used to determine the surface position accurately.
- Load segment: the indenting procedure can be load control, displacement control, or dP/P.
- Unload segment: 70 % of the maximum load is removed.
- Hold segment: the load is held constant at 30% of the peak load for 60s for the purpose of thermal drift correction.
- Unload segment: the unloading is completed.

There are different test modes available in this instrument which is summarized as follows:

Load control: The increase of load per second is constant.

Displacement control: The increase of penetration per second is constant.

Constant strain rate (dP/P) control: The ratio of dP/P during indentation is constant, which is useful to remove creep effects.

Continuous stiffness measurement (CSM): This involves superimposing a small sinusoidal oscillation on the primary indentation loading signal (see Fig. 4.3) and analysing the response by means of a lock-in amplifier. By measuring the amplitude ratio and phase shift between the force and displacement oscillations, a continuous record of stiffness and damping at different contact penetration can be obtained. A continuous record of elastic moduli and hardness at different penetration can be obtained by analysis the unloading portion of each cycle.

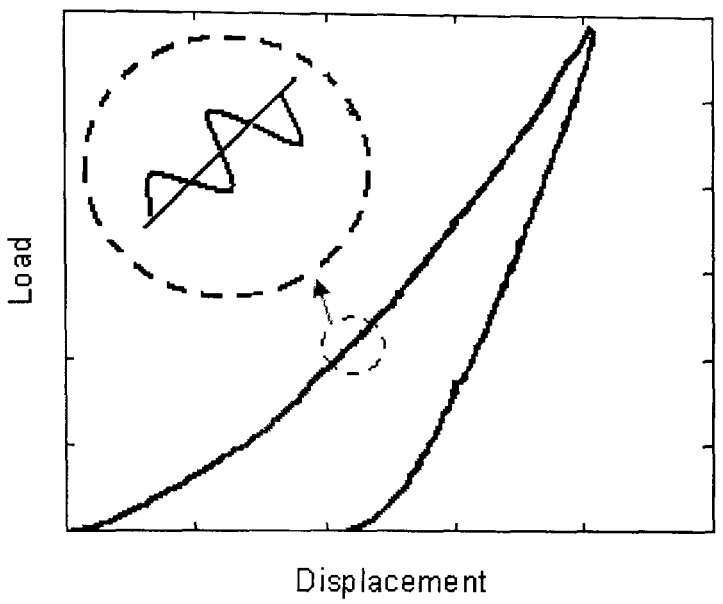

Fig. 4.3 Schematic of the CSM nanoindentation mode.

For the sake of studying fracture behaviour, displacement control is used in this study which will be explained in more detail in the next section.

4.3.2. Hysitron Triboindenter

4.3.2.1 Instrument

A Hysitron Triboindenter® (Minneapolis, MN, USA) with in-situ AFM is used for a lower load (<10mN) tests in this work. This machine is less than five years old. It consists of three main components: the transducer module, an x-y positioning table, and the Hysitron control unit and a data acquisition computer. The head is mounted on an AFM scanner and can be used for imaging (see Fig. 4.4).

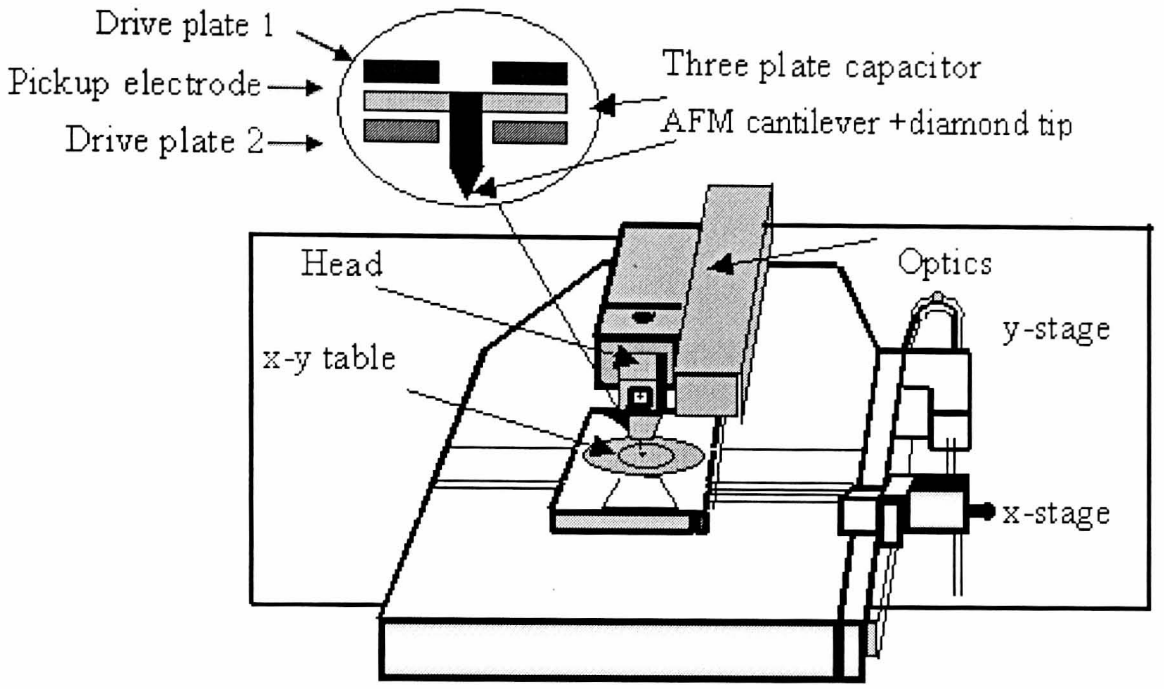

Figure 4.4: Schematic of the head and the positioning table where the main parts in a Hysitron triboscope.

The transducer module consists of the transducer head and an assembled circuit board which is the heart of the Triboindenter system. The transducer head consists of a three-plate capacitative force/displacement transducer which can provide relatively high sensitivity, a linear force (or displacement), relatively large dynamic range, and an output signal.

The transducer generates and simultaneously records the applied load and the corresponding displacement of the indenter. The force resolution is less than 1nN and the displacement resolution is approximately 0.04nm. When a voltage is applied, an electrostatic force is generated between the pickup electrode and drive plates (as depicted in Fig. 4.4), resulting the movement of the pickup electrode between the drive plates.

On the bottom of the transducer head, the diamond tip (a cube corner diamond and a Berkovich indenter are used in this work) is placed. This diamond tip operates with two functions (i.e. acting as the indenter and also as an AFM tip). *In situ* AFM allows the imaging of very small indentations which are impossible to locate under a

microscope once the sample is removed from the system. A reflected light vedio microscope system with magnification of 100X is incorporated in the system in order to select the indentation position. The Triboindenter head together with the microscope sit on a granite base to minimise vibration effects and this sits on an active piezo-driven anti-vibration table. Finally, everything is placed in an acoustic enclosure cabinet to minimize acoustic noise. The enclosure also works as a thermal buffer to help eliminate drift. The whole system is placed in a clean room with good temperature and relative humanity control.

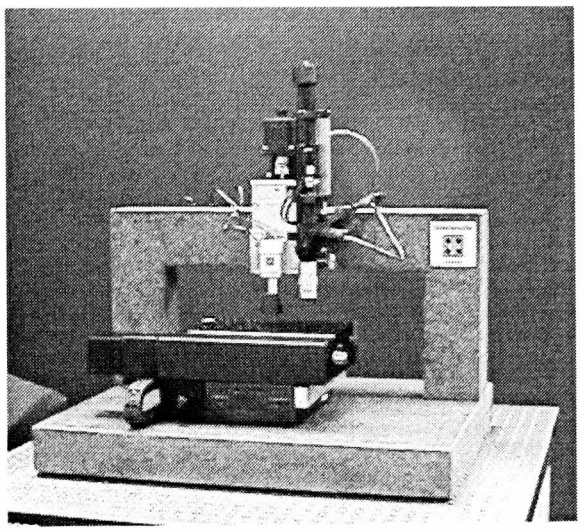

Figure 4.5. Triboindenter head together with optics on the granite base.

4.3.2.2 Different test modes

Conventional nanoindentation is an open loop method which uses voltage applied for a fixed time period to generate the required load. It is basically a force control system, but it does not perform a real-time correction for the internal spring in the transducer. This means that when a particular force is requested, part of the force will be used by the internal spring in the transducer, resulting in the force in the sample

not being the same as requested. It is precisely controlled by time only. Due to a small portion of the load absorbed by the springs of the transducer, it presents great challenges in doing creep studies because it does not maintain a constant load when holding at peak load. (see model curve in Fig. 4.6a). Closed loop control expands the scope of testing by offering improved control over the testing parameters. A closed loop indentation is run by feedback control. When running in closed loop control (force control or displacement control), there is actually a digital feedback loop that is controlled by the computer. The closed loop force control corrects internal spring force in real time, so the force applied to the sample is exactly as the user requests. In all cases, the actual displayed force and displacement after the indent is finished will be correct unless the material response faster than the feedback loop (e.g. in the presence of fast fracture). In Displacement Control, the indentation is driven based on the displacement that the user requests, and thus measures the force. In Load Control (open loop or closed loop), the indentation is driven by the force that the user requests, and measures the displacement.

If a stress relaxation test is to be performed (e.g. assessment of cracking, creep *etc*), displacement control is preferred as the case of this study. A software-driven feedback system has been developed that operates as a high-frequency feedback loop allowing true load and displacement control in the Hysitron Triboscan 6.0 control software. The feedback control loop operates at a greater frequency than the bandwidth of the transducer, producing a digital signal to actuate an analogue control signal for the transducer (Kuhn, 2004).

Typical load versus displacement curves are shown in the model curves in Fig.4.6 for all types of test. Note a hold period at peak load or displacement is used to illustrate the differences between them.

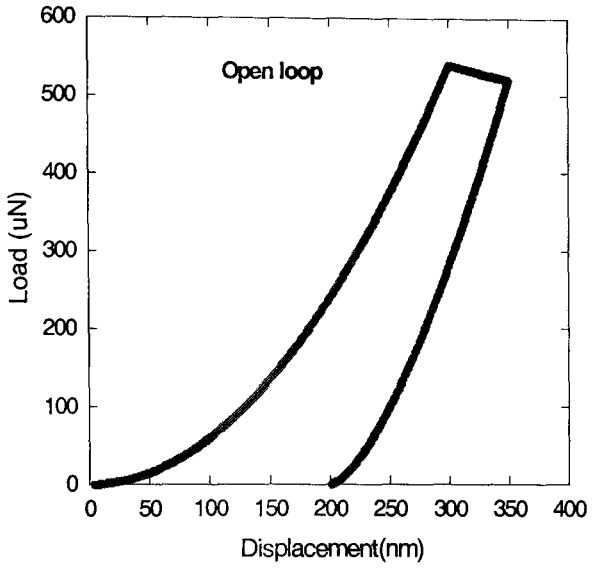

(a)

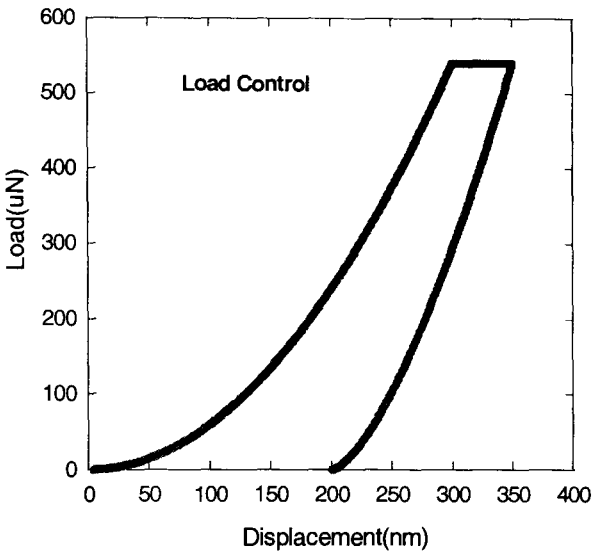

(b)

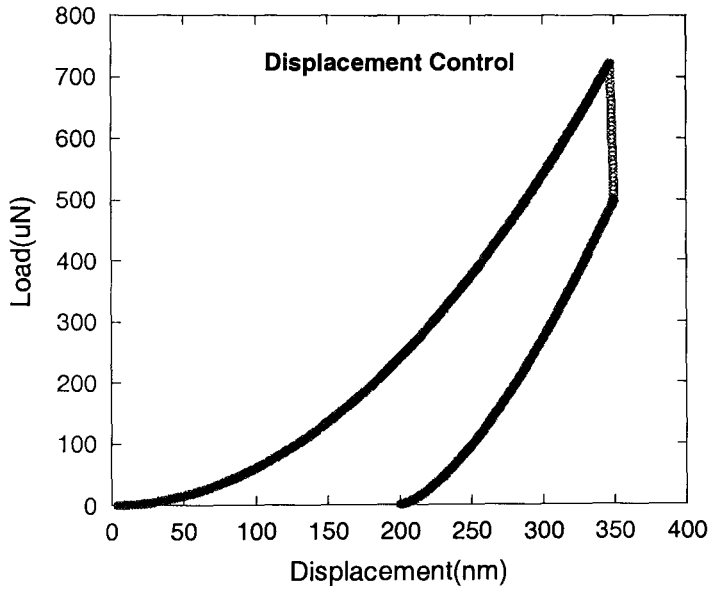

(c)

Fig.4.6. Schematic of the Load vs. displacement curve under (a) open loop control (b) load control (c) displacement control.

When there is a crack or a burst of dislocations, there will be an excursion in the load vs. displacement curve under the general load control (open loop). However, there will be load drop under displacement control (i.e. Fig 4.7).

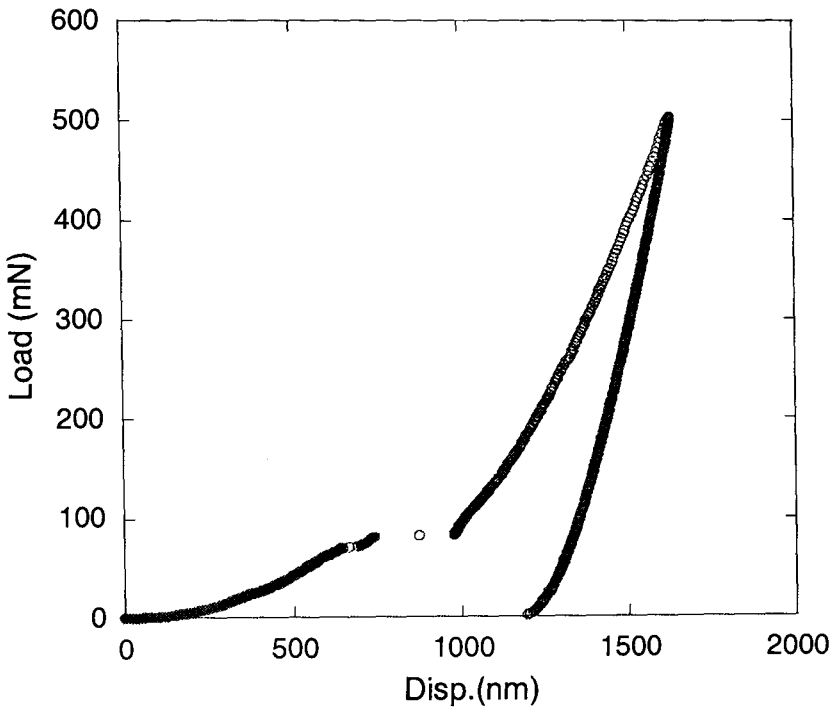

Fig. 4.7a: Excursion in the load-displacement curve associated with cracking in CN_x on sapphire.

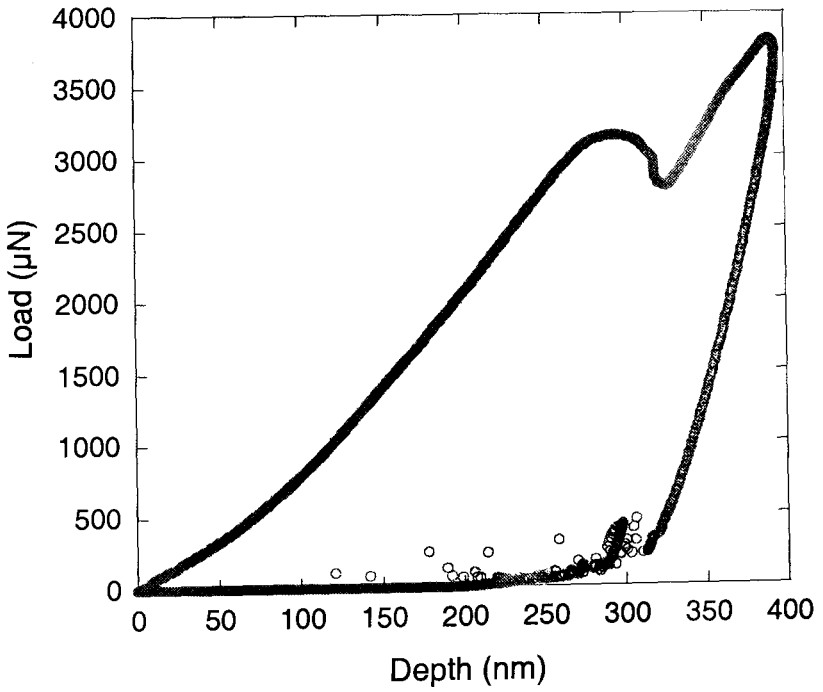

Fig. 4.7b Load drop in the load-displacement curve which is related to fracture in a solar control coating on glass tested under displacement control.

The equipment also incorporates the dynamic stiffness measurements mode, which utilizes sinusoidal loading concurrent with the quasi-static loading which is useful to test materials that display viscoelastic behaviour (e.g. polymers (Chakravartula and Komvopoulos, 2006), fullerene like CN_x (Palacio and Bull, 2004) by measuring loss modulus and storage modulus. It works in the same way as the CSM mentioned in previous section.

4.4 Microscopy

Although nanoindentation techniques are powerful tools, in order to gain more information about deformation mechanisms microscopy techniques are necessary. (Czernuszka and Page, 1985), (Page et al., 1998), (Page et al., 1992). This section describes the microscopic techniques used in this study: Reflected light microscopy (RLM), Scanning Electron Microscopy (SEM) and Atomic Force microscopy (AFM); the latter two will be described in more detail since they are the main techniques used in this work.

4.4.1 Reflected Light Microscopy.

This technique is very easy to use and works in a simple way. The light passes vertically to the sample through the microscope objective and reflects back to an eye piece, camera or TV monitor. An Olympus BH2 light microscope was used in this study to find the relatively big indentation array. It gives magnification up to 1000 times through the eye piece or up to 4000 times on the TV monitor. Nomarski interference microscopy is available on this system. This mode can give significant contrast when imaging indentations which arises from the interaction of plane-polarized light with a birefringent specimen to produce two individual wave components that are each polarized in mutually perpendicular planes. The interference colours produced are related to height differences on the sample. Reflected light

microscopy is very useful to explore densification underneath (e.g. Fig. 4.8a) an indent and subsurface cracking such as lateral cracking and delamination at the interface (e.g. Fig. 4.8b) which has a strong contrast in the image. This is largely due to the fact that the glass substrate and coatings on it are transparent in the visible.

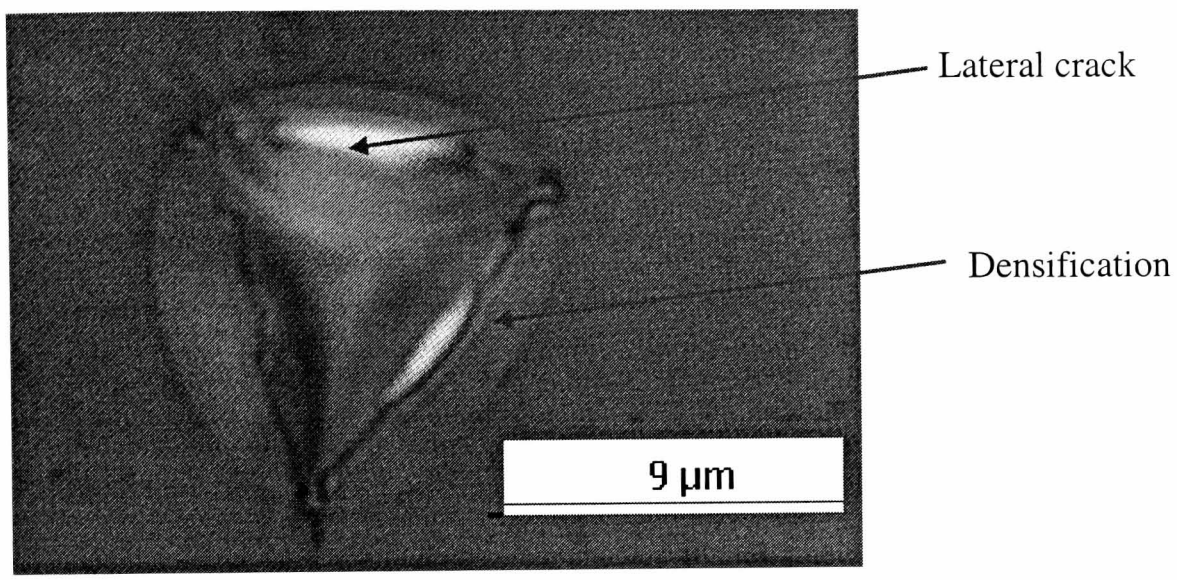

Fig. 4.8. Reflected light micrograph of fused silica indented at 500mN, which shows densification and lateral cracking caused by indentation.

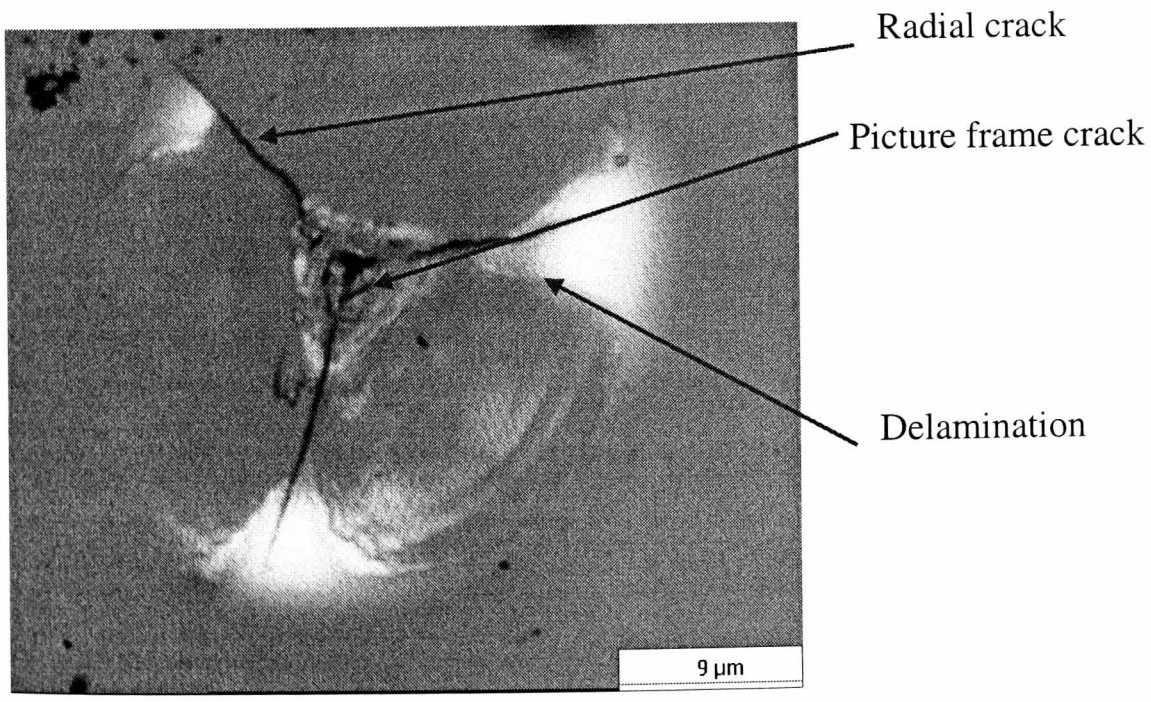

Fig. 4.8b. Reflected light micrograph of 1000nm SiC on Si (100) indented at 500mN which shows radial cracking, picture frame cracking and delamination at the interface.

4.4.2 Atomic Force Microscopy (AFM)

In this study, a commercial AFM (Park M5 Autoprobe, Park Scientific Instruments, and Sunnyvale, California) and the in-built AFM in the Triboindenter were used. The former scans the surface of the sample with a sharp tip (diameter less than 10nm in this study) which provides high resolution images compared to the latter which scans with the indenter tip (radius of a new cube corner tip is 40nm and radius of the used Berkovich tip is about 100nm). For the park AFM, the tip is placed at the free end of a cantilever. The forces between the sample surface and the tip will make the cantilever bend (see Fig. 4.9). A detector measures the cantilever deflection when the tip is moving over the samples and the computer uses a feedback loop to keep the curvature constant. The feedback signal is used to provide the image of surface topography. A range of different cantilevers can be used; in this study a sharpened silicon cantilever (Ultralever®) has been used. The scanner consists of a piezoelectric ceramic tube and the ScanMaster® hardware closed-loop scan control which allows quick and accurate zooming in features of interest without drift or distortion and corrects for unavoidable creep, and hysteresis in piezoelectric scanning systems.

There are different imagining modes available with the Autoprobe M5, which is discussed in the following. The force most commonly associated with the atomic force microscope is the van der Waals interaction force, which varies with the distance between the tip and the sample (see Fig.4.10). This allows three main imaging modes.

Contact AFM mode (C-AFM): When the distance between the cantilever and the sample is less that a few angstroms, the Van der Waals force is repulsive. As the scanner traces the tip across the sample, the contact force causes the cantilever to bend as a result of changes in topography. This provides the best resolution image but it may result in the contamination or damage of the sample. Also it may damage the tip when analysing a very hard surface or a surface with extreme topography.

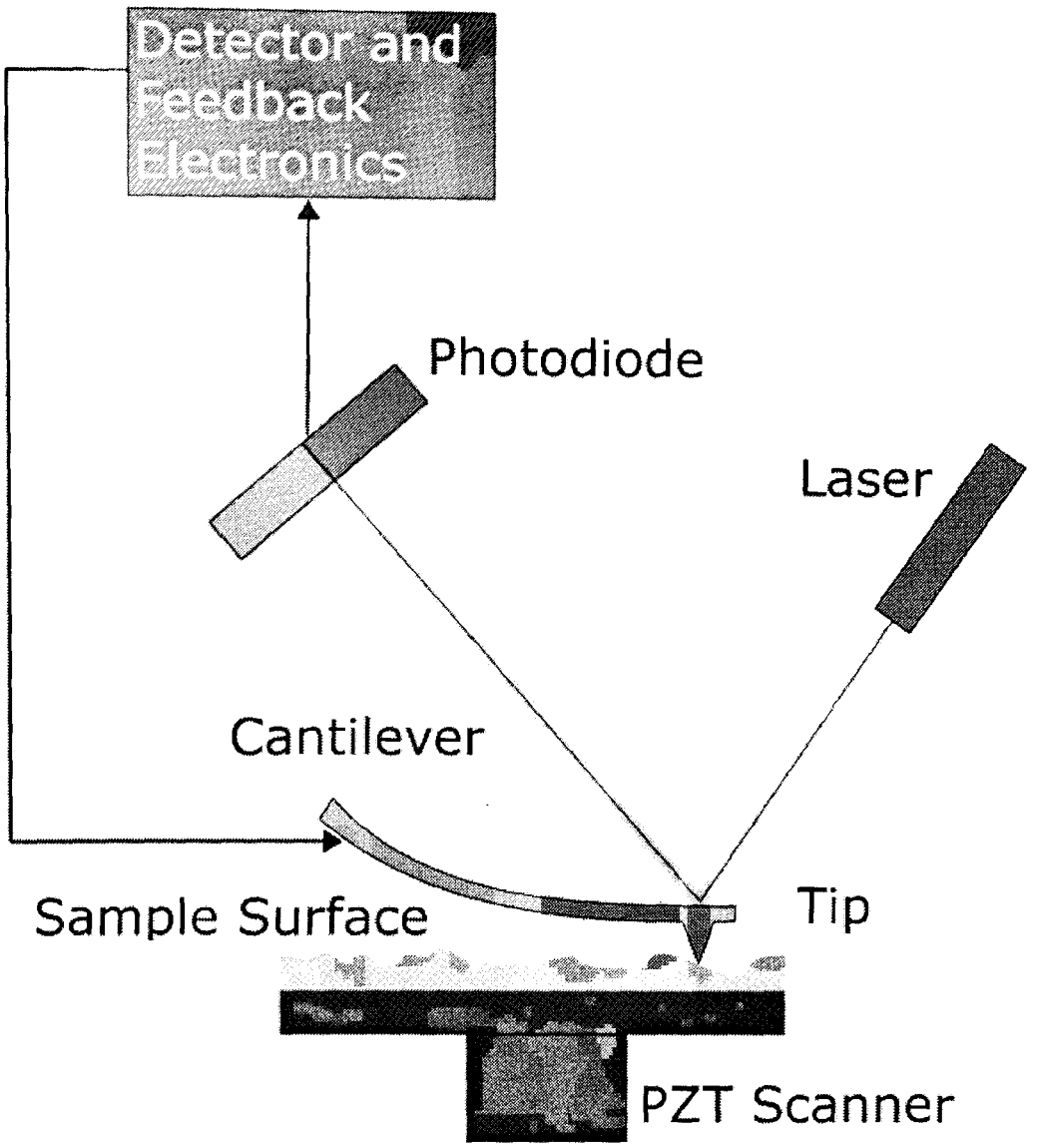

Figure 4.9: A schematic of an Atomic Force Microscope probe.

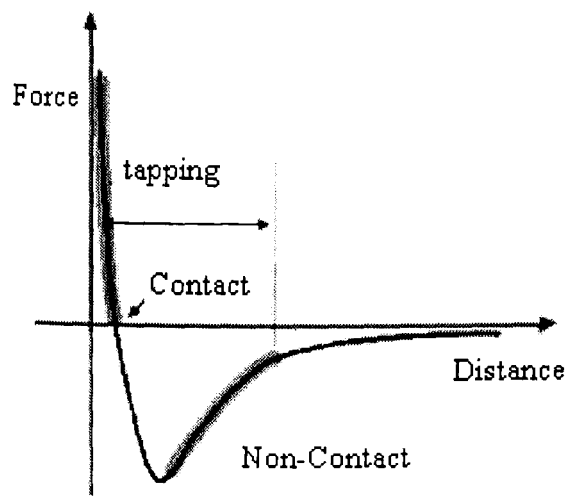

Figure 4.10: Interatomic force vs. distance curve.

Non-contact AFM mode (NC-AFM): If the distance between the tip and sample surface is relatively large (e.g. tens to hundreds of Angstroms), the van der Waals forces are attractive, and the microscope operates in non-contact mode. In this mode the cantilever is vibrated near the sample surface at its resonant frequency with amplitude that is smaller than the tip to surface distance. Changes of the resonant frequency or vibration amplitude during the tip scanning the sample surface are detected. Such changes in the resonant frequency of the cantilever reflect the changes in the spacing between the sample and the cantilever so that a map of surface topography can be generated. It does not provide very good resolution compared to C-AFM but it is very suitable for soft samples and gives reasonable resolution without contamination of the sample surface.

Intermittent AFM contact (IC-AFM, sometimes called "tapping mode): This is similar to the non-contact mode, but it also briefly contacts the sample surface every cycle. It is less likely to damage the sample compared to the contact mode since it eliminates lateral force between the tip and the sample and it has been found that IC-AFM is more effective than NC-AFM in the case of larger scan sizes that may contain greater variations in sample topography. Its resolution is intermediate between contact and non-contact mode.

In this study, the best resolution is the main concern. In addition, the samples analysed here are neither very hard nor soft so contact mode has been used in this study. The best lateral resolution condition is about 0.5nm and the Z resolution is 0.2nm.

The major merit of AFM is that it allows quantitative 3D dimensioned measurements easily, which cannot be achieved by SEM (see Fig.4.11 and 4.12). Also it allows the imaging of very small indentations which are almost invisible in the SEM in particular for insulators. However, adsorbed environmental species (e.g. water) can influence the image. For example, water absorbed in cracks by capillary forces will act as bridge when an AFM tip is scanning the surface leading to invisibility of the crack (see example in Chapter 8). Therefore, scanning electron microscopy (SEM) was also used which will be explained in the next section.

With regard to the in-situ AFM in the Triboindenter, although the resolution is limited, it allows the imaging of very small indentations (see Fig. 4.12), which are almost impossible to locate under off-line AFM or SEM.

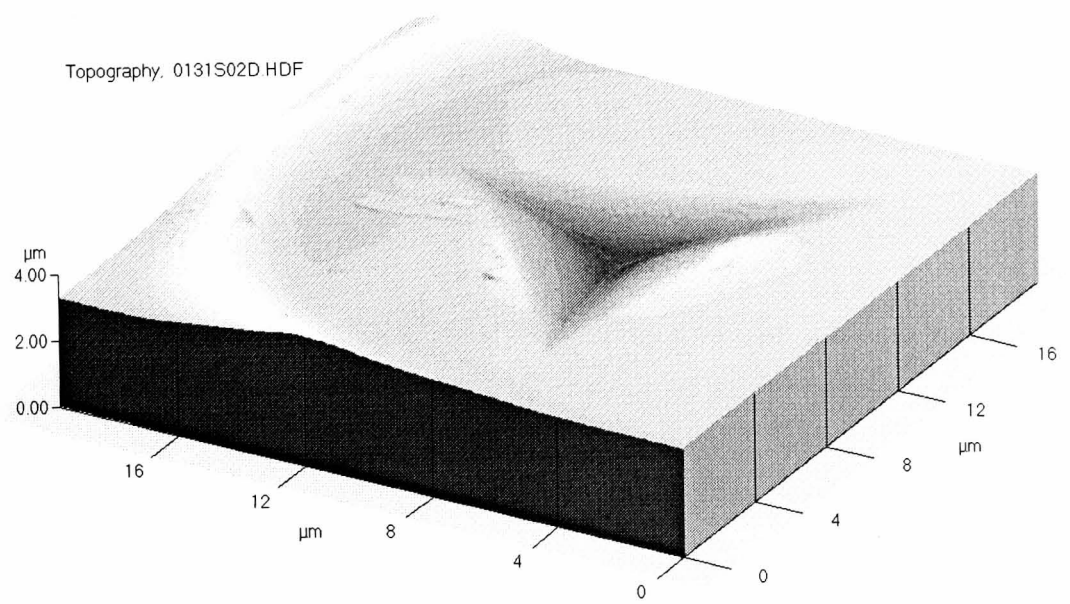

Fig. 4.11. AFM topography image of an indent in 400nm ITO on glass.

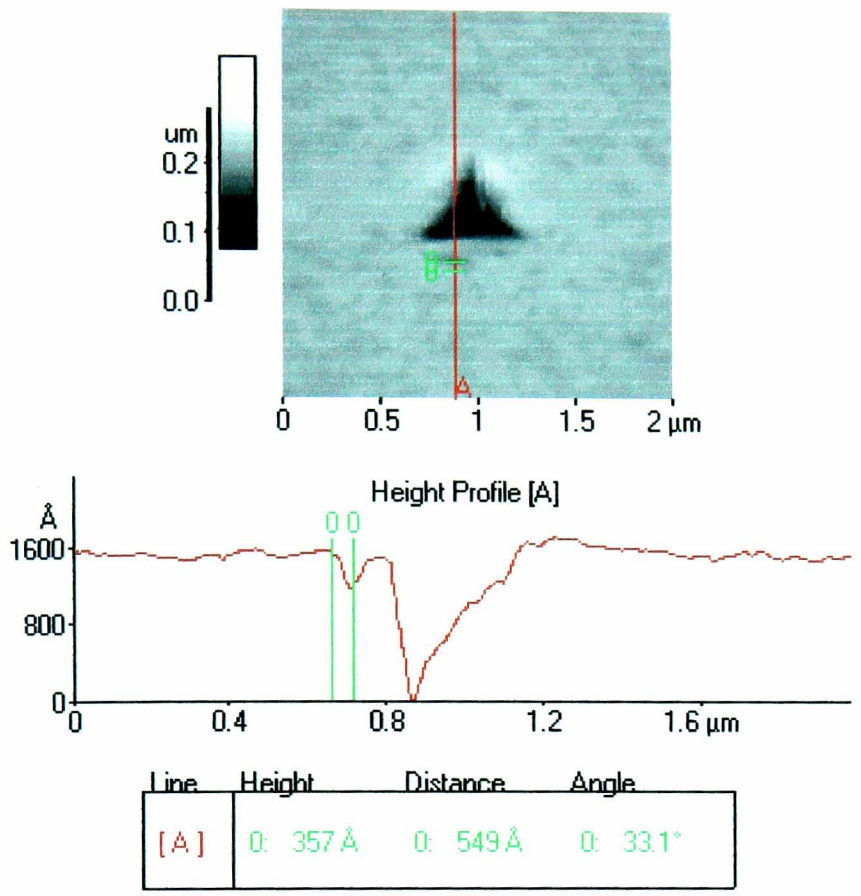

Fig. 4.12 . Line profile measurement of a small indentation by AFM.

4.4.3 Scanning Electron Microscopy (SEM)

The SEM is a powerful and versatile technique. Its versatility stems from the ability to use many different signals to create an image such as secondary electrons, backscattered electrons, X-rays, Auger electrons etc. As a consequence, it allows the characterization of surface topography at sub-micrometer scale, information about composition, crystallography, electrical information, magnetic information etc. In addition to metals, SEM can also be used to view bulk ceramics, ceramic coatings and ceramic composites (e.g. (Page, 1993)) or biological materials (Ayo-Yusuf et al., 2005), (Schupbach et al., 2005) although this may require a thin conducting coating or low voltage imaging.

A schematic diagram of the main components of a SEM is depicted in Fig. 4.13. A beam of electrons generated from a filament tip is attracted towards an anode, passes

through an aperture into the microscope column where it is, shaped by a condenser lens system and focused on the sample by the objective lens. The beam can be electrostatically scanned on the specimen surface via scanning coils fed with signals from a scan generator. When the electron beam hits the sample, different types of signal (secondary electrons, back-scattered electrons, X-rays, Auger electrons and photons of various energies) are produced and collected by detectors; these signals are converted to a voltage and amplified to modulate the brightness of the cathode-ray tube (CRT) thus yielding a 'brightness-modulated' image synchronously displayed by the CRT as the beam is scanned on the specimen.

SEM studies in this thesis were carried out using a CamScan S4-80DV [(Page, 1993)], fitted with a high brightness LaB_6 electron source, capable of high resolution at modest electron accelerating voltages (~4nm at 15kV). The specimen chamber is pumped to ~ 1×10^{-6} torr using a diffusion pump and equipped with a specimen airlock to minimise contamination when placing the samples into the SEM chamber. The electron gun is differentially pumped to ~ 2×10^{-7} torr using an ion pump. An integrating framestore, providing effective means of image processing and noise integration, is used to capture images via a number of detection systems (high sensitivity silicon back scattered electron detector (KE Developments), an Oxford CL system with monochromator, a LINK LZ4/eXL EDXsystem and a Cambridge Technology scanning electron acoustic attachment) depending on the signal required.

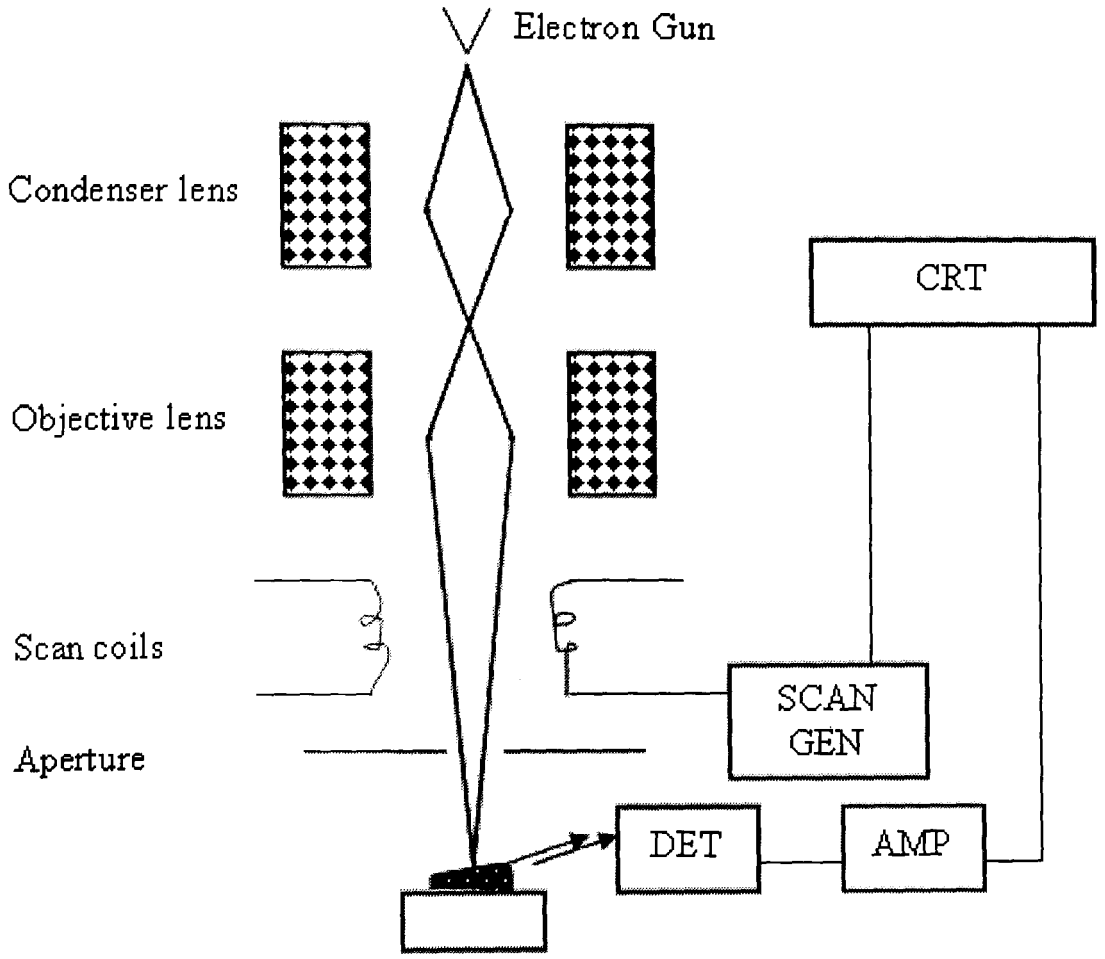

Fig. 4.13. Schematic diagram of the main components of SEM.

SEM can operate in different modes depending on the type of signal analysed and it can provide different kinds of information. Figure 4.14 summarizes the range and spatial resolution of their various signals produced.

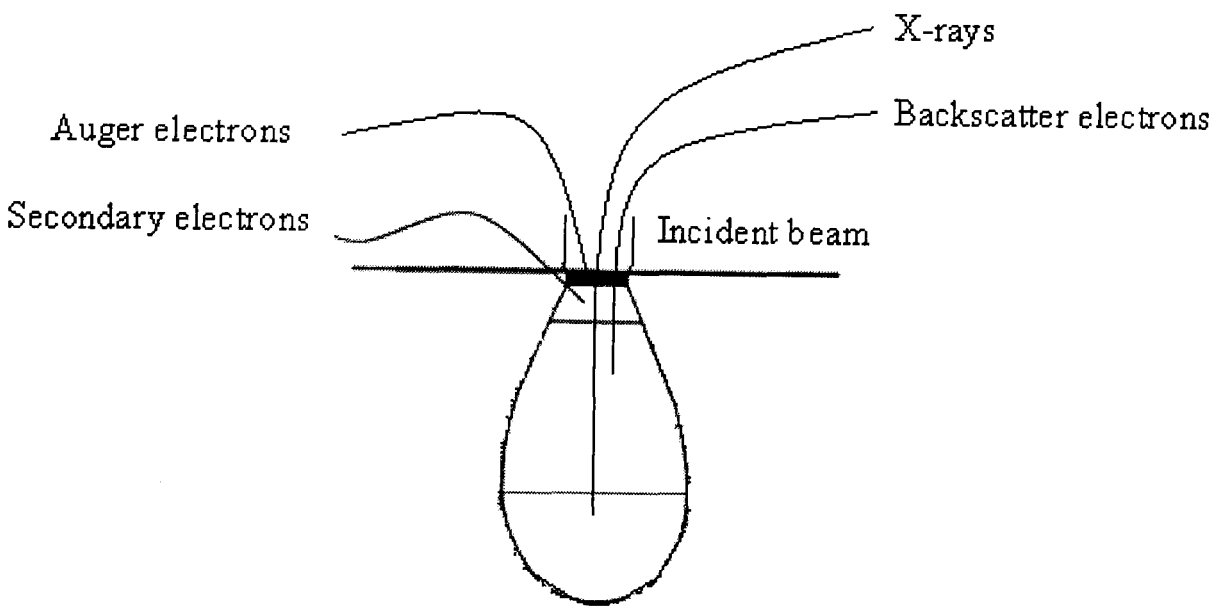

Figure 4. 14: Summary of the range and spatial resolutions for the different signals produced when an electron the beam interacts with the sample surface.

I. Secondary electron imaging (SEI)

Secondary electrons are low energy electrons (E<50 eV) which are formed as a result of excitation by the high–energy primary beam of loosely bound from sample atoms electrons. This mode allows imaging the surface features with a few nanometres diameter (topography). Since metals emit less secondary electron than insulators, different phases may be identified due to the different contrast levels. The disadvantage of this mode is that the low energies of the secondary electrons make them particularly susceptible to specimen charging. Therefore, if the specimens are not very conductive, they can attract polarisable gaseous contaminants which agglomerate on the sample surfaces and thus can lead to progressive image

degradation. This can be avoided by coating the specimen with a conductive layer (such as gold).

However, when imaging ceramic and ceramic coated samples, it is desirable not to use the conductive coating because it can obscure the microstructural detail, which is, in particular, crucial for the detection of cracks with ultra small crack opening displacement. The use of low accelerating voltages (< 2kV) to prevent charging effects (Oatley, 1972) could be a possible solution, but it will lead to a loss of resolution due to poor signal to noise ratio. For example, when imaging the ceramic coatings on glass in this study, charging results in poor resolution and image drift. Therefore, it requires skill to locate the indentation in the electron beam and focus very quickly so that good images are obtained; also a conductive paint at the edges of sample is useful to help leak away buried charge. Low voltage imaging is not an option with these samples because it will lead to poor contrast levels.

II. Back Scattered imagines (BEI)

Compared to secondary electrons, back scattered electrons are high-energy (E=10-20keV) primary electrons which are reflected from the surface and are much less abundant. Backscattering is sensitive to the atomic number and the density of the material, so this mode is very suitable to identify different phases in the specimen, cracks in coatings or bulk materials, and interfacial failure, which is usually impossible to be obtained by SEI alone. Atomic number contrast has been also used to identify through-thickness cracks in coating, where the substrate material could be identified at the crack bottoms without the distraction of SEI edge contrast (Twigg, 1996). It usually provides much better resolution than SEI for crack imaging. (e.g. Fig.4.15)

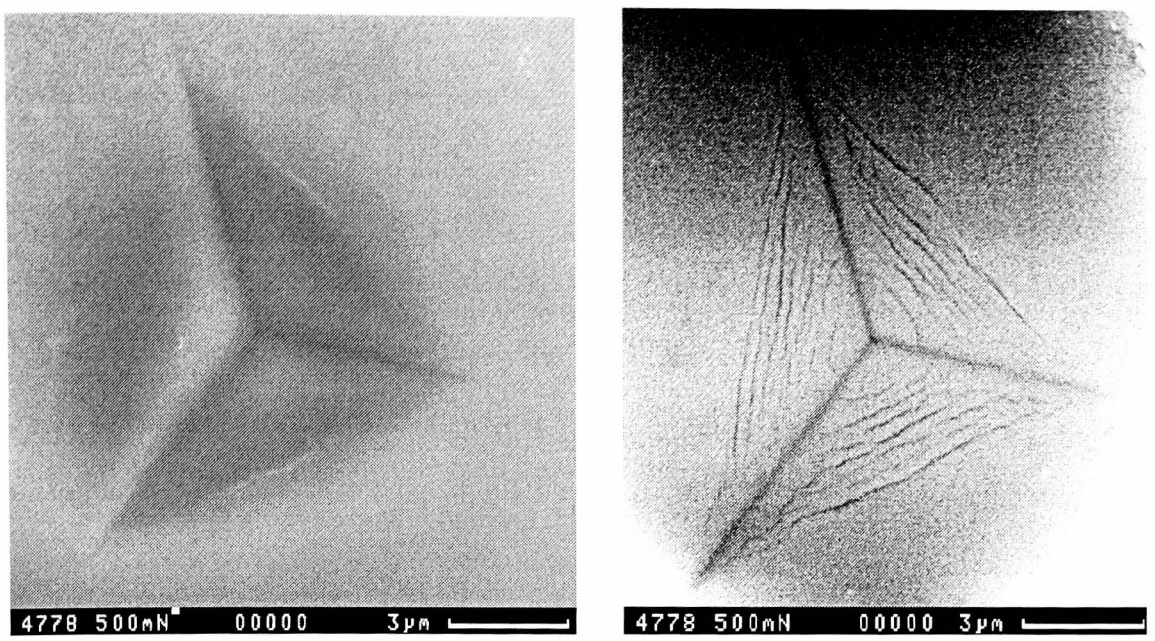

(a) (b)

Fig. 4.15. Scanning Electron Micrographs : (a) SEI and (b) BEI of an indentation in a 400nm ZnO multilayer on glass. It is obvious that BEI gives a better image for fracture analysis.

III. X-Ray emission (EDX technique)

When inner shell elctrons are ionised by the primary beam, there is the possibility for a single electron to drop from an outer shell to that inner ionised shell hole. The energy is released in the form of a photon, with energy given by the energy difference between the two states. An energy Dispersive X-ray (EDX) spectrometer can be used to perform qualitative and quantitative analyses for elements comprising a material by measuring the characteristic X-rays emitted from elements in the sample. EDX is non-destructive and therefore can be used for a range of applications[e.g. (Amin, 2006),(Ayo-Yusuf et al., 2005),(Goldstein et al., 1992)]. This technique is primarily used for chemical analysis rather than imaging (Goodhew and Humphreys, 1988).

IV. Auger emission

This is an important surface analytical technique, but auger emission electrons are of low energy and are so easily absorbed that they require ultra high vacuum systems and specialized equipment for efficient application (Goodhew and Humphreys, 1988). They can be used to provide compositional information about the outmost surface

layers. Auger electron spectroscopy has been used for quantitative composition analysis during the development of the coatings studied in this study.

There are also other techniques associated with SEM such as scanning electron acoustic microscopy (SEAM)(Page and Shaw, 2004), selected area channelling patterns (SACP) (Wells, 1974) and cathodoluminscience (CL) imaging which were not used in this work and will not be discussed further.

4.5. Nanoindentation tests

Prior to the nanoindentation tests, the as-received coated glass samples are cut into smaller pieces (about $2cm \times 3cm$). A sample is mounted on an aluminium holder by low melting point wax (Lakeside 60). Given that the substrate glass is insulator and the coatings are mainly poor conductors, a layer of silver paint is applied around the edges of the sample in contact with the Aluminium holder to reduce the problem of charging during SEM analysis.

4.5.1 Low load tests

The low load tests were carried out using the Triboindenter. Initially, a Berkovich indenter was used, however, no evidence of cracking in load-displacement curves and AFM images was observed at the highest load available (10mN) using this instrument. It has been found that when using a cube corner tip the cracking threshold for many brittle materials can be reduced by at least 10 times compared to a Berkovich or Vickers indenter (Pharr, 1998). Therefore, a cube corner tip (for a new tip, tip end radius is 40nm) was selected for the assessment of fracture.

As previously mentioned displacement control is very suitable for stress relaxation and fracture assessment, so it was adopted to study the cracking behaviour in this

work. To test such coatings without excessive substrate effects, it requires a very low load test (<5mN).

For the fracture assessment, this work focused on the systems with a relatively thick cap layer (400nm thick) in which the through-thickness crack is easier to form and observe. Also it is more practical to minimise the substrate deformation influence for the thicker coating. The description of the test procedure used is summarized in the following.

It was suggested that many coatings flex elastically up to displacements approximately equal to the coating thickness when the onset of fracture may occur [(Page and Hainsworth, 1995), (McGurk et al., 1994)]. Therefore, the maximum displacement control set point is 400nm which is equal to the thickness of the thick top layer (except for the sample with 240nm ITO coating). The tests were performed at range of penetration depth from 40nm to 400nm. The loading rates were varied from 5nm/s (for low penetration) to 40nm/s (for high penetration). Each test is repeated at least 5 times in different positions. The hold time at peak load for each case is 5 seconds. Fig. 4.16 shows a typical control function for a nanoindentation test under displacement control.

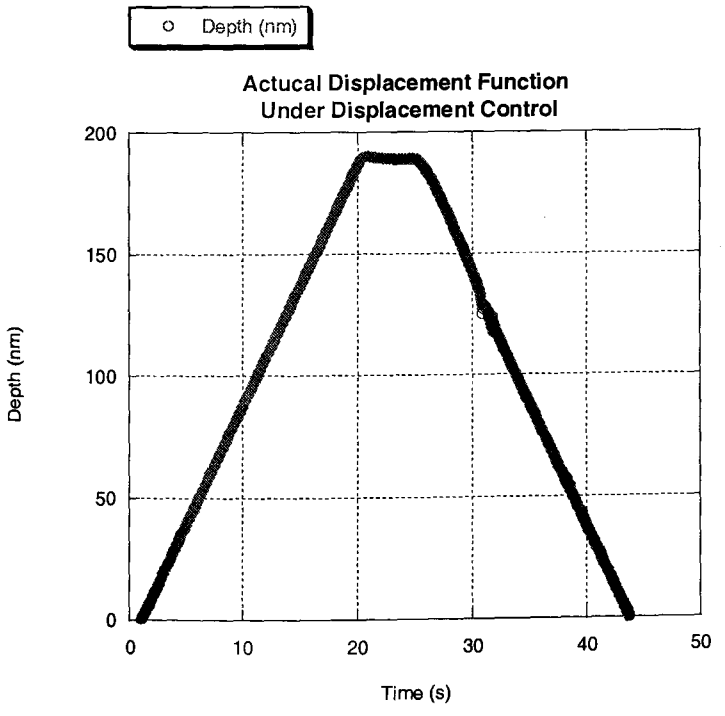

Fig. 4.16. An input displacement function vs. time under displacement control.

4.5.2 High load tests

Although evidence of cracking was observed in both load-displacement curves and AFM images at higher loads (>2mN), no distinct well-established crack pattern was observed in the in-situ AFM image due to its limited resolution. In order to obtain further insight into the indentation fracture of such a complex coating stack, it is necessary to investigate the fracture behaviour at different scales. Therefore, high load tests were performed on the coated and uncoated glass, fused silica, silicon and coated silicon using a Nanoindenter II (MTS, Knoxville, TN, USA) fitted with a Berkovich indenter (tip end radius ~250nm) at a range of loads from 10mN to 500mN. Ten indentations were made at each load. The distance between every indentation was at least ten times the indentation diameter to avoid interaction between the residual stress fields of neighbouring indents. Displacement control was used throughout; the displacement rate was 50nm/s for peak loads bigger than 300mN and 10nm/s for lower loads. Hold segments of 60s at peak load and 70% of peak load during unloading were used to assess the possibility of creep (minimal) and to correct for the influence of thermal drift. The indentation area function was carefully calibrated using a fused silica standard sample prior to testing. In order to measure the fracture dimensions, scanning electron microscopy (SEM, Camscan) and atomic force microscopy (AFM, Park M5) were used.

4.6. Summary

The chapter began with the description of the samples investigated in this thesis. Indentation instruments (Nanoindenter II and Hysitron Triboindenter) and microscopy techniques (reflected light microscopy, atomic force microscopy and scanning electron microscopy) used to characterise the indentation response of the samples have been discussed. Finally, the details of nanoindentation tests at low loads and high loads were presented.

Chapter 5 will present a new model to assess coating toughness which is based on extrapolating total work versus displacement curve (i.e. W_t-dp method).

Reference:

Amin, M. A. (2006) Weight loss, polarization, electrochemical impedance spectroscopy, SEM and EDX studies of the corrosion inhibition of copper in aerated NaCl solutions,*Journal of Applied Electrochemistry,* **36,** 215-226.

Ayo-Yusuf, O. A., Driessen, C. H. and Botha, A. J. (2005) SEM-EDX study of prepared human dentine surfaces exposed to gingival retraction fluids,*Journal of Dentistry,* **33,** 731-739.

Chakravartula, A. and Komvopoulos, K. (2006) Viscoelastic properties of polymer surfaces investigated by nanoscale dynamic mechanical analysis,*Applied Physics Letters,* **88**.

Czernuszka, J. T. and Page, T. F. (1985) The Importance of Microscopy in Studying the Wear Behavior of Ceramic Surfaces,*Journal of Microscopy-Oxford,* **140,** 159-169.

Goldstein, J. L., Newbury, D. E., Echlin, P., Joy, D. C., Romig, A. D., Lyman, C. E., Fiori, C. and Lifshin, E. (1992) *Scanning Electron Microscopy and microanalysis,* Plenum, New York.

Goodhew, P. J. and Humphreys, F. J. (1988) *Electron microscopy and analysis,* Taylor and Francis.

Kuhn, L. (2004), Private communication

McGurk, M. R., Chandler, H. W., Twigg, P. C. and Page, T. F. (1994) Modeling the Hardness Response of Coated Systems - the Plate-Bending Approach,*Surface & Coatings Technology,* **68,** 576-581.

Oatley, C. (1972) *The scanning electron microscope,* Cambridge University Press, Cambridge.

Page, T. F., Oliver, W. C. and McHargue, C. J. (1992) The Deformation-Behavior of Ceramic Crystals Subjected to Very Low Load (Nano)Indentations,*Journal of Materials Research,* **7,** 450-473.

Page, T. F. (1993) In *Electron Microscopy and Analysis 1993*, pp. 295-300.

Page, T. F. and Hainsworth, S. V.1995 Procedures for the nanoindentation testing of coated systemsSan Diego, CASpecial Publication of the National Institute of Standards & Technology, (Gaitherburg, USA)

Page, T. F., Pharr, G. M., Hay, J. C., Oliver, W. C., Lucas, B. N., Herbert, E. and Riester, L. (1998) In *Fundamentals of Nanoindentation and Nanotribology*, Vol. 522, pp. 53-64.

Page, T. F. and Shaw, B. A. (2004) Scanning electron acoustic microscopy (SEAM): A technique for the detection of contact-induced surface & sub-surface cracks,*Journal of Materials Science,* **39,** 6791-6805.

Palacio, J. F. and Bull, S. J. (2004) Dynamic indentation measurements on amorphous materials,*Zeitschrift Fur Metallkunde,* **95,** 335-339.

Pharr, G. M. (1998) Measurement of mechanical properties by ultra-low load indentation,*Materials Science and Engineering a-Structural Materials Properties Microstructure and Processing,* **253,** 151-159.

Schupbach, P., Glauser, R., Rocci, A., Martignoni, M., Sennerby, L., Lundgren, A. and Gottlow, J. (2005) The human bone-oxidized titanium implant interface: A light microscopic, scanning electron microscopic, back-scatter scanning electron microscopic, and energy-dispersive X-ray study of clinically retrieved dental implants,*Clinical Implant Dentistry and Related Research,* **7,** S36-S43.

Twigg, P. C. (1996) Mechanical degradation of Ceramic coaitngs and surface,University of Newcastle Upon Tyne

Wells, O. C. (1974) *Scanning electron microscopy,* mcgraw Hill, New York.

Chapter 5:

W_t-dp model to assess coating toughness during nanoindentation

Chapter 5: W_t-dp model to assess coating toughness during nanoindentation

As discussed in Chapter 2, the conventional indentation models (CIM) may not work well for coated systems, in particularly for thin films, due to the influence from the substrate such as substrate plastic deformation and membrane stress due to the constraint imposed by the substrate. With the intention to eliminate the substrate influence, a relatively low load is preferred and this may lead to small cracks which can be even confined to the indent impression, in which case, the conventional indentation methods (CIM) are not valid. Therefore, energy based models are proposed as alternative options to estimate the fracture toughness as discussed in Chapter 2. In this chapter, the main part will be focused on the models based on analysing individual load-displacement curves. Initially, the model of extrapolating load-displacement curves (denoted as ld-dp method) is briefly reviewed. Because there are some disadvantages and limitation of this model, it has been further developed by extrapolating the total work vs. displacement curve (denoted as the W_t-dp approach in the same way as in Chapter 2) which will be discussed in the second half of this Chapter. A brief introduction and comment about these two approaches was covered in Chapter 2 but is emphasised in this Chapter. Detailed comparisons between these two models and the other energy based models are also discussed.

5.1. Ld-dp model

The ld-dp model (Li and Bhushan, 1998, Li et al., 1997) is based on extrapolating the loading curve when there is a step associated with through thickness fracture in it. In this model the load-displacement curve is extrapolated from the step start point (assumed to be the onset of fracture) to its end point, and the difference between the

extrapolated curve and the measured curve is regarded as the fracture dissipated energy (see details in Chapter 2). However, this model was questioned by several authors (e.g. (den Toonder et al., 2002)). It is found that this model is difficult to apply to small cracks which may not cause significant displacement excursions under load control. Also this method cannot be applied to displacement control tests. This model completely ignores the difference in mechanical properties between an uncracked coated system and its cracked systems counterpart. In order to solve these problems, the so-called W_t-dp method has been developed here. The initial intention for the development of the W_t-dp method was to deal with small cracks in coatings; therefore, how the experiments were designed to produce small cracks is discussed prior to the description of the W_t-dp method.

5.2. Experimental design

Indentation experiments were performed under displacement control using a Hysitron Triboindenter fitted with a cube corner indenter (radius is 40nm for a new tip). The maximum displacement was set in the range 40nm to 400nm. The hold period at maximum displacement was 5s and afterwards the indenter was withdrawn at the same rate as during the loading cycle. The crack length and profiles of the indentation impression were analysed by AFM using the tip which made the impression. Brittle coatings and glass were selected for investigation. The properties of the coatings are listed in Chapter 4. Samples with relatively thick coatings (i.e. >200nm) on top were investigated here because there are no obvious events in the P-δ curves for the samples with normal thickness (i.e. in the range of 7nm to 20nm for individual layers) of solar control coatings. As mentioned previously, it is difficult to assess small cracks. Primarily, special techniques are required to form the small crack under the condition that it can be used for toughness assessment. In the next section, it will be explained why the displacement control test with a sharp cube corner tip was necessary.

5.2.1 Why displacement control tests?

In this part, I only concentrate on the issue of why displacement control is preferred to assess fracture behaviour. More details about displacement control and load control were covered in Chapter 4.

It is often argued that the step in the load-displacement curve under load control (see Fig. 5.1a) indicates the loss of contact caused by a transient event such as fracture in brittle materials, but it cannot ensure the energy dissipated during displacement excursion is accounted by the transient event only because of the possible additional permanent deformation associated with it (Warren and Wyrobek, 2005). In contrast, the load drop in a displacement-controlled curve (see Fig.5.1b) was argued to be unambiguously related to loss of contact attributed to spalling accompanying fracture. If only the load-displacement curves were analysed, additional work was done by indenter during the displacement excursion under load control and no work was done by the indenter during load drops under displacement control tests which was also argued elsewhere (den Toonder et al., 2002). If the feedback control of the instrument is perfect, the load drops to ensure the exactly desired displacement and thus no additional work is done during a fracture event under displacement control. However, in practice the feedback control is not perfect and a load drop may accompany an excursion (see Fig.5.1b). For example, if examining the total work versus displacement curve (which can be obtained by integrating the load-displacement curve), it can be seen that additional permanent deformation may occur under both test conditions (see Fig. 5.2).

However, it is obvious that the displacement control should eliminate the additional deformation inherent in load control (see Fig. 5.2). In addition, as discussed in Chapter 3, the displacement control test is more sensitive to fracture compared to load control, therefore, displacement control tests were adopted here.

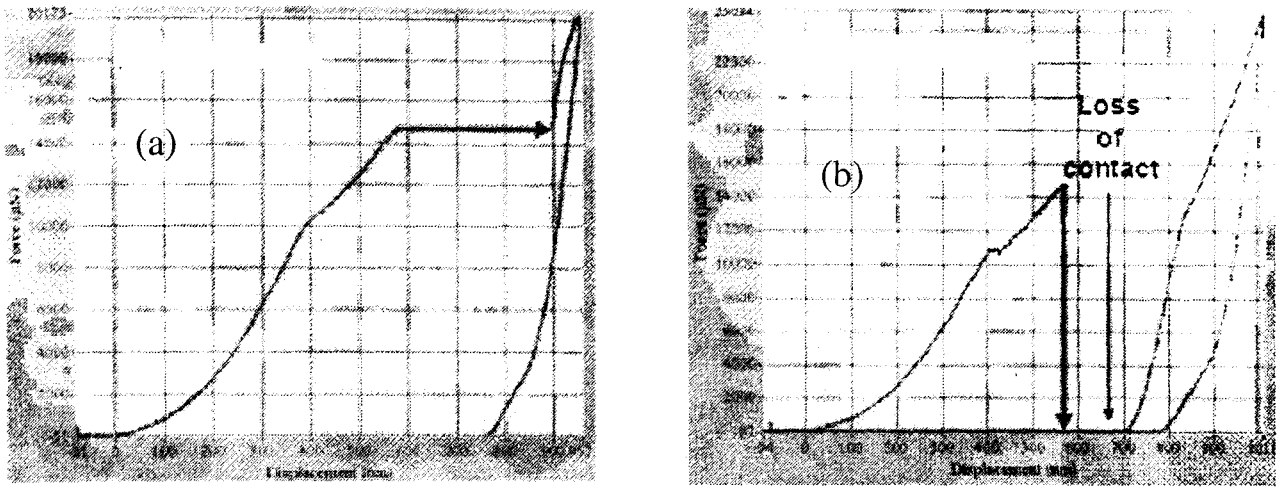

Fig.5.1. (a) Displacement excursion in the load-displacement curve associated with spalling in proprietary brittle coating on Si under load control and (b) load drop under displacement control, after (Warren and Wyrobek, 2005).

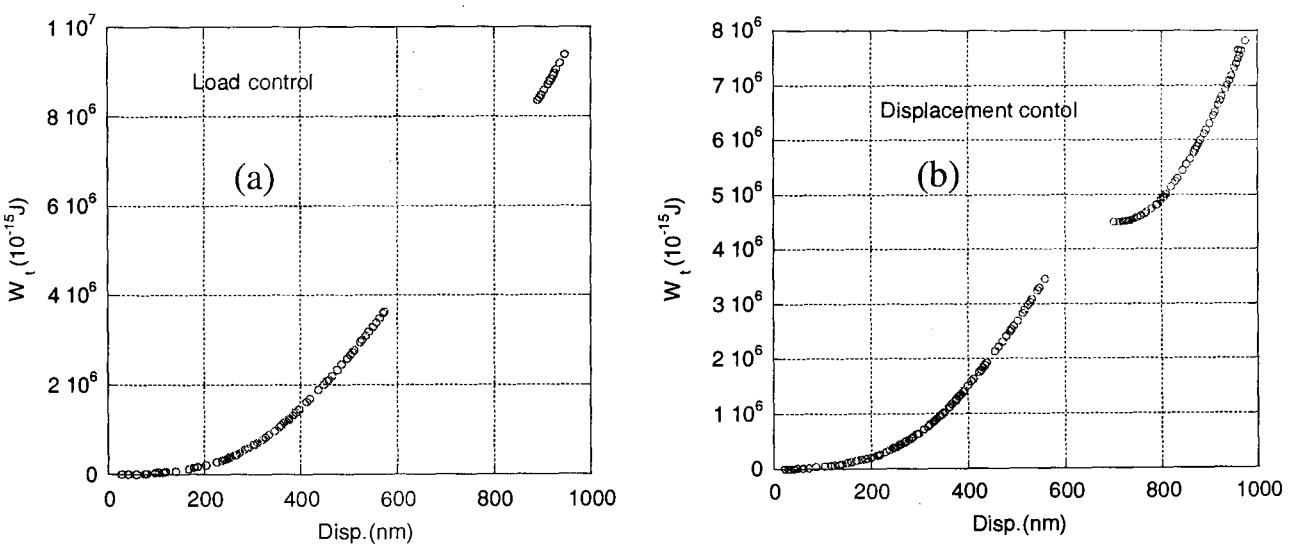

Fig. 5. 2. Total work versus displacement curves for (a) load control and (b) displacement control from data in Fig. 5.1.

5.2.2. Why a cube corner tip ?

When intending to eliminate substrate effects, it is preferred to make small indentations which requires relatively low loads in which case fracture may not occur when using the normal Berkovich tip. However, the application of cube corner tips

can significantly reduce the threshold for cracking (Pharr, 1998) (see example in Figure 5.3) so that this problem can be overcome. Another merit of cube corner tips is that the plastic deformation zone is more confined compared to Berkovich indenters at a given penetration (Stein, 2005) so that the influence from the substrate can be further reduced and smaller cracks can be produced at scales where they are not influenced by the plastic deformation zone. Therefore, a cube corner tip is good for investigating the cracking behaviour in thin films (<500nm in thickness).

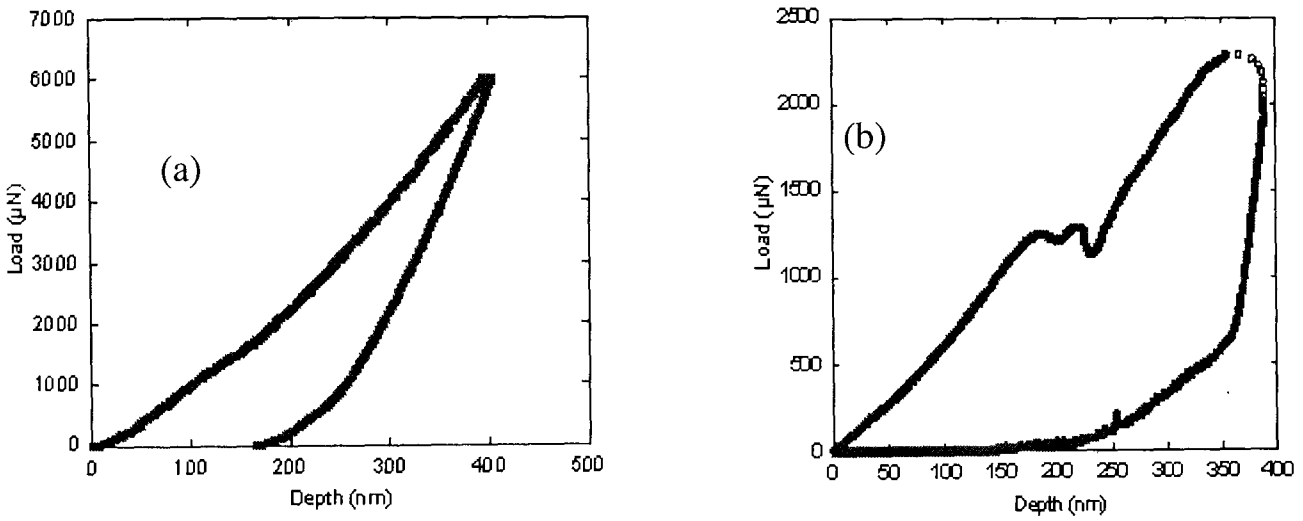

Fig.5.3. Load-displacement curve for 400nmTiOxNy/glass indented using (a) a Berkovich and (b) a cube corner tip under displacement control in which the maximum displacement is 400nm. There is no obvious excursion in load-displacement curve using a Berkovich tip, in contrast, significant load drops were observed in the P-δ curve using a cube corner tip.

5.3. Model of Extrapolating W_t-δ curve

As discussed in Section 5.2, plastic deformation of the coated system is usually inevitable during the events in the load-displacement curve for both load control and displacement control. However, the ld-dp method cannot separate these effects and it cannot deal with small cracks. Therefore, this model is further developed in this study.

5.3.1. Description of W_t-dp model and the fracture mechanisms for hard coatings on a hard substrate

It is proposed to assess the coating toughness based on a plot of total work of indentation vs. displacement (W_t-dp) which can be obtained by integrating the load-displacement curve (see example in Fig. 5.2). The method to determine fracture events is explained in Figure 5.4. First, it is suggested to extrapolate the initial W_t-dp curve from the cracking start point A to the cracking end point C, to get the work difference CD after fracture; then extrapolating the W_t-dp curve after cracking (i.e. curve XD in Fig.5.4) backward to the cracking start point and thus obtaining the work difference AB at the onset of fracture where point B has the same depth as point A. AB represents the difference of elastic-plastic deformation behaviour of the material prior to and post fracture whereas CD represents the total work difference caused by the presence of cracking which consists of the change of elastic-plastic deformation behaviour between the uncracked system and cracked system plus the fracture dissipated energy. The difference between the two (i.e. CD minus AB in Fig.5.4) will be the fracture dissipated energy.

From a thermodynamics point of view, the change of total Gibbs free energy during a fracture event results from the compliance change of the system, exchange of elastic strain with plastic strain, and change in crack area (Stevens and Guiu, 1991). The decrease of the stiffness of the coating and the change of the elastic-plastic strain field for the whole coated system can be additive (see Figure 5.4a, for a typical hard coating on a softer substrate) or counteract each other (see Figure 5.4b, for a typical hard coating on a harder substrate) depending on the actual coated systems and test conditions. It can be shown that for most materials CD-AB will not be zero provided load drops or plateaux are associated with fracture in the load-displacement curve (see next section).

During a through thickness fracture event in a brittle coated system, the following changes of the mechanical properties of the coated systems may occur,

(1) The stiffness of the coating decreases,

(2) Plastic deformation of the substrate is more likely or even dominates,

(3) Redistribution of the elastic and plastic strain may occur. The stored elastic energy in cracked coating is consumed, thus, in the further deformation; this part of coating is possibly elastically deformed rather than carrying on the plastic deformation.

(4) Any membrane stress is released.

Fig.5.5. displays the schematic of cross-section of an indentation with through thickness cracking by a sharp tip illustrating the processes which might occur.

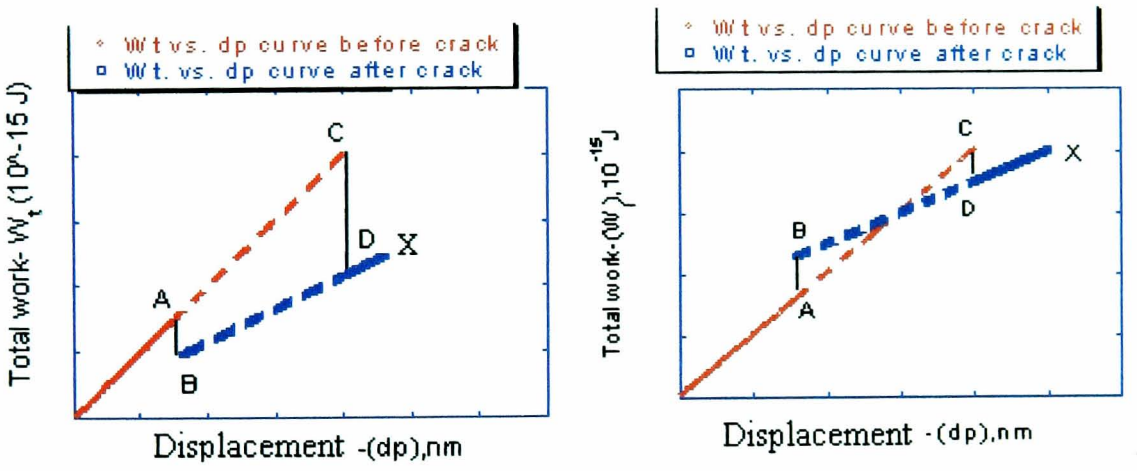

(a) (b)

Fig.5.4. Schematic of extrapolating the total work vs. displacement curve before and after cracking to determine the fracture dissipated energy CD-AB. Compared to CD, AB can be (a) positive as displayed in or (b) negative as depicted in depending on the actual coated systems (see text).

When a brittle coating on hard substrate is indented by a very sharp tip, say a cube corner tip, radial cracks easily initiate at the indent corners. When through thickness cracking occurs, the compressive stress and membrane stress (in Region I in Fig. 5.5) of the uncracked coating is released. The compliance of the cracked coating and its adjacent uncracked coating decreases. More load is supported by the substrate so the plastic deformation of the substrate is more likely to play an important role during further indentation. The cracked coating which was plastically deformed will still

support the load imposed by indenter; after the stored elastic energy is released by through thickness fracture it may be elastically deformed again prior to carrying on plastic deformation during further indentation. After through thickness cracking the bending stress caused by conforming to the substrate may be released.

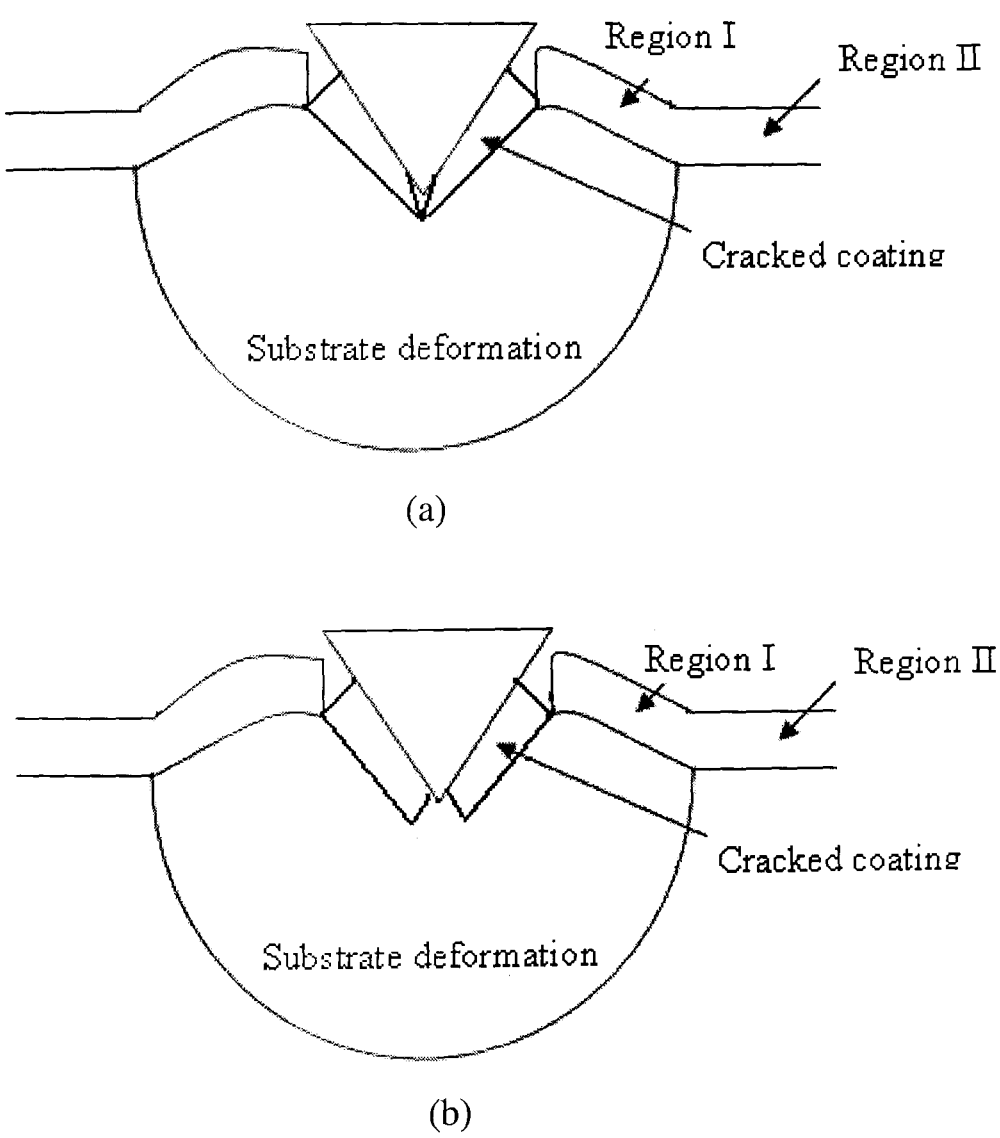

Fig. 5. 5. Schematic of the cross-section of an indention with through-thickness cracking by a sharp tip. (a) High tensile stress at the wedge tip causes fracture and (b) after increasing the load a bending effect on the coatings imposed by the substrate to increase the crack opening displacement. The upthrust of the coating and the plastic deformation of substrate is exaggerated in this figure.

All these mechanisms will lead to a change in the apparent hardness and modulus of the system during a crack event, thus altering the load-displacement curve (or the W_t-dp curve). It means it is not realistic to expect that the load-displacement curve or the W_t-dp curve after cracking will follow the same rule as the case prior to cracking. The second step, i.e. extrapolating the W_t-dp curve backward, described in the previous section is to account for such deviations. That AB in Fig. 5.4 can be positive or negative compared to CD is accounted for by the fact that the actual curve may be above or below the extrapolated curve. This is the reason why the second extrapolation process in W_t-dp model is necessary. Can the similar operation be made for ld-dp model under load control? The answer is no. The reason is that the energy (work) can be treated as the linear summary of elastic work, plastic work, fracture dissipated energy plus energy dissipated by heat etc (which is usually neglected), whilst, the load cannot be separated in this way. It is often the case that a second step in load-displacement curve will lead to a negative value of toughness (see such an example in Fig. 5.1).

5.3.2 Mathematical validity of the predictions and comments in W_t-dp method

In this section, the comments in Section 5.3.1 that CD-AB is unlikely to be zero will be analysed. For the sake of comparison with the ld-dp model, only the case of an excursion in the P-δ curve under load control is discussed in this section.

Assuming that there is no obvious slope change before pop-in, and the load-displacement curve (P-δ) can be described by a power law equation of the type,

$$P = k_1 \delta^2 \tag{5.1}$$

Then the total work done by the indenter at Point A in Fig.5.6, W_A, can be obtained by integrating the load-displacement curve,

$$W_A = \frac{1}{3} k_1 \delta_1^3 \tag{5.2}$$

For simplification, it is assumed that the total work versus displacement curve can be expressed as,

$$W = \frac{1}{3} a\delta^3 + \frac{1}{2} b\delta^2 + c \tag{5.3}$$

It is obvious that c>0 according to its physical meaning because the totoal work at the excursion end point (i.e. area OADN in Fig.5.6) is always bigger than the area under the load-displacement curve (ie. area ODN in Fig.5.6).

Thus P-δ curve after fracture can be expressed as

$$P(\delta) = a\delta^2 + b\delta \tag{5.4}$$

where *a,b,c* are dimensionless coefficients.

In order to determine the value of coefficients *a* and *b*, two initial conditions should be satisfied. For a plateau in the P-δ curve under load control experiments (here the ideal excursion is considered), the load P_{cr} where the pop-in occurs should be identical at Point A and Point B (see Fig. 5.6),

$$a\delta_2^2 + b\delta_2 = P_{cr} = k_1 \delta_1^2 \tag{5.5}$$

The total work at Point D expressed by integrating the equation should be the same as is measured,

$$W_D = \frac{1}{3} a\delta^3 + \frac{1}{2} b\delta_2 + c = \frac{1}{3} k_1 \delta_1^3 + P_{cr}(\delta_2 - \delta_1) \tag{5.6}$$

For convenience, let $\delta_2 = \lambda\delta_1$, where $\lambda > 1$ when pop-in occurs.

Combining equations (5.5) and (5.6), we can obtain,

$$a = \frac{k_1}{\lambda^2} - \frac{4k_1\delta_1^3(\lambda - 1) - c}{\lambda^3\delta_1^3} \tag{5.7}$$

$$b = \frac{4k_1\delta_1^3(\lambda - 1) - c}{\lambda^2\delta_1^2} \tag{5.8}$$

Then AB as depicted in Fig.5.4 is given by,

$$AB = \frac{1}{3}k_1\delta_1^3 - \left(\frac{1}{3}a\delta_1^3 + \frac{1}{2}b\delta_1^2 + c\right) \tag{5.9}$$

$$CD = \frac{1}{3}k_1\delta_2^3 - \left(\frac{1}{3}a\delta_2^3 + \frac{1}{2}b\delta_2^2 + c\right) \tag{5.10}$$

Now I need to prove that $CD - AB > 0$.

From equations (5.9) and (5.10), we obtain,

$$\begin{aligned} CD - AB &= \frac{1}{3}k_1(\delta_2^3 - \delta_1^3) - \left(\frac{1}{3}a(\delta_2^3 - \delta_1^3) + \frac{1}{2}b(\delta_2^2 - \delta_1^2)\right) \\ &= \frac{\delta_1^2(\lambda - 1)}{6}\left(2\delta_1(\lambda^2 + \lambda + 1)(k_1 - a) - 3b(\lambda + 1)\right) \end{aligned} \tag{5.11}$$

Combining equations (5.7), (5.8) and (5.11) , we get ,

$$CD - AB = \frac{(\lambda - 1)}{6\lambda^3}\begin{pmatrix} 2k_1\delta_1^3\lambda^5 + 2k_1\delta_1^3\lambda^4 - 4k_1\delta_1^3\lambda^3 - 2k_1\delta_1^3\lambda^2 \\ +10k_1\delta_1^3\lambda \ -8k_1\delta_1^3 + c\lambda^2 + c\lambda - 2c \end{pmatrix} \quad (5.12)$$

Since $\lambda>0$, the sign parameter in equation (5.12) is the complex term in the big bracket. Denoting,

$$f(\lambda) = \begin{pmatrix} 2k_1\delta_1^3\lambda^5 + 2k_1\delta_1^3\lambda^4 - 4k_1\delta_1^3\lambda^3 - 2k_1\delta_1^3\lambda^2 \\ +10k_1\delta_1^3\lambda \ -8k_1\delta_1^3 + c\lambda^2 + c\lambda - 2c \end{pmatrix} \quad (5.13)$$

Thus the derivative of $f(\lambda)$ is ,

$$f'(\lambda) = \begin{pmatrix} 10k_1\delta_1^3\lambda^4 + 8k_1\delta_1^3\lambda^3 - 12k_1\delta_1^3\lambda^2 - 4k_1\delta_1^3\lambda \\ +10k_1\delta_1^3 \ +2c\lambda \ +c \end{pmatrix} \quad (5.14)$$

and the derivative of $f'(\lambda)$ is given by,

$$f''(\lambda) = \left(40k_1\delta_1^3\lambda^3 + 24k_1\delta_1^3\lambda^2 - 24k_1\delta_1^3\lambda \ -4k_1\delta_1^3 + 2c\right) \quad (5.15)$$

The derivative of $f''(\lambda)$ is given by,

$$f'''(\lambda) = \left(120k_1\delta_1^3\lambda^3 + 48k_1\delta_1^3\lambda - 24k_1\delta_1^3\right) \quad (5.16)$$

Since $\lambda>1$, it is obvious that $f'''(\lambda)>0$. Thus $f''(\lambda)$ is a monotonic increasing function of λ. Therefore,

$$f''(\lambda) = \left(40k_1\delta_1^3\lambda^3 + 24k_1\delta_1^3\lambda^2 - 24k_1\delta_1^3\lambda - 4k_1\delta_1^3 + 2c\right) > f''(1) > 0 \tag{5.17}$$

Hence, $f'(\lambda)$ is a monotonic increasing function of λ. Therefore,

$$f'(\lambda) = \begin{pmatrix} 10k_1\delta_1^3\lambda^4 + 8k_1\delta_1^3\lambda^3 - 12k_1\delta_1^3\lambda^2 - 4k_1\delta_1^3\lambda \\ +10k_1\delta_1^3 + 2c\lambda + c \end{pmatrix} > f'(1) \tag{5.18}$$

Also, $f(\lambda)$ is a monotonic increasing function of λ. Therefore,

$$f(\lambda) = \begin{pmatrix} 2k_1\delta_1^3\lambda^5 + 2k_1\delta_1^3\lambda^4 - 4k_1\delta_1^3\lambda^3 - 2k_1\delta_1^3\lambda^2 \\ +10k_1\delta_1^3\lambda - 8k_1\delta_1^3 + c\lambda^2 + c\lambda - 2c \end{pmatrix} > f(1) = 0 \tag{5.19}$$

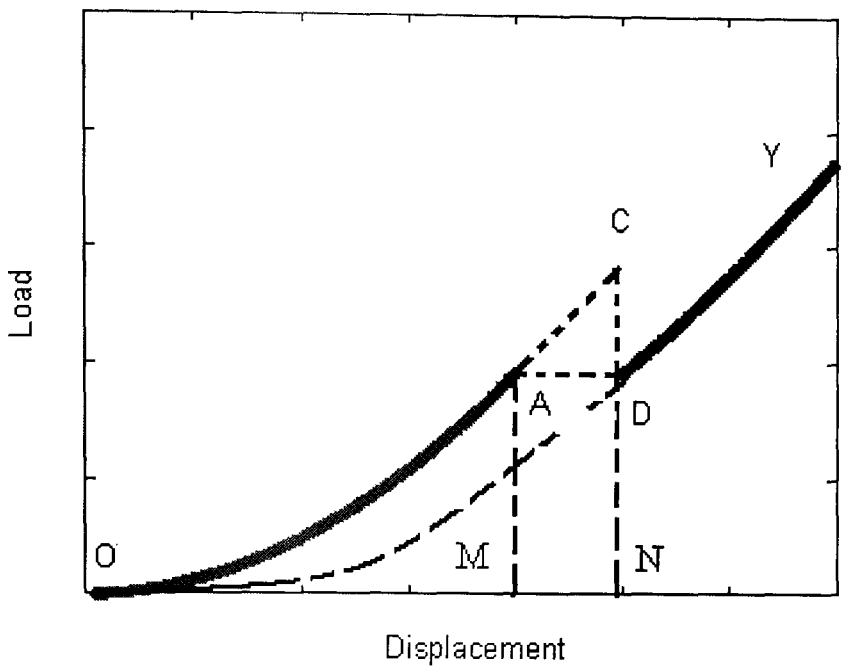

Fig. 5.6. Schematic of ideal load-displacement curve with an excursion due to crack in a coated system under load control discussed in this section.

It is necessary to point out that it is almost impossible to include in the mathematical analysis all the complex factors which influence behaviour in the coated systems which experience the fracture. The mathematical proof here is for an ideal simplified situation. For the actual coated systems, the argument that CD-AB>0 may be expected to be valid in wide range of cases which is confirmed by the experimental investigations. The purpose of the next section is to demonstrate this.

The same idea can be also applied to the simple purely linear elastic behaviour in which the fracture occurs which is discussed in Appendix.

5.4. Examples of model application

In this section, the fracture behaviour and the fracture toughness for brittle coated systems in different categories is discussed. Two cases are considered.

Type 1: Stiffer and harder coatings on a hard substrate, i.e. Solar control coating coatings on glass as described in Chapter 4; carbon coatings deposited on Si by different techniques from the literature is assessed.

Type 2: Softer coatings (but still hard materials) on harder and stiffer substrates, examples include CN_x coatings on various ceramic substrates such as sapphire.

Experimental measurements and data from the literature are used to examine the reliability of the W_t-dp method.

5.4.1 Solar control coatings on glass

5.4.1.1 Observations of fracture

Fig.5.7 shows the load-displacement curves for a 400nm TiO_xN_y single layer on glass with peak displacements of 100nm and 400nm. There is no evidence for fracture at the lower penetration but clear load drops are visible in the load-displacement curve for the deeper penetration. There is also some evidence of uplift next to the bigger indent (circled in Figure 5.7d) which could be an evidence for coating detachment since this material does not show appreciable pile-up and the substrate shows neither significant plastic deformation nor the significant constraint of plastic deformation in the coating. In order to analyse the possibility of cracking further line profiles have been extracted from Figure 5.7d and are presented in Figure 5.8. It can be seen that there is a possible open through-thickness crack (arrested) which is much deeper compared to valley in the surface roughness measurement. This is likely to be due to the detachment and lateral displacement of the coating. The origin of this detachment might be a picture-frame crack at C (see Fig.5.8) possibly at the transition between region I and region II as depicted in Fig.5.5.

The first event i.e. Event A-B-C in Fig.5.7c is accounted by the radial crack, whilst, the second event, i.e. Event D-E in Fig. 5.7c is expected to be related to interfacial

failure. The up-thrust in Fig.5.7d provides evidence of interfacial failure. The extra linear partion in the unloading curve in Fig. 5.7c is very likely caused by the rebound of the delaminated coating which implies that the delamination event occurs during the loading half cycle. Further, it is found that interfacial failure tends to occur after radial cracking for this sample, therefore, the second event which has different character from first event can be assumed to have a different fracture mechanism and it is possibly due to the interfacial failure. For the other samples without upthrust in the AFM image and graded slope change in their corresponding line profile measurement, radial cracking was assumed.

To provide further evidence for the size and location of fracture in these samples, analogy is made with the indentation tests done under high load (50mN~500mN) by a Berkovich indenter. At higher loads using a Berkovich indenter two crack systems are observed in these kinds of coatings using high resolution scanning electron microscopy (Berasategui, 2003). Initially, radial cracks were observed along the edges of the indenter where the coating is bent around the indenter edge. These are followed by picture-frame cracks at the edge of the impression once sufficient bending has occurred, which is usually observed at a relatively high load (>100mN). Since the use of a cube corner indenter can lower the threshold load for fracture initiation more than 10 times compared to a Berkovich indenter for many brittle materials (Pharr, 1998), it is reasonable to expect the presence of fracture at a few mNs. It might be expected that similar cracks are produced by the cube corner indenter at lower loads. However, it is noticed that the picture frame cracks in coatings are usually enhanced by the bending effect caused by the plastic deformation of the substrate which is more likely to occur for blunt tip at high load in which case the substrate will have been sufficiently plastically deformed.

For very low load tests, especially for the tests here which intend to eliminate the substrate influence, it can be expected the bending effect imposed by the plastic deformation of substrate is not significant. Further, given the sharp geometry of cube corner tip (with a small tip radius as well), the high stress intensity should result in the appearance of radial cracking. The crack pattern in this study is difficult to verify by microscope such as SEM or in-built AFM due to the limitation in resolution of these microscopy techniques. Also it is tricky to locate such small indentations in the SEM

or post-facto high resolution AFM measurement. In-situ transmission electron microscopy may be necessary to confirm the crack pattern and provide accurate crack imaging under such circumstances.

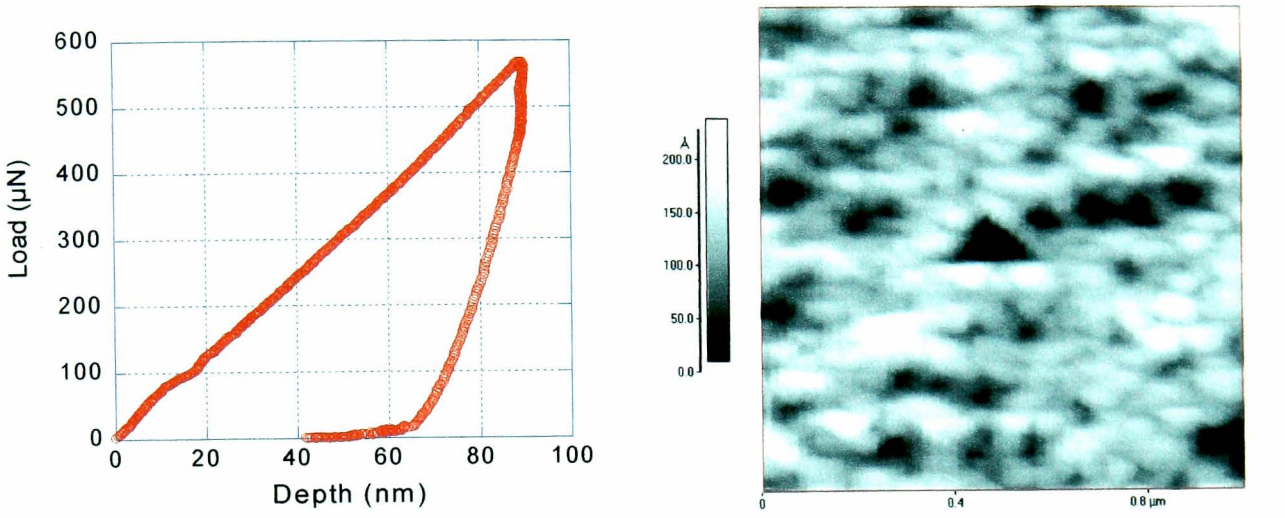

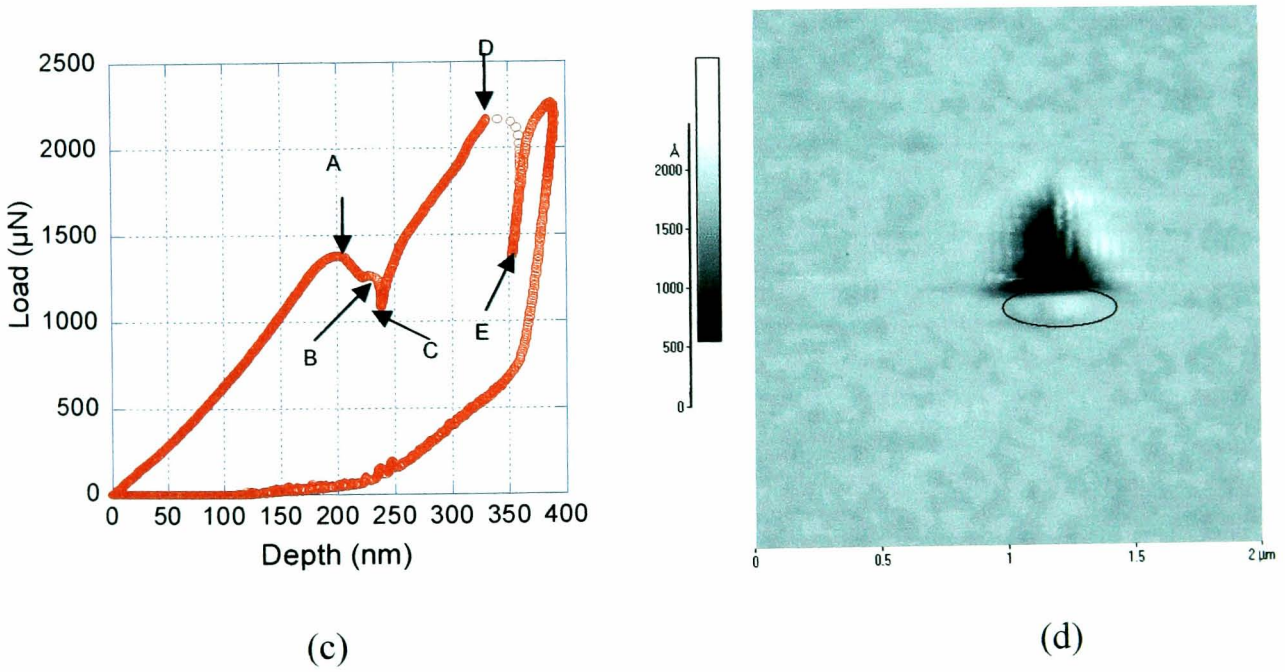

Figure 5.7. (a, c) Load-displacment curves and (b, d) AFM images of a 400nm TiO_xN_y coating on glass substrate (a, b) without cracks and (c, d) with cracks, respectively. The coating was indented by a cube corner tip under displacement control at 100nm maximum displacement (a, b) and 400nm maximum displacement (c, d). The circle in (d) marks an area of uplift associated with through-thickness and interfacial fracture. In (c), position A is regarded to be the position where plastic deformation extends to the softer substrate which is reasonable since the estimated plastic deformation exceeds 400nm based on the analysis by; points B and C are the start point and end point of through-thickness cracking, respectively; D and E are the start point and end point of interfacial fracture.

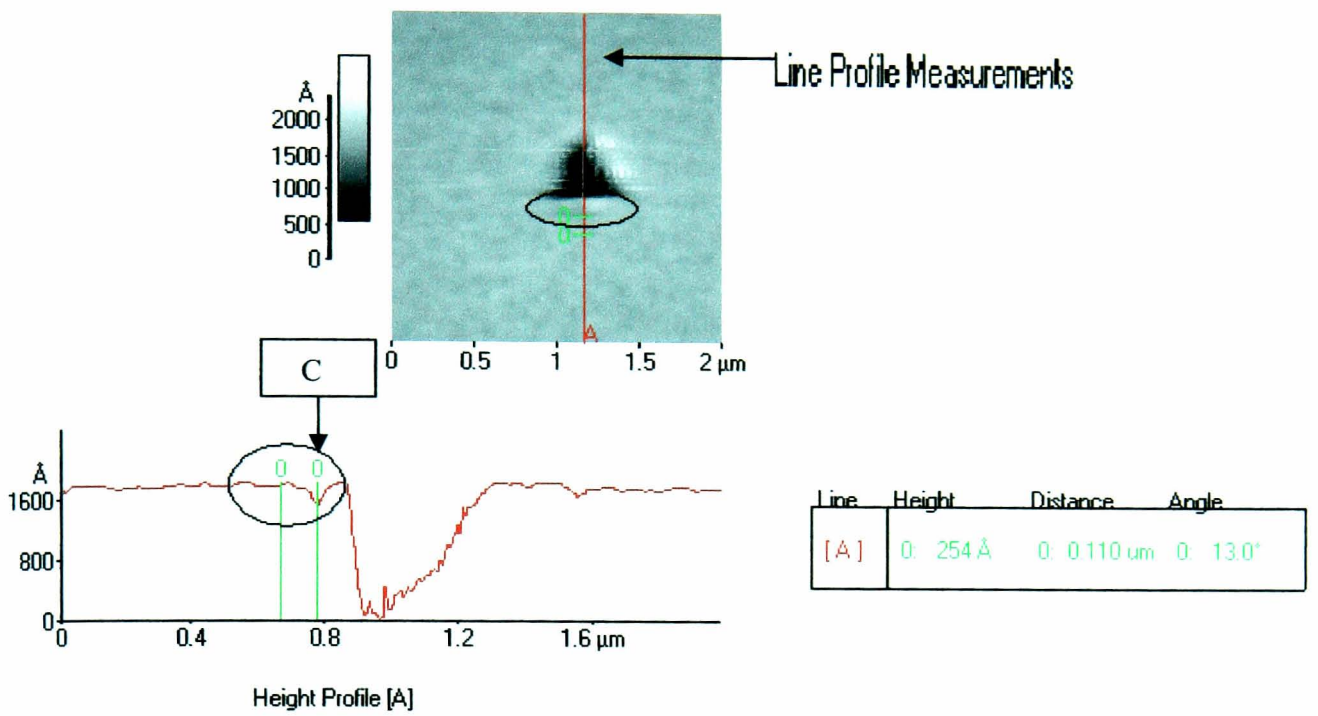

Figure 5. 8. AFM line profile measurement corresponding to Fig.5.6(d). An open through-thickness crack is visible at point C.

The experimental observations suggest that it is better to assess coating toughness under 400nm control because at such a displacement (relatively higher load), there is visible fracture in AFM images and analysable W_t-dp curves for all the samples investigated here. In addition, it was proposed (McGurk et al., 1994) that when the penetration is approaching the coating thickness during the fracture events, the cracks are likely to propagate through the complete coating thickness. Therefore, it is more convenient to assess the coating toughness based on the 400nm control tests and complete through-thickness cracking is used as a basis for toughness assessment.

The W_t-dp curve and its corresponding load-displacement curve for a 400nm TiO_xN_y on glass are plotted in Fig. 5.9. Two significant discontinuities are observed. It is obvious that these two events may be related to different fracture mechanisms. The first one, a small discontinuity, is related to radial cracking and the second one, a big jump, is likely to be accounted by interfacial failure. The reasons are discussed in previous paragraph.

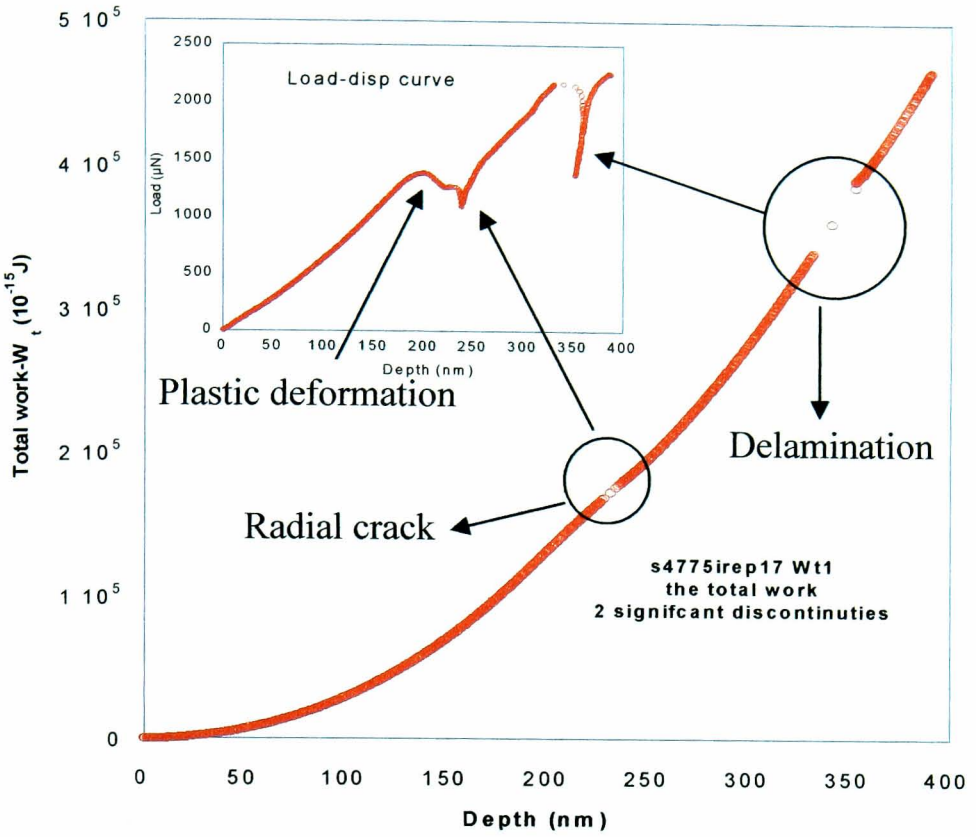

Fig. 5.9. Total work versus displacement curve for a 400nm TiO_xN_y on glass. Two significant discontinuities are observed. It is obvious that these two events are related to different fracture mechanisms (see text).

5.4.1.2 Energy release rate and toughness

Conventional indentation methods for measuring fracture toughness (Anstis et al., 1981) are not suitable for the thin coatings in particular for cracking confined to indent due to factors such as substrate effects, membrane stress, the domination of near-field stress in the case of small cracks. However, it is treated as first approximation in this study for comparison purposes. For Berkovich and Vickers indenters, χ=0.016 in Eq. (2.1). In this Chapter, a constant of 0.0335 was used for the cube corner indenter which was derived based on the scale relationship between the coefficient and the geometry parameter as mentioned in Chapter 2.

The strain energy release rate in Chapter 2 and fracture toughness can be determined based on Eq. (5.43) which is the same as that used in ld-dp model.

$$K_{IC} = [\frac{E_f U_{fr}}{(1-\nu^2)A_{crack}}]^{\frac{1}{2}} \tag{5.20}$$

Where U_{fr}, and A_{crack} are the fracture dissipated energy and the fracture area; E_f and ν are Young's modulus and Poisson's ratio of the coating.

In order to do this we need an accurate measurement of crack area. In this study the calculation is based on radial fracture following the indenter edges; it is assumed that the crack horizontal dimension is equal to the indentation radius (because no evidence of well-extended radial cracking was observed by in-situ AFM) and the vertical dimension is equal to coating thickness as discussed in previous section. Since there are three indenter edges, this dimension must be multiplied by 3 to get the total crack area which assumes uniform fracture around the indentation. All these results are summarized in Table 5.1. The comparison between the new method proposed here and the CIM is also plotted in Fig.5.9.

From Table 5.1, it can be seen the energy release rate of these kinds of ceramic coating are in the range 15 to 45 J/m^2 which is reasonable. By comparing the toughness determined by CIM and the new method developed here, they are of the same order of magnitude. However, the results for all the samples determined by the conventional method are almost identical to the toughness of uncoated glass (except for tin oxide). But these coatings suppress the fracture of the glass at higher loads, which implies that they are tougher than the glass substrate. The results determined by the W_t-dp method developed here support this observation. Although the sub-threshold cracking has been investigated elsewhere (Jung et al., 2004a), it requires many tests on a well-documented material to calibrate the constants in the model which is feasible for bulk material but not for thin coatings because their mechanical properties are usually not well known.

Table 5.1. The energy release rates and toughness calculated for the solar control coating components investigated in this study based on the radial through-thickness fracture.

	Energy release rate of coating G_{IC} (J/m^2) calculated by the W_t-dp model	Toughness of coating K_{IC} ($MPa\sqrt{m}$)	
		W_t-dp model	Estimated by CIM
400nm TiO_xN_y top layer single layer stack	24.4 ± 1.4	1.8 ± 0.2	0.9 ± 0.1
240nm ITO top layer mutilayer stack	36.3 ± 8.2	2.2 ± 0.3	0.9 ± 0.1
400nm ITO top layer mutilayer stack	32.7 ± 4.4	2.1 ± 0.2	0.7 ± 0.1
400nm TiO_xN_y top layer mutilayer stack	24.1 ± 7.8	1.8 ± 0.2	1.0 ± 0.1
400nm SnO_2 top layer mutilayer stack	29.3 ± 9.8	1.9 ± 0.3	1.3 ± 0.1

It might be argued that the fracture events which lead to features in the load-displacement curves are actually picture-frame cracking events. In this case the area of crack can also be shown to be dependent on the size of the indent and is about $\sqrt{3}$ times the area determined for radial cracks The strain release energy will thus be reduced by a factor of $1/\sqrt{3}$ and is thus in the range 9 to 26 J/m^2 which is also reasonable.

When it comes to the residual stress in the coating, unlike in the case of interfacial fracture or radial fracture for very brittle coatings with relatively large residual stress (e.g. sol-gel coating in (den Toonder et al., 2002)), it only plays a minor role in the contribution to radial fracture in this study. For such through-thickness cracking, it can be expected the upper volume limit of the coating whose stored strain energy U_r will contribute to the fracture is a disc with the radius of crack length as depicted in Fig. 5.11.

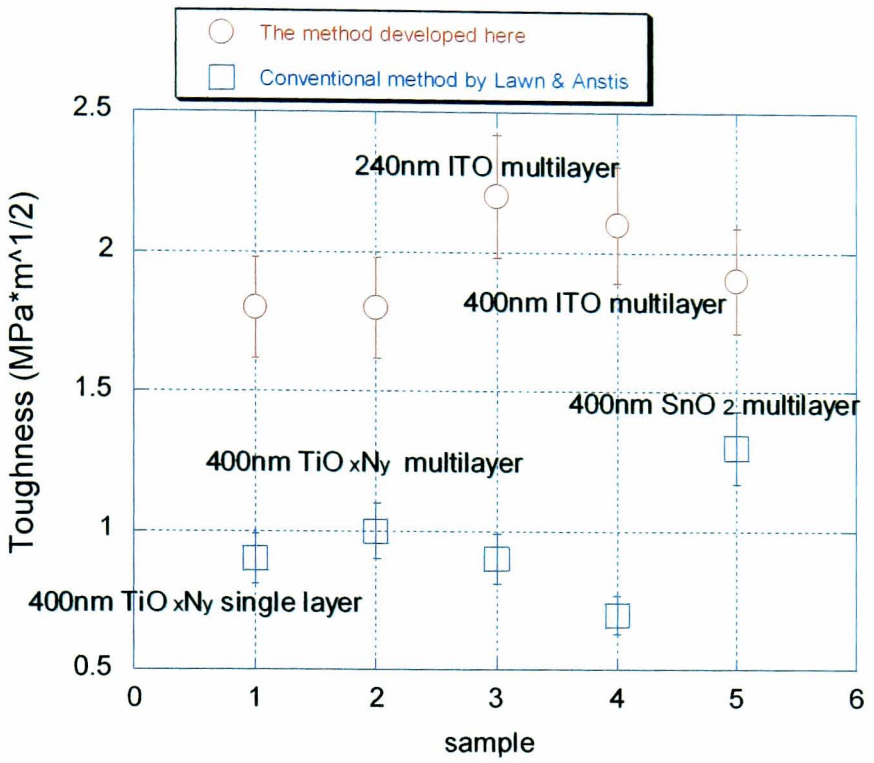

Figure 5.10. Comparison of toughness values determined by the conventional indentation method and the new method developed here.

The region around the crack undergoes stress relaxation due to the decease of stiffness where the region depicted in Fig.5.11 is the upper limit of the stored strain energy (U_r) because the tensile stress decrease dramatically with the distance , thus is given by,

$$U_r = \frac{1}{2}\frac{\sigma_r^{\,2}}{E}\pi c^2 t \tag{5.21}$$

Thus the contribution of U_r to the energy release rate of fracture is given by,

$$G_r = \frac{U_r}{3ct} \tag{5.22}$$

Where σ_r is the residual stress in the coating (for 400nm TiO_xN_y top layer with residual stress is around 200MPa); E, c, t are Young' modulus, crack length (for 400nm TiO_xN_y top layer, the crack length is about 480nm) and coating thickness,

respectively. According to Equations (5.21) and (5.22), we obtain 0.94 J/m^2 which is significantly smaller than the value of 24J/m^2 in Table 5.1. An alternative argument is that , based on the value of the strain energy release rate G estimated here, using the Equation (5.23) developed by Lawn et al (Lawn and Wilshaw, 1975), the stress σ_{tip} at the crack tip is about 2400MPa which is much bigger than the residual stress (~200MPa). For a crack which is not well-developed, σ_{tip} can be expected to be bigger than 2400MPa in this study because this sub-threshold crack is unstable (Jung et al., 2004b), whilst, Eq.(5.23) was proposed based on equilibrium cracking.

$$\sigma_{tip} = [\frac{EG}{(1-\nu^2)\pi\Omega c}]^{\frac{1}{2}} \tag{5.23}$$

where E, ν, c are as defined before, and the geometric constant Ω is $4/\pi^2$ for an ideal fully developed penny crack in an infinite medium.

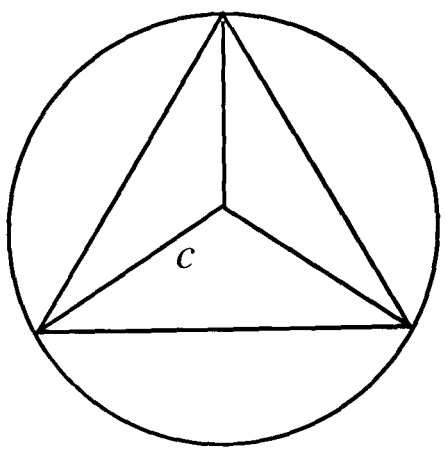

Fig. 5.11. Schematic of cross-section of a disc encaved the cracked coating which is regarded to be an upper limit volume contributes to coating fracture.

The arguments above provide the evidence that the residual stress in these coatings is much smaller than the indentation stress which contributes to the fracture in this study and thus it may be ignored here with reasonable accuracy.

In the same way, the energy release rate for interfacial failure for 400nm TiO_xN_y/glass, and 240nm ITO multilayer/glass is 30±14J/m^2, 19±9J/m^2, respectively, where the delamination area is assumed to be πc^2. As it was found that interfacial failure in the former sample (i.e. TiO_xN_y coating on glass) occurs at higher load than the cracking in the coating, this indicates that the interface toughness is comparable to the coating toughness if not greater. The energy release rate for interfacial failure is similar to that for the coating itself, which agrees with the comments above. Experimental observation shows delamination at the edge of the sample prior to the indentation which is caused by the high residual stress in the ITO coating introduced during deposition and the additional stress during glass cutting which confirms the relatively poor interfacial toughness for 240nm ITO multilayer/glass. It is reasonable to expect that such an interface is weaker than that of the TiO_xN_y coating on glass which is consistent with the calculations here. It may also be expected that the interface is weaker than the coating itself which is also suggested by the calculations here. More details about assessment of interfacial failure will be addressed in Chapter 8.

5.4.2 Toughness results for other coated systems

It is more convincing if this method can be successfully applied to different coated systems with different crack behaviour under different test conditions.

Figure 5.11 depicts the W_t-dp curve and its corresponding fracture image by SEM for a 1μm fullerene-like CN_x coating on an Al_2O_3 substrate under 500mN load control. The step in the load-displacement curve and jump in the W_t-dp curve are caused by the through-thickness cracking of the coating since blistering without coating detachment shows no jump in the loading curve. In this case, the area in Eq. (5.43) is determined by the extent of through-thickness fracture after interfacial failure. The

toughness results for the CN_x coating on different substrates obtained by various models are summarized in Table 5.2.

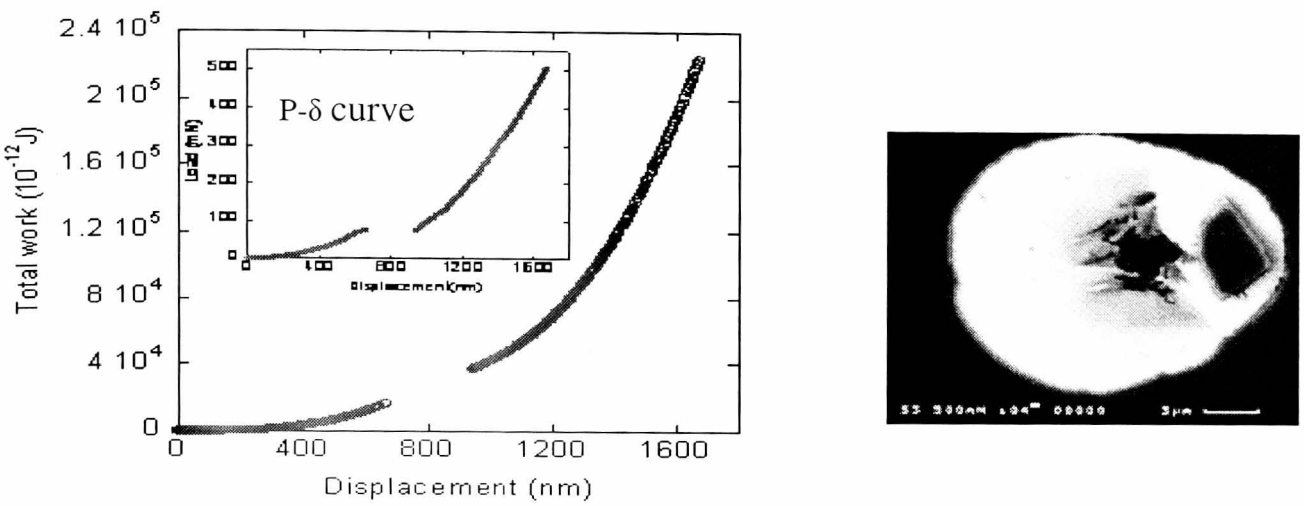

Fig. 5.12. The total work vs. displacement curve and SEM image for coating deposited on Al_2O_3 substrate where through thickness fracture occurs. The maximum load is 500mN.

It is necessary to point out that the crack morphology of CN_x on sapphire is slightly different from the previous samples. For the other samples, the area of cracking can be assumed as $3\times 2\pi C_R$ as suggested by den Toonder et al (den Toonder et al., 2002), (see details in Chapter 2), whilst, for CN_x on sapphire, the crack area is more reasonably calculated as $2\pi C_R$ since fracture is approximately circular.

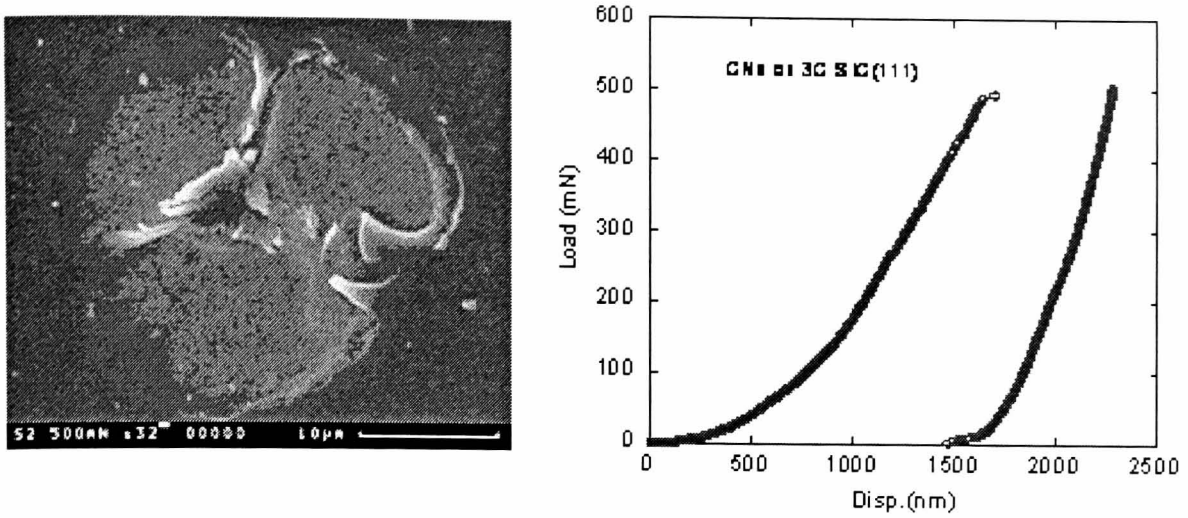

Fig. 5.13. SEM micrographs and corresponding P-δ curve of a 500mN applied load on 1µm CN_x coating deposited on 3C SiC(111) showing through-thickness fracture and chipping of the coating. The load where excursion occurs is almost the maximum load. After (Fernandez-Palacio et al., 2004).

Table 5.2. Comparison of 1µm fullerene like CN_x on different stiffer and harder substrate between different models based on fracture dissipated energy method.

Substrate	K_{IC}, $MPa\sqrt{m}$	
	Ld –dp model	*W_t-dp method here*
Si(001)	2.9 ± 0.1	*3.8 ± 0.2*
Al_2O_3	4.2 ± 0.2	*5.7 ± 0.2*
3C SiC(001)	5.5 ± 0.2	*5.6 ± 0.2*
3C SiC(111)	4.9 ± 0.1	*5.4 ± 0.2*

From Table 5.2, it can be seen that the ld-dp model tends to underestimate the fracture toughness for the first two sets of samples which agrees well with the prediction that ld–dp method may underestimate the fracture toughness for a typical softer coating on harder and stiffer substrate in the previous section (i.e Section 5.2). For the other two samples, the results obtained by the ld-dp method and W_t-dp model are almost identical, the reason is that the load where displacement excursion occurs is approaching the maximum load (also the highest limit of Nanoindenter II available in Newcastle), which leads to the restriction of the second extrapolation process as discussed in the previous section. This happened to the latter two samples and there are no obvious slope changes prior to the excursion, in which case, the W_t-dp method gives similar results to the ld-dp method. However, when other features (such as slope

changes) occur prior to the excursion, the W_t-dp method is preferred because it tends to reduce their influence. An example of this is discussed in the following paragraph.

An examination was carried out for experimental data from carbon coatings deposited on Si which were initially used in the development of ld-dp model in the work of Li et al (Li et al., 1997) , (Li and Bhushan, 1998). The comparison of the fracture toughness for different carbon coatings on Si determined by ld-dp method and W_t-dp method is summarized in Table 5.3 from which it can be seen that more reasonable results are provided by means of the W_t-dp method. From Table 5.3 the toughness of cathodic arc carbon coating on Si determined by the ld-dp method (Li et al., 1997) was 10.9MPam$^{1/2}$ which was higher than the toughness (~7.9 MPam$^{1/2}$) of bulk diamond (Field and Pickles, 1996). This is not realistic since the coating is usually more brittle compared to its bulk form because of the pre-existing stress and relatively abundant defects in coating. However the W_t- dp method provides the result of 6.2 MPam$^{1/2}$ which is more reliable. The difference in toughness for ion beam carbon coating indented by the conical tip and the cube corner tip obtained by the ld-dp method is about 10%, in contrast, the difference drops to 4% when using the W_t-dp method. The overall results of these two carbon coatings are in the range 5.5~6.2 MPam $^{0.5}$ which is identical to the toughness range (5~6MPam $^{0.5}$) of diamond coatings reported in literature (Field and Pickles, 1996). It is reasonable to make such comparison because these coatings are highly cross-linked which is close to the structure of diamond coatings. The main errors of calculation will result from fracture measurement in the initial paper; the overall errors in the calculations by the W_t-dp method will be similar to those in the ld-dp method.

As addressed previously in the case that the critical load for fracture is approximately the maximum load, in which the second item (i.e. AB in Figure 5.4) will vanish then the ld-dp method will be identical to the W_t-dp method. However, this is only true for the ideal case, i.e. the load is proportional to displacement squared (or an equivalent polynomial relationship) up to the critical load where excursion occurs, in other words, no obvious slope change occurs prior to the excursion. A slope change may occur before an excursion in the load-displacement curve, in particularly for a brittle coated system consisting of a hard coating on a softer substrate, in which case, the W_t-

dp model could smooth the curve and eliminate the fitting errors thus leading to more stable results as indicated in Table 5.3.

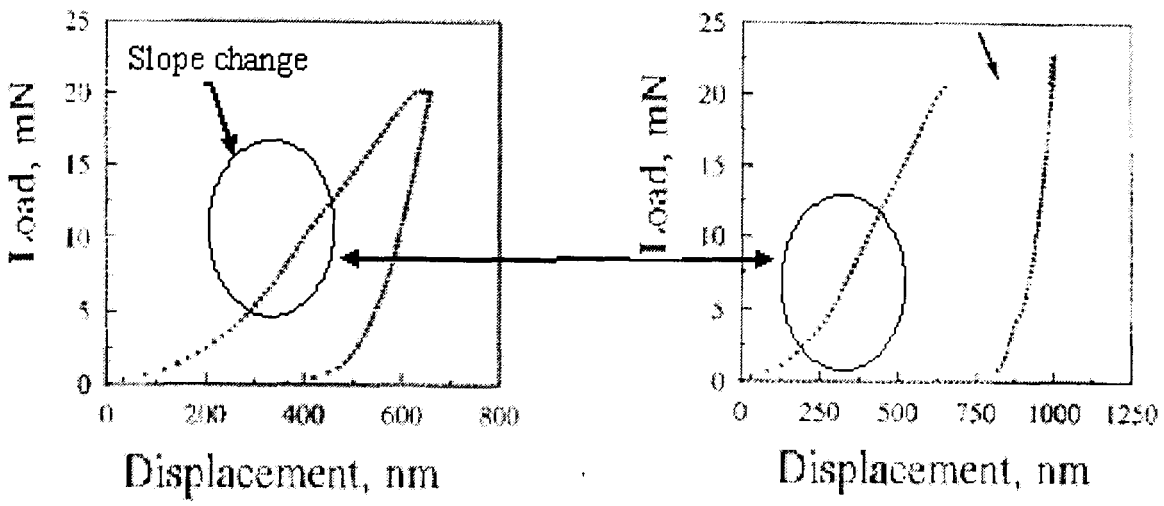

Fig. 5.14. *P-δ* curve for ion beam carbon coating indented by a cube corner tip. It is obvious that a slope change occurs prior to the excursion. After Li et al (Li et al., 1997).

Table 5.3. The comparison of toughness of carbon coating deposited on silicon by cathodic arc and ion beam between ld-dp method and W_t-dp method.

	Maximum load, mN	K_{IC}, $MPa\sqrt{m}$	
		Ld-dp method	W_t-dp method
Ion beam conical tip	30	5.4	5.8
Ion beam cube tip	22.5	4.9	6.0
Cathodic arc cube tip	200	10.9	6.2

Compared to the ld-dp model and the other energy based models addressed in Chapter 2, the W_t-dp method can separate other deformation mechanisms from fracture dissipated energy and can deal with different cracking patterns based on a single curve given that the link of the events in the W_t-dp curve to the fracture mechanism is known. Although this method was initially developed to deal with small cracks, it is also applicable to well-developed cracking. In addition, it can be equally applied to

load control and displacement control tests. The disadvantage of W_t-dp method is that the two-step extrapolation may lead to more fitting errors.

5.5. Summary

This Chapter has explained why tests performed under displacement control with a cube corner tip are necessary to assess small cracks confined in very thin films. The development of an energy based model (i.e. the W_t-dp method) to assess coating toughness was described. The conclusions are summarized as follows:

(1) Nanoindentation under displacement control by a cube corner tip is suitable to investigate the small-scale fracture behaviour of submicron coated systems.
(2) The W_t-dp method provides reasonable results for various coated systems with different cracking patterns under different test conditions and it shows promise for wider application compared to the ld-dp method.
(3) The W_t-dp method shows promise to investigate different fracture behaviours for coated systems based on the response in an individual test.
(4) The W_t-dp method helps to give the insight into the different fracture mechanisms during the fracture event (such as the two predictions in Section 5.2).

Usually, for most energy based models to assess coating toughness, it requires features such as a displacement excursion or load drop in P-δ curve. In the next Chapter, another model used to predict the boundary values of coating toughness is presented based on the events in P-δ curve with the difference that it does not require any extrapolation process.

References :

Anstis, G. R., Chantikul, P., Lawn, B. R. and Marshall, D. B. (1981) A Critical-Evaluation of Indentation Techniques for Measuring Fracture-Toughness .1. Direct Crack Measurements,*Journal of the American Ceramic Society,* **64,** 533-538.

Berasategui, E. G. (2003) Determining the mechanical properties of thin coated systems by nanoindentation,University of Newcastle Upon Tyne

den Toonder, J., Malzbender, H., de With, G. and Balkenende, R. (2002) Fracture toughness and adhesion energy of sol-gel coatings on glass,*Journal of Materials Research,* **17,** 224-233.

Fernandez-Palacio, J., Arce-Garcia, I. and Bull, S. J. (2004) Indentation response of fullerene-like CNx,*Tribology International,* **37,** 929-940.

Field, J. E. and Pickles, C. S. J. (1996) Strength, fracture and friction properties of diamond,*Diamond and Related Materials,* **5,** 625-634.

Jung, Y. G., Pajares, A., Banerjee, R. and Lawn, B. R. (2004a) Strength of silicon, sapphire in the subthreshold flaw and glass region,*Acta Materialia,* **52,** 3459-3466.

Jung, Y. G., Pajares, A. and Lawn, B. R. (2004b) Effect of oxide and nitride films on strength of silicon: A study using controlled small-scale flaws,*Journal of Materials Research,* **19,** 3569-3575.

Lawn, B. R. and Wilshaw, T. R. (1975) *Fracture of Brittle Solids,* Cambridge University Press, London.

Li, X. D., Diao, D. F. and Bhushan, B. (1997) Fracture mechanisms of thin amorphous carbon films in nanoindentation,*Acta Materialia,* **45,** 4453-4461.

Li, X. D. and Bhushan, B. (1998) Measurement of fracture toughness of ultra-thin amorphous carbon films,*Thin Solid Films,* **315,** 214-221.

McGurk, M. R., Chandler, H. W., Twigg, P. C. and Page, T. F. (1994) Modeling the Hardness Response of Coated Systems - the Plate-Bending Approach,*Surface & Coatings Technology,* **68,** 576-581.

Pharr, G. M. (1998) Measurement of mechanical properties by ultra-low load indentation,*Materials Science and Engineering a-Structural Materials Properties Microstructure and Processing,* **253,** 151-159.

Stein, W. (2005), Private communication

Stevens, R. N. and Guiu, F. (1991) Energy-Balance Concepts in the Physics of Fracture,*Proceedings of the Royal Society of London Series a-Mathematical Physical and Engineering Sciences,* **435,** 169-183.

Warren, O. L. and Wyrobek, T. J. (2005) Nanomechanical property screening of combinatorial thin-film libraries by nanoindentation,*Meas. Sci. Technol.,* **16,** 100–110.

Chapter 6:

Modelling the limits for coating toughness

Chapter 6: Modelling the limits for coating toughness

In Chapter 5, an energy based model, i.e. the W_t-dp method was developed to estimate coating toughness. In practice, it is very helpful to have the knowledge of the limits to coating toughness based on reliable and convenient calculations. The methods described in Chapter 5 rely on curve fitting (extrapolating the ld-dp curve or W_t-dp curve), whilst, in this section, the methods to predict the toughness are performed without extrapolation and some fundamental universal equations are derived. As discussed in Chapter 2, the initial bound model to predict the upper and lower limit of coating toughness is briefly described which is followed by the explanation of the modified model. The introduction of and comparison between these two methods was partly covered in Chapter 2.

6.1. Initial bound model

The lower and upper bound method which was first proposed by den Toonder et al (den Toonder et al., 2002) provides a simple and concise expression to determine the bound values of fracture dissipated energy. It was assumed that before cracking and after cracking the load (P) scales with displacement squared (δ^2) in the loading part and in the unloading procedure. At the same time, it is supposed that either fully elastic behavior (i.e. final depth $\delta_f=0$) or fully plastic behaviour (i.e. $\delta_f=\delta_m$, where δ_m is the maximum depth) occur in the coated system before and after crack events to determine the lower bound or upper bound for fracture dissipated energy under load control (see Fig.6.1). The upper bound of fracture dissipated energy under displacement control was obtained by assuming the final depth after fracture is zero (see Fig.6.2). The detailed description of this model was outlined in Chapter 2.

Unlike in load control, the initial bound method failed to provide any lower limit of the fracture toughness for displacement control. As mentioned in Chapter 2, there are some conflicts between the assumptions for these expressions which are addressed in the following paragraphs.

As argued previously that the plastic deformation (in coating or substrate) always occurs when indented by a sharp tip before the point where fracture which leads to the result that the final indentation depth cannot be zero. Real situations therefore do not agree with the assumptions and it is not reasonable to regard the area OAB (see Fig.6.1) as the lower bound of fracture dissipated energy. Actually, area OAB is the upper boundary under the assumption of purely elastic behaviour for both load control and displacement control. However, for actually coated systems indented by a sharp tip, plastic deformation is usually evitable. The argument that ABDC is not a reasonable upper bound because it is mainly attributed to the plastic deformation under the assumption of fully plastic behaviour. Thus a modified bound model is developed here and it is explained in the following section.

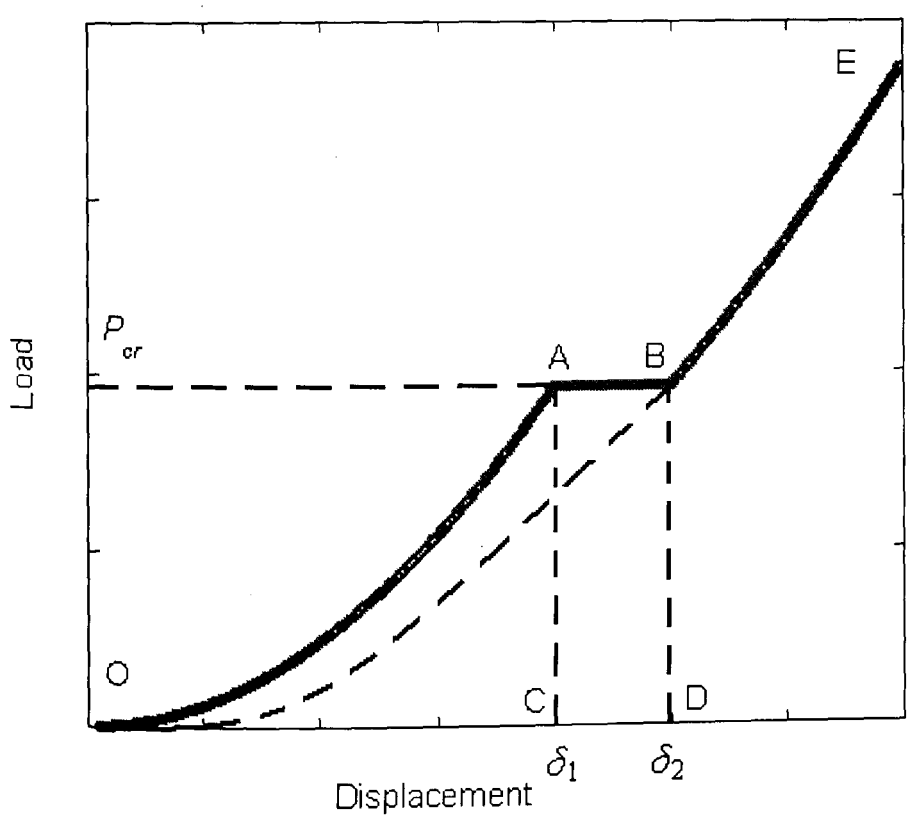

Fig.6.1. Schematic of the lower bound method by den Toonder et al under load control. The areas OAB and ACDB are regarded as the lower and upper bound of fracture dissipated energy, respectively.

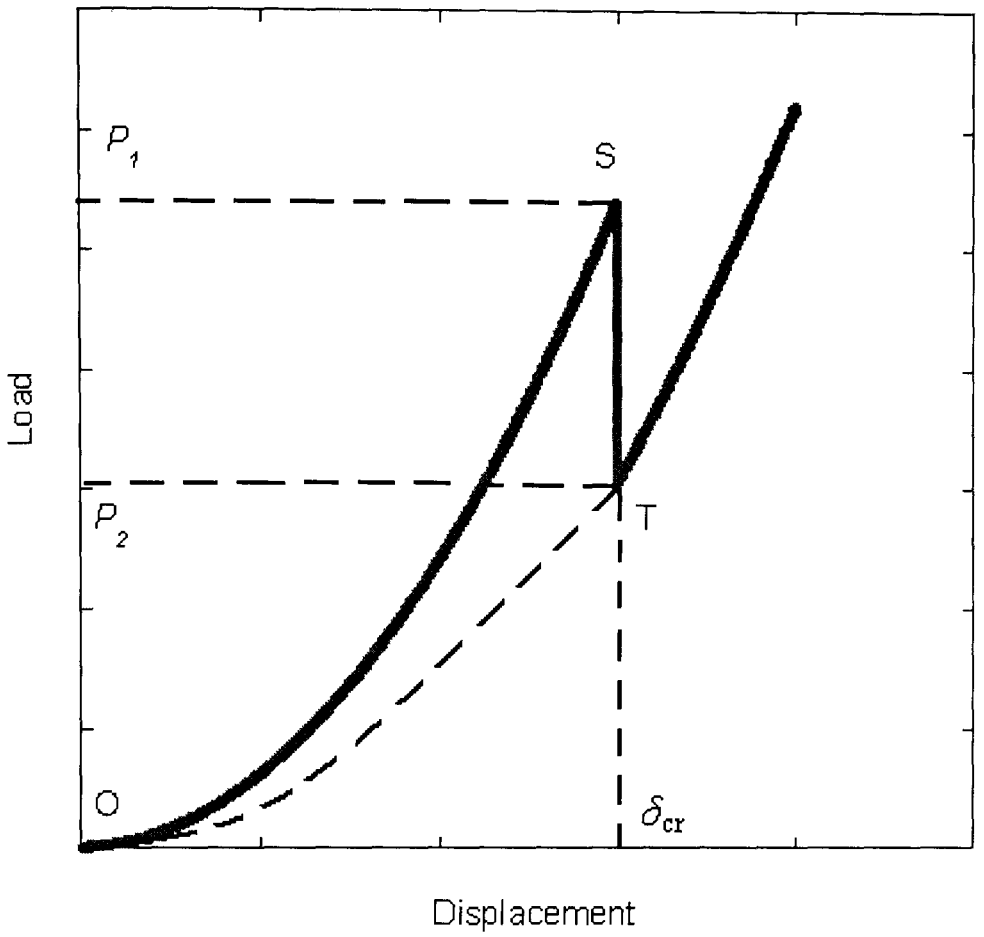

Fig.6.2. Schematic of the upper bound method by den Toonder et al under displacement control. The area of OST is regarded as the upper bound of fracture dissipated energy.

6.2 New bound model

In this section, in combination with existing numerical analysis and phenomenological models, a modified model is proposed based on analysing the unloading curves at the points where the crack starts and ends which more reliably represents the behaviour of coated systems in practice. The modified method gives the lower and upper bound of fracture dissipated energy for both load control and displacement control. Actually, the real lower bound is very difficult to be obtained. The lower and upper bound discussed here will be the lower and upper limits of the upper bound. The model developed here has been successfully applied to fullerene-like CN_x coatings deposited on various substrates such as Si, SiC, Al_2O_3 and it is also

suitable for other coated systems (e.g. sol-gel coatings on glass) given that a discontinuity related to fracture occurs in load-displacement curve.

The explanation of this modified bound model is divided in two parts in the following.

6.2.1 Step in load –displacement curve under load control

First of all, imagine unloading the load-displacement curve at the start point of a discontinuity to obtain the imaginary unloading curve AE (see Fig. 6.3). It can be expected that after fracture events the final depth of the imaginary unloading curve will be between δ_f and δ_2 (see Fig.6.3). The energy dissipated by fracture is supplied by the stored elastic strain energy and the work done by the indenter during fracture. Thus the possible maximum energy, U_{max}, which could be dissipated by cracking is the stored elastic strain energy before cracking plus the work done by the indenter. And the minimum dissipated energy U_{min} equals U_{max} minus the residual stored elastic energy after fracture. In other words, the areas AEB and AEFB in Fig.6.3 are the lower and upper bound of energy dissipated by fracture, respectively.

Then the key issue is how to determine the areas AEB and AEFB in Fig.6.3.

(1) It is assumed that the imaginary unloading curves (i.e. AE and BE in Fig.6.3) before cracking and after cracking can be fitted by a power law equation, i.e. $P_1 = A(\delta - \delta_{f1})^m$, $P_2 = B(\delta - \delta_{f2})^n$, respectively. The final part of the fully unloading curve may diverge from this expression but the contribution from it can be ignored in energy based models.

Thus, four independent parameters (e.g. δ_{f1}, δ_{f2}, m, n) are needed to be determined.

(2) Before the prediction of δ_{f1}, it is assumed that there is no microcracking (or its influence is negligible) disturbing the elastic–plastic behaviour before the step (plateau or load drop) occurs in the load-displacement curve.

For bulk materials without fracture, Cheng et al (Cheng et al., 2002) developed the following linear relationship between the ratio of δ_f to δ_m and the ratio of H to E,

$$\frac{\delta_f}{\delta_m} = 1 - \lambda \frac{H}{E} \tag{6.1a}$$

$$\lambda = 1.50\tan(\theta) + 0.327 \qquad \text{for } 60^o \le \theta \le 80^o \tag{6.1b}$$

For a Berkovich indenter, λ=4.5. In this case, $\delta_m = \delta_1$ in Fig.6.3. Thus the value of δ_f can be determined. Actually, from numerical analysis in conjunction with analytical assessment, the relationship between the H/E ratio and δ_f/δ_m is not linear as discussed in Chapter 3. However, within the range of H/E of the materials investigated here, Eq.(6.1) is a very good approximation and it is easy to apply. Although the expressions above are not strictly valid for a coated system, it can be approximately applied when substrate-dominated deformation is well-established. Using the hardness and elastic modulus of the coated system which can be measured or calculated by a reliable model (Bull, 2001, Bull et al., 2004, G-Berasategui et al., 2004), a reasonable agreement to equation (6.1a) is maintained for the coated system tested in this study. A similar relationship was also found by Malzbender et al for their coated systems(Malzbender and de With, 2000). In addition, previous studies indicate that the ratio of δ_f to δ_m, Young's modulus E of the coated systems and hardness H are almost identical to the values of corresponding substrates in this study when the load is over 100mN (Arce-Garcia, 2002). Therefore, equation (6.1a) can be approximately applied in such coated systems as in this study, where the critical load for excursion is much higher than 100mN except for CN_x on Si (100) which is further discussed in Section 6.4.

It is obvious that the area ABQE is the upper bound of the fracture dissipate energy because it is maximum irreversible work done during the events of fracture which can be fracture dissipated energy and plastic deformation associated with fracture. The lower and upper limit of the area ABQE can be determined because Point Q should be between Point E and F as depicted in Fig.6.3.

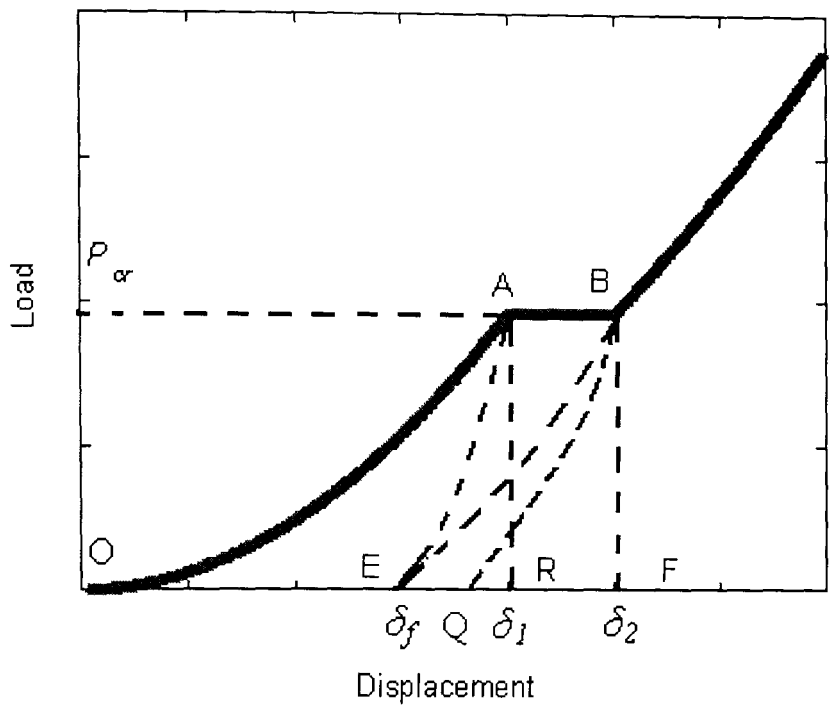

Fig. 6.3. Schematic of the lower bound method under load control developed in this thesis. The areas EAB and EABF are regarded as the lower and upper limits of the upper bound of fracture dissipated energy (i.e. the area AEQB), respectively. The reason is that the final depth associated with Point B (i.e. Point Q) will be in the range between E and F.

Then, the lower limit is given by,

$$U_{\min} = \int_0^{P_{cr}} ((\frac{y}{B})^{1/n} - (\frac{y}{A})^{1/m}) dy \tag{6.2}$$

$$U_{\max} = \int_{\delta_f}^{\delta_1} A(x - \delta_f)^m dx + P_{cr}(\delta_2 - \delta_1) \tag{6.3}$$

where $$A = \frac{P}{(\delta_1 - \delta_f)^m} \qquad B = \frac{P}{(\delta_2 - \delta_f)^n}$$

The next target is to estimate m and n, which is described in the following.

A few workers (Cheng et al., 2002),(Malzbender and de With, 2000),(Lawn and Howes, 1981), (Marx and Balke, 1997) find that there is a linear relationship between

W_{irr}/W_t and δ_f/δ_m by experiments or numerical analysis. Combining finite element analysis and scaling relationships, Cheng et al (Cheng et al., 2002) give the relationship between the ratio of irreversible work and total work W_{irr}/W_t and the ratio of final depth and maximum depth as follows,

$$\frac{W_{irr}}{W_t} = 1.27\frac{\delta_f}{\delta_m} - 0.27 \qquad \text{for } \frac{\delta_f}{\delta_m} > 0.4 \tag{6.4}$$

When a Berkovich indenter is used, the condition that $\frac{\delta_f}{\delta_m} > 0.4$ corresponds to the requirement that H/E is less than 0.19 which is satisfied by the CN_x coating and the substrates investigated (see Table 6.1) in this study but not with more recent CN_x films which can have H/E ~0.25 (Palacio et al., 2006).

If it is assumed that the load P scales with δ^2 in the loading curves before cracking (i.e. fracture does not occur before well-developed plastic deformation) and that the unloading curves can be fitted by the power law as previously, i.e. $P = A(\delta - \delta_f)^m$, the following relationship can be obtained (Mencik and Swain, 1994),

$$\frac{W_{irr}}{W_t} = \frac{3}{m+1}\frac{\delta_f}{\delta_m} - \frac{2-m}{m+1} \tag{6.5}$$

For ideal case, equation (6.5) can be obtained by finite element simulations as well. Thus it can be assumed this relationship is identical with Eq.(6.4), and it gives m=1.362. Ideally, this value of m can be used in this study. Since it is very difficult to directly predict the value of n independently, it is supposed that n=m=1.362, so that the lower bound and upper bound can be obtained. Such an assumption is reasonable when fracture propagation has ceased. Actually, the variance of the values of m, n will

not lead to considerable change of results of coating toughness which is discussed in Section 6.4.

6.2.2 Load drop in load-displacement curve under displacement control

In the same way, the Point V should be between Point E and G, thus the lower and upper bound of area ABVE (i.e. area AEB and area AEG in Fig. 6.4 respectively) of fracture dissipated energy is given by,

$$U_{\min} = \int_{\delta_f}^{\delta_{cr}} (A(x-\delta_f)^m - B(x-\delta_f)^n)dx \tag{6.6}$$

$$U_{\max} = \int_{\delta_f}^{\delta_{cr}} A(x-\delta_f)^m dx \tag{6.7}$$

The interpretation of U_{min} and U_{max} are the same as in Section 6.3.1.

In fact, by rewriting the equations for U_{max} (i.e. equation (6.3) and (6.7)) and U_{min} (i.e. i.e. equations (6.2) and (6.6)), we get a universal expression for both the step under load control and the ideal load drop under displacement control,

$$U_{\max} = W_t - W_{p1} \tag{6.8}$$

$$U_{\min} = U_{\max} - \int_{\delta_f}^{\delta_2} B(x-h_f)^n dx \tag{6.9}$$

where W_t can be directly obtained by integrating the load-displacement curve (i.e. the area OAG in Fig. 6.3 and Fig.6.4); W_{p1} (i.e. the area OAE in Fig. 6.3 and Fig.6.4) can be determined by equation (6.4), alternatively, it can be obtained using area OAR minus area AER in Fig. 6.3 or area OAG minus AEG in Fig. 6.4 where the latter is preferred.

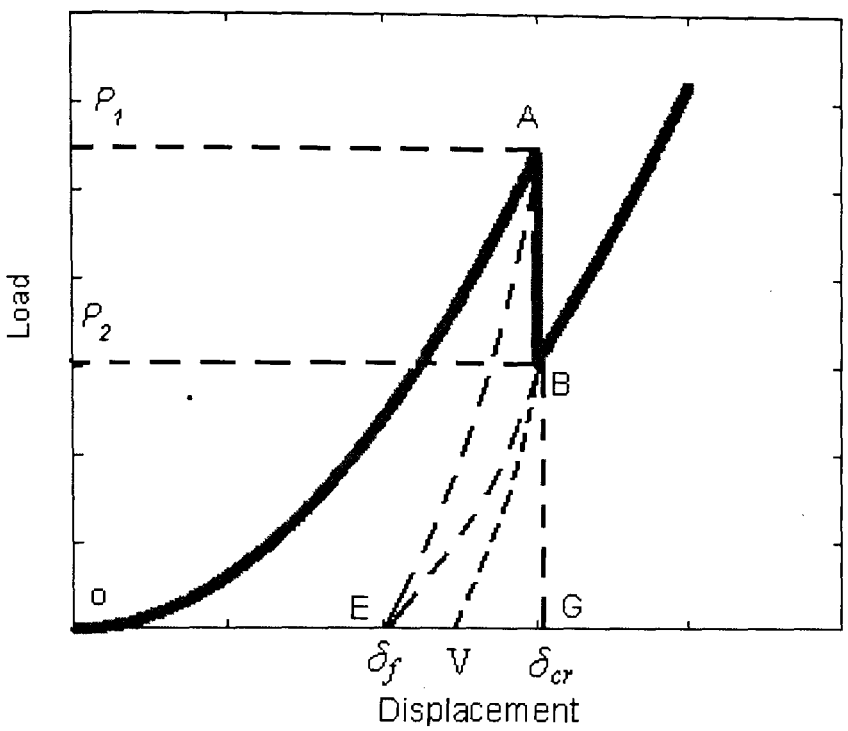

Fig. 6.4. Schematic of the upper and lower bound methods in this work under displacement control. The areas AEB and AEG are regarded as the lower and upper limits of the upper bound of fracture dissipated energy (i.e. the area AEVB), respectively.

6.2.3 Non ideal excursion in load-displacement curve under displacement control

The excursions discussed above are so-called ideal excursions (i.e. P_{cr} in Fig. 6.3 equals the load where the excursion stops and the δ_{cr} in Fig.6.4 equals the depth where load drop ceases). However, in the realistic case, non-ideal excursions as depicted in Fig. 6.5 may occur.

This non-ideal case was ignored in the initial bound model. The same solution in section 6.3.2 is still applicable to this case.

It is necessary to state that the reasonable lower limit of the fracture toughness is difficult to obtain. But it is still very helpful to obtain the lower and upper bound of the upper limit of the fracture toughness as discussed in this study, which is very useful for engineering design.

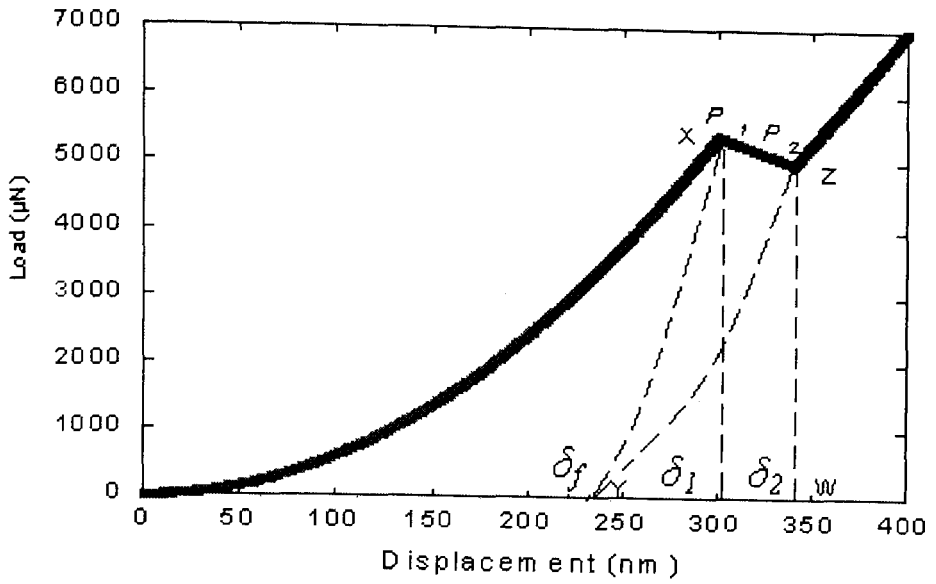

Fig. 6.5. Schematic of a non-ideal feature in a load-displacement curve.

6.3. Experimental assessment

6.3.1. Nanoindentation tests of CN_x coating

Fullerene-like CN_x coatings with a thickness of 1μm were deposited at Linkoping University on different substrates including Si(001), Al_2O_3, 3C SiC(001) and 3C SiC(111) using unbalanced magnetron sputtering. The deposition temperature was around 350°C. Nanoindentation was carried out using a Nanoindenter Π ™(Nano Instruments, Knoxville,TN, USA) fitted with a Berkovich indenter (with tip end radius of ~250nm) at a range of peak loads from 100μN to 500mN. The constant loading rate was 500μN/s for the maximum applied loads greater than 100mN and 50μN/s for the lower load tests.

Table 6.1. Hardness and reduced Young's modulus as well as H/E ratio of the CN_x coating and substrates obtained from 1mN nanoindentation tests using a well-calibrated Berkovich indenter (Arce-Garcia, 2002).

Material	H (GPa)	E(GPa)	H/E
CN_x	9	100	0.090
Silicon	11.5	130	0.093
SiC	42	450	0.093
Al_2O_3	20.1	345	0.058

6.3.2 General experimental observations and toughness results

At 500mN applied load, chipping (e.g. Fig.6.6) in all samples was observed. A step in the load-displacement curve (e.g. Fig.6.7) which correlates to chipping of the coating was found. Thus the fracture toughness is given by,

$$K_{IC} = \sqrt{\frac{U_{fra} E}{(1-\nu^2) 2N\pi C_R t'}} \tag{6.10}$$

Where, C_R is the radial dimension of the chipping, for the chipping of coating caused by a pyramid indenter N=3 if the chipping morphology is approximately three circular disc; N=1 if the fracture morphology is close to one circular discs. Such a difference has been observed in experiments as shown in the following paragraph. The effective coating thickness $t' = t/\sin\beta$ is used instead of the coating thickness t as discussed in Chapter 2. The average angle β of chipping edge was estimated by optical profilametry.

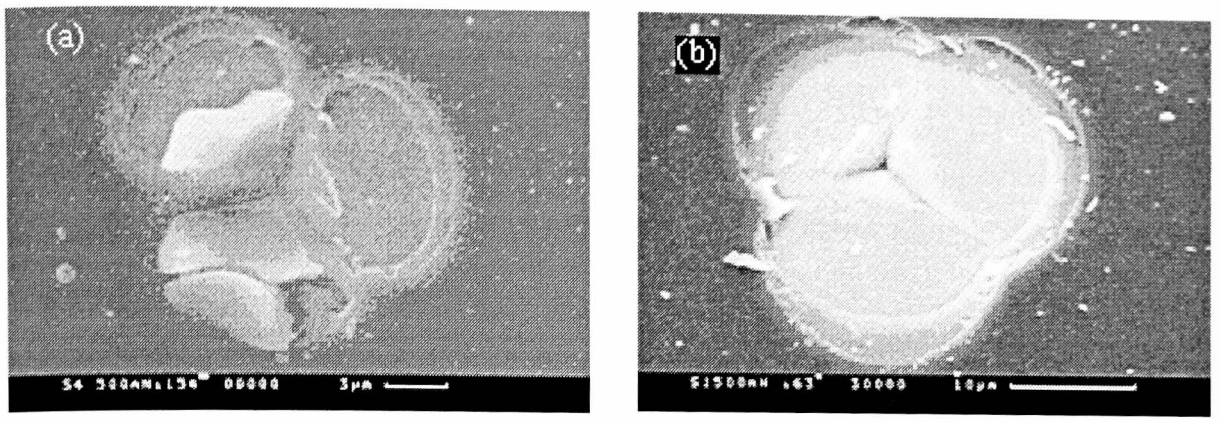

Fig. 6.6. SEM micrographs of 500mN maximum load indents in a 1μm CN_x coating deposited on (a) Si(001) and (b) 3C SiC(100) showing through-thickness fracture and chipping of the coating. After (Arce-Garcia, 2002).

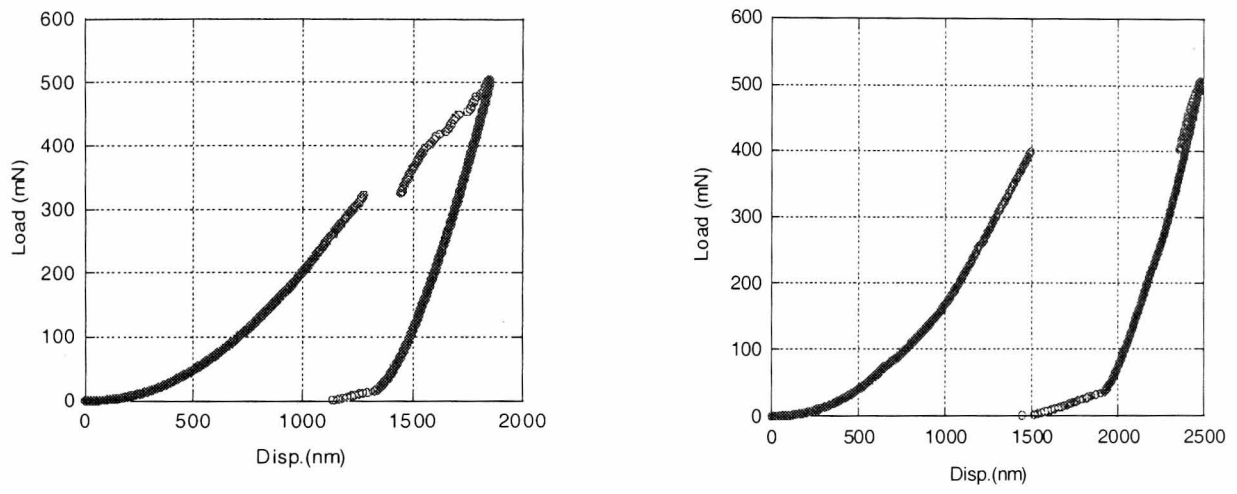

(a) (b)

Fig. 6. 7 The load displacement (P-δ) curve corresponding to Fig.6.6 for a 1μm CN_x coating deposited on (a) Si(001) and (b) 3C SiC (100), respectively. The steps in the P-δ curves are related to chipping.

For comparison, the summary of toughness results for these samples determined by different models is provided in Table 6.2.

It should be pointed out that for the all the substrates except sapphire, the H/E ratio is similar to the coating and the critical load for the excursion is much higher than the threshold where substrate deformation dominates behavior, in which case , the application of Eq. (6.1a) is reasonable. However, for the sapphire substrate, the H/E ratio of the substrate is much less than that of the CN_x coating and the critical load for

excursion in the load-displacement curve is in the range that coating and substrate deformation play important role together rather than the substrate deformation dominating or only coating deformation occurring. Therefore, it is more realistic to consider the H/E ratio of the CN_x coating and substrate sapphire to estimate the limiting value of toughness.

Table. 6. 2. Comparison of the fracture toughness of a 1 μm CN_x layer on different stiffer and harder substrates determined by different energy based models.

	K_{IC}, $MPa\sqrt{m}$				
Substrate	The ld-dp model	Initial Lower and Upper bound		Modified bound model	
Si(001)	2.9±0.1	5.3±0.2	6.5±0.2	5.0±0.2	9.2±0.3
Al_2O_3	4.2±0.2	4.3±0.2	5.4±0.2	4.1±0.1	6.4±0.3
3C SiC(001)	5.5±0.2	5.5±0.2	6.7±0.2	5.0±0.2	7.5±0.3
3C SiC(111)	4.9±0.2	5.7±0.2	7.0±0.3	5.3±0.2	8.2±0.3

From Table 6.2, it can be seen that the toughness of the samples as determined from the methods in the previous chapter fall into the range of the modified model rather than the initial bound model, which shows that the modified model is more reasonable. Although the lower limit determined by the modified model is close to that determined by the initial bound method, logically, the modified model tends to describe the real system more reliably due to the reasons discussed in Section 6.3. The toughness of CN_x on Si does not lie in the range of the upper and lower bound which is possibly due to the fact that the ld-dp model or the W_t-dp method cannot include the influence of the phase transformation of the substrate silicon (Pharr et al., 1991), ((Hainsworth et al., 1994, Haberl et al., 2004). In addition, it is should be borne in mind that the toughness of substrate silicon (100) is much lower (~0.91 $MPa\sqrt{m}$) compared to the coating toughness, which makes it possible that the substrate may crack before the discontinuity in the loading curve. In such case, it can be expected that the ld-dp model or Wt-dp will underestimate the coating toughness. Such

significant deviation may not occur for the other substrates with much higher toughness (usually >2.7 $MPa\sqrt{m}$).

Further, well-developed fracture in bulk silicon can occur at a load (e.g. Fig. 6.8 b) lower than the critical load for excursion in the coated case and it does not lead to any excursion in the P-δ curves (see Fig. 6.8a). Even when the applied load is up to 500mN and the bulk silicon is seriously damaged (see Fig. 6.8 d), it does not result in any excursion in P-δ curve (see Fig. 6.8 c). All these indicate that the cracking in the silicon substrate is very likely in the sample consisting of CN_x and silicon indented at 500mN. Since the cracking in substrate cannot be distinguished in the P-δ curve, it is difficult to separate this factor from the dissipated energy by coating fracture.

This method has also been applied to sol-gel coatings on glass. For example, when using the data taken from the literature (Malzbender and de With, 2002), (Malzbender et al., 2002), the toughness of a sol-gel coating (see detailed composition in (Malzbender et al., 2002) on soda-lime glass is 0.08~0.16 $MPa\sqrt{m}$, while the literature result is 0.14 $MPa\sqrt{m}$ (Malzbender et al., 2000) which falls within this bound.

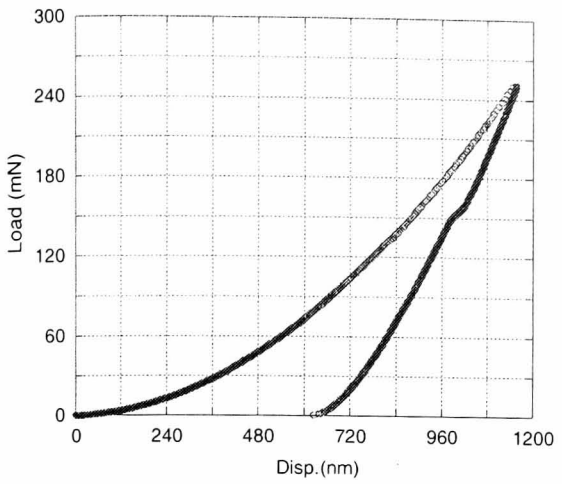

(a)

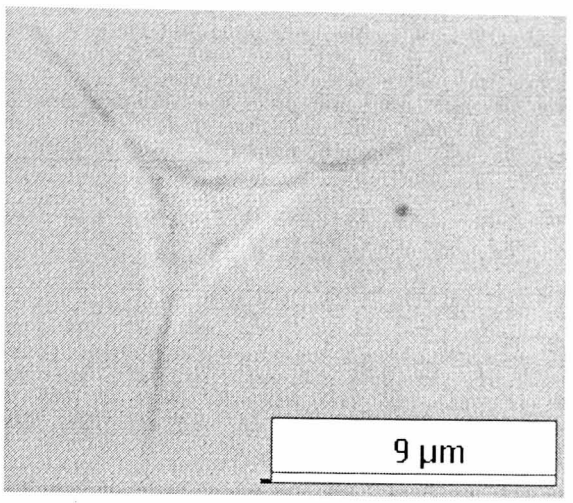

(b)

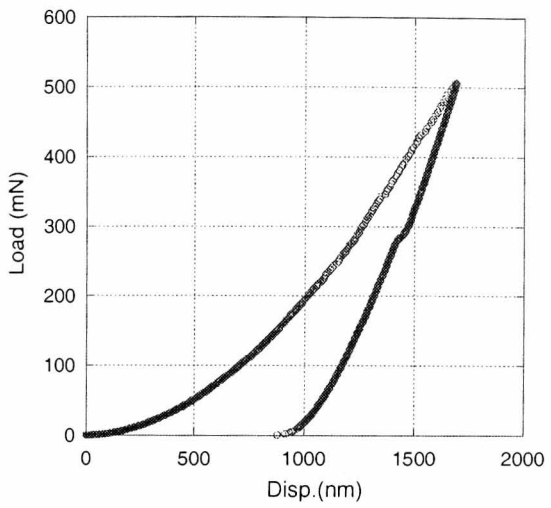

(c)

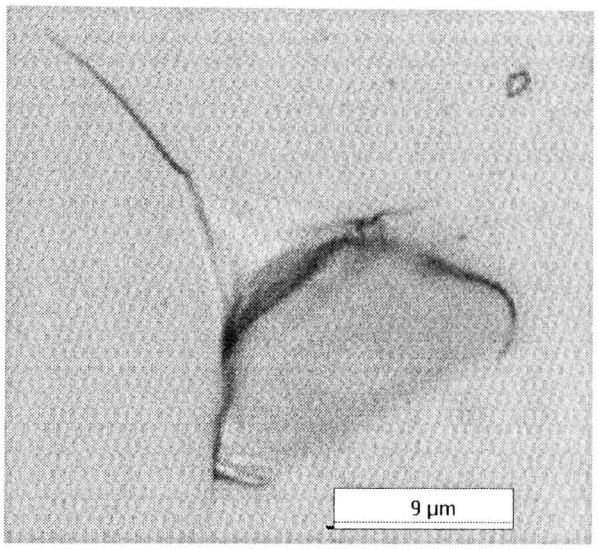

(d)

Fig. 6.8. The P-δ curves and reflected light micrographs of Si at high loads of (a,b) 250mN and (c,d) 500mN by Nanoindenter II fitted with a Berkovich tip. The elbow occurring in unloading curve is caused by phase transformation in Si.

6.3.3. Discussion on the influence of different m and n

Although it has been shown that it may be reasonable to assume the exponents in Eq.(6.2) to Eq.(6.3) and Eq.(6.6) to Eq.(6.7), are $m=n=1.36$, it is not easy to know their exact values. The value of n may deviate from m; and both of them may not be equal to 1.36. They may vary for different coated systems and/or the coated systems prior to and post fracture, which is tricky to verify by experimental results. Therefore, it is necessary to examine if the results are sensitive to m, n or not.

The correlation between the relationship of *m, n* and the bound results of toughness are analyzed in three cases which covers all possibilities. For this, *m* is assumed to vary from 1.2 to 2. This assumption is reasonable for most brittle materials which is confirmed by experimental work and numerical simulations.

(1) $m=n$

(2) $m>n$; in this case, two examples are taken. One is $m=n+0.05$, the other is $m=n+0.1$

(3) $m<n$; Again, two examples are taken. One is $m=n-0.05$, the other is $m=n-0.1$

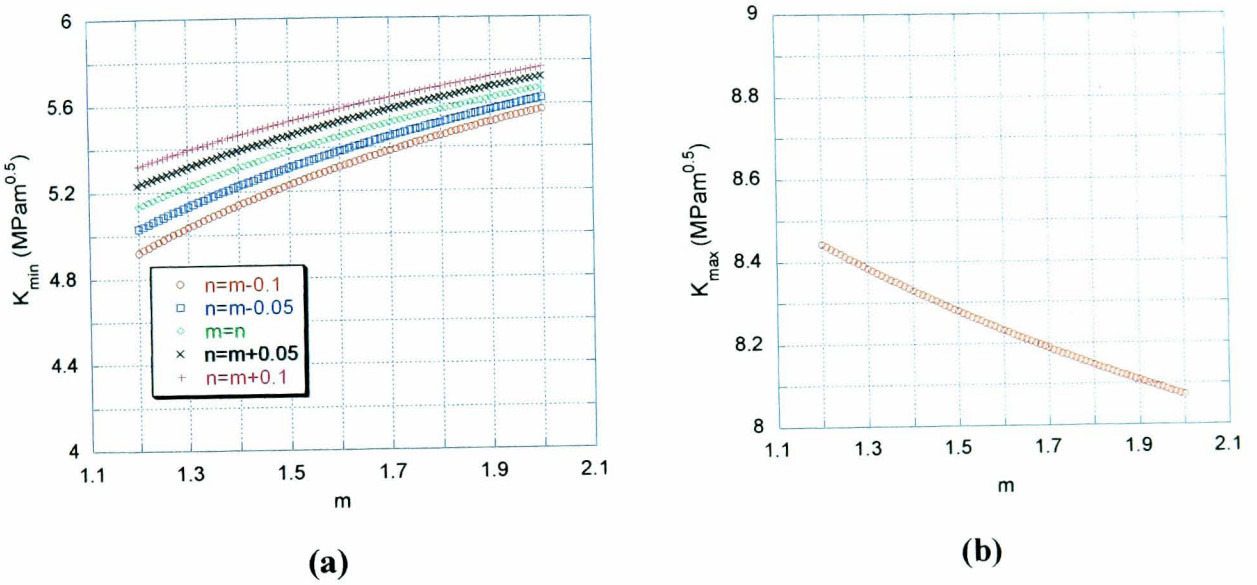

Fig. 6.9 Comparison of (a) the lower and (b) upper bound of coating toughness of CN_x on 3C SiC (111). For the values of m given above, there is no big difference between the different cases. (Error bars are removed for clarity).

The plot of values of upper and lower bound versus the value of *m* for CN_x on Si (100) and 3C SiC (111) are displayed in Fig. 6.9 and Fig. 6.10. In the case that *n* is bigger than *m*, the results are least sensitive to the value of m. Given the value of *m*, the bigger the value of *n* the bigger is the minimum toughness K_{min}. When *m* increases, all the curves (see Fig. 6.9 and Fig. 6.10) approach each other. The variance of K_{min} is less than 15% when m increases from 1.2 to 2.0 which indicates that the lower bound of toughness is not very sensitive to the values of *m*. Also, the relationship between *m* and *n* will not considerably change the results at least within the range discussed here. With an increase of *m*, the difference in the results

decreases. K_{max} depends on m only. Form Fig. 6.9b and 6.10b, it can be seen that the variance of K_{max} is less than 10% when m increases from 1.2 to 2.0. From Fig.6.11 and 6.12, it can be seen that it does not cause much difference (<5%) in K_{min} and K_{max} no matter what the value of H/E of the CN_x coating or the Sapphire substrate.

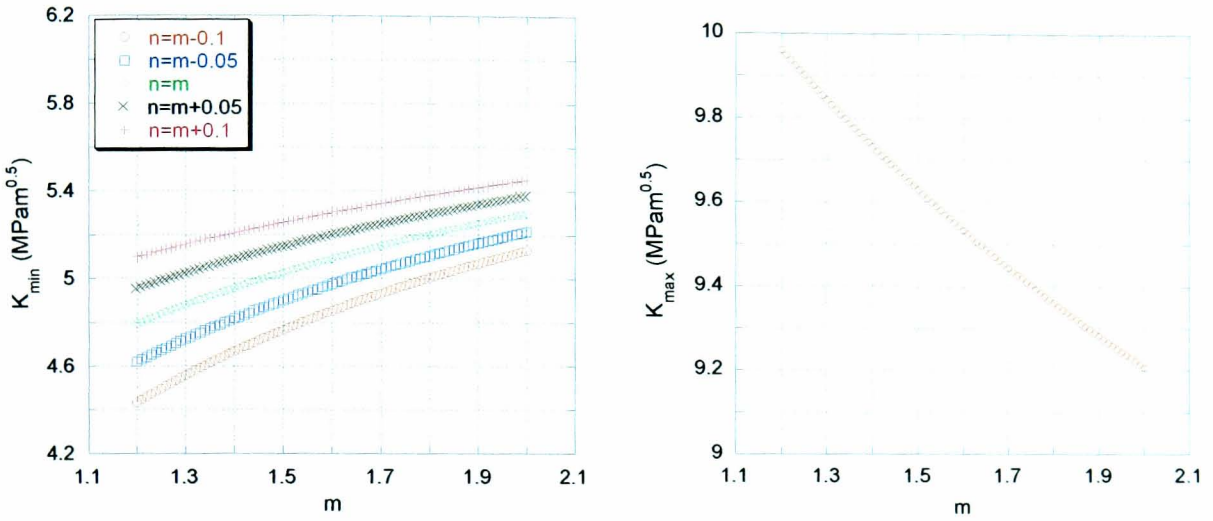

Fig. 6.10 Comparison of (a) the lower bound and (b) upper bound of coating toughness for CN_x on Si (100). For the values of m given above, there is no big difference between the different cases. (Error bars are removed for clarity)

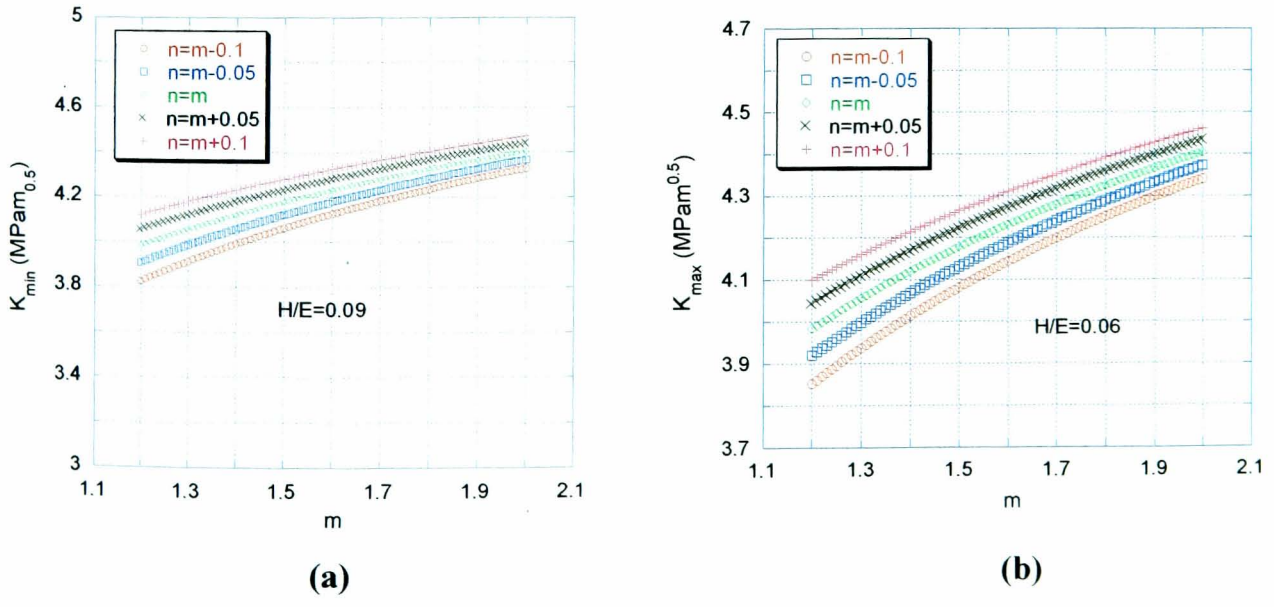

Fig. 6.11. Plot of K_{min} versus m for 1μm CN_x on Sapphire (a) H/E=0.09 for the CN_x coating and (b) H/E=0.06 for the sapphire substrate (Error bars are removed for clarity).

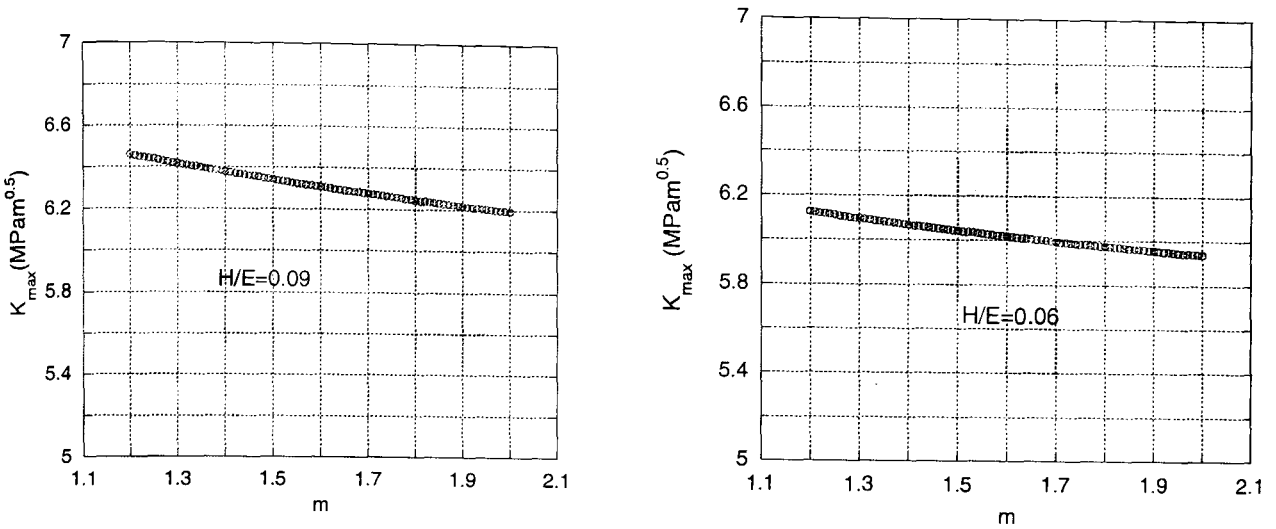

Fig. 6.12. Plot of K_{max} versus m for the CN_x on Sapphire in the case of (a) H/E=0.09 for CN_x coating and (b) H/E=0.06 for the sapphire substrate (Error bars are removed for clarity).

6.3.4. Comparison between initial bound model and modified model

Compared to the initial bound model, the new model does not require the ideal displacement excursion under load control and ideal load drop under displacement control as depicted in Fig.6.1 and Fig.6.2, respectively. In practical conditions, the ideal features in *P-δ* curves seldom occur. In contrast, the modified model does not depend on the path of the displacement excursion and load drop, in other words, it can deal with non-ideal features (i.e. a load drop associated with displacement excursion as depicted in Fig. 6.2, or a displacement excursion accompanied by a load increase as depicted in Fig.6.1) in P-δ curves. Alternatively, for the convenience of the application of the modified bound model, the use of Equation (6.1) can be replaced by performing indentation with the critical load as maximum load thus the value of δ_f can be directly obtained so that the application of the modified bound model can be extended. Principally, the modified model can be extended into most coated systems by adjusting the parameters in this model given that a step in the load displacement occurs corresponding to a fracture event and it may be helpful for coating design and selection in industry.

In order to obtain more precise results, it will be necessary to unload the curve at the excursion start point and end point ,which will be the future work.

6.4. Summary

In this chapter, a new upper and lower limit model to estimate the coating toughness has been presented. By combing an existing numerical analysis and the investigation of the energy dissipated during indentation, it more reliably represents the actual coated system behaviour. The comparison between the toughness of a CN_x coating on various substrates determined by different methods indicates this modified model is reasonable. Furthermore, the new model provides the upper and lower limit for load control as well as displacement control and gives a universal explanation for the bound, which the initial bound model does not adequately describe, at the cost of more complicated calculated procedure. However, further work is necessary to apply the model to bulk materials which show steps or load drops in the loading curve associated with fracture if the toughness is to be correctly calibrated.

The models presented in this chapter and the previous chapter are based on an excursion in the P-δ curve. However, it is not unusual that fracture in coatings may not lead to an excursion in P-δ curve. In such cases, can the energy based model still be an option? An attempt to deal with this problem is discussed in the next Chapter.

Reference:

Arce-Garcia, I. (2002) Mechanical properties of fullerene-like CNx : Ph. D Dissertation, ,University of Newcastle Upon Tyne

Bull, S. J. (2001) Modelling the hardness response of bulk materials, single and multilayer coatings,*Thin Solid Films,* **398,** 291-298.

Bull, S. J., Berasetegui, E. G. and Page, T. F. (2004) Modelling of the indentation response of coatings and surface treatments,*Wear,* **256,** 857-866.

Cheng, Y. T., Li, Z. Y. and Cheng, C. M. (2002) Scaling, relationships for indentation measurements,*Philosophical Magazine a-Physics of Condensed Matter Structure Defects and Mechanical Properties,* **82,** 1821-1829.

den Toonder, J., Malzbender, H., de With, G. and Balkenende, R. (2002) Fracture toughness and adhesion energy of sol-gel coatings on glass,*Journal of Materials Research,* **17,** 224-233.

G-Berasategui, E., Bull, S. J. and Page, T. F. (2004) Mechanical modelling of multilayer optical coatings,*Thin Solid Films,* **447,** 26-32.

Haberl, B., Bradby, J. E., Swain, M. V., Williams, J. S. and Munroe, P. (2004) Phase transformations induced in relaxed amorphous silicon by indentation at room temperature,*Applied Physics Letters,* **85,** 5559-5561.

Hainsworth, S. V., Whitehead, A. J. and Page, T. F.1994Snowbird, UtahPublishers Plenum Press

Lawn, B. R. and Howes, V. R. (1981) Elastic Recovery at Hardness Indentations,*Journal of Materials Science,* **16,** 2745-2752.

Malzbender, J. and de With, G. (2000) Energy dissipation, fracture toughness and the indentation load-displacement curve of coated materials,*Surface & Coatings Technology,* **135,** 60-68.

Malzbender, J., de With, G. and den Toonder, J. M. J. (2000) Elastic modulus, indentation pressure and fracture toughness of hybrid coatings on glass,*Thin Solid Films,* **366,** 139-149.

Malzbender, J. and de With, G. (2002) Indentation load-displacement curve, plastic deformation, and energy,*Journal of Materials Research,* **17,** 502-511.

Malzbender, J., den Toonder, J. M. J., Balkenende, A. R. and de With, G. (2002) Measuring mechanical properties of coatings: a methodology applied to nano-

particle-filled sol-gel coatings on glass,*Materials Science & Engineering R-Reports,* **36,** 47-103.

Marx, V. and Balke, H. (1997) A critical investigation of the unloading behavior of sharp indentation,*Acta Materialia,* **45,** 3791-3800.

Mencik, J. and Swain, M. V. (1994) Micro-Indentation Tests with Pointed Indenters,*Materials Forum,* **18,** 277-288.

Palacio, J. F., Bull, S. J., Neidhardt, J. and Hultman, L. (2006) Nanoindentation response of high perfonnance fullerene-like CNx,*Thin Solid Films,* **494,** 63-68.

Pharr, G. M., Oliver, W. C. and Harding, D. S. (1991) New Evidence for a Pressure-Induced Phase-Transformation During the Indentation of Silicon,*Journal of Materials Research,* **6,** 1129-1130.

Chapter 7:

W_{irr}-W_p model to assess coating toughness during nanoindentation

Chapter 7: W_{irr}-W_p model to assess coating toughness during nanoindentation

In previous chapters, the assessment of fracture toughness is based on the excursions in load-displacement curves. In this Chapter a new method to estimate the fracture toughness is presented in the case that no excursions are observed in the load-displacement curve.

7.1. Introduction

The methods to estimate the coating toughness can be generally divided into three branches. One is an empirical model which relates the toughness to applied load and cracking length when well-developed radial or median cracking occurs in a sufficiently thick coated system (i.e. the conventional indentation method). The second is energy based models which estimate the fracture dissipated energy based on pop-ins or jumps in load-displacement curves (as reviewed in Chapter 2) or total work vs. displacement curves (as described in Chapter 5) thus obtaining the fracture toughness of the coatings. However, if picture frame cracking rather than a well-developed radial/median crack pattern is observed during indentation, the first model becomes invalid; if the picture-frame fracture does not lead to any excursion in the load-displacement curves or total work vs. displacement curves, the second method fails. The third method is possible a stress analysis model which becomes even more complex in the coated systems since the very complex stress field produced is modified by the presence of fracture. The question therefore arises can we measure the coating toughness based on picture frame cracking which does not lead to any obvious discontinuities in the load-displacement curve. This Chapter is devoted to answering this question.

7.2. Experimental observations of picture frame cracking

The experiments were carried out on the coated and uncoated glass (as described in Chapter 4) using the Nanoindenter II ™ (Nano Instruments, Knoxville, TN, USA) fitted with a Berkovich indenter (radius ~250nm). A wide range of loads was applied to each sample (from 10mN to 500mN) in order to investigate the cracking behaviour in the coated system. Displacement control was used throughout. The loading rate was 50nm/s for the peak loads bigger than 300mN and 10nm/s was used for lower loads. In order to measure the fracture dimensions, off-line SEM (Camscan) and AFM (Park M5) were used. The H/E ratio of the main components of solar control coatings and the substrate are given in Table 7.1. This is required for the analysis developed later.

Table 7.1. *H/E* ratio of the main component of solar control coatings and the glass substrate obtained by nanoindentation from 100μN to 1mN load using a well-calibrated sharp cube corner indenter .

	E_r (GPa)	H (GPa)	E_r/H
Uncoated soda-lime glass	79	6.5	12.2
ZnO coating	114	15	7.6
SnO_2 coating	131	14	9.4
ITO coating	133	12	11.1
TiO_xN_y coating	117	9	13.0

*All the E used in this study is the reduced Young's modulus ,i.e. E_r without notion.

Except for the sample with a thick cap layer of TiO_xN_y, the picture-frame cracks were clearly observed in SEM image in all samples when the load is bigger than 200mN, which is discussed in the following section. Interfacial detachment was only found in coated glass with a 400nm ITO cap layer which indicates the relatively poor adhesion between the cap layer and substrate, which is verified by the observation that a 400nm ITO cap layer will spontaneously delaminate after deposition in some locations (as shown in Chapter 8).

Fig. 7.1 displays the picture-frame cracks for a 400nm ZnO cap layer indented at loads in the range of 200mN to 500mN where the picture-frame cracks are clearly observed. The associated P-δ curves are presented in Fig. 7.2. It is clear that no excursions resulting from fracture were observed. Fig. 7.3 and Fig.7.4 display the SEM images of a 240nm ITO and 400nm SnO_2 indented with peak load between 200mN and 500mN, from which well-established picture frame cracks are also observed. From Figures 7.1, 7.3 and 7.4, the density of picture-frame cracks for the 240nm ITO multilayer and 400nm SnO_2 multilayer is significantly less than for ZnO. In addition, the samples show less crack opening displacement compared to ZnO coating which will be explained in Section 7.4.

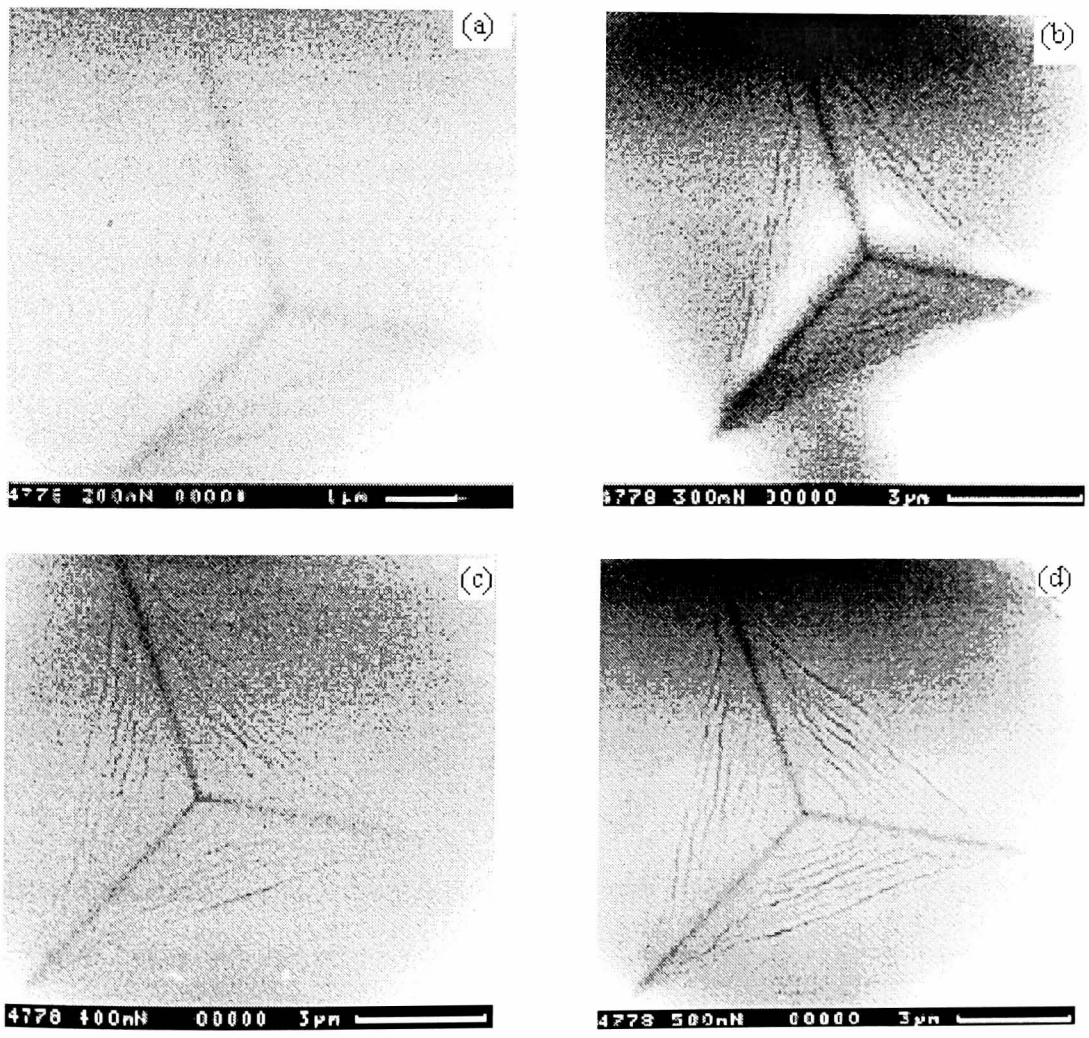

Figure 7.1. SEM (backscatter) micrographs showing the picture frame cracks for multilayer coated glass with a 400nm ZnO cap layer. The peak nanoindentation loads are (a) 200mN, (b) 300mN, (c) 400mN, and (d)500mN, respectively.

Picture frame cracks were not observed in the TiO_xN_y coating (see Fig. 7.5a and 7.5b) either as a single layer or as a multilayer stack which will also be explained in Section 7.4. Evidence of lateral cracking (possibly occurring at the interface) was observed in the 400nm ITO coated sample (Fig.7.5c). No evidence of fracture was found in the substrate glass as depicted in 7.5d. Also, no evidence of picture frame cracks were observed in all the samples with ultra thin single layer or multilayer coatings (individual layer thickness varies from 7nm to 20nm) as depicted in Fig.7.6. It is not clear whether the dark diagonal of the indent is related to sub-threshold radial cracking or significant plastic deformation at the indenter edges.

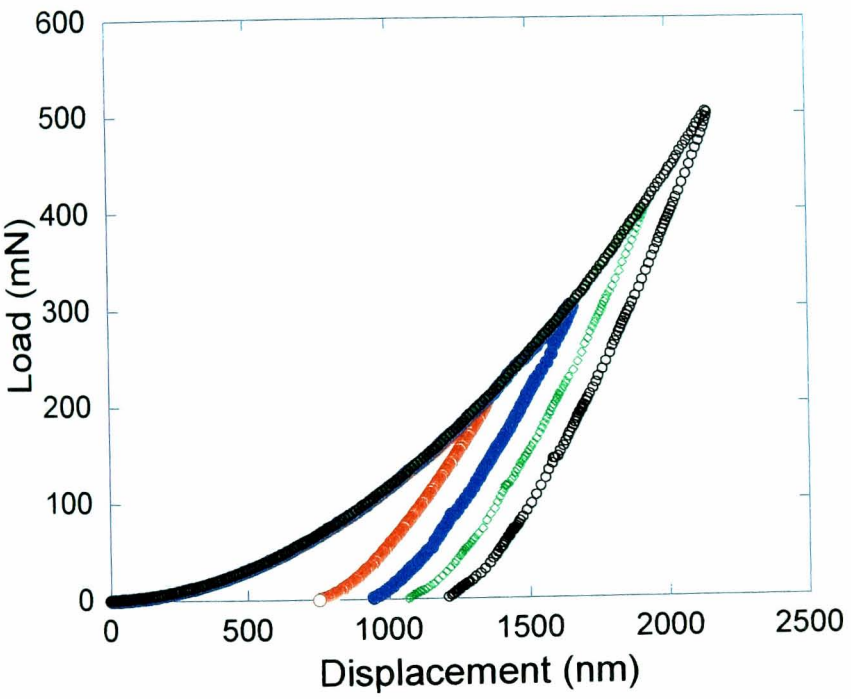

Figure 7.2. The load –displacement curves corresponding to Fig. 7.1. No obvious excursions in the *P*-δ curves were observed.

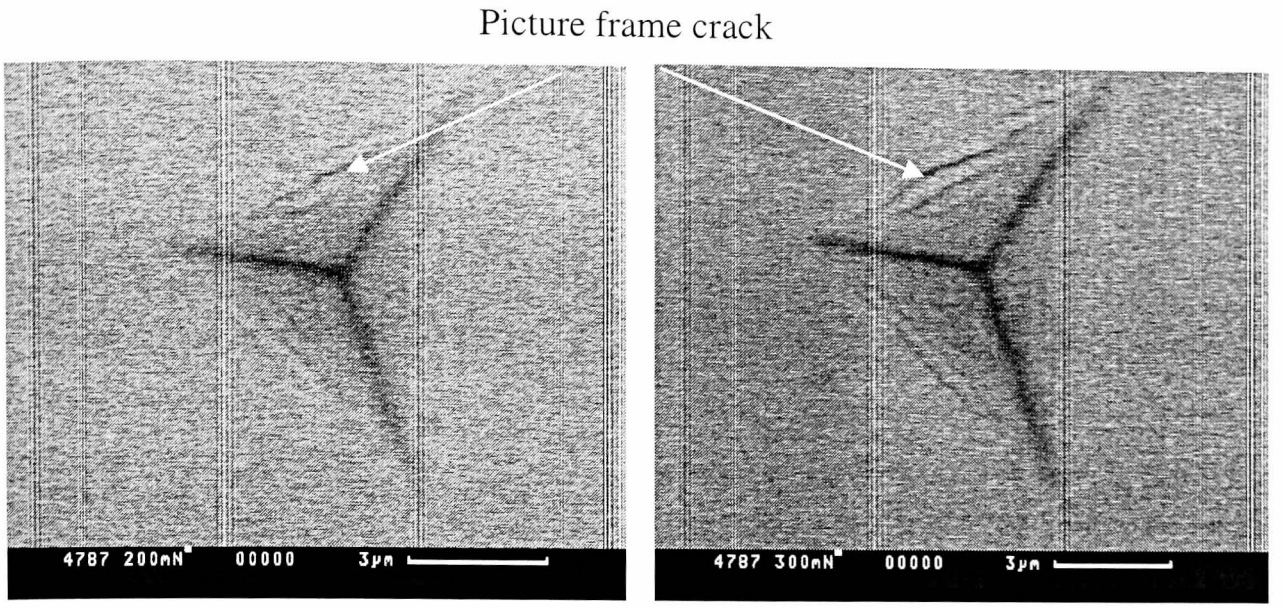

Figure 7.3. SEM (backscatter) micrographs showing the picture frame cracks for multilayer coated glass with a 400nm SnO_2 cap layer. The peak nanoindentation loads are (a) 200mN, (b) 300mN, (c) 400mN, and (d) 500mN.

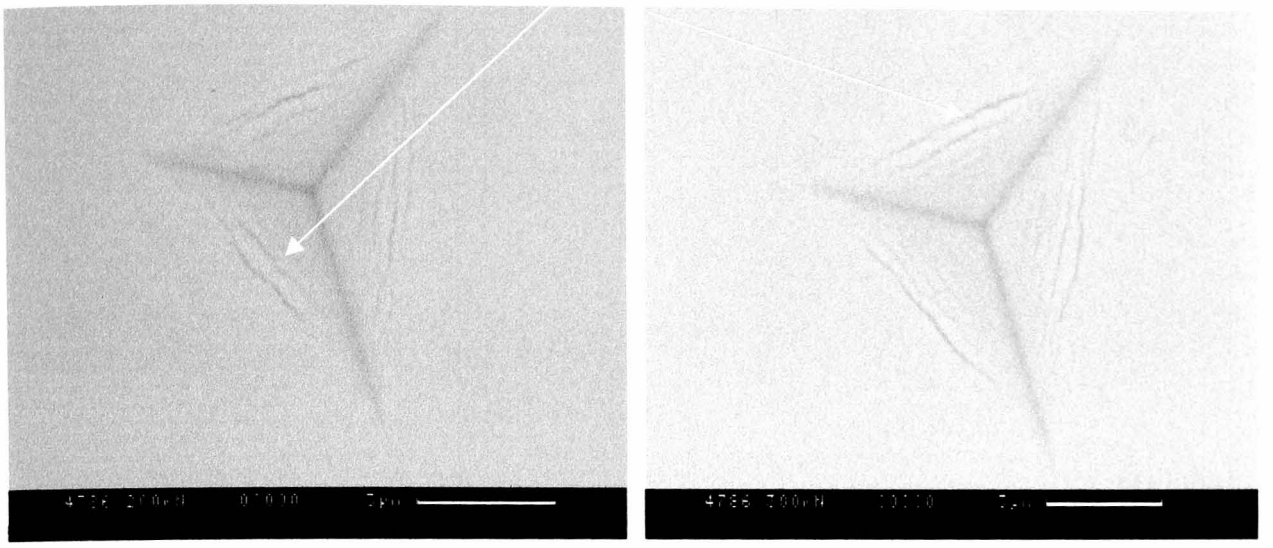

(a) **(b)**

(c) **(d)**

Fig. 7.4 SEM (backscatter) micrographs showing the picture frame cracks for multilayer coated glass with a 240nm ITO cap layer. The peak nanoindentation loads are (a) 200mN, (b) 300mN, (c) 400mN, and (d) 500mN.

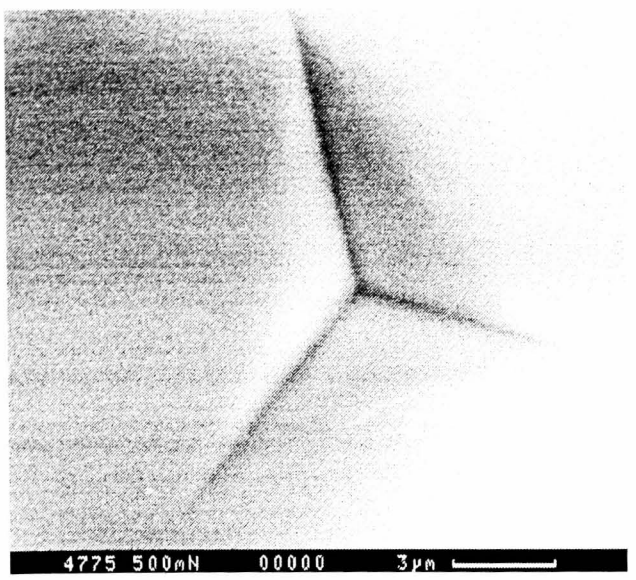

(a)

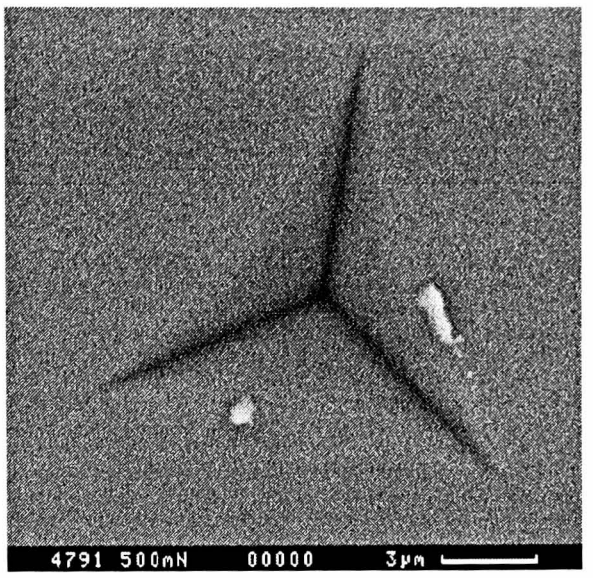

(b)

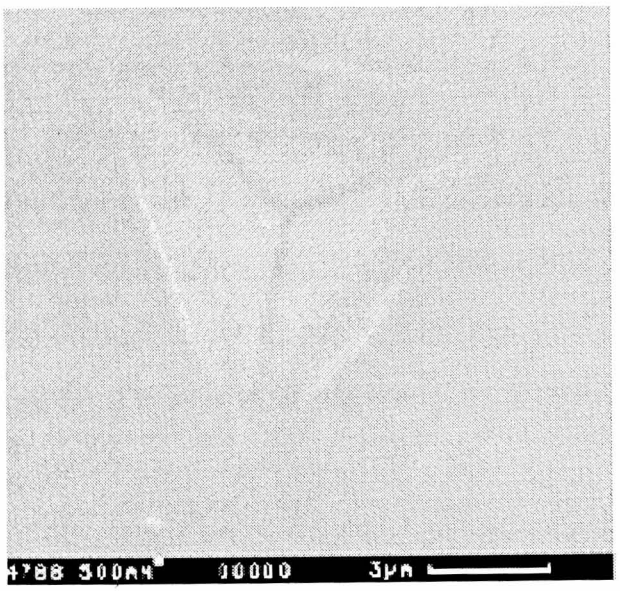

(c)

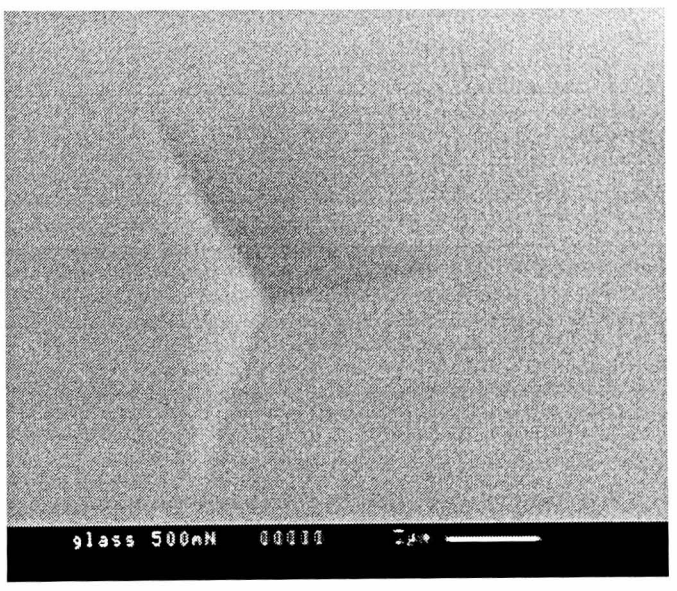

(d)

Figure 7.5. SEM micrographs for coated glass (a) 400nm TiO_xN_y monolayer (b) 400nm TiO_xN_y multilayer (c) 400nm ITO multilayer (d) uncoated glass, which are indented at 500mN peak load.

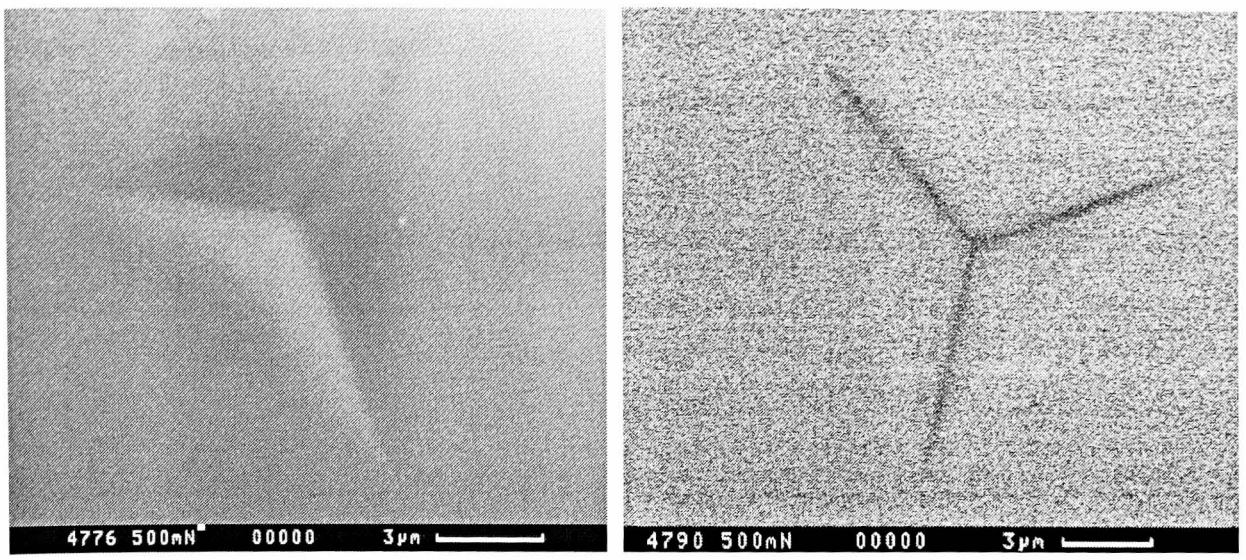

Figure 7.6. SEM micrographs of ultra thin coated glass (a) single layer (b) multilayer.

No evidence of picture frame cracking and radial cracking was observed by AFM for all the samples (see example in Fig. 7.7). A possible reason is that the crack opening displacement is too small for even a sharp AFM tip to penetrate. In addition, the water absorbed in the crack by capillary forces will act as bridge when AFM tip is scanning the surface. The combined effect of this is that the tip displacement associated with cracking is less than the surface roughness and the crack is not visible.

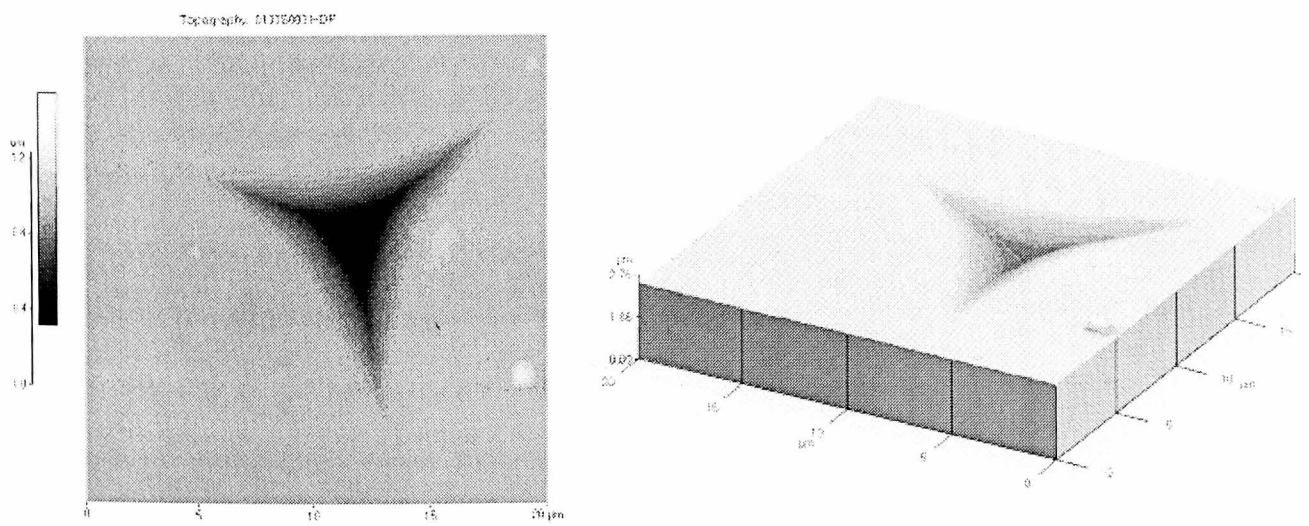

(a) (b)

Figure 7. 7. (a) AFM contact mode topographic map and (b) 3D image of a Berkovich indentation in a 240nm ITO coated glass sample at 500mN, which does not show obvious evidence of cracking.

7.3. W_{irr}-W_p method

7.3.1 Irreversible work analysis for uncracked materials

A few workers (Cheng and Cheng, 1998, Cheng et al., 2002), (Mencik and Swain, 1994) find that there is a linear relationship between the ratio of irreversible work to total work, W_{irr}/W_t, and the ratio of final indentation depth to maximum depth, δ_f / δ_m for a bulk material without cracks. For example, by combining the finite element result and scaling relationships, the following expression is given by Cheng et al (Cheng and Cheng, 1998),

$$\frac{W_{irr}}{W_t} = (1+\gamma)\frac{\delta_f}{\delta_m} - \gamma \qquad \text{for } \frac{\delta_f}{\delta_m} > 0.4 \tag{7.1}$$

For a Berkovich indenter, $\gamma = 0.27$. In this case, the W_{irr} can be also regarded as plastic work W_p.

If it is assumed the load P scales displacement squared in the loading curves before cracks and the unloading curves can be fitted by a power law, i.e. $P = A(\delta - \delta_f)^m$ (Oliver and Pharr, 1992), the following relationship can be obtained (Mencik and Swain, 1994),

$$\frac{W_P}{W_t} = \frac{3}{m+1}\frac{\delta_f}{\delta_m} - \frac{2-m}{m+1} \tag{7.2}$$

Since both equation (7.1) and the fundamental equations to derive (7.2) can be verified by finite element simulations for a range of bulk materials, it is reasonable to assume that these two equations are identical, thus it gives m=1.362.

However, it should be noted that the numerical analysis may not represent the actual behaviour for bulk materials at any situation. For example, it is found that there is 3~4% percent deviation when applying this numerical analysis in soda-lime glass in this study as explained in Fig.7.9b, which may be caused by the difference between the ideal materials used in the numerical simulations and actual materials. Also the factor of a truncated tip in practice may also result in some deviation form the numerical result.

If the coated systems have similar *H/E* in both coatings and substrates and their *H* and *E* do not deviate much from each other in the composite, it is very likely that there will be no slope change in the load-displacement curve after plastic deformation is fully developed in the substrate and *H/E* will not vary with the load. In such a case, the whole coated system can be approximately treated as an equivalent bulk material and the relationships in equations (7.1) and (7.2) can also be applied.

The ratio $\delta_f/\delta_m>0.4$ for the samples investigated here meets the requirement for equation (7.1) to be valid. Here, the work difference between actual irreversible work and the irreversible work measured by equation (7.1), ΔW_{irr}, is less than 4% of the total work and less than 8% of the actual irreversible work (see Fig.7.8), which may be due to possible microcracks in glass and the intrinsic system errors between the experimental work and numerical analysis. It may indicate that if the fracture dissipated energy as small as the difference of measured and calculated W_{irr}, this method will break down.

Although no obvious evidence for cracks in the uncoated glass was observed in the SEM images in this study, it cannot be proved that no cracking in the glass occurs under high load tests (>100mN). It has been found that the critical load for cracking in glass indented by a sharp Berkovich indenter is about 20mN with associated critical flaw size is about 600nm (Lawn and Evans 1977). However, it was also reported elsewhere that the threshold for cracking initiation in glass by a Vickers indenter is about 250 to 500mN (Pharr 1998). The threshold load for fracture may depend on many factors such as the size and distribution of the potential flaws and the tip radius. For the substrate glass underneath the coating, it has been sufficiently cleaned before

coating deposition so that the critical load for cracking initiation in substrate glass may be higher than expected. When the through-thickness fracture in the coatings forms, the load is easier to be transmitted to the substrate and the debris of coatings may act as a suitable intermediate flaw for fracture initiation in the substrate glass. Therefore, sub-threshold cracking in the substrate glass is expected to mainly contribute to the deviation of W_{irr} from the theoretical value for the coated samples investigated here. Therefore, for the calculation in this study, this deviation is subtracted and it is assumed this systematic error is mainly caused by the substrate and it is identical in the different coated systems and the uncoated glass. This assumption is reasonable since the deformation is dominated by substrate under the test conditions used with high loads when fracture occurs and the H and E in coatings and substrate do not differ much from each other.

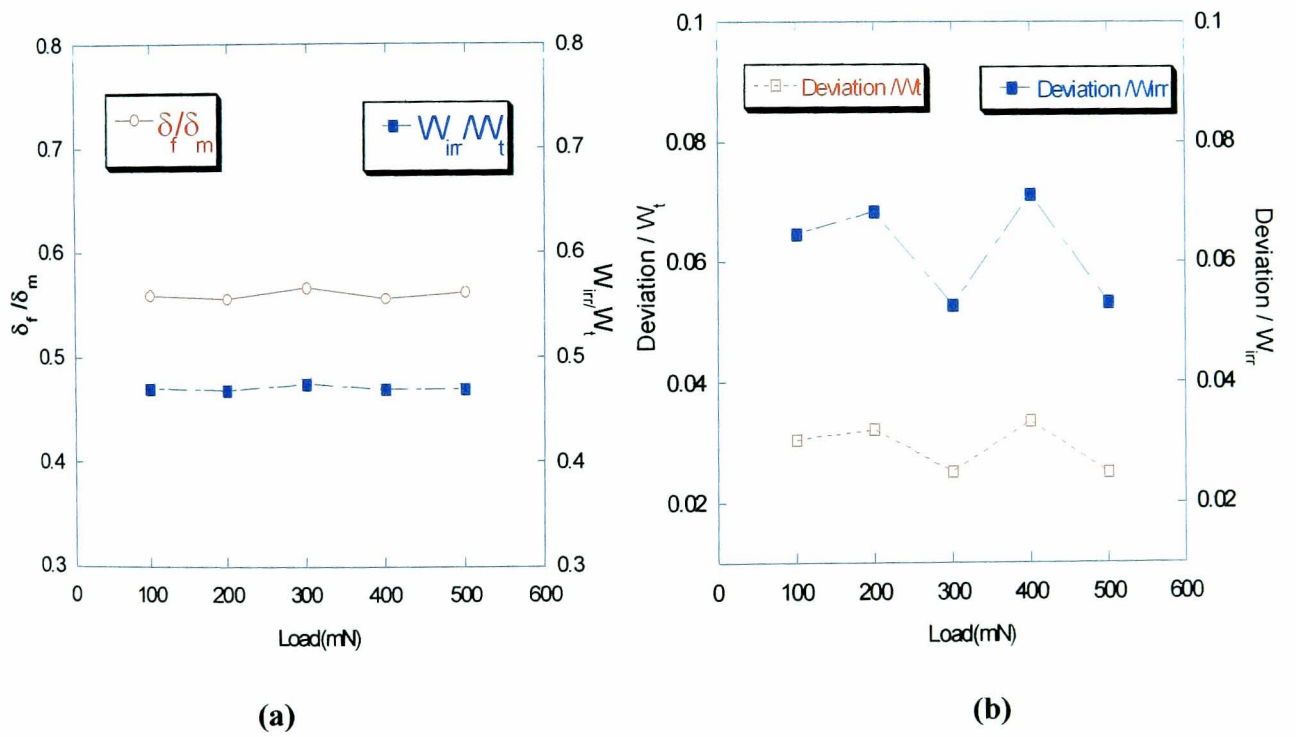

Figure 7.8. (a) Plot of δ_f/δ_m and W_{irr}/W_t versus load, and (b) plot of $\Delta W_{irr}/W_t$ and $\Delta W_{irr}/W_{irr}$ versus load for an uncoated glass at a range of loads (i.e. from 100mN to 500mN).

7.3.2 Description of W_{irr}-W_t method

The work of indentation can be written as,

$$W_t = W_P + U_{fra} + W_e + W_{other} \tag{7.3}$$

where W_t is the total work, W_P is work of plastic deformation, W_e is work of elastic deformation, U_{fra} is the fracture dissipated energy, W_{other} represents other items such as heat dissipated during indentation, creep and possible microcracks. The sum of all the other items in Eq.(7.3) except W_e is the irreversible energy W_{irr} (here, we ignore any reversible plastic behaviour). Given an indentation procedure, W_t and W_e can be easily measured. If W_P and W_{other} can be determined, the fracture dissipated energy U_{fra} can be obtained. The following section explains how to achieve this target.

The method of irreversible work difference (denoting as W_{irr}-W_p) is explained as follows.

1. The load-displacement curve shows no evidence for fracture, either in the form of large excursions in the loading or unloading curve or smaller invisible excursions which lead to an increase indenter displacement at a fixed load on loading. This will be compared with the experimental data which shows evidence of cracking.
2. Therefore, the influence of cracking on the mechanical properties of the whole coated system after cracking applies to the whole loading part of the experimental curve, i.e. averaging the crack influence on the plastic and elastic deformation over the whole loading cycle. This is a reasonable assumption since *E/H* remains almost constant despite the presence of fracture in the case that no excursion and no slope change in the P-δ curve are observed.
3. In such case the coated system can be treated as equivalent to a bulk material.

4. Ignoring the energy dissipated by heat etc, $W_t = W_P + U_{fra} + W_e$, the fraction of plastic work remains the same as in the equivalent bulk materials i.e. $W_t = W_P + W_e^{'}$ (where $W_e^{'} = U_{fra} + W_e$). The total work does not change because fracture only plays a role in converting some stored elastic energy into irreversible work under displacement cotrol.

Since the fracture influence on the elastic-plastic deformation of the whole system in the indenting procedure is averaged, this turns the initial system into an imaginary system without a crack but with the same plastic deformation work (W_P). For the ideal curve constructed here, the work of plastic deformation can be approximately determined by equation (7.1). Also the deviation introduced into W_{irr} by microcracking in substrate needs to be subtracted according to the analysis in Section 7.3.1. Thus the U_{fra} can be obtained, which represents the dissipated energy used to create new crack surface. The approach can separate the influence of elastic-plastic deformation mechanism from fracture given coated systems with features similar to what has been described here. It needs to be emphasised that the fracture must not make any contribution to the total work under displacement control. The contribution of fracture is to convert part of W_e into $W_{irr.}$

The coating toughness is then given by,

$$K_{IC} = \sqrt{\frac{U_{fra} E}{(1-\nu^2) A_{fra}}} \tag{7.4}$$

where ν and E are the Poisson's ratio and Young's modulus of coating, respectively. A_{fra} is the total area of fracture. In this study, ν=0.25 is used in the absence of better data for the coatings of interest.

7.4. Application of the model

7.4.1 Toughness analysis of coated glass

Using the analysis in previous section, the toughness of coatings of ZnO, SnO_2 and ITO as well as the interfacial toughness of the sample with 400nm ITO cap layer was determined. No obvious evidence of fracture in the substrate was found in this study. In order to estimate the coating toughness based on Eq. (7.4), a careful measurement of fracture area is required. Assuming that crack initiation can be described by a critical strain criterion, it can be expected that the crack spacing is uniform(Tuck and Korsunsky, 2000). Provided that picture frame cracking is well established and the outer picture-frame crack is very much bigger than the initial one, it can be shown that the total fracture area of the picture frame cracks is given by,

$$A_{fra} = \frac{3a^2}{2s}t \tag{7.5}$$

where a is the radial dimension of the indentation, s and t are the spacing between the cracks and the coating thickness shown in Fig.7.9.

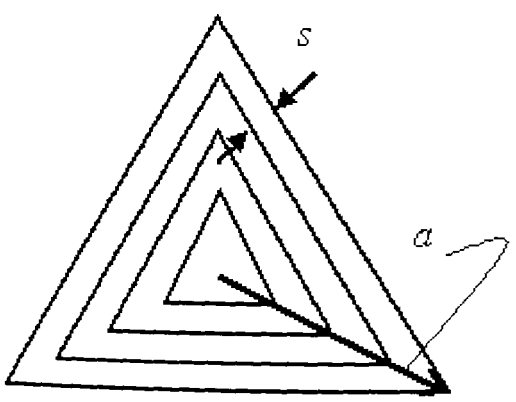

Figure 7.9: Schematic of the picture-frame crack geometry induced by a Berkovich indenter.

The interfacial crack area is given by,

$$A_{\text{int}} = \pi c_R^2 \tag{7.6}$$

where C_R is the measured interfacial crack radius.

Table 7.2. The energy release rate and toughness of the coatings determined by the new method here.

	Spacing (nm)	Young's Modulus (GPa)	*Energy release rate (J/m^2)	*Toughness ($MPam^{0.5}$)
400nm ZnO cap layer	239 ± 28	117	10.3 ± 3.8	1.1 ± 0.2
400nm SnO_2 cap layer	412 ± 54	133	19.9 ± 6.3	1.6 ± 0.3
240nm ITO cap layer	313 ± 30	131	39.4 ± 15.9	2.2 ± 0.5

*Both energy release rate and toughness is the mean value under the loads from 200mN to 500mN.

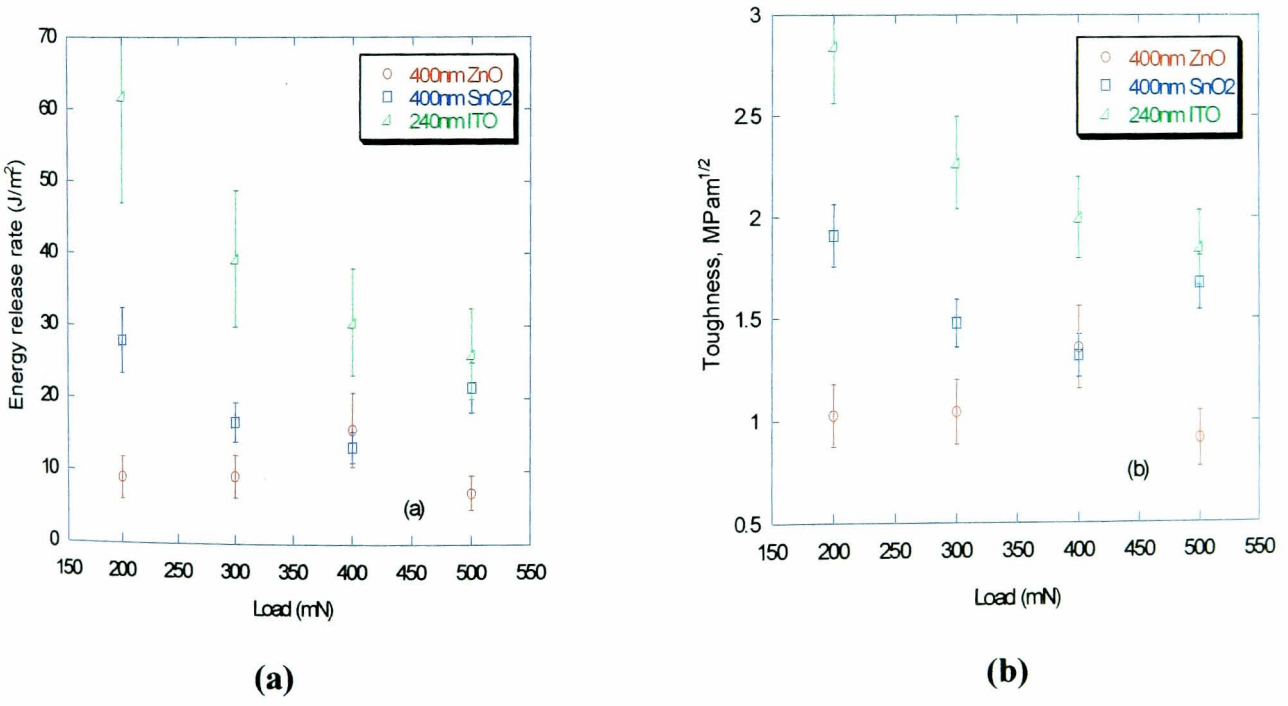

(a) **(b)**

Figure 7.10. (a) Plot of energy release rate and (b) toughness for ZnO, SnO_2 and ITO cap layers measured by nanoindentation under different applied loads (from 200 to500mN).

As discussed in the following chapter (i.e. Chapter 8), the lateral cracking induced interfacial failure is likely to occur in coated glass capped with 400nm ITO layer (see Fig.7.3) It is also possible to estimate the fracture toughness of the interface of ITO, where the Young's modulus of the coating will be replaced by a so-called interfacial modulus defined by Hutchinson and Suo (Hutchinson and Suo 1992),

$$\frac{1}{E_{\text{int}}} = \frac{1}{2}\left(\frac{1}{E_c} + \frac{1}{E_s}\right) \tag{7.7}$$

where E_c and E_s are the Young's modulus of coating and substrate, respectively. Here, the E_s is the effective substrate consisting of substrate glass and the other thin layers underneath the cap layer which is determined by the model developed by Bull et al [(Bull, 2001),(Bull et al., 2004)]. The interfacial toughness is 0.64 ± 0.07 $MPam^{1/2}$ which agrees with the results determined by different methods as discussed in Chapter 8.

From Table 7.2, it can be seen that the ITO coating is relatively tough compared to the ZnO coating. All of these coatings are tougher than glass, which was consistent with our previous results in Chapter 5. The toughness results for ITO and SnO_2 agree with our previous results determined by the W_t-dp method when assessing ultra small cracks in such coatings under low loads (<5mN) indented by a cube corned tip. The toughness of the ZnO cap layer determined here is around $1.1 \pm 0.2\ MPa\sqrt{m}$, which is consistent with results in the literature such as $0.8 \pm 0.11\ MPa\sqrt{m}$ (Mukhopadhyay et al., 2001) for ZnO powder and $1.4\ MPa\sqrt{m}$ for bulk ZnO (Ruf and Evans, 1983). Previous tests (Bull et al., 2003) show that the critical loads for first acoustic emission (AE) event well after plastic deformation initiation in ZnO and SnO_2 are similar, which implies that their toughness will be similar if it is assumed that the flaw size distribution is similar. The results in Table 7.2 agree with this observation. The toughness error for ITO is relatively big which is possibly due to the non-uniform distribution of residual stress and flaws in it. The energy release rate and toughness at loads for different samples is displayed in Fig.7.10. The values do not vary much with loads which indicates that the model presented here is reasonable.

7.4.2 Why no evidence of picture frame cracks in TiO_xN_y coatings ?

As described in the previous section (see Fig.7.5), no obvious evidence of picture-frame cracks in TiO_xN_y was observed in SEM micrographs. Two possible reasons could account for this.

One is the poor conductivity of TiO_xN_y compared to other coatings which degrades image quality in the SEM and limits the visibility of picture-frame cracks since the opening displacement is small (<10nm). Another reason to explain why no picture-frame cracks are visible in the SEM micrographs of TiO_xN_y on substrate is provided in the following, which is more likely to account for this phenomenon.

If a thin hard coating (usually associated with high yield stress) is well bonded to a softer substrate, the softer substrate is likely to yield first (Burnett and Rickerby, 1987). In such case, the substrate may add a bending influence on the deformation of the coating.

When $\frac{E_f}{H_f} < \frac{E_s}{H_s}$, the plastic zone of the substrate underneath the coating enhances the bending of the coating thus helping to produce the picture-frame cracks and tends to increase the crack opening displacement (see Fig. 7.11a). This is also the reason that the crack opening displacement (COD) is relatively significant in ZnO whose E/H ratio is lowest among all the coatings (see Table 7.1). However, in the reverse case, i.e. $\frac{E_f}{H_f} > \frac{E_s}{H_s}$ (see Fig. 7.11b), the plastic zone in substrate does not have much contribution to the bending of the coating so that the COD in TiO_xN_y coatings may be too small to be observed in the SEM used in this study.

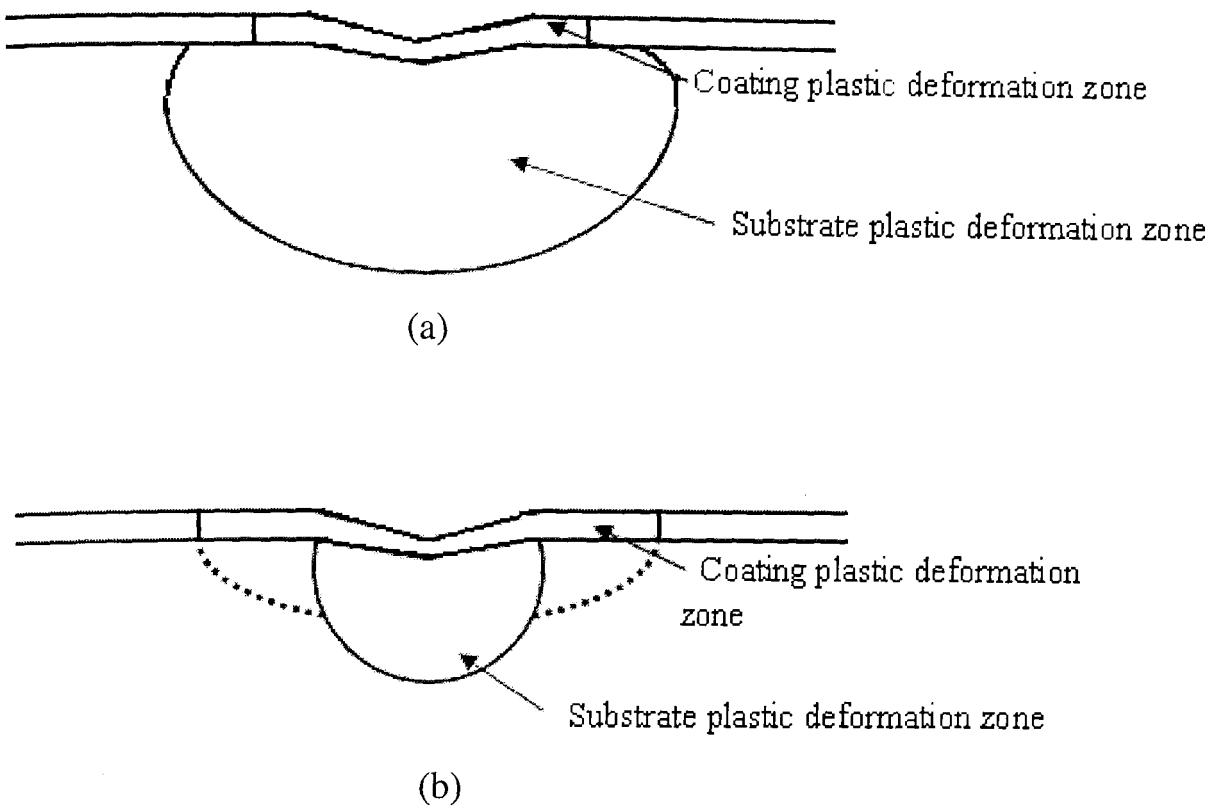

Figure 7.11. Relative plastic zone volumes envisaged for the coated system (a) $E_f/H_f<E_s/H_s$ (b) $E_f/H_f>E_s/H_s$ as proposed by Burnett and Rickerby (Burnett and Rickerby, 1987).

7.4.3 Application of the model to bulk materials

In order to further examine its utility, the model has also been applied to some bulk materials. In this case, radial cracking, rather than picture frame cracking, dominates the fracture response and the areas of these cracks are used in toughness calculations (assuming they are quadrants of a circle). For SiC and Si (100) tested by the Nanoindenter II ™(Nano Instruments, Knoxville,TN, USA) fitted with Berkovich indenter under 500mN load control, the toughness evaluated by this new model is ~3.7 MPa$\sqrt{m}$, and ~1.3 MPa$\sqrt{m}$, respectively, similar to the results ~4.1 MPa$\sqrt{m}$, and ~0.9 MPa $\sqrt{m}$, determined by the conventional indentation model (CIM). Considering that the accuracy of the conventional indentation model is more than 25%, the values determined by CIM and the method presented here are in reasonable agreement. In addition, since different types of cracks exist (such as radial cracks and lateral chipping as depicted in Fig.7.12), the interaction between the various crack

systems may disturb the initial radial cracking stress field which might lead to a deviation when using the conventional indention model.

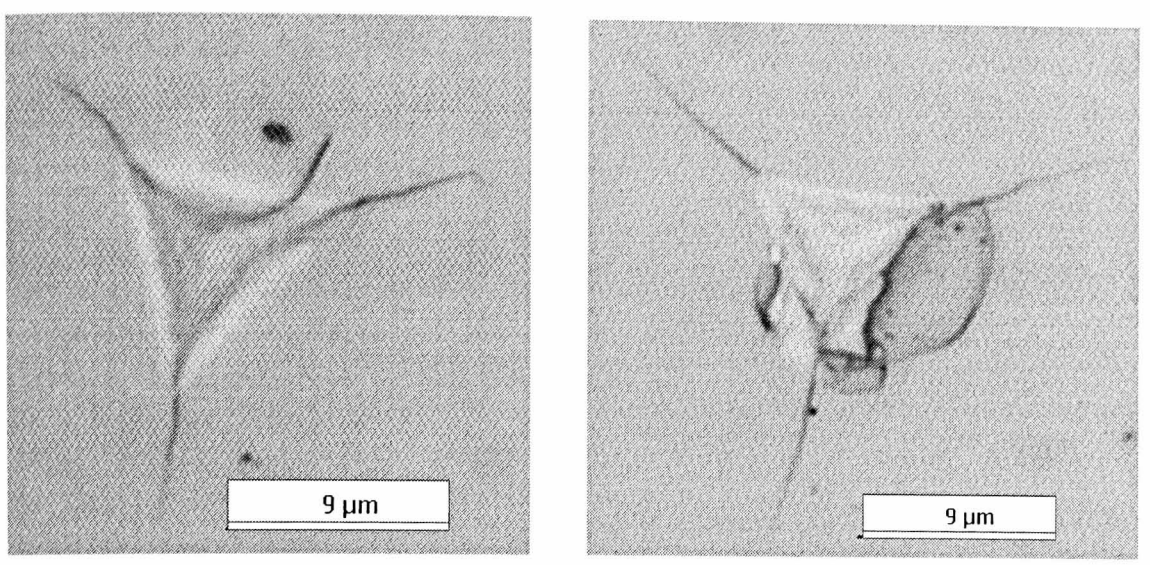

(a) **(b)**

Figure 7. 12. SEM micrograph of the radial cracking and chipping in (a) Si (100) and (b) SiC indented at 500mN peak load using a Berkovich indenter.

Although different coated systems and typical brittle bulk materials have been selected to verify the W_{irr}-W_p method, it should remembered that it is not reasonable to trust the method developed here in all structures because the properties of some coated systems (e.g. hard and brittle coating on very soft substrate) will conflict with the assumptions in this model.

7.5. Summary

A new model is presented in this Chapter to measure the coating toughness based on picture frame cracks which shows comparable results to those reported in the literature which indicates the model is reasonable. It can be also extended to the other coated systems or bulk materials given that the assumptions in the model are valid. The values of the coating toughness determined here agree well with previous results

obtained by W_t-dp method (see Chapter 5). Compared to the other fracture dissipated energy based models, i.e. extrapolating the discontinuity in P-δ curve or the W_t-dp curve which require a discontinuity or step in these curves, the new model presented here fills the gap to measure the coating toughness when investigating the load-displacement curve under the condition that no obvious discontinuity occurs. The calculation errors are mainly caused by the determination of the length and area of the crack since the crack geometry is not ideal.

References:

Bull, S. J. (2001) Modelling the hardness response of bulk materials, single and multilayer coatings,*Thin Solid Films,* **398,** 291-298.

Bull, S. J., Arce-Garcia , I., G-Berasategui, R. E. and Page, T. F.2003Indentation fracture ,acoustic emission and modelling of the mechanical properties of thin ceramics coatingsHouston,TXpp21-42

Bull, S. J., Berasetegui, E. G. and Page, T. F. (2004) Modelling of the indentation response of coatings and surface treatments,*Wear,* **256,** 857-866.

Burnett, P. J. and Rickerby, D. S. (1987) The Mechanical-Properties of Wear-Resistant Coatings .1. Modeling of Hardness Behavior,*Thin Solid Films,* **148,** 41-50.

Cheng, Y. T. and Cheng, C. M. (1998) Scaling approach to conical indentation in elastic-plastic solids with work hardening,*Journal of Applied Physics,* **84,** 1284-1291.

Cheng, Y. T., Li, Z. Y. and Cheng, C. M. (2002) Scaling, relationships for indentation measurements,*Philosophical Magazine a-Physics of Condensed Matter Structure Defects and Mechanical Properties,* **82,** 1821-1829.

Hutchinson, J. W. and Suo , Z. (1992) Mixed mode cracking in layered materials.,*Adv. Appl. Mech.,* **29,** 63–191.

Lawn, B. R. and Evans , A. G. (1977) A Model for Crack Initiation in Elastic/Plastic Indentation Fields,*J. Mater. Sci.,* **12,** 2195.

Mencik, J. and Swain, M. V. (1994) Micro-Indentation Tests with Pointed Indenters,*Materials Forum,* **18,** 277-288.

Mukhopadhyay, A. K., Chaudhuri, M. R., Seal, A., Dalui, S. K., Banerjee, M. and Phani, K. K. (2001) Mechanical characterization of microwave sintered zinc oxide,*Bull. Mater. Sci.,* **24,** 125-128.

Oliver, W. C. and Pharr, G. M. (1992) An Improved Technique for Determining Hardness and Elastic Modulus Using Load and Displacement Sensing Indentation Experiments,*Journal of Materials Research,* **7,** 1564-1583.

Ruf, H. and Evans, A. G. (1983) Toughening by monoclinic zirconia,*J.Am.Ceram. Soc.,* **66,** 328-332.

Tuck , J. R. and Korsunsky, A. M. (2000) In *13th European Conference on Fracture, http://www.eng.ox.ac.uk/~ftgamk/ecf13.pdf 27Nov.2004*san sebastian, Spain.

Chapter 8:

Adhesion assessment

Chapter 8 Adhesion assessment

There are a lot of techniques to estimate the adhesion of a coating on a substrate , such as the pull-off test, superlayer method, bending, bulge and blister tests, Double Cantilever Beam tests, scratch and indentation (nanoindentation) tests which have been reviewed in Chapter 2.

As mentioned in Chapter 2, there is no universal model or test to assess adhesion. Some specific methods may generate different phenomena in different coated systems. In some systems adhesive failure occurs during indentation tests. This Chapter describes some new methods to estimate the adhesion based on these experimental observations.

This Chapter begins with a brief review of energy-based models for adhesion assessment. Then the method based on extra linear recovery during unloading is presented followed by the assessment based on lateral crack induced interfacial failure. The rest of the Chapter is devoted to evaluation of adhesion in the case of spontaneous blister formation and a summary of the results from all tests.

8.1. Energy based models

There are several energy based models (e.g. the ld-dp method as reviewed in Chapter 2 and W_t-dp method as described in Chapter 5) to assess the fracture toughness of a coating. If the feature in the load-displacement curve is related to delamination, these energy based models are still valid (e.g. Fig.8.1). For example, the W_t-dp method gives the energy release rate of $30\pm14 J/m^2$ and $19\pm9 J/m^2$ for a 400nm TiO_xN_y /glass

interface and 240nm ITO multilayer on glass, respectively. These are reasonable results for such coated systems.

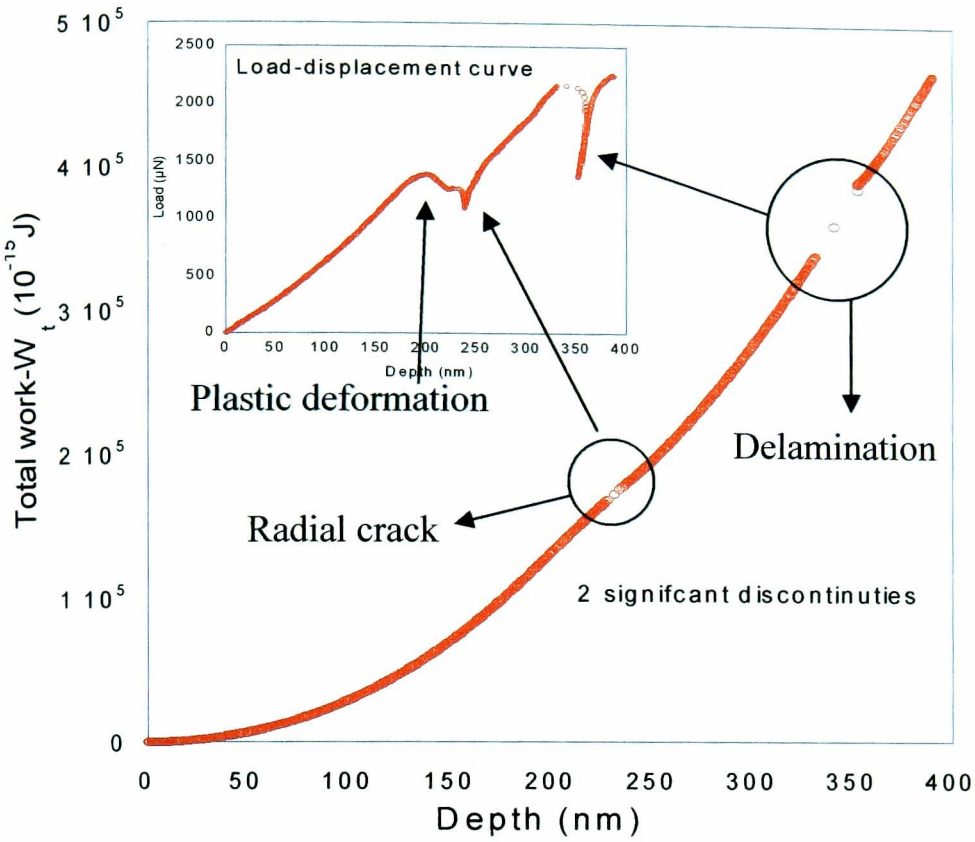

Fig. 8.1. Total work versus displacement curve for a 400nm TiO_xN_y coating on glass. Two significant discontinuities are observed. It is obvious that these two events are related to different fracture mechanisms. The second one is caused by delamination (see Chapter 5). Its associated AFM image can be found in Fig. 5.6d or Fig.8.3b.

Another alternative energy based model was presented by Malzbender and de With (Malzbender and de With, 2000) based on plotting irreversible work W_{irr} versus applied load. For thicker sol-gel coatings in (Malzbender and de With, 2000) a slope change of curve of W_{irr} versus applied load (W_{irr} -P curve) was observed when delamination occurred. Thus the energy ΔW_{irr}^{d} (see Fig.8.2) was assumed to be the energy dissipated by delamination which is the difference between the energy at a given delamination dimension C_R and the extrapolated energy for the plastic deformation of the coating system before delamination.

Then the energy release rate for delamination G_{int} is given by,

$$G_{\text{int}} = \frac{\Delta W_{irr}^{d}}{\pi C_R^2} \tag{8.1}$$

and the interfacial toughness K_{int} is given by,

$$K_{\text{int}} = \sqrt{G_{\text{int}} E_{\text{int}}} \tag{8.2}$$

where E_{int} is a so-called interfacial modulus which is given by (Hutchinson and Suo 1992),

$$\frac{1}{E_{\text{int}}} = \frac{1}{2}\left(\frac{1}{E_c} + \frac{1}{E_s}\right) \tag{8.3}$$

where E_c and E_s are the Young's modulus of the coating and substrate, respectively.

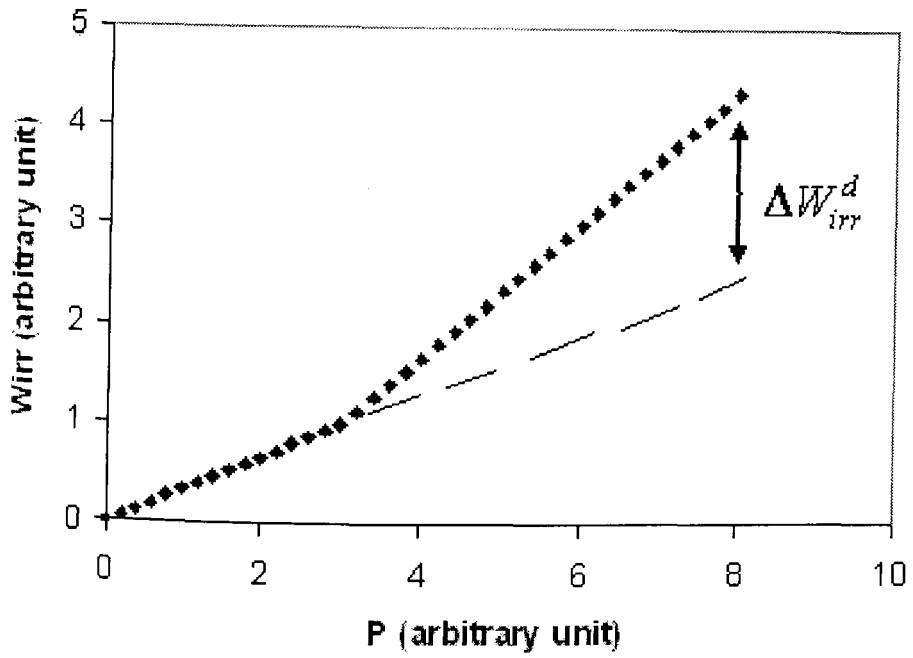

Fig.8.2 Schematic of the irreversible energy dissipated as a function of applied load during indentation (Malzbender and de With, 2000).

However, this method is not as accurate as expected as documented in Chapter 2. In addition, such a method requires many tests at a number of loads which is quite time consuming and not economic for practical application. It is necessary to point out that actually the W_{irr} method is also only valid in the case of an adhesion related feature in load-displacement curve otherwise a slope change may not be observed thus leading to the failure of the method (see the example for inorganic-organic coating on glass in (Etienne-Calas et al., 2004)).

Furthermore, it is necessary to point out that fracture does not always lead to an obvious excursion in the load-displacement curve (P-δ curve). In this case, if the energy difference between plastic work and irreversible work can be distinguished and is related to the fracture, then the fracture toughness can still be measured by the energy based model described in Chapter 7. Combining numerical simulations and calibration on realistic materials, the plastic work can be estimated and the irreversible work can be easily calculated from the load-displacement curve. Then the difference between plastic work and irreversible work is regarded as the fracture dissipated energy. The interfacial toughness for 400nm ITO/glass is 0.64 ± 0.07 $MPam^{1/2}$ by this model (see Chapter 7) which is very close to 0.44 $MPam^{1/2}$ determined by a different method in the following section.

In fact, under certain conditions, i.e. rebound after delamination leading to extra linear recovery in the unloading part of the P-δ curve, the adhesion may be assessed by a different method which will be discussed in detail in this Chapter.

The linear part (as marked in Fig.8.3 or 8.4) occurring near the end of unloading procedure is believed to be accounted by rebounding during unloading. In this case the coating detached from the substrate (with crack radius of C_R) acts as a spring, pushing the indenter out of the impression and generating load at lower depths than normal elastic unloading. The area of debonding during unloading is given by πC_R^2. By extrapolating the initial part before transition point of the unloading curve to the completely unloaded point, the difference between the extrapolated unloading curve and the actual unloading curve can be regarded as an approximation of the fracture

dissipated energy for delamination (see the marked portion in Figures 8.3 and 8.4). The mechanism can be explained as follows (see Fig.8. 5).

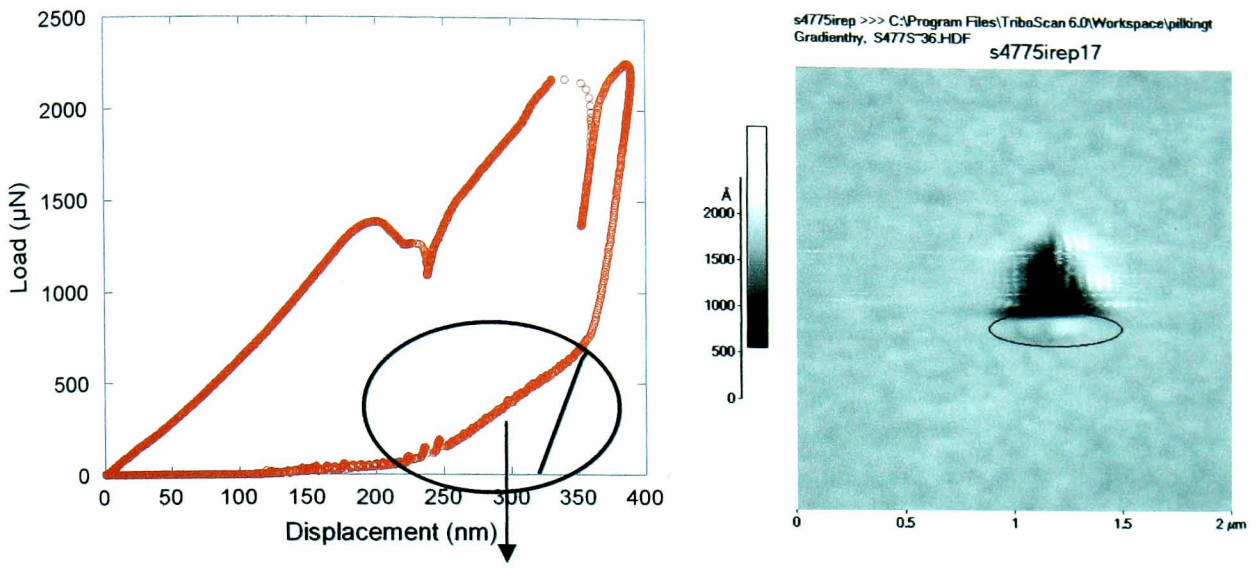

(a) **(b)**

Fig.8.3. (a) Extra linear elastic recovery in the load-displacement curve is observed during unloading for a 400nm TiO_xN_y coating on commercial soda-lime glass and (b) its corresponding AFM image.

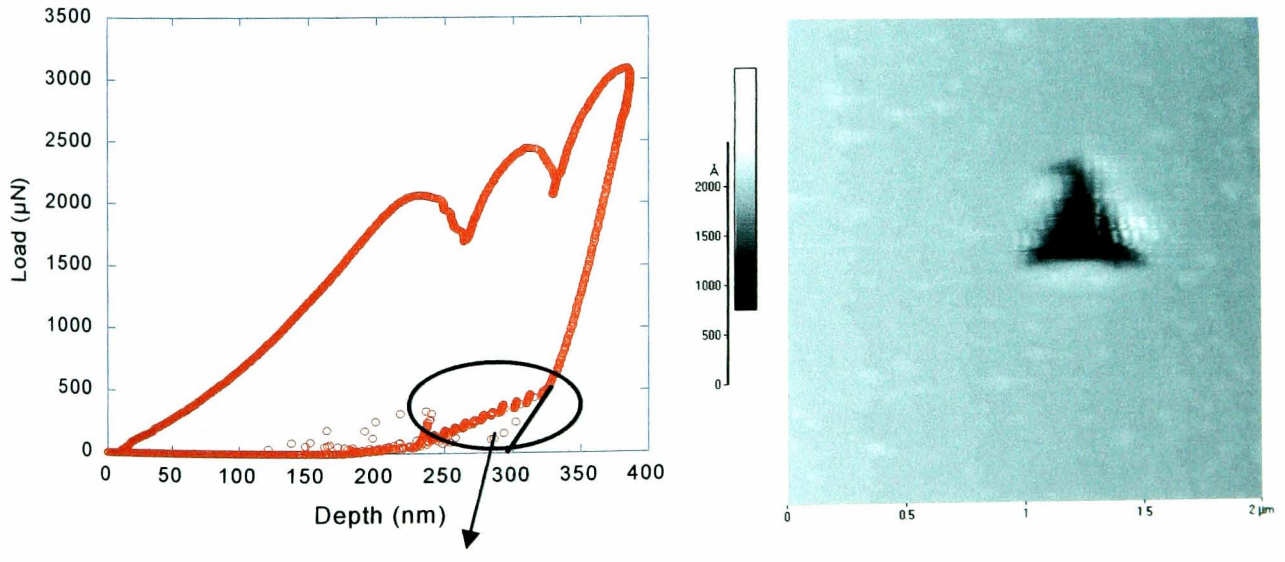

(a) **(b)**

Fig.8.4. (a) Extra linear elastic recovery in the load-displacement curve is observed during unloading for a 240nm TiO_xN_y coating on commercial soda-lime glass and (b) its corresponding AFM image.

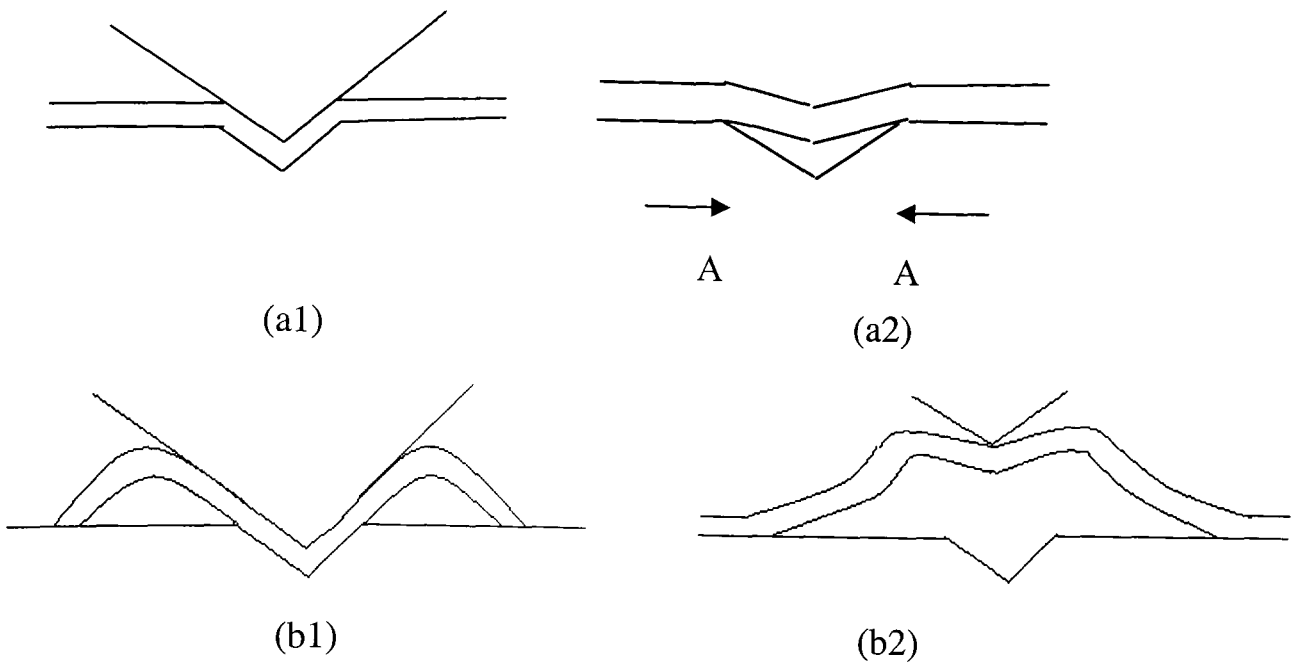

Fig.8.5. Schematic of the rebound of the detached material on unloading (a) good adhesion and (b) poor adhesion. The coating within the region A-A is involved in short-range rebounding as shown in Fig.8.3.

The coating underneath the indenter deflects into the impression in the substrate under load, causing the tensile stress at the edges and the buckling during loading if the adhesion is poor but the compressive stress at the tip causes the coating within the region A-A (see Fig.8.5) to remain pressed against the substrate. During unloading the film in this area will buckle upwards, pushing the indenter ahead of it. The case in Fig. 8.5b is more difficult to analyse as the energy consumed in fracture on loading is not easy to determine.

Another model based on equilibrium theory and solution of a centrally loaded disc to assess debonding was proposed to deal with the same phenomena by Hainsworth et al. (Hainsworth et al., 1998). In contrast to the model presented here, it is assumed the fracture dissipated energy associated with debonding equals the elastic energy stored in the flexed annular coating segment while ignoring the extra recovery area in the unloading curve.

The energy dissipated by debonding is given by,

$$W_d = W_f = \frac{2\pi E t^3 (\delta_m - \delta_r)^2}{3C_R^2} \tag{8.4}$$

$$G_{\text{int}} = \frac{W_d}{\pi C_R^2} = \frac{2E t^3 (\delta_m - \delta_r)^2}{3C_R^4} \tag{8.5}$$

However, it dramatically overestimated the results. For example, for a 4μm TiN/ZrN multilayer on steel indented at 500mN, the G_{int} =173 to 716J/m^2 with regard to the debonding length of 5~7 μm. In addition, it is extremely sensitive to the measured debonding length since the exponent of C_R in Eq.(8.5) is 4. When applying this method to the ceramic coatings in this study, it gives around 20000 J/m^2 for 400nm TiO_xN_y and 240nm ITO, which is obviously unrealistic. In contrast, the method presented here provides a reasonable approximation which gives the fracture dissipated energy 32 to 64 J/m^2 for TiN/ZrN which is more sensible for a ceramic/metal interface. Also for the coated glasses in this study, it gives 79.7 ±17.6 J/m^2 for TiO_xN_y / glass interface, thus the interfacial toughness is approximately 2.8±0.3 MPam$^{1/2}$ (according to Equations (8.1) to (8.3)). For the ITO/ZnO/Ag interface, the values of fracture dissipated energy and toughness are 35.8 ±14.1 J/m^2, 1.9±0.3 MPam$^{1/2}$, respectively. These results agree reasonably with those determined by the different method (i.e. W_t-dp) provided in previous section. For the 240nm ITO coating, the relatively high pre-existing residual stress in the coating and interface may make it more likely to fail at the ITO/Ag interface rather than the other weak interface in the coating stack (ZnO/Ag). It can also be argued that the ITO coating acts as a superlayer which causes the ZnO/Ag interface to fail.

The reason that the model by Hainsworth et al significantly overestimates the values of interfacial toughness is that the through-thickness cracking prior to the debonding means that the stored elastic energy U_e in the cracked coating segment has been at least partly released. The analysis of the extra recovery area during unloading as the

work done by the indenter is more reasonable. If the release of elastic energy in the coating is what causes detachment and the buckling of the coating then the work done pushing the indenter out should be the same as this. The recovery work is assumed to be equal to the extra recovery area (including the effects of residual stress in the film) but some other energy dissipation mechanisms may also contribute (crack tip plasticity, microcracks, energy stored in bending) which will limit the accuracy of the result.

8.2 Method based on analysis of lateral crack induced interfacial failure

The models above deal with the blister formation or delamination, while, interfacial failure can be also caused by a lateral crack occurring at the interface or adjacent to interface.

Based on the expanding cavity model as used in the analysis of the radial/median crack pattern (Lawn et al., 1980) and a simple plate theory, Marshall et al proposed a model to relate the toughness of brittle bulk materials to the depth where lateral cracks occur and the driving force P_r due to the residual stress during unloading. It was found that the lateral cracking tended to occur near the elastic-plastic boundary. Although P_r can be described in terms of the applied load P, there are three coefficients needed for the model which are very difficult to determine. This model has been further developed to link the toughness to the threshold fracture load and the other basic parameters such as hardness, elastic modulus, giving (Marshall et al., 1982),

$$K_c^4 = \frac{P_0 A_0^2}{\delta_0}(\cot\theta)^{\frac{2}{3}}\left(\frac{H^4}{E}\right) \tag{8.6}$$

Where P_0 is threshold load for lateral cracking; A_0 and δ_0 are dimensionless constants (A_0 =3/4 and δ_0 =1200) and θ is the half-included angle for the indenter.

With the aid of nanoindentation, this method can be simply applied to coated systems since indents may be produced with suitable plastic zone sizes. Under certain circumstances, this method can be used to assess the interfacial failure of a coated system if the lateral crack occurs at a relatively weak interface compared to the toughness of the coating and substrate.

For the coated glass investigated here, the lateral cracking was only observed in coated glass capped with a 400nm ITO layer. The lateral crack observed was shorter than the indentation size (see Fig. 8.6). Since the interface for the 400nm ITO coated glass was relatively weak, it can be expected that the lateral cracking occurs at this interface. The lateral cracking is unlikely to occur in substrate because there is no evidence of lateral cracking in all the other samples including uncoated glass indented at 500mN. It is reasonable to assume that the critical load for the lateral cracking can be obtained when the plastic deformation zone reaches the interface. As suggested by Chen and Bull (Chen and Bull, 2006b), for ceramics the radius of the plastic deformation zone is about five times the residual indent depth. The residual depth is around 80nm and then the critical load is about 3mN. Based on Equation (8.6), a first approximation of interfacial toughness, 0.44 $MPam^{1/2}$ (or G_c=1.9J/m^2), can be obtained. It is a reasonable result compared to the values of interfacial toughness for similar ceramics/silver in the literature (Barthela et al., 2005).

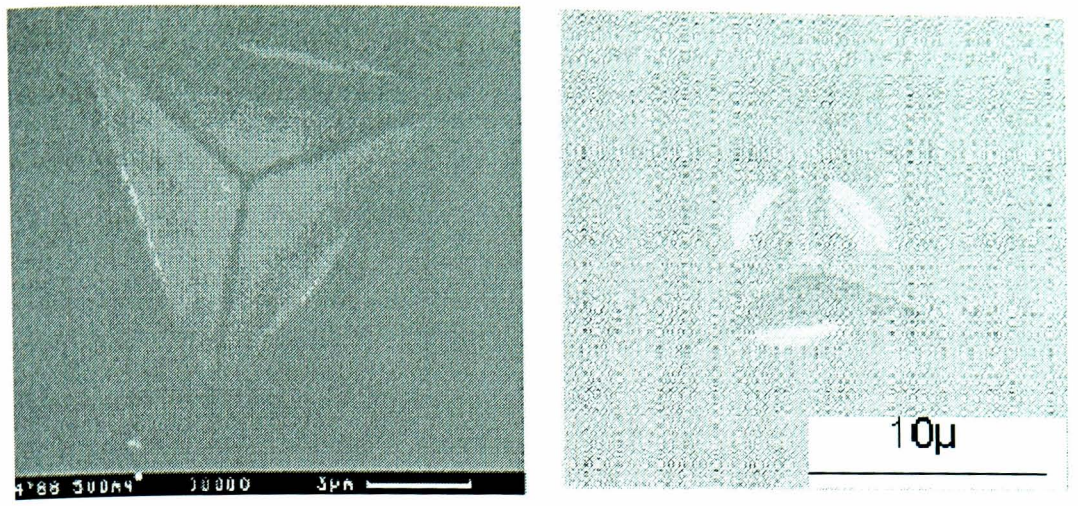

(a) (b)

Figure 8.6. (a) SEM (secondary electron) micrograph and (b) reflected light micrograph showing lateral cracking for a 400nm ITO cap layer on glass.

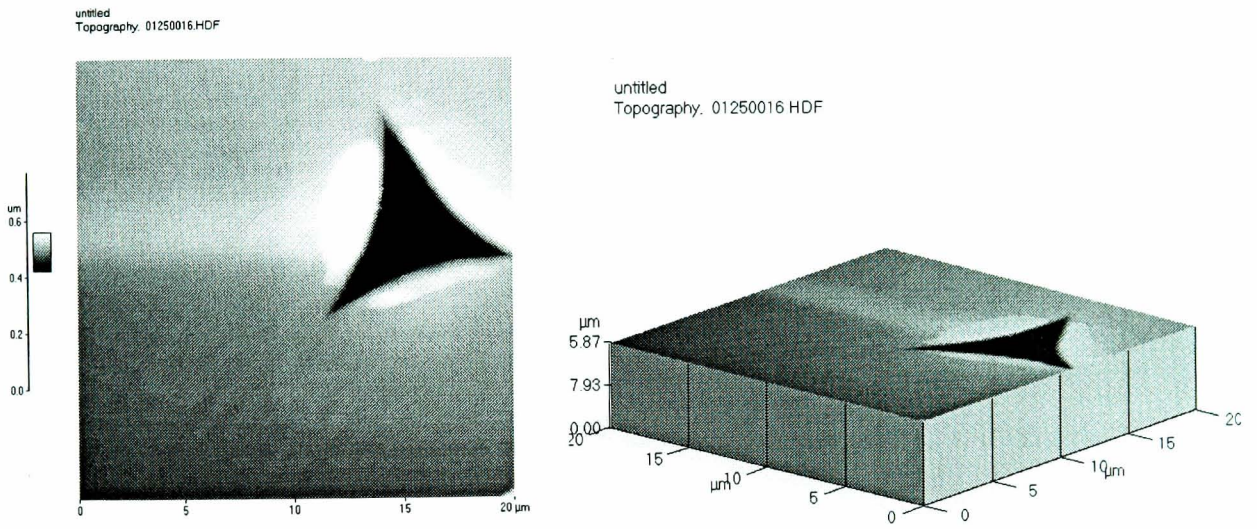

(a) (b)

Figure 8.7. AFM image of lateral cracking in a 400nm ITO multilayer stack on glass (a) topography (b) 3D image.

8.3 Method based on spontaneous blister

If a spontaneous blister occurs in a coated system (e.g. Figures 8.8 and 8.9), the interfacial toughness can be directly estimated without additional tests. The method

considers the contribution to energy release rate G_{int} for the interface by the critical buckling stress σ_c and driving stress σ_r of the film (i.e. the residual stress in the coating) and the relationship between them is given by Hutchinson and Suo (Hutchinson and Suo 1992),

$$G_{\text{int}} = \left[\frac{(1-\nu^2)t}{2E}\right](\sigma_r - \sigma_c)(\sigma_r + 3\sigma_c) \tag{8.7a}$$

$$\text{Where } \sigma_c = \frac{kE}{12(1-\nu^2)}\left(\frac{t}{a}\right)^2 \tag{8.7b}$$

$$\sigma_r = \sigma_c\left[c_1\left(\frac{h}{t}\right)^2 + 1\right] \tag{8.7c}$$

Where h is the bulge height, c_1=0.75, for a spontaneous blister, $k = \pi^2$.

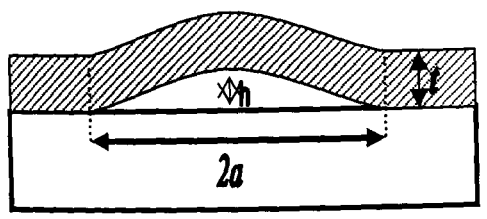

Fig. 8.7. Schematic of a cross section of a spontaneous blister in a coated system.

For a newly-developed CN_x coating (1μm in thickness) on M2 steel, Eq. (8.7) leads to the energy release rate of 3.3±0.1 J/m^2 which is reasonable(Palacio, 2006). Such spontaneous blistering has been observed across the surface of a 400nm ITO multilayer stack on glass (see Fig.8.8 and 8.9), the energy release rate for adhesion is around 2.7±0.1J/m^2 given by Eq. (8.7), which agrees well with the value of 1.9J/m^2 determined by equation (8.6) in the previous section.

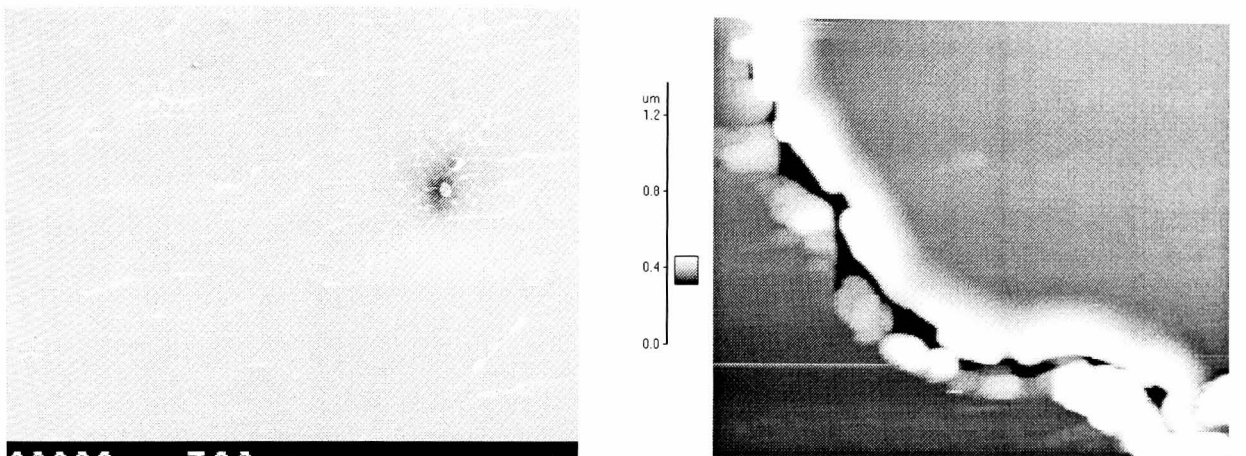

(a) **(b)**

Fig.8.8. (a) SEM and (b) AFM image of spontaneous blister in 400nm ITO on glass.

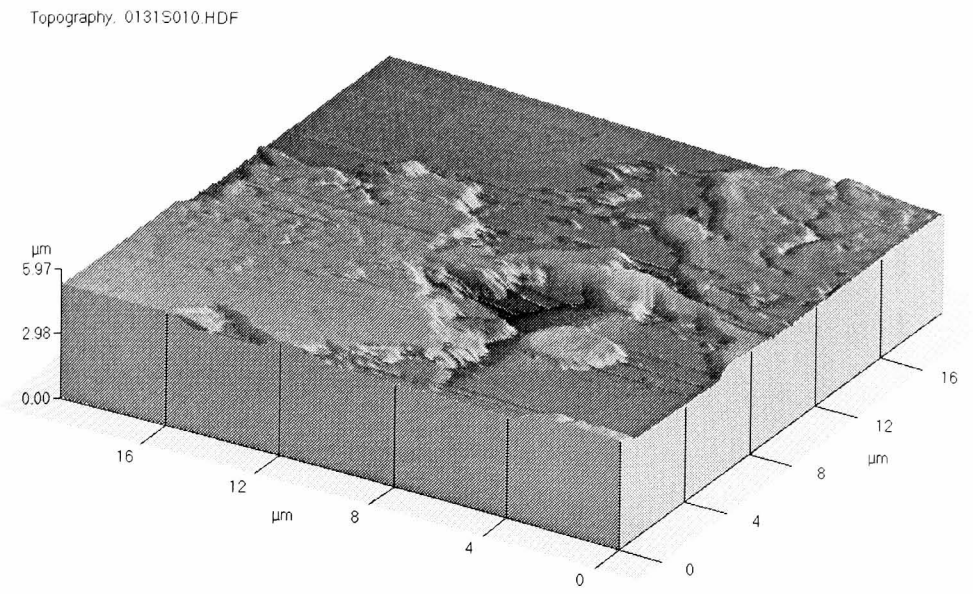

(a)

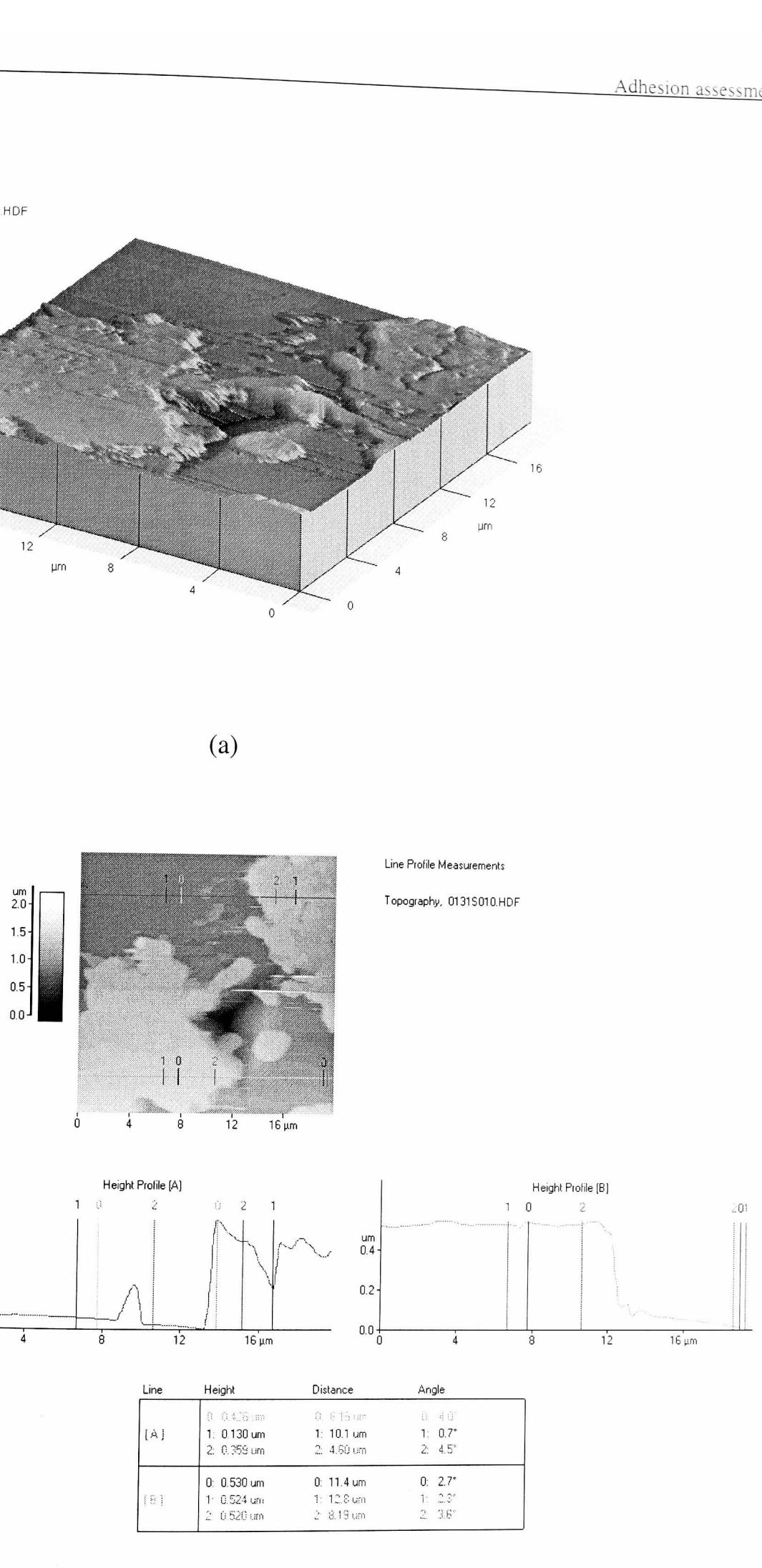

(b)

Fig.8.9. (a) AFM image and (b) line profile measurement of a spontaneous blister around an indent.

8.4 Comparison

Double cantilever beam (DCB) testing has previously been used to assess the adhesion of relatively thick coatings. Recently, it was found that it can be also used to assess the adhesion between ultra thin films (down to 10nm) and a glass substrate. By DCB, Barthel et al (Barthel et al., 2005) obtained the adhesion energy of 1.4~2.8 J/m^2 for a Glass/ZnO (TiO_2 or SnO_2)/Ag/ZnO stack with the crack path in ZnO/Ag interface. Density-functional calculations in the absence of mechanical energy dissipation at the ZnO/Ag interface (Bristowe and Lin, 2006) provides similar results. Barthel et al (Barthel et al., 2005) stated that that the adhesion energy between SnO_2 (or TiO_2) and Ag may be at least 50% higher than that of ZnO/Ag for the similar layer stack on glass. The weak interface in the study is one with silver either Ag/ZnO or Ag/ITO which is difficult to verify. Because there is high residual stress in ITO, it may be expected that ITO/Ag fails first. It is reasonable to expect that adhesion ITO/Ag is similar to that of SnO_2 and it is in same order of magnitude of ZnO/Ag. For this regard, no matter which interface really fails (either ITO/Ag or Ag/ZnO) the value of G_{int} obtained for ITO/Ag/ZnO interface here based on spontaneous blister agrees very well with the results by DCB for similar coating stack reported in the literature. The driving force of the spontaneous blister is around 3GPa which is a reasonable estimation of the residual stress in the coating.

For the delamination produced by a sharp cube corner indenter analysed by the W_t-dp method, the result is between 10 to 28J/m^2 which overestimates the adhesion energy due to the inevitable plastic deformation associated with the delamination during loading. The adhesion energy assessed by extra linear elastic recovery for such a coating stack is about 20 to 40J/m^2 which overestimates the interfacial toughness as well. The reason for the overestimation is that only part of stored elastic energy drives crack propagation and what this fraction is is unknown. However, this method is useful for qualitative comparison.

For a 400nm TiO_xN_y single layer on glass, its adhesion is relatively high compared to the coating stack with oxide/Ag interfaces. This is possibly due to the fact that the mismatch between the oxides and glass is smaller than that between the oxides and Ag.

8.5. Summary

Adhesion assessment of various coatings on glass has been made by a number of indentation techniques. The interfacial toughness estimated by different methods has achieved reasonable agreement, which indicates the results and the methods are reasonable.

From Chapter 5 to this chapter, all the models and methods have been presented to assess the toughness of coating and coating/substrate interface. In the next chapter, a detailed analysis of the P-δ curves to investigate how loading rate influences the fracture behaviour is discussed.

Reference:

Barthel, E., Kerjan, O., Nael, P. and Nadaud, N. (2005) Asymmetric silver to oxide adhesion in multilayers deposited on glass by sputtering,

Thin Solid Films **473,** 272- 277.

Barthela, E., Kerjana, O., Naela, P. and Nadaudb, N. (2005) Asymmetric silver to oxide adhesion in multilayers deposited on glass by sputtering,

Thin Solid Films **473,** 272- 277.

Bristowe, P. and Lin, Z. (2006), Private communication

Etienne-Calas, S., Duri, A. and Etienne, P. (2004) Fracture study of organic-inorganic coatings using nanoindentation technique,*Journal of Non-Crystalline Solids,* **344,** 60-65.

Hainsworth, S. V., McGurk, M. R. and Page, T. F. (1998) The effect of coating cracking on the indentation response of thin hard-coated systems,*Surface & Coatings Technology,* **102,** 97-107.

Hutchinson, J. W. and Suo , Z. (1992) Mixed mode cracking in layered materials.,*Adv. Appl. Mech.,* **29,** 63–191.

Lawn, B. R., Evans, A. G. and Marshall, D. B. (1980) Elastic/Plastic Indentation Damage in Ceramics: The Median/Radial Crack System,*J. Am. Ceram. Soc.,* **63,** 574.

Malzbender, J. and de With, G. (2000) Energy dissipation, fracture toughness and the indentation load-displacement curve of coated materials,*Surface & Coatings Technology,* **135,** 60-68.

Marshall, D. B., Lawn, B. R. and Evans, A. G. (1982) Elastic/Plastic Indentation Damage in Ceramics: The lateral crack system,*J. Am. Ceram. Soc.,* **65.,** 561.

Palacio, J. F. (2006) "Mechanical properties of high performance fullerene-like CNx coatings assessed by nanoindentation": Ph. D thesis,,University of Newcastle Upon Tyne

Chapter 9:

Loading rate influence on fracture behaviour during nanoindentation

Chapter 9: Loading rate influence on fracture behaviour during nanoindentation

Previous chapters were devoted to investigations of the fracture toughness of the coated systems. This chapter will concentrate on loading rate effects on the fracture behaviour of these brittle coated systems.

9.1 Introduction

As mentioned previously, fracture may lead to load drops in load-displacement curves under displacement control. Different analysis methods may be used to determine the fracture onset such as inspection of load-displacement *(P-δ)* and P/δ^2 vs. δ, $\partial P / \partial(\delta^2)$ vs. δ and these may be used to investigate detailed features of the fracture process. When analysing the loading rate on the fracture initiation load, significantly different behaviour was observed for some materials and the possible mechanisms are discussed in this chapter.

9.2. *P-δ* curve analysis

For all the coated glass samples (as previously, the main emphasis is again on the thicker coatings), it was found that within the penetration rate range used in this study the higher the penetration rate, the higher the fracture threshold (see Fig. 9.1 for example). Such observation agrees well with the literature for brittle bulk materials and coatings at high loads (>20N) (Lee et al., 2002).

A possible reason to account for such rate-dependent behaviour is the competition between fracture and dislocation mobility in these brittle materials. At high loading rate, it is difficult to find a suitable flaw for fracture nucleation since the well-established plastic deformation prior to fracture rapidly continues its development and obliterates the layer defects. When very high stress intensity is reached, even a relatively small flaw (which does not contribute to crack initiation at lower load) can provide suitable nucleus for fracture. In contrast, at a lower displacement rate, the flow of the materials is slow, there is more opportunity for a suitable flaw size to remain in the location where large stress concentration occurs (usually underneath the indenter), thus fracture may occur at lower loads. At lower penetration (<200nm), no load drops were observed regardless of the displacement rate.

It is obvious that more fracture events occur at lower loading rates. The span of the region where load drops occur is wider at higher rates compared to lower ones. This may be explained by the following mechanism: (1) when the loading rate is high enough, it is difficult to find favorable flaws for crack nuclei at low load in such a short time until the elastic stored energy is high enough, when an unfavorable flaw can act as the nucleus of a crack which leads to the failure of coating at higher load in the end; (2) Once a crack is generated, the high stored elastic energy imposes strong driving force for fracture propagation so that a significant drop of the loading rate occurs over a relatively big depth range. In contrast, it can be expected that a lower threshold load and many small fracture events will occur at lower loading rates.

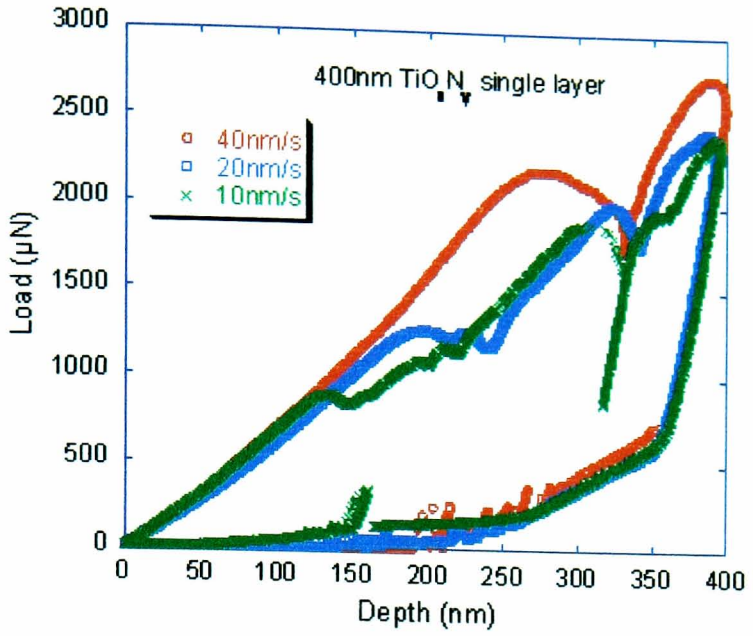

(a)

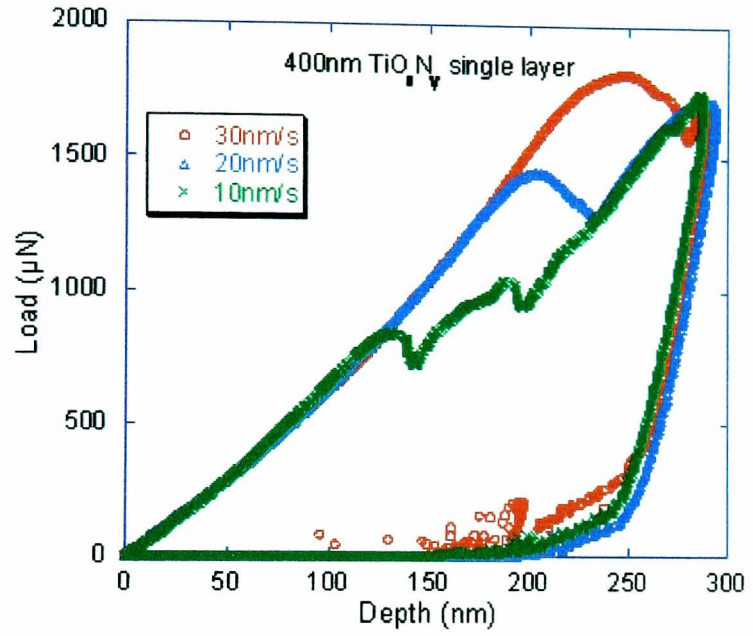

(b)

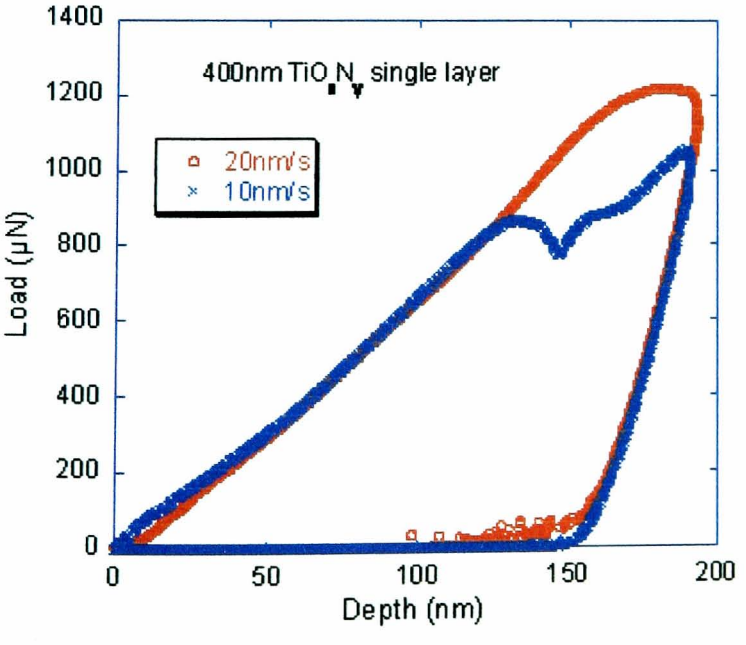

(c)

Fig. 9.1. Plot of load-displacement curves for a 400nm TiO_xN_y single layer on glass indented at different penetration rates to a range of maximum penetration depths: (a) 400nm; (b) 300nm; (c) 200nm.

9.3 *P-δ^2 analysis*

Although the loading curve may display load drops which are related to fracture behaviour when the brittle samples are indented by a sharp indenter under displacement control (e.g. Fig.9.2(a)), in some cases such obvious load drops do not occur during fracture events under the same indentation conditions (e.g. Fig. 9.2(b)).

In order to analyze the nanoindentation response of coated systems, Hainsworth *et al* (Hainsworth et al., 1996) proposed a plot of P/δ^2 vs. δ *(or* δ^2*)*. This analysis was based on the following relationship which was developed for a monolithic material indented by a geometrically self-similar indenter such as the conical or pyramidal tips used in this study,

$$P = E(\varphi\sqrt{\frac{H}{E}} + \phi\sqrt{\frac{E}{H}})^{-2}\delta^2 = K_m\delta^2 \qquad (9.1)$$

where E and H are the Young's modulus and the hardness, respectively. The constants $\varphi = 0.194$ and $\phi = 0.930$ were experimentally determined for a Berkovich indenter. Similar equation were derived for a perfect Berkovich tip elsewhere (Malzbender et al., 2000).

It was shown that P/δ^2 vs. δ (i.e. K_m) curve can be expected to identify the transition from coating-dominated deformation behaviour at low displacement (usually less than the coating thickness) to substrate-dominated deformation. But such model is not sensitive enough to detect fracture behaviour, therefore, it was further developed by McGurk and Page (McGurk and Page, 1999), i.e. a plot of $\partial P/\partial(\delta^2)$ vs. δ, known as K_{exp} curve. Analysis of the plot of $\partial P/\partial(\delta^2)$ vs. δ was found to work well for hard coatings on different steels. Fig. 9.3a displays the K_{exp} curve *of* 2.81μm NbN on stainless steel, from which it can be seen that three drops in the K_{exp} *curve* are visible when the penetration is bigger than 600nm. Such drops stop when they reach the baseline of the substrate steel. It can be expected that such events are related to through thickness fracture in the coated steel which has been verified by SEM

analysis (see Fig. 9.3b). Some spikes were also observed in the region between 250nm and 400nm which are caused by the imperfect geometry of the tip (McGurk and Page, 1999). However, this may not be the complete story, it could be related to the dislocation burst in substrate steel at the onset of substrate plastic deformation.

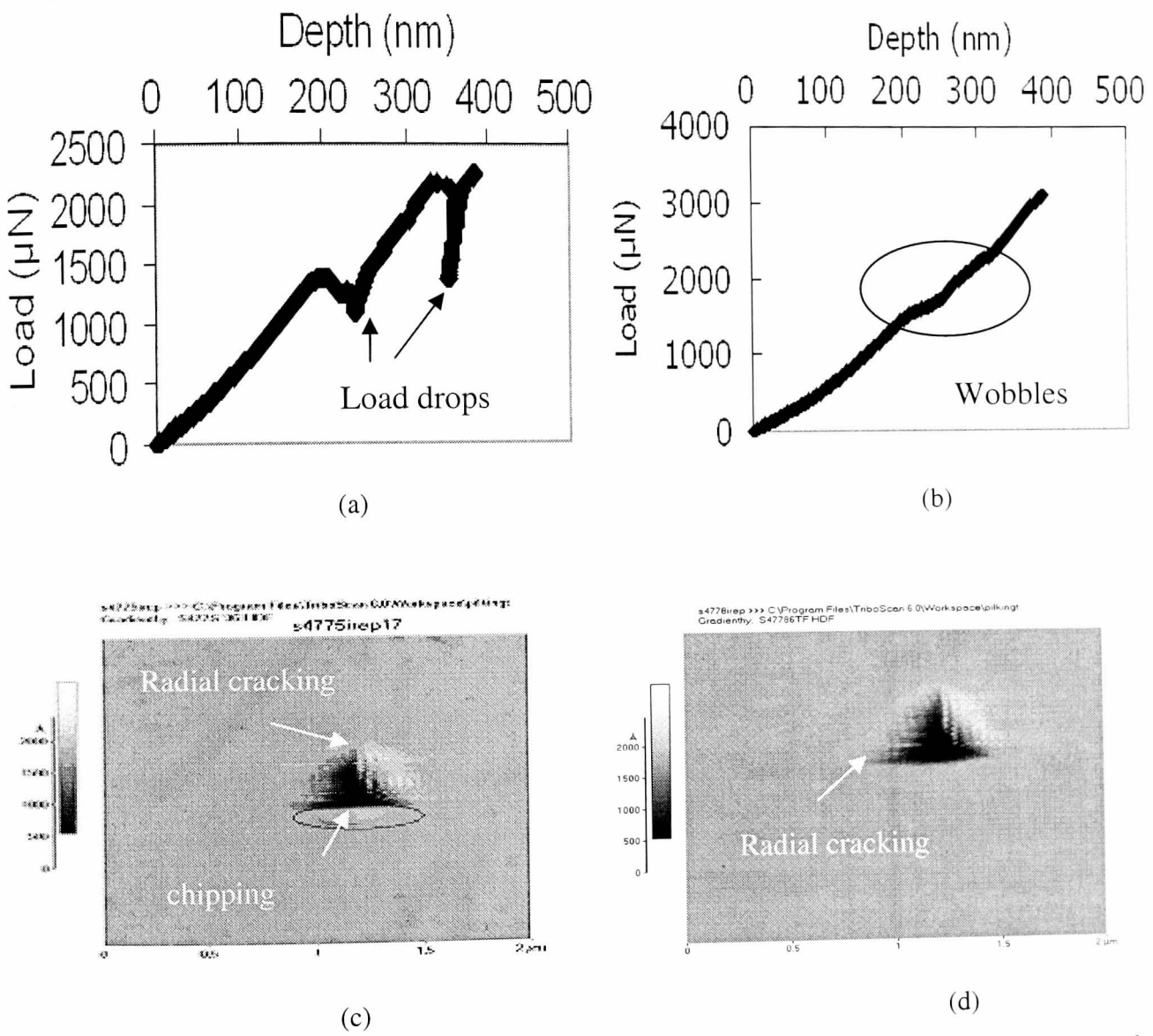

Fig. 9.2. (a-b) The loading curves and (c-d) AFM images of a 400nm TiO_xN_y single layer and a 400nm ZnO multilayer, respectively. Features in the load displacement curves are associated with fracture and delamination.

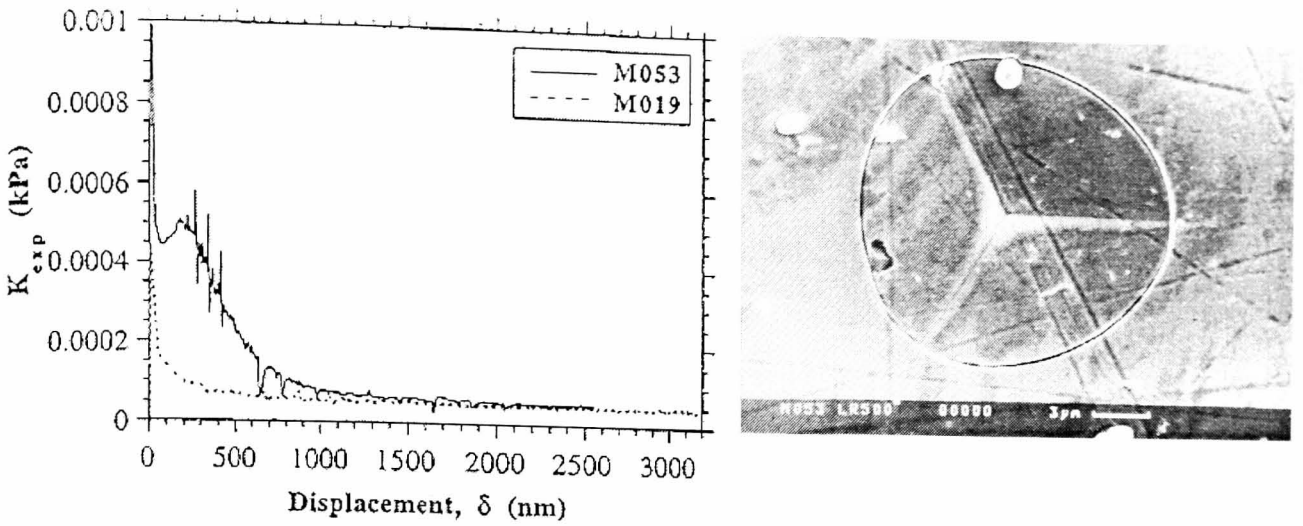

Fig. 9.3. (a) The K_{exp} curve and (b) SEM image for 2.81μm NbN on stainless steel.The solid line and dashed line correspond to the coated steel and substrate, respectively. After McGurk et al (McGurk and Page, 1999).

The method of analysing the K_{exp} curve does not work well for brittle coated systems because it leads to quite noisy curves. For example, when it is applied to sol-gel coating on glass (Malzbender and de With, 2000) and solar control coatings on glass (Bull et al., 2003, Berasategui, 2003) in Fig.9.4, the K_{exp} curve is too noisy to provide any useful information in both brittle coated systems. It is well known that acoustic events (AE) can be used to detect fracture initiation, rapid phase transformation, and dislocation bursts during static indentation [e.g. (Breval et al., 1995), (Belmonte et al., 2003), (Dyjak and Singh, 2006), (Rogers, 2005)]. For the TiO_xN_y coatings, no evidence of phase transformation occurs when indented by a relatively blunt Berkovich tip. Therefore, the AE events occurring after plastic deformation are likely to be due to the fracture initiation in these amorphous brittle coating systems. As displayed in Fig.9.4 (b), it is obvious that there are many more excursions in a plot of K_{exp} vs. δ than AE events and the correlation between them is poor.

In order to remove the noise influence, Malzbender et al (Malzbender and de With, 2001) suggested smoothing the data. However, it is difficult to choose a reasonable smoothing interval which can effectively remove the noise influence without changing the nature of loading curve and retaining the useful information. In fact, it is

found that any smoothing procedure will change the nature of the indentation response which is discussed in next section. Furthermore, Malzbender et al (Malzbender and de With, 2001) argued that the smoothed K_{exp} curve did not provide more information than the plot of P/δ^2 vs. δ in their sol-gel coatings. In addition, neither K_m nor *the derivative of* K_m always has a distinct physical meaning. For example, in the region where elastic deformation dominates or fracture influence is significant, the second order polynomial relationship between load and displacement in equation (9.1) becomes invalid so that K_m do not have any physical meaning and the resultant $\partial P / \partial(\delta^2)$ does not mean the change of K_m in a finite region.

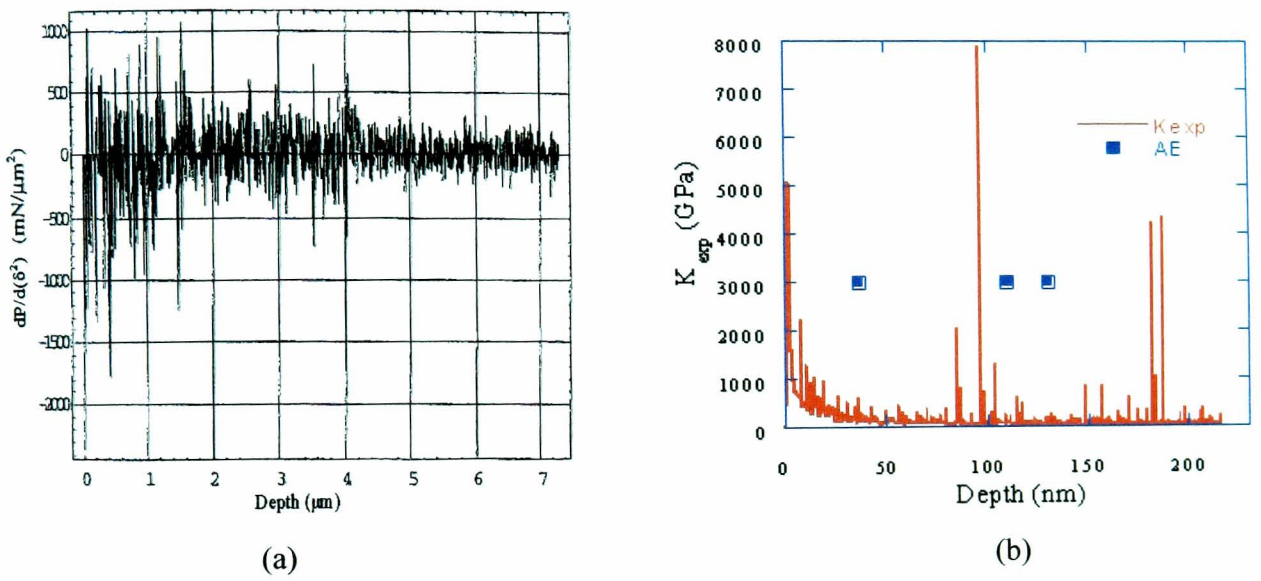

Fig. 9.4. The K_{exp} curve of (a) sol gel coatings on glass (Malzbender and de With, 2000) and (b) 200nm TiO_xN_y single layer on glass (Berasategui, 2003). The curves are quite noisy.

9.4. Instantaneous loading rate curve

To solve this problem,here it is suggested plotting the instantaneous loading rate curve, $\partial P / \partial t$ vs. δ to assess the fracture behaviour caused by nanoindentation in brittle coated systems. This method avoids the presence of a singularity and it is quite sensitive to the change of mechanical deformation during nanoindentation.

Figure 9.5 displays plots of $\partial P/\partial(\delta^2)$ vs. δ at different averaging levels (i.e. number of data points for the moving average) and a scatter plot of $\partial P/\partial(\delta^2)$ for a 240nm ITO cap layer multilayer stack on glass.

In Fig. 9.5 (a), the raw line plot of K_{exp} curve is very noisy from which is difficult to obtain useful information about fracture. Although the noise can be removed with a smoothing interval of 50 data points in Fig. 9.5(e), the K_{exp} curve after smoothing deviates from the initial one considerably. It is obvious that the second event is more significant than first one in the scatter plot (i.e. Fig.9.5 (f)), however, this phenomena has been reversed in the smoothed line plot Fig.9.5 (e). In Fig. 9.5(f), there is a smooth region between the first event and second event, whilst, the first event is immediately followed by second event in Fig.9.5 (e). In contrast, the plot of instantaneous loading rate provides good information without smoothing. It makes the events easier to be detected and it maintains all the initial information obtained during indentation.

It will also improve the sensitivity to detect fracture events during indentation (see Fig. 9.6). Figure 9.6 displays the comparisons of all the methods described above to detect events. In order to make them more readable, the K_m, K_{exp} and scatter plot of $\partial P/\partial(\delta^2)$ curves are plotted on a log scale (i.e. Fig. 9.6d, 9.6f, 9.6h). Although there are obvious events in the K_{exp} and scatter $\partial P/\partial(\delta^2)$ curves, it is difficult to reliably distinguish the fracture initiation point from them. However, it is much easier to find the fracture initiation point based on the events in the instantaneous loading rate curve. In addition, when making a plot in log scale, the non-positive data points have to be removed, which means that some useful information may be lost in the K_m , K_{exp} curves. From Fig. 9.6(b) we can see a significant drop in the loading rate in some regions or even negative loading rates. This may be due to slow crack growth in such brittle coatings which is not obvious in the in-situ AFM image due to its limited resolution. The negative values of K_{exp} in Fig.9.6 (a-f) make no physical sense, whilst, the loading rate decreasing to a negative value indicates the load drops which is likely to occur when cracks open in such brittle coated systems. The irregular shape of the AFM images (such as Fig. 9.2(c) and 9.2(d)) provides further evidence for fracture.

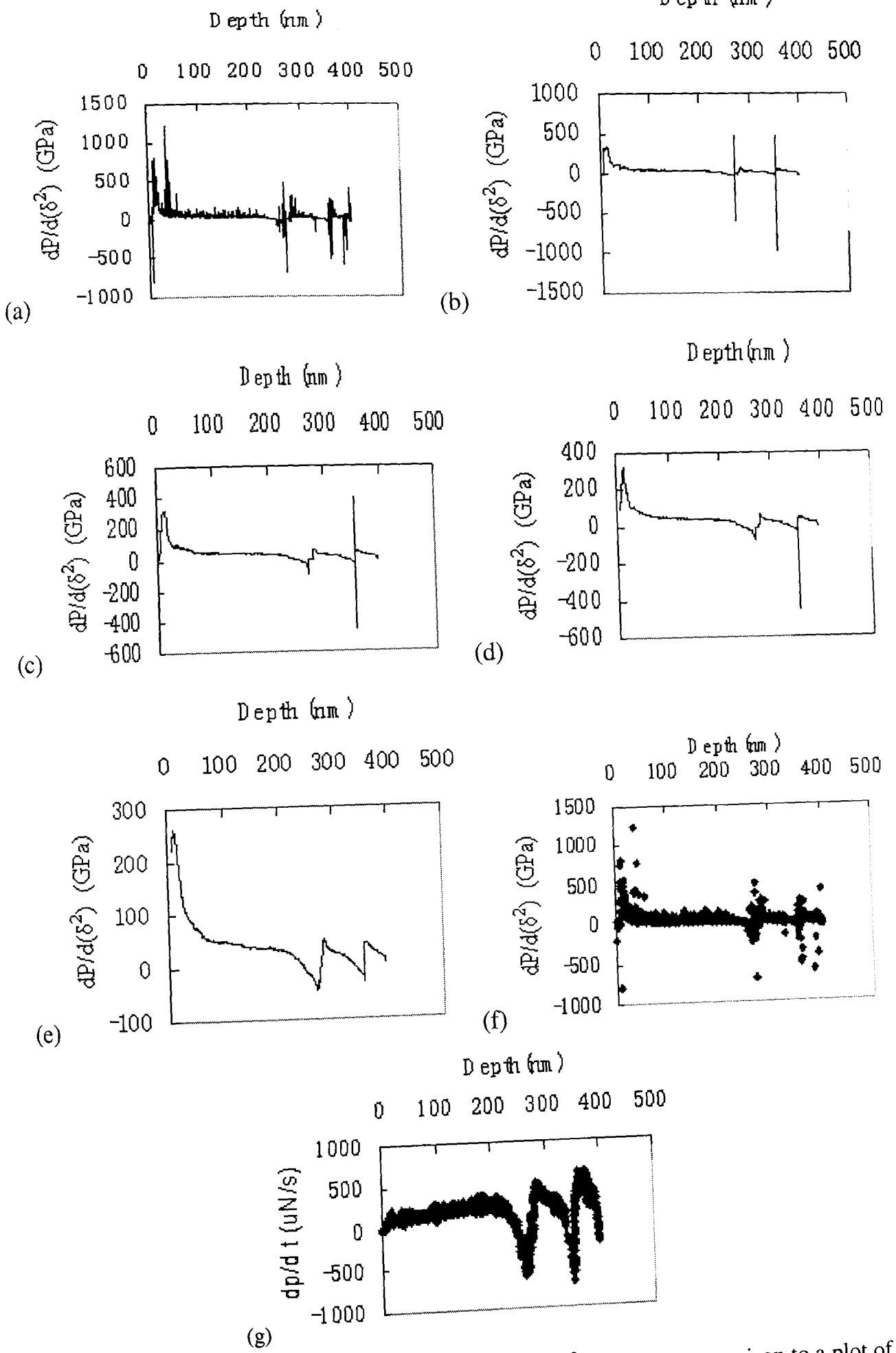

Fig.9.5. (a-e) Line plots and (f) a scatter plot of $\partial P / \partial(\delta^2)$ vs. δ, in comparison to a plot of (g) $\partial P / \partial t$ vs. δ for a 240nm ITO cap layer multilayer stack on glass. The various smoothing levels are (a) 0, (b) 10, (c) 20, (d) 30, (e) 50.

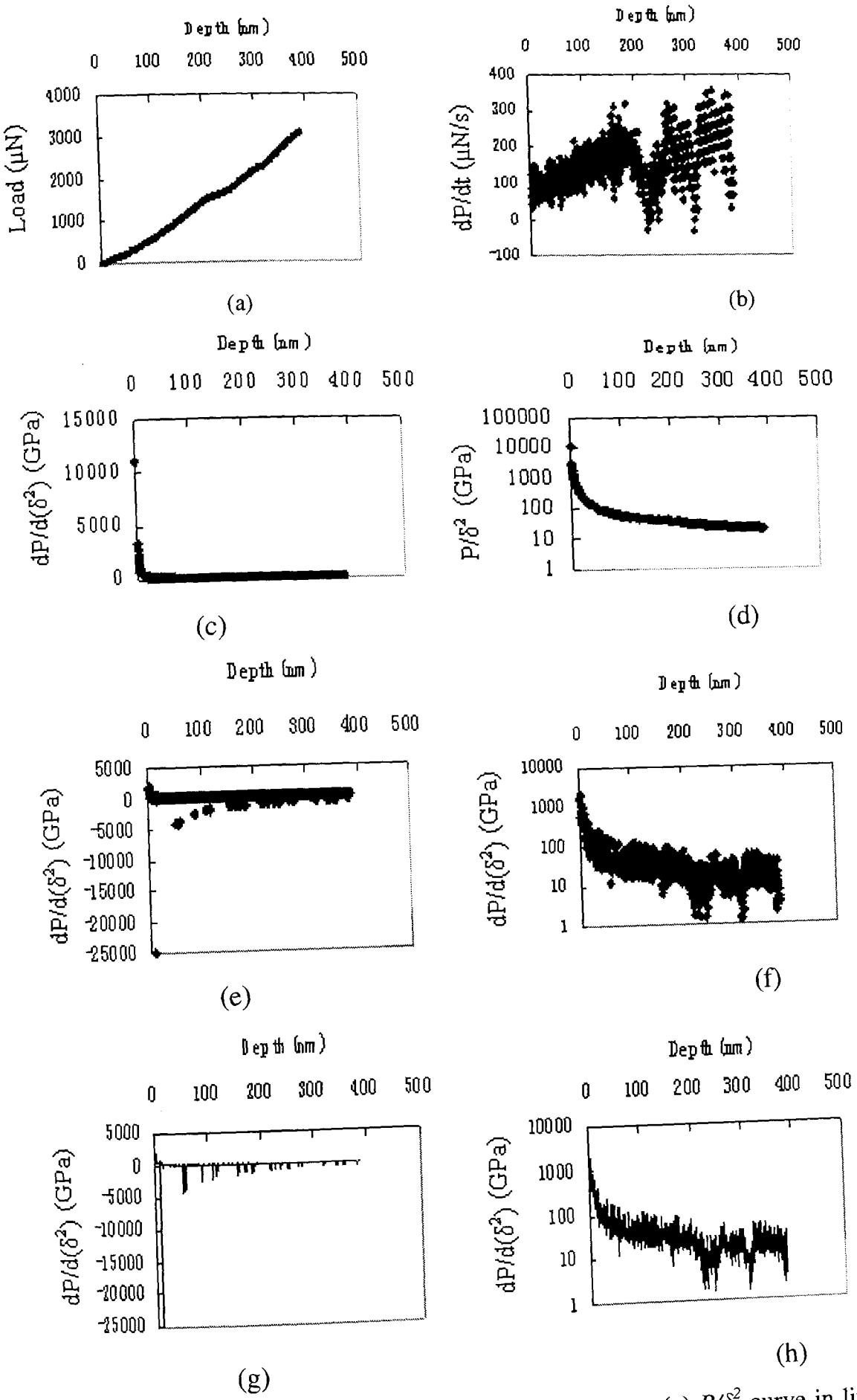

Fig. 9.6. Plots of (a) loading curve, (b) loading rate curve, (c) P/δ^2 curve in linear scale and (d) in log scale, (e) $\partial P/\partial(\delta^2)$ scatter plot in linear scale and (f) in log scale, (g) K_{exp} curve in linear scale and (h) in log scale for a 400nm ZnO cap layer multilayer stack on glass. The maximum control depth was set at 400nm.

The possible mechanisms for the loading rate drop can be described as follows. The change of loading rate could be due to the domination of plastic deformation and the transition from coating dominated behaviour to softer substrate dominated behaviour. If both coating and substrate are brittle, the decrease of loading rate may be an indicator for fracture initiation or propagation. When fracture behaviour plays a minor role in the total deformation, the loading rate drops but remains positive. If the fracture behaviour dominates, the loading rate will drop to a negative value, the indenter loses contact with the fracture surface briefly as the displacement control feedback loop tends to keep it out of contact by applying a retarding force against the system support spring.

General observations show that the loading rate recovers to the previous value when the fracture propagation stops, which may suggest that the substrate influence is important immediately before fracture. The trend that the loading rate almost remains at a constant level after the fracture event indicates that the deformation is dominated by substrate with only a small contribution from the coating at the high displacements where fracture occurs.

With the aid of the $\partial P / \partial t$ vs. δ method presented here, the fracture initiation point (FIP), i.e. the displacement at which fracture first occurs (which assumes it is strain controlled) can be easily determined (see Fig. 9.7(a)). In order to examine the validity of FIP obtained here for different samples (identified in Chapter 4,Table 4.1) it is useful to make comparison between the toughness values determined here and the results determined by different methods as shown in Chapter 5. In order to make them comparable, we convert them into relative toughness as shown in Fig.9.7(c) by normalising with results for uncoated glass. When converting FIP into relative toughness, it is assumed that the flaw distribution and critical flaw size is identical for all the samples. Furthermore, it is assumed that only radial cracking occurs in this study.

Table 9.1. Samples of the solar control coating stopped after each different layer in the multilayer stack with the final thickness increased to 400nm. N.B., this leads to spallation of the ITO so an extra sample was produced with a 240nm thickness top layer. Note the samples with the thicker cap layer are the emphasis of this study.

Sample 1: TiO_xN_y (400nm top layer) on substrate glass
Sample 2: TiO_xN_y / ZnO/ Ag/ ITO / SnO_2 /TiO_xN_y (400nm top layer) on substrate glass
Sample 3: TiO_xN_y / ZnO/ Ag/ ITO (240nm top layer) on substrate glass
Sample 4: TiO_xN_y / ZnO/ Ag/ ITO (400nm top layer) on substrate glass
Sample 5: TiO_xN_y / ZnO/ Ag/ ITO /SnO_2 (400nm top layer) on substrate glass
Sample 6: TiO_xN_y / ZnO (400nm top layer) on substrate glass

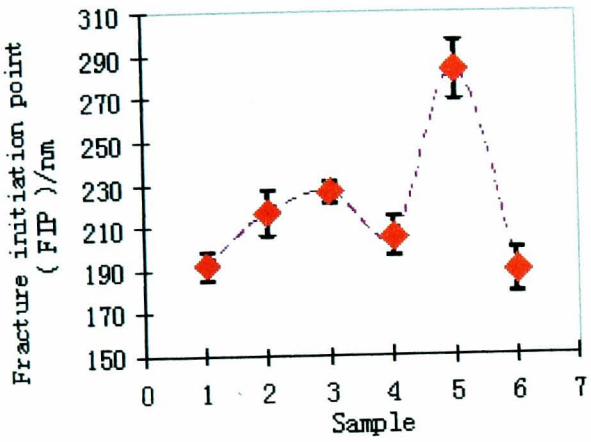

(a)

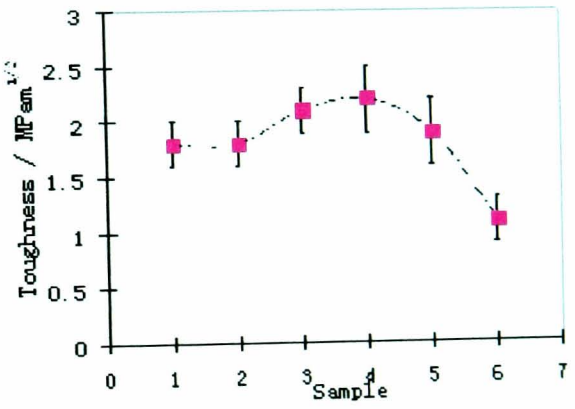

(b)

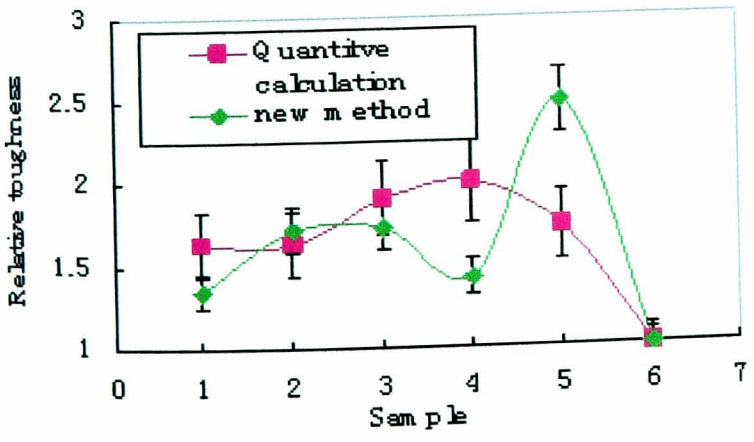

(c)

Fig. 9.7. Plots of (a) fracture initiation point as defined in this chapter, (b) toughness determined previously and (c) comparison between the relative toughness predicted by FIP in this chapter and previous results. All these data correspond to 20nm/s rate, 400nm maximum depth displacement control.

It can be seen that the results of relative toughness determined by FIP in this study and previous results agree well with each other except for sample 4 (i.e. with cap layer of ITO) and sample 5 (with cap layer of SnO_2) (see Table 9.1). This is because there is larger residual stress in these two samples, which was ignored in the calculations. In addition, the critical flaw size may vary significantly in these samples since it was shown there is some debris on the surface in sample 4 (i.e. 400nm ITO cap layer on glass) in a previous study.

9.5 Rate influence on maximum load achieved under displacement control

The displacement rate also has an impact on the overall indentation response thus influencing the maximum load achieved at a given displacement. For instance, it was found that a 400nm ITO multilayer stack on glass shows the lowest maximum load under the same displacement control conditions for all the samples. This is not surprising because the relatively thick ITO coating easily delaminates due to the high residual stress caused by the deposition process and the detachment occurs during the deposition cycle. In such a case, the indenter contacts the very thin films underneath (varying from 7nm to 20nm for individual layer) and the substrate glass dominates the response. Therefore, in this section the ITO coating refers to the 240nm ITO coating. Here, the focus is on the variation of the maximum load caused by different displacement rates.

Fig.9.8 shows the comparison of the load-displacement curves for different coatings at different displacement rates. The SnO_2 coating and ITO significantly differ from the other layers. Fig.9.9a displays the comparison between the maximum loads for different samples tested at different rates. It can be seen that in the case of the SnO_2 and ITO coatings only, the maximum loads at the highest rate rise considerably (by a factor of more than 20%), most noticeably for SnO_2 (where the increment is up to 35%), when the displacement rate increases from 20nm/s to 40nm/s. No significant

difference of peak load between displacement rates of 20nm/s and 10nm/s was observed for these samples. This is possibly due to the fact that no fracture occurs at the displacement rate of 40nm/s for these two samples, whilst, the presence of cracking significantly reduces the peak load by relaxing the indentation residual stress for the displacement rate of 20nm/s and 10nm/s. It is necessary to point out that such sensitive rate-dependent behaviour was not observed at lower loads in the case of the absence of fracture (i.e. $\leq$200nm in this study, see Fig. 9.9b), also it was not observed when testing using a Berkovich tip in which case no evidence of fracture was observed within the load limit of Hysitron Triboindenter. To further examine the phenomenon, nanoindentation tests at high loads (up to 500mN) were performed using the Nanoindenter II and the fracture was clearly observed by SEM, however, no events were observed in the load-displacement curves (see Chapter 7). This highlights the fact that the feedback control mechanisms for displacement control are different for the two machines and the instrumental response time is too slow for the older machine (Nanoindenter II).

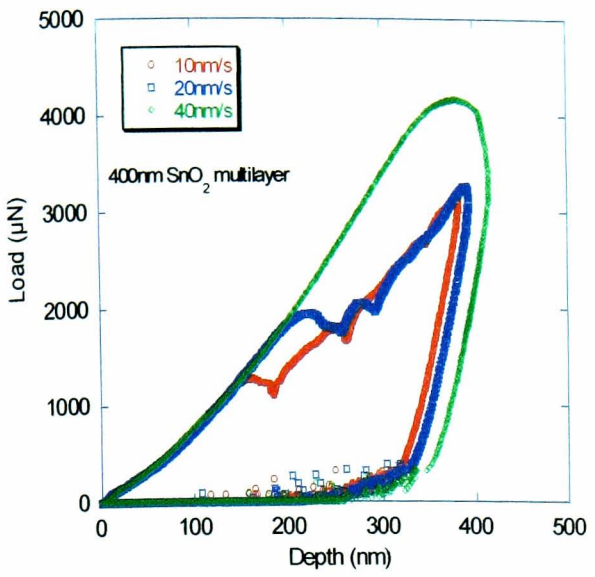

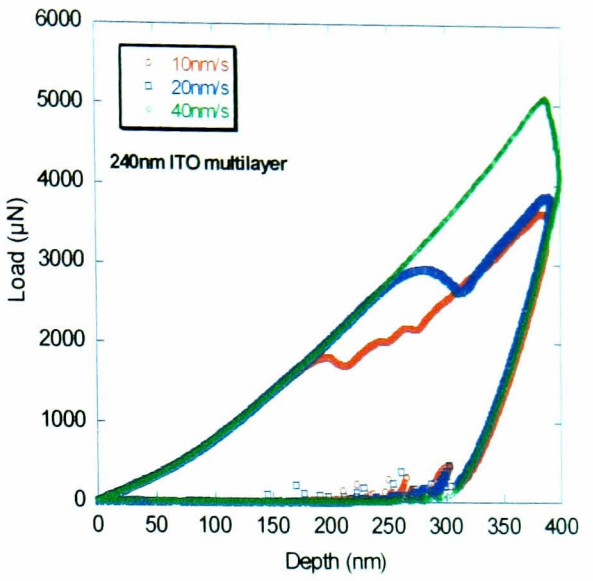

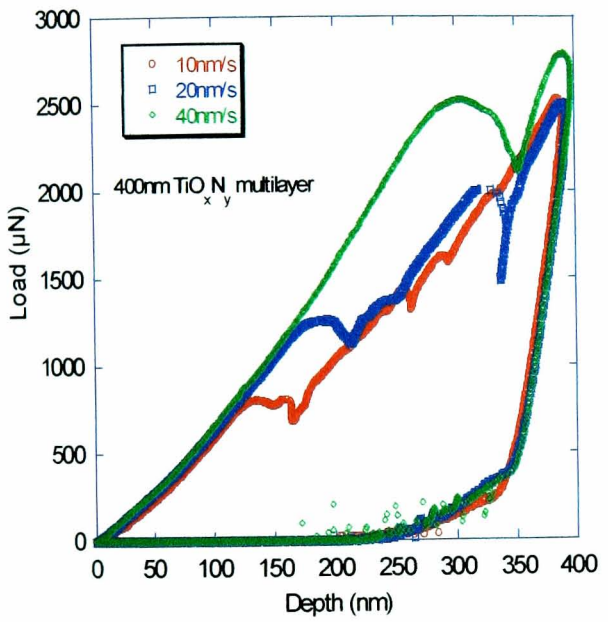

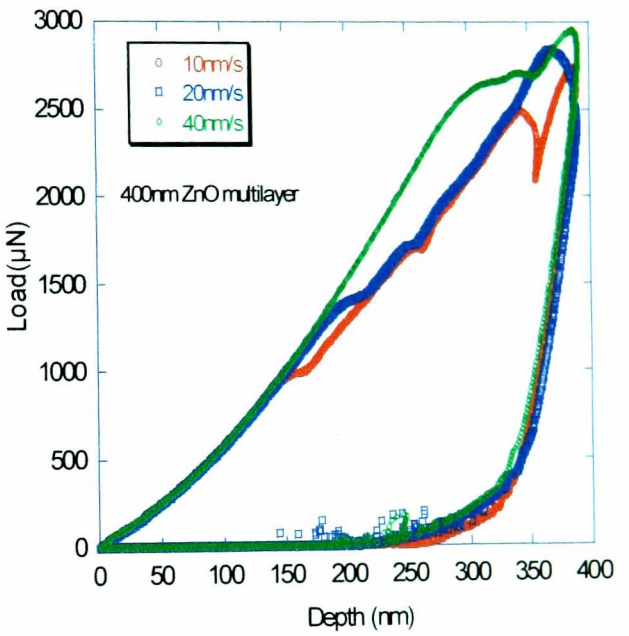

Fig.9.8. Comparisons of load-displacement curves at different loading rates for different coatings and glass.

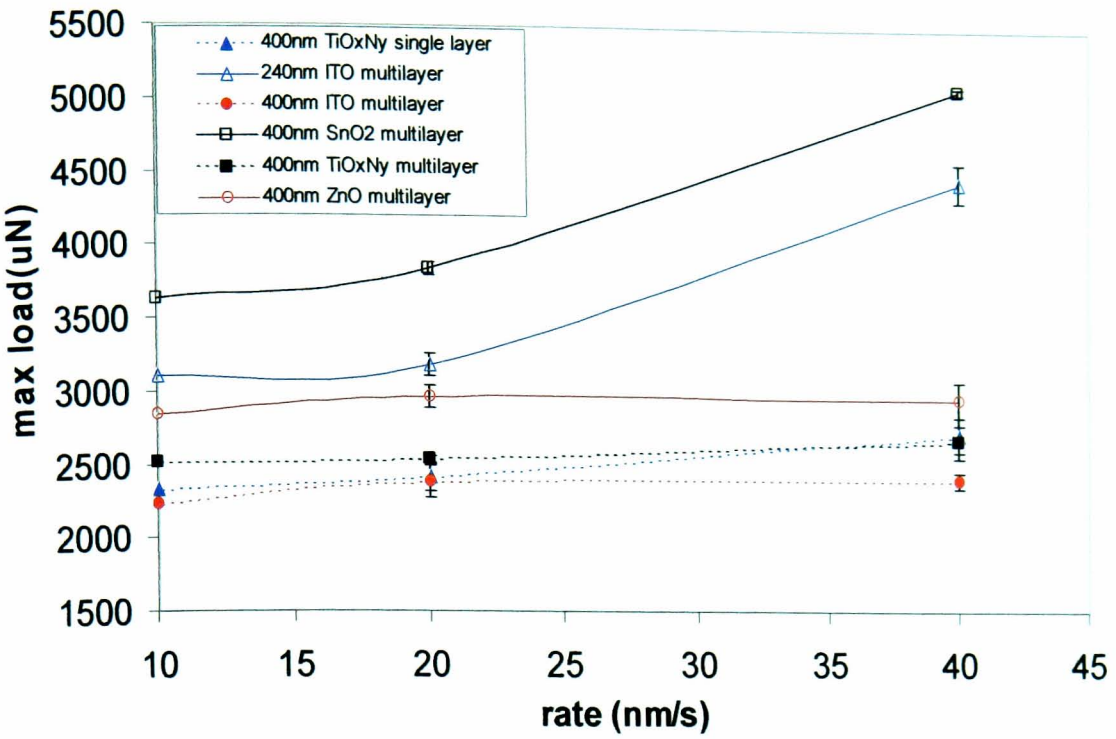

Fig.9.9 a The maximum load attained for different samples indented at different loading rate under 400nm displacement control.

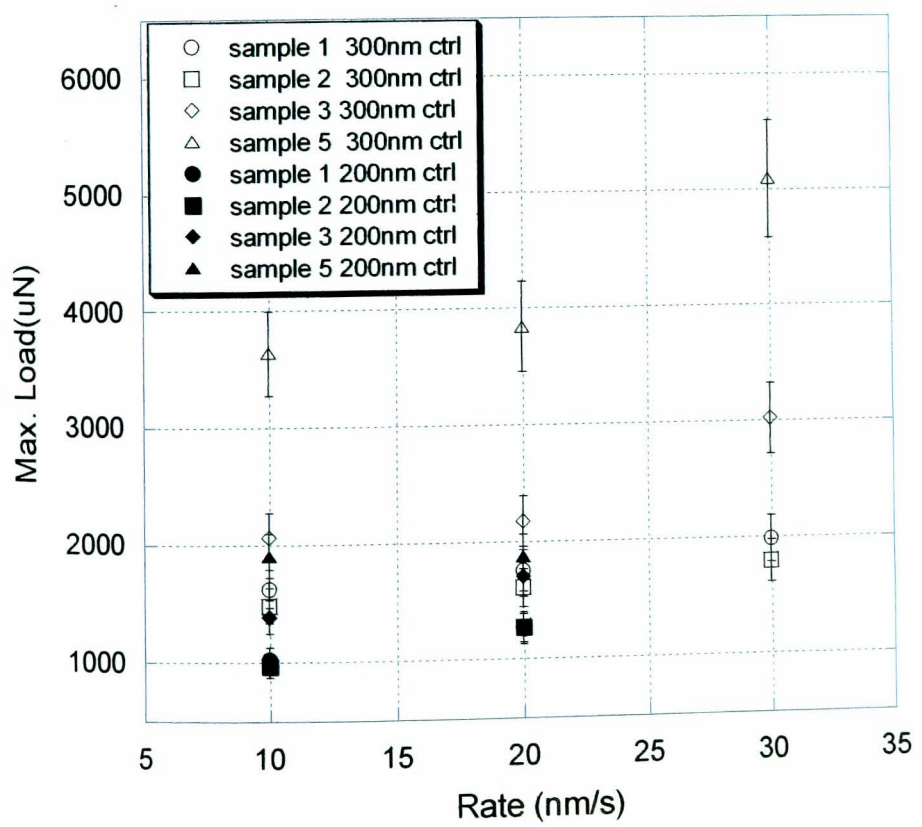

Fig. 9.9b. The comparison of maximum load versus loading rate for different samples at lower penetrations (<400nm). See sample description is Table 9.1.

Another mechanism was proposed for this sort of behaviour in thick thermal barrier coatings (~200μm), as it was found that the loading rate will influence the indentation response when inter-column sliding occurs (Guo and Kagawa, 2004). However, this mechanism is unlikely in thin coatings and most of the ones assessed in this study are amorphous and poorly columnar. Even if the inter-column sliding effect exists, due to the low coating thickness, its influence will be less significant than the substrate influence and can be ignored.

9.6 Possible mechanisms for the different behaviour of SnO_2 and ITO

This is the first observation of such enormous rate-dependent behaviour in tin oxide coatings during nanoindentation by a sharp cube corner tip. The fact that the behaviour of these coatings is almost independent of the displacement rate at low displacement where no fracture occurs indicates that the rate-dependent behaviour is actually associated with the fracture. Therefore, the different behaviour of the tin oxide must be related to differences in the fracture process, e.g. fracture propagation rate, environmental influences, or even phase transformation under very high pressure. Tin oxide has the lowest thermodynamic stability of all the oxide materials investigated here which implies that environmental effects (e.g. chemomechanical effects) could be significant but these have been shown to be small in these tin oxide based materials (Belde and Bull, 2006). Thus, phase transformation is probably the most likely explanation. Rate-dependent phase transformation has been found in silicon by (Juliano et al., 2003). In addition, for bulk Si, the phase transformation accompanies fracture (e.g. (Jang et al., 2004), (Baek et al., 2006), (Pharr, 2005)). It can be expected that similar behaviour will occur in the tin oxide coating reported here.

Tin oxide coatings sputtered on glass are generally amorphous structure and crystalline material (Warren, 2005, Wang et al., 2001), which may provide an

favourable situation for phase transformation under very high-pressure, e.g. amorphous to crystalline transition. As mentioned previously, such loading rate-dependent behaviour was not observed during the test by a relatively blunt Berkovich indenter (with the tip radius of ~250nm) which produces much lower stress at the same penetration. It is necessary to point out that the flaw state and its distribution is more critical for a cube corner indenter test since the contact area is much smaller compared to a Berkovich tip at a given penetration. A similar phenomenon but less significant was observed for ITO which was not surprising because ITO is indium doped tin oxide.

Natural tin oxide has the rutile structure and a new phase was found at 50GPa~74GPa during room temperature (RT) compaction (Shieh et al., 2005). The relatively open crystal structure can be easily densified. This high pressure cannot be produced underneath the tip during nanoindentation by a sharp cube corner tip with radius of about 40nm unless there is a large stress concentration at a defect. However, transformation from amorphous to crystalline SnO_2 could occur at a lower pressure, particularly if this is nucleated on pre-existing crystalline material. At high loading rate, it can be expected that there is competition between phase transformation, crack initiation and plastic deformation at the site of highest stress concentration. For the latter two, this requires a suitable pre-existing flaw or dislocations with reasonable mobility, which may not be achieved. However, for the phase transformation, the pre-existing mixture of amorphous and crystalline material in tin oxide makes it easier; in other words, it may lower the critical pressure for transformation. Pressure-induced phase transformation in bulk ceramics (such as Si, Ge) during indentation is not unusual and a well-known example is silicon in which the phase transformation (e.g. from Si-I to Si-II) can be observed at the pressure higher than 10GPa at room temperature (RT) (Jang et al., 2004). Estimates for the threshold pressure for phase transformation will be outlined in the following.

For bulk silicon, the phase transformation can be identified by in-situ XRD or Raman spectroscopy in a high pressure test (e.g. the diamond anvil,(Wiederhorn, 1974), (Domnich and Gogotsi, 2002)). The test conditions can be quasi-hydrostatic or nonhydrostatic. It is found that the application of nonhydrostatic stress (as under an indenter) can significantly lower the critical pressure for phase transformation

(Domnich and Gogotsi, 2002), (Hu et al., 1986). In addition to such experiments, the critical pressure can also be determined by theoretical simulations (e.g. simulations by *ab initio* methods (Yin and Cohen, 1982), (Yin and Cohen, 1980), (Chang and Cohen, 1985), (Needs and Martin, 1984), which was found to be in good accord with the different experimental results (Olijnyk et al., 1984), (Hu et al., 1986), (Domnich and Gogotsi, 2002). The critical values of pressure for phase transformation in Si-I~Si-II during compression is 9 to 16GPa as summarized in (Domnich and Gogotsi, 2002).

For thin films, the experimental methods and theoretical calculations which were used in bulk silicon become even more complicated. Therefore, in this section a simple estimation was made.

To model indentation plasticity, a model based on the expansion of a cavity was proposed by Johnson (Johnson, 1970), (Johnson, 1985) who assumed that the hemispherical core was incompressible. The mean pressure p_m is given by,

$$\frac{p_m}{Y} = \frac{2}{3}\left[1 + \ln\left(\frac{\frac{E}{Y}\cot\theta + 4(1-2\nu)}{6(1-\nu)}\right)\right] \tag{9.2}$$

Where Y and E are yield strength and Young's modulus, respectively, ν is Poisson's ratio and θ is the semi-apical angle of the indenter.

Johnson's model has been further developed by considering the hemispherical core as compressible and a term to account for the heat dissipated by plastic deformation is added (Tanaka, 1987),

$$\frac{p_m}{Y} = \frac{2}{3}\left[1 + \ln\left(\frac{\frac{E}{Y}\cot\varphi}{12(1-\nu)}\right)\right] + \alpha \qquad (9.3)$$

The value of the material constant α is given as 1/3 for ceramics and 1 for metals and polymers (Tanaka, 1987).

Actually, calculations using both equations above result in a mean pressure approximately equal to the hardness measured by nanoindentation. For example, for the tin oxide coating investigated here, the mean pressure is 11.7GPa by Eq. (9.2) and 14.6GPa by equation (9.3) close to its measured hardness of 14GPa.

By analysing the instantaneous load and its associated contact depth in combination with the analysis of contact depth and elastic flexure depth proposed by Oliver and Pharr (Oliver and Pharr, 1992), the critical pressure for phase transformation can also be estimated at a particular point on the load-displacement curve (Juliano et al., 2003). The stiffness was assumed to be the same as that under the maximum load, which is reasonable for bulk materials, whilst, for coated systems, it is necessary to perform additional tests with a peak load at the critical load for the phase transformation and its associated contact depth will be assumed to remain the same for the higher load tests. In this way, the critical pressure for the possible tin oxide phase transformation is about 10.3GPa. There is good agreement for the phase transformation pressure from the different methods. In addition to the pre-existing mixed phase, the relatively high shear stress within coating under the test conditions in indentation may also lower the critical pressure for phase transformation as mentioned previously.

The displacement rate of 20nm/s in the tests reported here seems to be a critical rate for SnO_2 within the range of test conditions in this study, since beyond it, the presence of fracture is significantly reduced thus resulting in the much higher apparent maximum load; below it, the maximum load does not change much although the presence of fracture is advanced. Rate dependent phase transformation was also

observed in Silicon (Juliano et al., 2003). For instance, it was shown that the Si-III to Si-XII transition occurs during slower unloading rate resulting in a pop-out in the load-displacement curve whereas α-Si forms at higher unloading rates showing an elbow or curvature change in the unloading curve. Usually, the higher the unloading rate, the lower the average pressure for a pop-out during unloading. The chance for amorphous silicon formation during unloading is increased at higher unloading rate (Juliano et al., 2003).

The reason that the other coatings do not display such phenomena may be due to the fact that their critical loading rate is outside the rate range used here. It is unlikely to be accounted by the different mechanical properties of the coatings because the mechanical properties of these coatings such as Young's modulus, hardness and toughness are similar. Possible phase changes might also be expected for TiO_2 coatings but the pressure of nitrogen in them increases their density and stability. The ZnO coating is most crystalline among the materials studied here and has a dense crystal structure where phase changes are unlikely. Thus it is the stress-induced phase transformation in SnO_2 and ITO that is more likely to lead to the difference from the rest of the coatings. No results have been reported with respect to effect of loading rate on phase transformation for Si so far. It can be expected that such rate–dependent phase transformation may occur during the loading cycle as well. The problem is that it is difficult to verify by experimental methods. In-situ Raman spectra or in-situ TEM are required for this.

9.7 Summary

Different techniques and analyses were adopted in this study in order to assess the loading rate influence on the nanoindentation response of brittle thin films on a hard substrate in the presence of fracture. It was found that the loading rate changes the load-displacement curve and fracture initiation point. It is very interesting to note that SnO_2 and ITO coating display quite different behaviour compared to the other coatings; at a given depth (i.e. 400nm in which case evidence of fracture was observed for all the coatings discussed in this study) the maximum load was found to

increase dramatically when the displacement rate increases from 20nm/s to 40nm/s, which was neither observed for the other coatings nor in test conditions where fracture was absent. The possible mechanisms to account for such abnormal behaviour for these two coatings were discussed. As suggested for silicon (Juliano, Gogotsi et al.), phase transformation during indentation is the most likely explanation but there is no direct evidence of phase transformation by microscopy. The contact geometry was also found to influence the phase transformation in Ge and Si (Jang et al., 2005). It was also shown that the cube corner tip is a better choice for promoting phase transformations (Jang et al., 2005) as was observed in this study.

This is the first report of the possibility of phase transformation in tin oxide coatings under indentation. Also it is the first report of the rate-dependence of the possible phase transformation during the loading cycle. This observation may be extended to Si and similar materials. In-situ TEM or in-situ Raman spectra is required to confirm that the rate-dependent behaviour under high pressure during nanoindentation is related to phase transformation.

References:

Baek, S., Koo, J. M. and Seok, C. S. (2006) In *Fracture and Strength of Solids Vi, Pts 1 and 2*, Vol. 306-308, pp. 601-605.

Belde, K. J. and Bull, S. J. (2006) Chemomechanical effects in optical coating systems,*Surface & Coatings Technology*, in press.

Belmonte, M., Fernandes, A. J. S., Costa, F. M., Oliveira, F. J. and Silva, R. F. (2003) Acoustic emission detection of macro-indentation cracking of diamond coated silicon,*Diamond and Related Materials,* **12,** 1744-1749.

Berasategui, E. G. (2003) Determining the mechanical properties of thin coated systems by nanoindentation,University of Newcastle Upon Tyne

Breval, E., Srikanth, V. and Subbarao, E. C. (1995) Acoustic-Emission and Microcracking in Sapphire, Sintered Al2o3, Al/Al2o3 Composite, and Aluminum,*Journal of the American Ceramic Society,* **78,** 2541-2544.

Bull, S. J., Arce-Garcias , I., G-Berasategui, R. E. and Page, T. F.2003Indentation fracture ,acoustic emission and modelling of the mechanical properties of thin ceramics coatingsHouston,TXpp21-42

Chang, K. L. and Cohen, M. L. (1985) Solid-solid phase transitions and soft phonon modes in highly condensed Si,*Phys. Rev.B,* **31,** 7819-7826.

Domnich, V. and Gogotsi, Y. (2002) Phase transformationations in Silicon under contact loading,*Rev. Adv.Mater. Sci.,* **3,** 1-36.

Dyjak, P. and Singh, R. P. (2006) Acoustic emission analysis of nanoindentation-induced fracture events,*Experimental Mechanics,* **46,** 333-345.

Guo, S. Q. and Kagawa, Y. (2004) Effect of loading rate and holding time on hardness and Young's modulus of EB-PVD thermal barrier coating,*Surface & Coatings Technology,* **182,** 92-100.

Hainsworth, S. V., Chandler, H. W. and Page, T. F. (1996) Analysis of nanoindentation load-displacement loading curves,*Journal of Materials Research,* **11,** 1987-1995.

Hu, J. Z., Merkle, L. D., Menoni, C. S. and I.L, S. (1986) Crystal data for high-pressure phase of silicon,*Phys. Rev.B,* **34,** 4679-4684.

Jang, J., Wen, S., Lance, M. I., Anderson, I. M. and Pharr, G. M.2004Cracking and Phase transformation in Silicon during nanoindentationBoston,MA

Jang, J. I., Lance, M. J., Wen, S. Q. and Pharr, G. M. (2005) Evidence for nanoindentation-induced phase transformations in germanium,*Applied Physics Letters,* **86**.

Johnson, K. L. (1970) Correlation of Indentation Experiments,*Journal of the Mechanics and Physics of Solids,* **18,** 115.

Johnson, K. L. (1985) *Contact Mechanics,* Cambridge University Press, Cambridge.

Juliano, T., Gogotsi, Y. and Domnich, V. (2003) Effect of indentation unloading conditions on phase transformation induced events in silicon,*Journal of Materials Research,* **18,** 1192-1201.

Lee, C. S., Kim, D. K., Sanchez, J., Miranda, P., Pajares, A. and Lawn, B. R. (2002) Rate effects in critical loads for radial cracking in ceramic coatings,*Journal of the American Ceramic Society,* **85,** 2019-2024.

Malzbender, J. and de With, G. (2000) The use of the loading curve to assess soft coatings,*Surface & Coatings Technology,* **127,** 266-273.

Malzbender, J., de With, G. and den Toonder, J. (2000) The P-h(2) relationship in indentation,*Journal of Materials Research,* **15,** 1209-1212.

Malzbender, J. and de With, G. (2001) The use of the loading curve to assess soft coatings (vol, 127, pg 266, 2000),*Surface & Coatings Technology,* **138,** 111-111.

McGurk, M. R. and Page, T. F. (1999) Using the P-delta(2) analysis to deconvolute the nanoindentation response of hard-coated systems,*Journal of Materials Research,* **14,** 2283-2295.

Needs, R. and Martin, R. M. (1984) Transition from ß-tin to simple hexagonal silicon under pressure,*Phys. Rev.B,* **30,** 5390-5392.

Olijnyk, H., Sikka, S. K. and Holzapfel, W. B. (1984) Structural Phase Transition in Si and Ge Under Pressures up to 50 GPa,*Phys.Lett.,* **103A**.

Oliver, W. C. and Pharr, G. M. (1992) An Improved Technique for Determining Hardness and Elastic Modulus Using Load and Displacement Sensing Indentation Experiments,*Journal of Materials Research,* **7,** 1564-1583.

Pharr, G. M. (2005), Private communication

Rogers, L. M. (2005) In *Damage Assessment of Structures Vi*, Vol. 293-294 TRANS TECH PUBLICATIONS LTD, Zurich-Uetikon, pp. 33-45.

Shieh, S. R., Kubo, A., Duffy, T., Prakapenka, and Shen, G. (2005) High-pressure phase transition in SnO2 to 117 GPa: Implications for silica; Mineral and rock Physics meeting 2005,,*www.agu.org/meetings/fm05/fm05-sessions/fm05_MR33B.html*.

Tanaka, K. (1987) Elastic Plastic Indentation Hardness and Indentation Fracture-Toughness - the Inclusion Core Model,*Journal of Materials Science,* **22,** 1501-1508.

Wang, T. G., Stahley, M. E., Pantano, C. G., Yang, D. H., Anderson, T. and Kuhn, L.2001Nanoindentation and Nanowear Studies of Sputter-Deposited Ultrathin Tin Oxide Films on Glass SubstratesBostonL.3.6.1

Warren, P. (2005), Private communication

Wiederhorn, S. M. (Ed.) (1974) *Subcritical crack growth in ceramics,* Plenum, New York,.

Yin, M. T. and Cohen, M. L. (1980) Microscopic Theory of the Phase-Transformation and Lattice-Dynamics of Si,*Physical Review Letters,* **45,** 1004-1007.

Yin, M. T. and Cohen, M. L. (1982) Theory of static structural properties, crystal stability, and phase transformations: Application to Si and Ge,*Phys. Rev.B,* **26,** 5668-5687.

Chapter 10:

Conclusions and Further work

Chapter 10: Conclusions and Further work

10.1 Conclusions

Firstly, a new energy-based model (W_t-dp method) to estimate coating toughness was developed based on the ld-dp method by Li et al, which has been successfully applied to predict the toughness of various thin coatings (such as SnO_2, ITO, TiO_xN_y etc) on soda-lime glass indented by a sharp cube corner tip. This model was also validated by experiments on different coated systems such as CN_x on silicon, sapphire, SiC and other coatings reported in literature. Compared to the ld-dp method, the W_t-dp method was found to provide more reliable results. The analysis predicts that the ld-dp method will overestimate the coating toughness for a typical coated system with a hard coating on a softer substrate and underestimate the coating toughness for a typical coated system with a softer coating on a hard substrate. This argument was confirmed by both experimental results and mathematical analysis. The analysis demonstrates that the W_t-dp method developed here can separate the energy dissipated in other deformation mechanisms from the fracture dissipated energy which has not been achieved by previous energy-based models.

In many cases, with regard to safe design, it is very useful to know the limiting value of the coating toughness. An initial boundary model was proposed by Toonder et al which gives precise formulae to achieve this goal. However, it was found that the assumptions in this model conflict with each other and they considerably deviate from realistic conditions. Therefore, the model was further developed in this work using assumptions that are more reasonable representations of the actual situation. Further, the initial boundary model gives upper and lower boundary of coating toughness for nanoindentation tests under load control, whilst, it only gives the upper boundary of coating toughness for nanoindentation tests under displacement control. In contrast,

the new boundary model can be equally applied to nanoindentation performed under load control and displacement control. The results demonstrate that the modified model proposed here is more reasonable than the initial boundary model.

Most energy based models including the two models developed in this study require an excursion in the nanoindentation load-displacement curve, whilst, the conventional indentation model developed by Anstis et al can only deal with well-developed radial /median crack systems. However, with the increasing complexity of coated systems, the radial /median crack system may not occur in the coating. Also, it is not unusual that the crack does not lead to an excursion in the load-displacement curve. Therefore, the previous models become invalid and a new method is required. A new method based on analysis of picture-frame cracking in coated glasses produced by a Berkovich indenter at higher loads and the difference in the calculated and measured irreversible work was advanced to address this problem. Reasonable results were obtained and they agree well with the results determined by different methods reported in the literature. The model was also successfully applied to deal with the radial cracks in bulk materials such as silicon, SiC etc, and gave reasonable results compared to values in the literature obtained using different methods.

The failure of a coated system is not only caused by coating toughness, it may also be caused by interfacial failure or substrate failure. In some cases, the delamination of coating may cause extra linear elastic recovery in the unloading curve. An attempt to estimate the interfacial toughness based on such observations was made by Hainsworth et al, however, a significant overestimation was found for both hard coatings on soft substrates (e.g. nitride coatings on steel) and hard coatings on a hard substrate (e.g. oxides on glass). An alternative method was suggested here which provides more reasonable results for different types of coated systems.

An advantage of the energy-based models is that no empirical parameters are required. However, a measurement of the area of cracking is necessary which can be difficult to achieve as the crack systems become smaller and more complex.

In addition to the fracture toughness of a coating or interface, other information about the fracture mechanism such as the fracture initiation point (FIP) or the loading rate influence on fracture behaviour during nanoindentation is also very important. Different techniques were applied to analyse the FIP in coated glass. The previous techniques were demonstrated to work well for hard coatings on a soft substrate but they cannot deal with brittle coatings on a brittle substrate. Thus, the plot of instantaneous loading rate against displacement was proposed to identify the FIP which turns out to be very efficient and easy to apply compared to the other methods. In addition, it can be used to find rate-dependent fracture behaviour in these ceramic coatings on glass. For all the coatings, within the displacement rate range used in this study, it was found that the higher displacement rate the higher the FIP. Also, at lower loading rates, the events in the load-displacement curves are relatively small but large in quantity which is due to slow crack growth in these coatings at low testing rates. When analysing the maximum load achieved at the same displacement but different displacement rates, it was found that the maximum load increases dramatically in SnO_2, when the displacement rate rises from 20nm/s to 40nm/s. Although the increase of the displacement rate will significantly delay the presence of fracture, the maximum loads do not change much for the rest of coatings. The possible reasons to account for this phenomenon were discussed, among which phase transformation under the high pressure associated with indentation was most likely. The critical pressure for the phase transformation was estimated by different methods and good agreement was achieved between them.

10.2. Further work

The energy based models presented here have been successfully applied to different crack patterns in different types of coated systems. With regard to the ultra small cracks caused by a cube corner indenter at low loads (<5mN), no evidence of the exact crack morphology was observed, thus more advanced microscopy techniques are required such as in-situ Transimission electronic microscopy (TEM) because it is

almost impossible to locate such small indentations under off-line SEM, AFM and TEM. SEM and AFM may not be able to investigate the exact crack morphology in many cases. Also, to assess the possible phase transformations in an ultra small volume under the indenter, in-situ TEM is necessary because Raman spectra are not sufficiently sensitive for such amorphous or semi-crystalline coatings in this work.

In order to further the understanding of the fracture mechanisms during indentation, it is valuable to know the size effect on fracture behaviour. The following questions will be very interesting. Will the coating thickness influence the fracture toughness and how? Will the coating thickness influence the fracture initiation point and how? How does the coating thickness affect the interface? Will the contact scale matter and how? There is some evidence that, as the contact scale is reduced, the apparent mechanical properties change and the deformation mechanism in very fine grained nanomaterials are considerably different from those in the bulk. Conventional continuum mechanics may no longer apply and even plasticity models based on dislocation dynamics will be invalid since the scale of the material microstructure is smaller than the dislocation core size. Under such condition, diffusion and other time-dependent processes will be significant.

In order to cope with these questions, multiscale modelling which combines finite element simulations and molecular dynamics is required to be carried out in the following few years.

With regard to the bound model, the future work is to perform nanoindentation tests to obtain the actual unloading curve at the excursion start point and excursion end point so that the upper bound of the fracture toughness can be obtained. Also work to obtain the reasonable lower bound of fracture toughness will be carried on.

The long term goal of exploring the fracture behaviour of complex coatings is to guide the design of new coatings and reduce the possibility of the failure of the

coating in service. The provision of reliable design data and predictive performance models for brittle coatings is made possible by the preliminary work in this thesis.

Appendix : Application of W_t-dp method in the case of an excursion associated with fracture in a purely linear elastic system in indentation

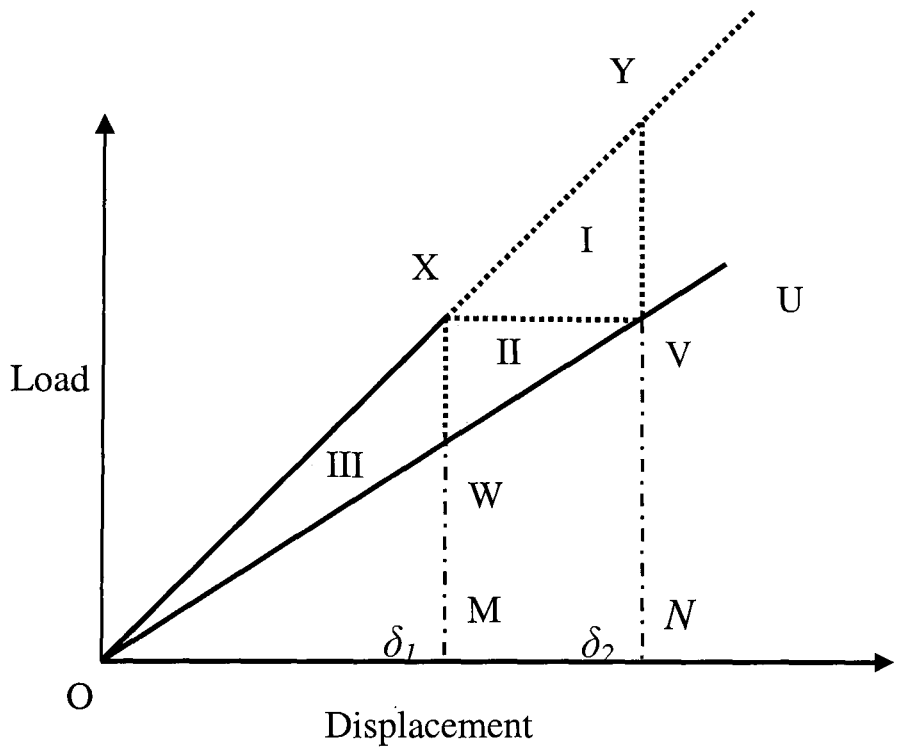

Fig. a. Schematic of excursion associated with fracture in a purely linear elastic system. It is assumed that the loading curve OX and the unloading curve UV are purely linear elastic in indentation.

Considering the simpliest condition, i.e. linear elastic, before an excursion and after an excursion (i.e. $P = k_1\delta$, $P = k_2\delta$) , then it can be expected that the area OXVO will be the upper bound of the fracture dissipated energy (if ignoring the heat or other factors, it will be fracture dissipated energy).

Now applying the W_t-dp method, the energy expenditure for fracture will be the area XYVMX. The area XYV is obtained by the first extrapolating process. If we consider the Point V as the reference point, the area of VXW will be the work difference obtained by second extrapolation.

At Point V, the total work difference between Point X and V is the area XVNM, while the total work difference between Point W and V is the area WVNM. Thus the work difference between Point X and Point W should be area XVW.

Applying the W_t-dp method, the fracture dissipated energy will be the sum of the area XYV and the area XVW (i.e. the area XYVW).

For convenience, we denote the areas XYV, XVW, and OXW as areas I, II, III as depicted in Fig. a. Also, we denote that $\delta_2/\ \delta_1=\lambda$, thus $k_1/\ k_2=\lambda$.

It is obvious that,

$$\frac{\mathrm{I}+\mathrm{II}}{\mathrm{II}}=\frac{(k_1-k_2)\delta_2+(k_1-k_2)\delta_1}{(k_1-k_2)\delta_1}=\frac{\delta_2}{\delta_1}+1=\lambda+1 \tag{A.1}$$

$$\frac{\mathrm{III}+\mathrm{II}}{\mathrm{II}}=\frac{k_1\delta_1}{(k_1-k_2)\delta_1}=\frac{k_1}{(k_1-k_2)}=\frac{\lambda}{\lambda-1} \tag{A.2}$$

$$\frac{\mathrm{I}+\mathrm{II}}{\mathrm{III}+\mathrm{II}}=\frac{(\lambda+1)(\lambda-1)}{\lambda} \tag{A.3}$$

It is then easy to obtain,

$$\begin{cases} \dfrac{\mathrm{I}+\mathrm{II}}{\mathrm{III}+\mathrm{II}} \geq 1, \lambda \geq \dfrac{1+\sqrt{5}}{2} \\ \dfrac{\mathrm{I}+\mathrm{II}}{\mathrm{III}+\mathrm{II}} < 1, 1 < \lambda < \dfrac{1+\sqrt{5}}{2} \end{cases} \tag{A.4}$$

Therefore, for a simple linear elastic system, the ratio of the fracture dissipated energy based on W_t-dp method proposed in Chapter 5 over the upper bound of the fracture dissipated energy as argued in chapter 6 is dependent of how big is the excursion in the load-displacement curve compared to indentation depth (i.e. the ratio of depth of the excursion start point and the excursion end point.)

In reality, the ratio of depth of excursion start point and excursion end point is seldom bigger than 1.62. For an elastic system, the excursion is usually very small compared to the depth where excursion occurs so that the λ is close to 1, in which case, the fracture dissipated energy determined by W_t-dp is always less than the upper bound and is reasonably close to it.